Analytic study of intrinsic flame and coupled intrinsic-acoustic instabilities in combustor models

by

Nalini Kanta Mukherjee

Submitted in accordance with the requirements for the degree of

Doctor of Philosophy

Keele University

School of Computing and Mathematics

June 2017

Acknowledgment

Abstract

The study is concerned with theoretical examination of thermo-acoustic instabilities in combustors and focuses on recently discovered flame intrinsic modes. These modes differ qualitatively from the thoroughly studied acoustic modes in a combustor. Despite being intensely studied, primarily numerically and experimentally, their properties remain poorly understood. Here an analytical investigation produced a comprehensive picture of the properties of linear intrinsic modes within the framework of a one-dimensional model of closed-open and open-open combustors with temperature and cross-section jump across the flame, and a linear $n - \tau$ law of heat release, where n is interaction index and τ is the time lag. It has been shown there is always an infinite number of intrinsic modes present. In the limit of small n the frequencies of these modes depend neither on the properties of the combustor nor on the position of the flame. For small n these modes are strongly damped and they become unstable only if n exceeds a certain threshold. Remarkably, on the neutral curve the intrinsic modes become completely decoupled from the environment. The main results of the study follow from the discovered decoupling on the neutral curve and include explicit analytic expressions for the exact neutral curve on the $n - \tau$ plane, and for the growth/decay rate dependence on the parameters of the combustor. A new type of thermo-acoustic instability has been discovered. The instability occurs out due to coupling between intrinsic and conventional acoustic modes. Unstable or weakly decaying

coupled acoustic modes behave exactly like an intrinsic mode, which increases the possible number of unstable intrinsic modes. The overall picture of intrinsic mode instabilities found for ideal boundary conditions has been shown to be robust with respect to modifications of the end boundary conditions. The explicit corrections to the position of the neutral curve and growth/decay rate have been found. The analytical results have been verified by numerics.

Contents

4.   Flame intrinsic instability for combustors with open-open end

conditions…………………………………………….....................184

x

Abbreviations

FTF: Flame Transfer Function

B.I.: Born Intrinsic

B.A.: Born Acoustic

Notations

x : Axial coordinate of the combustor

t : Time

L : Length of the combustor

x_q : Flame location

T : Uniform mean temperature, when there is no temperature jump assumed across the flame

T_1 : Mean temperature of the flow of upstream of the flame

T_2 : Mean temperature of the flow of downstream of the flame

S : Uniform cross-section of combustor, when there is no cross-section jump across the flame

S_1 : Cross-section of combustor upstream of the flame

S_2 : Cross-section of combustor downstream of the flame

c : Uniform speed of sound within combustor, when there is no temperature jump assumed across the flame

c_1 : Speed of sound upstream of the flame

c_2 : Speed of sound downstream of the flame

ρ : Uniform mean density of the reactants and products of combustion, when there is no temperature jump assumed across the flame

ρ_1 : Mean density of the reactant mixture upstream of the flame

ρ_2 : Mean density of the product gases of combustion downstream of the flame

k : Uniform wave number, when there is no temperature jump assumed across the flame

k_1 : Wave number upstream of the flame

k_2 : Wave number downstream of the flame

$\tilde{p}_1$: Acoustic pressure upstream of the flame

$\tilde{p}_2$: Acoustic pressure downstream of the flame

$\tilde{u}_1$: Acoustic velocity upstream of the flame

$\tilde{u}_2$: Acoustic velocity downstream of the flame

$\tilde{q}$: Flame heat release rate perturbation per unit volume

c_p : Specific heat of ideal gas at constant pressure

c_v : Specific heat of ideal gas at constant volume

γ : Ratio of the specific heats (c_p/c_v)

R : Specific gas constant of ideal gas

v : Specific volume

u : Specific internal energy

n : Interaction index

τ : Time lag between acoustic velocity perturbation upstream of the flame and flame heat release rate perturbation

n_{th}^{i} : Threshold of interaction index (n) for intrinsic mode instability

n_{th}^{a} : Threshold of interaction index (n) for acoustic mode instability

m^{i} : Mode number of the intrinsic modes

m^{a} : Mode number of the acoustic modes

ω : Eigen-frequencies or modal frequencies of the combustor

$f(\omega)$: "Detuning" function for the dispersion relation of the closed-open combustor

$g(\omega)$: "Detuning" function for the dispersion relation of the open-open combustor

ω^{i} : Modal frequencies of the intrinsic modes

ω^{a} : Modal frequencies of the acoustic modes

ω_{0}^{i} : Modal frequency of the intrinsic mode in the limit of $n \to 0$

ω_{0}^{a} : Modal frequency of the acoustic mode, when $n = 0$

ω_{c}^{i} : Deviation of the modal frequency of the intrinsic mode on the neutral curve from the modal frequency in the limit of $n \to 0$

ω_{1}^{i} : Growth rate of the intrinsic modes

ω_{1}^{a} : Growth rate of the acoustic modes

$m_{(+\pi,0)}$: Intersection point number of the neutral curve segments $\omega_c^i \tau = 0$ and $\omega_c^i \tau = \pi$,

with $m_{(+\pi,0)} = 0$ being the rightmost intersection point

$m_{(-\pi,0)}$: Intersection point number of the neutral curve segments $\omega_c^i \tau = 0$ and $\omega_c^i \tau = -\pi$

, with $m_{(-\pi,0)} = 0$ being the rightmost intersection point

$\tau_{n(+\pi,0)}$: Time lag at the intersection of neutral curve segments $\omega_c^i \tau = 0$ and $\omega_c^i \tau = \pi$,

valid for large τ

$\tau_{n(-\pi,0)}$: Time lag at the intersection of neutral curve segments $\omega_c^i \tau = 0$ and $\omega_c^i \tau = -\pi$,

valid for large τ

$n^i_{th(+\pi,0)}$: n - threshold at the intersection of neutral curve segments $\omega_c^i \tau = 0$ and $\omega_c^i \tau = \pi$

, valid for large τ

$n^i_{th(-\pi,0)}$: n - threshold at the intersection of neutral curve segments $\omega_c^i \tau = 0$ and

$\omega_c^i \tau = -\pi$, valid for large τ

R_1: Acoustic reflection coefficient at $x = 0$ of the combustor

R_2: Acoustic reflection coefficient at $x = L$ of the combustor

$\varepsilon_1 r_1$: Perturbation of the acoustic reflection coefficient at $x = 0$ of the combustor, where

ε_1 is a small parameter and r_1 is a complex number

$\varepsilon_2 r_2$: Perturbation of the acoustic reflection coefficient at $x = L$ of the combustor,

where ε_2 is a small parameter and r_2 is a complex number

Chapter 1

Introduction

1.1.   Fundamentals of thermo-acoustics

A major proportion of the energy produced in the modern era comes from the combustion of fossil fuels, which is also a dominant contributor to air pollution. Air pollution is one of the major environmental threats to our industrialized society. Control of air pollution has been a major concern for the European Union, since the late 1970s. Substantial efforts to curb the emissions of pollutants, such as Sulphur and Nitrogen Oxides, have ensured that the serious urban smog and acid rains that we used to witness in the past, do not currently occur at the same rate and intensities. But even after so much effort, as per the European Commissions' report,

'*Every year, more than 400 000 people in the EU die prematurely due to the consequences of air pollution: this is more than 10 times the toll of road traffic accidents. Another 6.5 million people fall sick as air pollution causes diseases such as strokes, asthma, and bronchitis. Air pollution also harms our natural environment, impacting both vegetation and wildlife: almost two-thirds of Europe's ecosystems are threatened by the effects of air pollution*'.

[http://ec.europa.eu/environment/air/cleaner_air/].

A parameter called 'Air Quality Index' (AQI) is used by governments to communicate to people how polluted the current air is and what the forecast for pollution is [https://www.airnow.gov/index.cfm?action=aqibasics.aqi]. The increase of AQI means a large percentage of the global population will experience adverse health effects. In the United States, the AQI is monitored based on five criteria pollutants under 'Clean Air Act'. These are: ground-level ozone, particulate matter, carbon monoxide, sulfur dioxide, and nitrogen dioxide. For countries in the European Union, the Common Air Quality index offers information regarding the hourly, daily and annual air quality. Three major pollutants (PM_{10}, NO_2 and O_3), as well as three additional pollutants (CO, $PM_{2.5}$ and SO_2), are used to monitor air pollution across Europe [http://www.airqualitynow.eu/about_indices_definition.php]. The Central and State Pollution Control Board of India [http://www.cpcb.nic.in/] monitors eight pollutants (PM_{10}, $PM_{2.5}$, NO_2, SO_2, CO, O_3, NH_3 and Pb), whereas the Ministry of Environmental Protection (MEP) of China monitors five pollutants (PM_{10}, SO_2, NO_2, O_3, CO) for measuring the level of air pollution.

[https://web.archive.org/web/20041018003319/http://www.sepa.gov.cn/quality/background.php]. Clearly, different countries use different parameters to measure air pollution. At the same time, developed and developing countries can no longer ignore their responsibility in controlling air pollution. It is a matter of concern for our planet and not just for individual countries.

As mentioned already, the main contributor to air pollution is combustion of fossil fuels, the primary source of energy in modern day combustors, which adds pollutants like the oxides of nitrogen (NO_X) to the environment. In modern day, combustors are used in various applications, e.g. in industrial power plants, rockets, and so on.
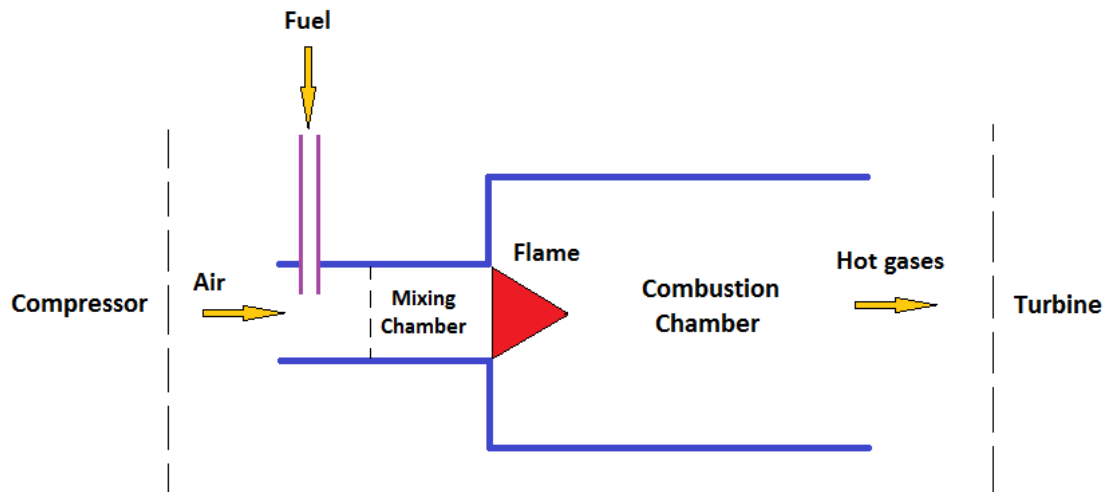
Figure 1.1: A schematic layout of an industrial gas turbine combustor.

Figure 1 shows a schematic layout of an industrial power plant combustor of the type used to produce electricity. There is a compressor at the upstream of the combustion chamber to supply air at high pressure. From a parallel fuel supply line fuel is supplied into the system. The air and fuel after being mixed in a premixed chamber go through the process of combustion, which gives rise to a flame. The hot products of combustion eventually go to the downstream nozzle (not shown in the figure) and hit the turbine blades. The rotating turbine shaft is coupled to a generator, which eventually produces electricity. Hence, for electricity production in a power plant, proper functioning of a combustion chamber is mandatory.

Due to strict pollution norms, combustors are compelled to reduce NO_X by reducing the temperature during combustion. Hence, lean premixed pre-vaporized (LPP) combustors were introduced [Warren (1966), Lee and Wimmer (1968)]. In LPP combustors, the equivalence ratio (ratio of the actual fuel/air ratio to the stoichiometric fuel/air ratio [McAllister et al. (2011)]) is kept close to lean flammability limit, which ensures the presence of large excess of air as a dilutant to minimize flame and exhaust temperature. Apart from the reduction in pollutant

formation, lean combustors, also, provide higher combustion efficiency. However, it comes at a cost of increased likelihood of 'combustion instability' during the combustion process [Putnam (1971), McManus et al. (1993)]. In thermo-acoustic combustion instability the flame heat release is coupled to one of the acoustic modes of the combustor, which gives rise to an increase of acoustic pressure within the combustor. Apart from that, there is one more mechanism via which combustion instability can occur. In this route, the flame heat release is coupled to one of the hydrodynamic modes of the combustor.

Thus, the instability mechanism within a practical combustion system takes place due to the three-way coupling of hydrodynamics, acoustics and the combustion (or the flame) itself, as sketched in figure 2 [Altunlu et al. (2014), Lieuwen et al. (2001)].
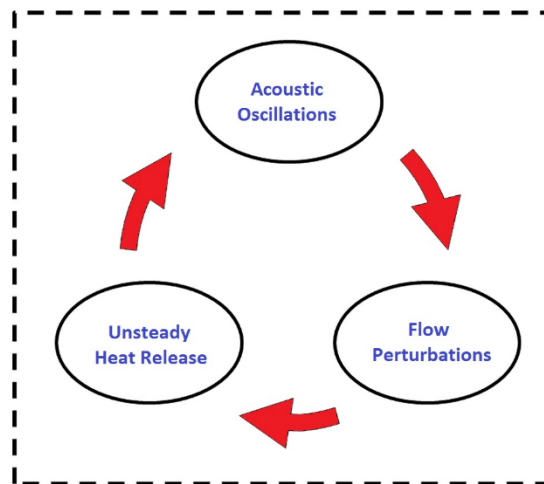
Figure 1.2: Three-way coupling between acoustic, flow perturbations and flame heat release rate perturbations in a combustion chamber [Altunlu et al. (2014), Lieuwen et al. (2001)]

As the already mentioned combustion instability is an undesirable phenomenon, as in large-scale gas turbine engines these instabilities entail growing heat release and pressure oscillation. These self-sustained, high amplitude instabilities can cause acoustic, mechanical and thermal loads to the combustor and its related parts, higher

pollutant emission, and even flame extinction. Such effects are extremely undesirable for an engine performance. Even though various active [Poinsot et al. (1988), Langhorne et al. (1990), Culick et al. (1991), Candel (1992)] and passive [Richards et al. (2003), Zhao and Morgans (2009), Noiray et al. (2009a), Noiray and Schuermans (2012)] measures are available to control combustion instabilities, the fundamental mechanisms of combustion instability are still a topic of on-going research.

The first observation on combustion instability was made by Higgins (1777) in the form of a 'singing flame'. Later Le Conte (1958) discovered a 'dancing flame' where musical beats were found to oscillate a flame in synchrony. For a vertical tube with both ends open, Rijke (1859) showed that sound can be produced by placing heated metal gauze inside the tube. The sound was heard, only when the gauze was kept in the lower half of the tube, specifically at a distance of a quarter of the tube length from the bottom. The basis of this 'flame heat release-acoustics interaction' was explained by Lord Rayleigh (1878), he formulated what is now known as the Rayleigh criterion. According to this criterion,

'*If heat is periodically communicated to, and abstracted from, a mass of air vibrating in a cylinder bounded by a piston, the effect produced will depend upon the phase of the vibration at which the transfer of heat takes place. If heat is given to the air at the moment of greatest condensation or to be taken from it at the moment of greatest rarefaction, the vibration is encouraged. On the other hand, if heat is given at the moment of greatest rarefaction, or abstracted at the moment of greatest condensation, the vibration is discouraged.*'

Mathematically, the acoustic pressure oscillation p', with time period T, can grow in a combustor with volume V (control volume), with a heat release oscillation q', if it satisfies the Rayleigh criterion as follows,

$$\int_0^T\int_0^V p'(x,t)q'(x,t)dvdt > 0.$$

x is the spatial coordinate. This integral is spatial (dv represents elementary volume) as well as temporal (t is time), which means that for a different flame location and time period, energy can be added or removed from the system, resulting in destabilizing or stabilizing the system. The Rayleigh Criterion implies that a thermo-acoustic instability can be optimally controlled by having heat release oscillations 180 degrees out of phase with pressure oscillations at the same frequency. If we consider the effect of energy dissipation in the system as well, the corresponding Rayleigh Criteria will take the following form,

$$\int_0^T\int_0^V p'(x,t)q'(x,t)dvdt > \int_0^T\int_0^V \varphi(x,t)dvdt.$$

To control combustion driven oscillations, a thorough understanding of the linear [Kim and Santavicca (2009)] and non-linear [Powell E. A. (1970), Zinn and Powell (1971)] dynamics of flame is needed. These linear processes determine the frequency and growth rate of the inherent disturbances of the combustor [Bellows et al. (2006)]. For higher amplitude oscillations, the non-linear processes kick in and take control of the combustion system, producing phenomena like the limit cycle of a self-excited oscillation. This concept of advent of the limit cycle [Strogatz (1994), Rabinovich and Trubetskov (1989), Kosztin (2013)] can further be clarified by figure 3 [Bellows et al. (2006)], where for an acoustic disturbance of amplitude A, the driving and damping processes within a combustor are described by hypothetical functions $L(A)$ and $D(A)$, respectively. The growth or decay of A depends on the relative magnitude of driving and damping. The amplitude grows if the driving process dominates and decays if the damping dominates. At low amplitude oscillation, $L(A)$ can be

approximated as a linear function. Prediction of limit cycle amplitude will further call for non-linear characteristics of $L(A)$ and $D(A)$. Figure 3 depicts a situation when $L(A)$ saturates, but $D(A)$ remains linear, and at the limit cycle, these two curves cross each other.
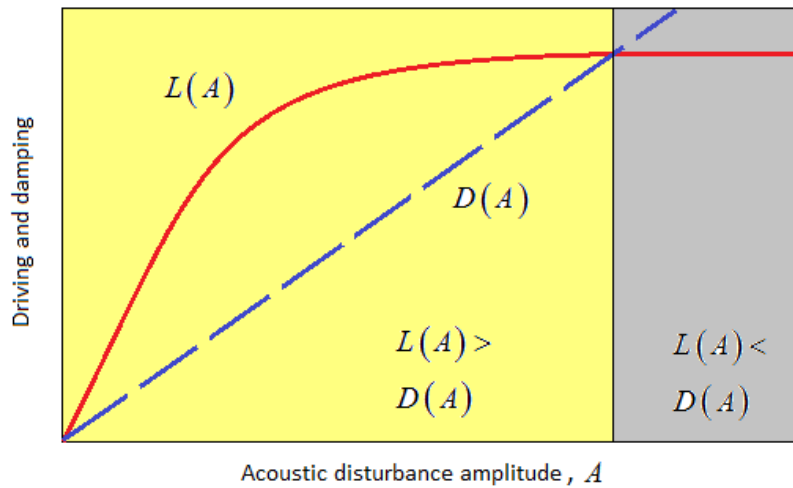
Figure 1.3: Dependence of acoustic driving, $L(A)$ and damping, $D(A)$ processes on the amplitude of acoustic oscillations, A [Bellows et al. (2006)]. These two curves cross at the limit cycle.

1.2. Brief overview of the background research in thermo-acoustic instability

1.2.1. Root cause of thermo-acoustic instability

The root cause of the thermo-acoustic instability is assumed to be the coupling of flame heat transfer, acoustics, and hydrodynamics of the combustion chamber. However, the mechanisms are still an on-going topic of research. In the literature, two specific mechanisms of combustion instability have been identified: (i) equivalence ratio fluctuation and input mass flux fluctuation [Lieuwen and Zinn (1998), Paschereit et al. (1999a)] and (ii) vortex shedding at the tip of the flame holder [Schadow and Gutmark (1992), Poinsot et al. (1987), Poinsot and Veynante (2004)]

1.2.1.1. **Thermo-acoustic instability due to equivalence ratio fluctuation**

Equivalence ratio fluctuation as the cause of heat release rate oscillation can be found in the work of Lieuwen and Zinn (1998) for a very lean premixed combustion system. Their consideration is based on time lag theory, which describes the effect of the phase difference in a combustor. In a practical situation, any acoustic oscillation present in the pre-mixer causes variation in the mass flux of air and the fuel supply, which leads to equivalence ratio fluctuation (refer figure 4). This equivalence ratio fluctuation is convected downstream to the flame, inducing flame heat release fluctuation. This creates a convective time lag. This quantity is given by $\tau_{conv} = L_i / \overline{u}$, where L_i is the distance from the fuel injector to flame front and $\overline{u}$ is the average flow velocity at the inlet [Lieuwen et al. (2001), Lieuwen (2003), Lieuwen et al. (2008)]. In addition to this, there is another time lag, known as a chemical time lag, τ_{chem}, which is the time for the air-fuel mixture to burn completely and generate the combustion products. Thus, the total time lag ($\tau_{total} = \tau_{conv} + \tau_{chem}$) is the transport time for oscillations from the injection point of air/fuel mixture, to the point when the air/fuel mixture burns at the flame front. Usually, the chemical time lag is order of magnitudes smaller than the convective time lag [Lieuwen and Zinn (1998)]. If heat release oscillation, induced by this equivalence ratio fluctuation at flame, is in phase with pressure oscillation at the flame, it will amplify the oscillation. If it is out of phase, oscillations will decay. It is assumed that the acoustic pressure oscillation in the combustion chamber causes velocity fluctuations and no change in flow variables, such as density and temperature. The equivalence ratio can be controlled to oscillate between two limits, to avoid thermo-acoustic instabilities, as observed in the work of Richards et al. (1999).
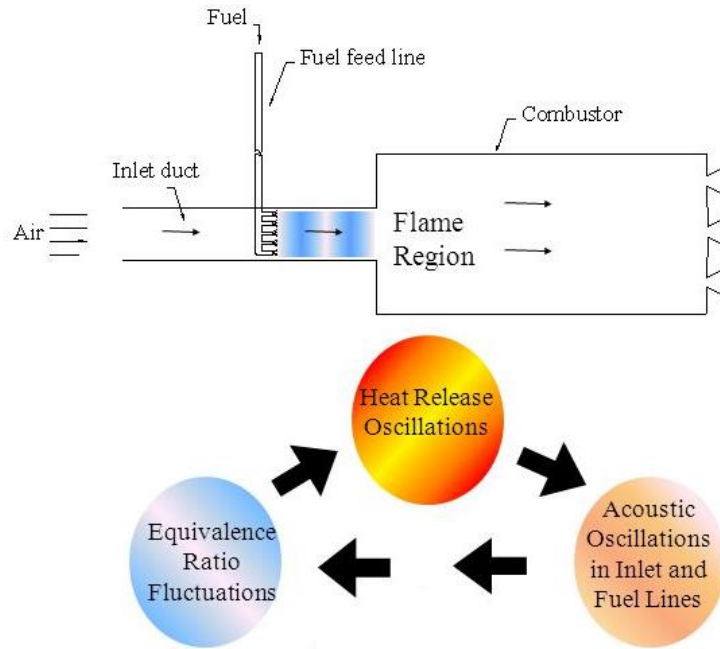
Figure 1.4: Mechanism for combustion instability due to equivalence ratio fluctuation
[Lieuwen and Zinn (1998)]

1.2.1.2. Thermo-acoustic instability due to Vortex rollup

Thermo-acoustic instabilities can also come into the picture, due to the large-scale coherent vertical structures, arising because of flow separation at the tip of the flame holder, as observed in the work of Dec et al. (1991). These flow instabilities are often referred to as vortex rollup. The combustion interacts with the unstable fluid flow as it moves downstream causing heat release fluctuations. The resulting acoustic field interacts with the flow oscillations at the boundary layer separation at the flame holder tip. Vortex shedding frequencies, in general, are much lower than the reaction rates during combustion.

In diffusion-type flames (in flames where the oxidizer mixes with the fuel by diffusion e.g. a candle) setup, large-scale coherent structures control the mixing between fuel and air. In a premixed flame (this flame is a result of the combustion between a premixed mixture of fuel and oxidiser, e.g. flame in LPP gas turbine and Spark Ignition engines) setup, these structures control the mixing between fresh air-

fuel mixture and hot combustion products [Paschereit et al. (1999b)]. A possible mechanism of vortex rollup, as a cause of combustion instability, can be found from Schluter (2001) [figure 5]. As per Schluter (2001) [and also Poinsot et al. (1987)], the vortex rollup near the burner captures some unburnt fresh gasses inside, increasing the flame surface area dramatically. This mechanism eventually leads to an enhancement of heat release rate, as heat release rate is found to be proportional to the flame surface area [Merk (1957), Boyer and Quinard (1990), Dowling (1999)]. The heat release fluctuation gives rise to acoustic perturbation after some time lag. The acoustic perturbation triggers subsequent vortex rollup in the shear layer at the tip of the burner.
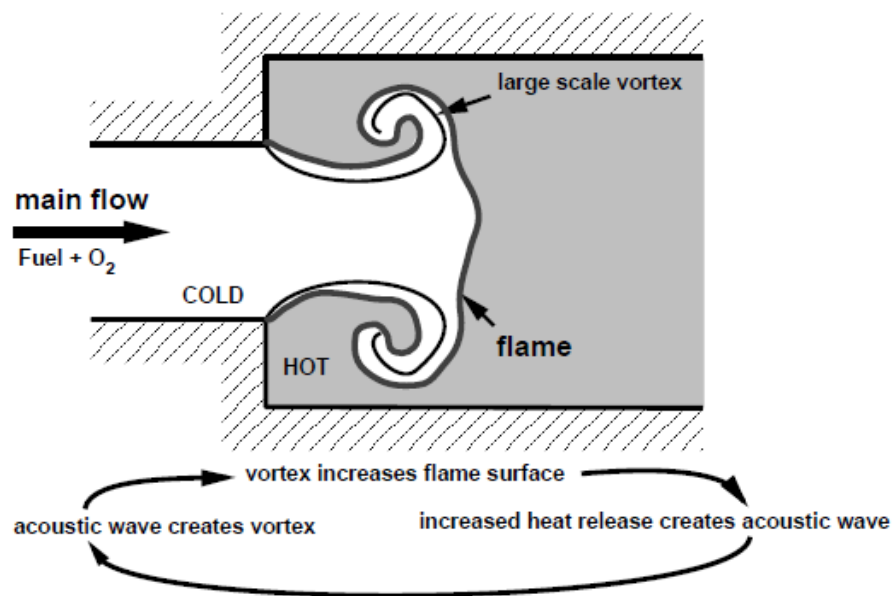
Figure 1.5: Schematic of large scale vortices as a driver of combustion instabilities [Schluter (2001)]

In general, the noise radiated from a combustor consists of a direct and an "indirect" component. Direct combustion noise is created due to isentropic pressure waves, produced by the unsteady heat release, a mechanism already explained in this section. Apart from that, there is indirect noise, also known as entropy noise [Dowling and Mahmoudi (2015)], which is caused by entropy waves that are perturbations in the

hot gas temperature. These are generated by the heat release of the flame via equivalence ratio fluctuations. A feedback mechanism can be formed if such a perturbation is convected into a choked or nearly choked nozzle at the combustor exit, where it is reflected as a pressure wave. The possible sources of direct and indirect combustion noise are further explained by the sketch in figure 6 [Dowling and Mahmoudi (2015)]. Combustion noise is found to be the third major contributor after fan and jet noise, in the context of turbojet engine noise [Dowling and Mahmoudi (2015)].
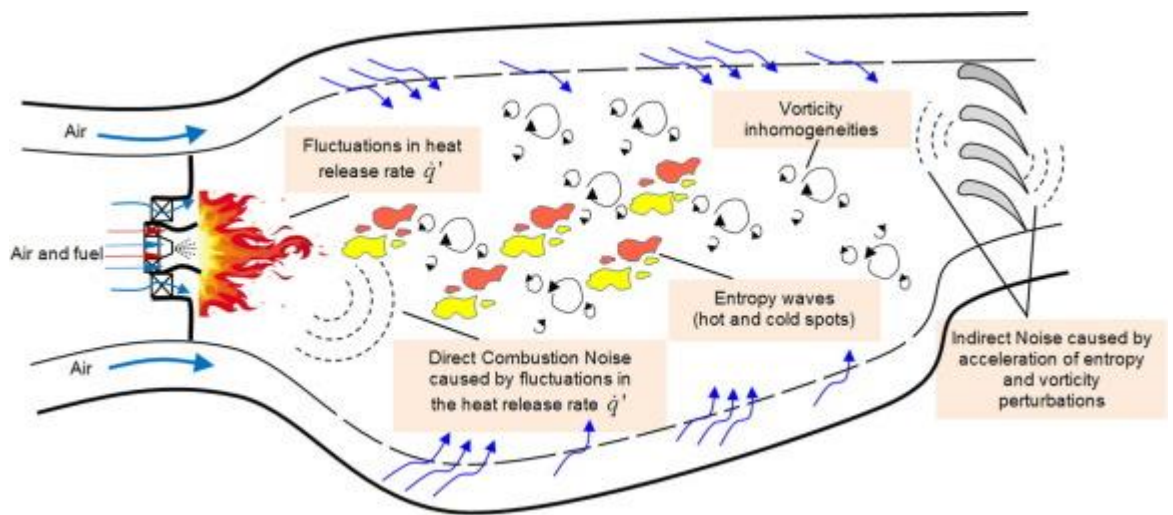
Figure 1.6: Generation of direct and indirect combustion noise in aero-engines [Dowling and Mahmoudi (2015)]

1.2.2. Modeling of flame and acoustics in combustion chamber

1.2.2.1. The modeling of flame

The theoretical modeling of the flame in a combustion system is an essential part of understanding the underlying mechanism of thermo-acoustic instability. However, theoretical modeling is restricted by the intrinsic nonlinear nature of the combustion process [Khanna (2001)]. Attempts have been made to identify the effect of flame heat release on velocity fluctuations through a mathematical parameter called flame

transfer function [Ducruix et al. (2000), Schuller et al. (2002, 2003), Polifke and Lawn (2007)], which is widely used for linear stability analysis of combustors. The flame transfer function (FTF) is the ratio of the heat release rate perturbation (Q') to acoustic velocity perturbation (u'), both normalized with respect to mean quantities ($\bar{Q}$ and $\bar{u}$),

$$Q'/\bar{Q} = f\left(u'/\bar{u}\right)$$

A Fourier transform of the above equation transforms it to the frequency domain,

$$Q'(\omega)/\bar{Q} = FTF(\omega)\left[u'(\omega)/\bar{u}\right]$$

$FTF(\omega)$ is known as the '*flame transfer function*' and is usually expressed as $FTF(\omega) = G(\omega)\exp\left[i\varphi(\omega)\right]$, where $G(\omega)$ is the gain and $\varphi(\omega)$ is the phase of the flame transfer function. The flame modeling, with the help of the flame transfer function, can be pinned down to several publications. The concept of the transfer function of flames was introduced in the work of Merk (1957), where the concept was used to analyze unstable combustion of laminar premixed flame. Experimental measurement of the FTF is done by taking luminescence signal of the excited OH (OH*) molecule, within the flame, as a representation of heat release rate, whereas, the velocity is recorded directly or by hot wire anemometry. The FTF is obtained at discrete frequency steps, with external excitation generated from a loudspeaker [Freitag (2009)]. References to the earlier works on the FTF measurements for a swirl stabilized burner, can be found in Buechner et al. (1993) and Khanna et al. (2001, 2002) (also referred as Flame Response Function). Previously, Bloxsidge and Dowling (1988) developed a flame transfer function that relates the fluctuation in local heat release rate per unit length of the flame, to the mean heat release rate at that location, the Strouhal number, and a time delay. They also studied the flame

12

dynamics of afterburners, where the combustion zone length was a significant fraction of the acoustic wavelength. The combustion process was modeled as a distributed source, with low instability frequency (20-90 Hz) supposedly appearing due to flow instabilities.

The concept of the flame transfer function was also used in the work of Fleifil et al. (1996) on laminar conical flames, where the steady field was modeled as a Poiseulle flow and the flame dynamics were derived by linearizing about the mean flame shape. When subjected to an acoustic wave at a given frequency, the solution generated temporal and spatial flame displacement with respect to mean position. Attention has been paid to model conical flames using the flame transfer function in different research works of Cuquel et al. (2011-2013). They described (2013a) the impact of flame base dynamics on the non-linear frequency response of conical flames. Unsteady heat transfer between the flame base and burner lips was considered to model the flame base response. This analysis demonstrates the important role of flame foot oscillations to control the saturation of the Flame Transfer Function phase lag. They also made a theoretical and experimental study of the flame transfer function of confined premixed conical flames (2011). The response of conical premixed flames to velocity perturbations for different flow operating conditions and burner nozzle geometries were examined. Afterwards, Campa et al. (2010) identified the influence of the flame and burner transfer matrix on thermo-acoustic combustion instability modes. They developed a 3-D finite element code, to predict acoustically driven combustion instability. The heat release was predicted by the $n - \tau$ flame transfer function model. The code could predict the frequency, as well as the growth rates at the onset of combustion instability, when assuming linear acoustic behavior.

Flame modeling can also be performed with the help of a '*flame describing function*' (that is a velocity amplitude dependent flame transfer function), as found from the work of Noiray (2007), Noiray et al. (2008, 2009b) and Boudy et al. (2011). In their work [Noiray et al. (2009b)], a method was developed to estimate the noise level of unstable combustion based on the flame describing function. It has been shown that non-linear phenomena such as frequency shift, triggering or hysteresis may be predicted by an analytical model, based on the flame describing function. Subsequently, triggering phenomenon was also explained by Boudy et al. (2011). Cuquel et al. (2013b) explained the prediction technique of the non-linear dynamics of a multiple flame combustor, by coupling the describing function methodology with a Helmholtz solver. Later, Campa et al. (2013) identified the influence of nonlinear flame models (using a nonlinear flame transfer function) on bifurcation process and limit cycles in gas turbine combustors. A simple cylindrical and a simple annular configuration of a combustor system was examined. The bifurcation diagrams of these flame models were obtained considering interaction index as the control parameter. The influence of time delay on both the hopf and fold bifurcation point was found. Previously, Bellows et al. (2006) identified the effect of imposed acoustic oscillations on the non-linear flame transfer function of a lean, premixed flame in a swirl-stabilized combustor. Both CH* oscillation amplitude and phase were found to have a strong dependence on imposed velocity. Different mechanisms were found to be responsible at different frequencies and flow rates. At low flow rates, the non-linear amplitude of CH* varied greatly with driving frequency, whereas, for high flow rates, the non-linear amplitude was independent of driving frequency. Two parameters: vortex rollup and flame lift-off, played a crucial role in controlling the saturation mechanism of the flame transfer function.

1.2.2.2. The acoustic modeling of combustion chamber

It has been mentioned previously that in a practical combustor, acoustics, flame and hydrodynamics are strongly coupled. Therefore, a combustor should be tested for a wide range of operating conditions to ensure its stability. Experiments and high fidelity direct numerical simulations are, in principle, capable of providing this stability testing. Nonetheless, these methods are generally time consuming and expensive. To tackle this problem, low order models are developed to predict stability features of the system with reasonable accuracy. These analytical models are easy to handle and can often be checked for accuracy aposteriori against the high-fidelity and comprehensive numerical simulations of the combustion systems. A very brief review of the literature from the analytical modeling of combustion systems can be cited in this regard.

Hubbard and Dowling (2001) developed a theory able to describe low-frequency acoustics in complicated combustor geometry of industrial gas turbines. Two main types of acoustic resonances have been identified: a "plenum" mode and another combustor mode (plenum represents the chamber volume at the upstream region of flame). Combustion chamber temperature did not seem to alter the plenum mode. It was observed that any Helmholtz resonator fitted upstream of the flame, altered the plenum mode if the resonator is tuned to the plenum mode. However, the resonator did not significantly alter the resonant modes of the combustion chamber. Later, Dowling and Stow (2003) performed linear acoustic analysis of gas turbine combustors. The coupling between heat input and unsteady flow had a crucial effect on modal frequency. The effect of mean temperature jump across the combustion zone was found to be significant for the modal frequency. However, mean flow

effects were not severe for Mach numbers less than 0.2. The modal coupling took place when the combustor geometry was not axisymmetric.

Hathout et al. (2000) have adopted a lumped parameter approach, to develop a reduced order model for flame dynamics, combining the effect of flame area oscillation and equivalence ratio fluctuation. It has been shown that the acoustic mode determines the heat-acoustic coupling mechanism. Schuermans et al. (1999) developed an analytical model of a burner with premixed swirl stabilized flame. The model is based on Bernoulli's equation, derived for the incompressible isentropic flow of an ideal gas through the burner. The model assumes that the acoustic fluctuations develop an equivalence ratio fluctuation, which propagates downstream of the injector to the flame, ultimately leading to a time lag. The altered heat release rate couples with combustion chamber acoustics and generates pressure oscillations.

Sujith (2001) and Sujith et al. (1995) found exact analytical solutions for one-dimensional sound propagation through a combustion zone, accounting for the effect of mean temperature gradient and oscillatory heat release. Using appropriate transformations, solutions were derived for the case of an exponential mean temperature gradient in terms of Bessel functions. A low order network model for combustor was developed by Mukherjee et al. (2014), where the vicinity of the flame holder was modeled as a lumped inertance. It was found that the temperature jump across the flame increased the modal frequency of the system, whereas the effect of the cross-section jump across flame is less straightforward. This feature was explained using pressure profile of modes. It was shown that the cross-section jump, when introduced at the point of increasing pressure (as per mode shape), decreases the modal frequency, whereas the cross-section jump, introduced at the point of reducing pressure (as per mode shape), increases the modal frequency.

Modeling of the flame is an essential component of analytical models of combustors. The flame modeling techniques have been covered briefly in § 2.2. However, it assumed that the flame behaves as a compact element. Some works discuss the condition under which the flame can be treated as compact, as well as the condition for which the mean flow of the system can be neglected. Dowling (1995) dealt with various flow effects on thermo-acoustic oscillations. It was found that one must be cautious when neglecting the mean flow, to avoid coupling of the entropy wave to the acoustic field. Under certain conditions, a relatively high Mach number flow can lead to significant drop in thermo-acoustic oscillation frequencies. The condition at which an axially distributed heat source can be treated as a compact source has been identified. It was observed that due to the small length scale, entropy waves are affected much more by axial heat distribution than acoustic waves. At low Mach number, or for mean temperature ratio close to unity, acoustic waves are not perturbed by entropy waves. Under these conditions, the heat source can be treated as a compact source. In this regard, Kato et al. (2005), using a 1-D linear model, concluded that instead of treating the flame as fixed and lying on a single axial flame, the level of accuracy of combustion oscillation frequencies is increased, if the flame heat release is modeled by some spatial distribution function. The spatial distribution function was assumed to depend on operation conditions such as the equivalence ratio and flow velocity.

Crocco and Cheng (1956) introduced a simple linear heat release model in terms of time lagged acoustic velocity perturbation $q(t) = nu(t - \tau)$, where n is the interaction index and τ is the time lag between the heat release and the velocity perturbation. Sirignano W. (document link is in the references) explained the effect of nonlinear combustion instability on the liquid propellant rocket. Using time lag theory by

17

Crocco and Cheng, the stability limits for longitudinal, transverse, as well as, radial acoustic modes were identified. As per the reported observation, at very low time lags, the system also retains stability for high interaction indexes. The applicability and limitations of a linear theory to predict thermo-acoustic oscillation frequency has been discussed by many authors. In particular, Lores M. E. (1972) performed a theoretical study of non-linear longitudinal combustion instability in liquid propellant rocket engines. As per their observation, the limit cycle oscillations of longitudinal instabilities are discontinuous waves. Near the linear stability limit, small amplitude oscillations can be observed. The oscillation becomes discontinuous as amplitude increases. Moreover, it was also observed, to second order in velocity, that the nonlinearities of the system do not change the regions of instability predicted by linear analysis. Following this, Dowling (1997) found that the non-linearity in the self-excited oscillations in a ducted flame originates from the saturation in the heat release rate. The work also explained why linear theory provides a good prediction of the frequency of oscillation and the mode shape.

Different modeling techniques to identify the effect of the flame, as well as the acoustic boundary conditions of the combustor on the combustor stability behavior, have been carried out by Schuller et al. (2009-2012). Schuller et al. (2009) tried to model non-linear boundary conditions using an Impedance Describing Function (IDF), which depends on pressure perturbation level or velocity fluctuation level. According to this work, the stability of the system is dependent, not only on the nonlinear response of the flame, but also on the non-linear response of the boundary conditions. Later, Schuller et al. (2012) defined an acoustic coupling index, dependent on the area ratio and the characteristic impedance ratio between the upstream and the downstream of the flame, to identify low-frequency acoustic

interactions in a generic combustion system. It was identified that the low-frequency combustion instabilities lock on to the plenum or upstream combustor mode and is weakly dependent on the changes downstream of the flame region.

The majority of the instabilities in practical combustors come in the form of limit cycles [Nayfeh and Mook (1995)], the frequency of which can be calculated with reasonable accuracy using low order analytical models [Lieuwen and Yang (2005)]. However, thermo-acoustic oscillations are often associated with transient energy growth, where, under certain conditions, limit cycles can be triggered to higher. Nagaraja et al (2009) studied the various aspects of transient energy growth during combustion instabilities. The Galerkin technique was used to simplify governing acoustic equations in the duct in the presence of localized heat source, modeled by the $n - \tau$ law. The transient energy growth was estimated by singular value decomposition. A parametric study was also performed, to identify the influence of the system parameters on the maximum transient energy growth. In a previous work, Balasubramanian and Sujith (2008) explained the non-normal and non-linear combustion-acoustic interaction for the diffusion flames. Non-normality aspects in thermo-acoustics are also discussed by Mariappan (2012).

In the work on transient energy growth and triggering in a horizontal Rijke tube, Juniper (2011) explained the link between linear transient growth (Balasubramanian and Sujith (2008)) and non-linear triggering (Ananthakrishnan et al., (2000)). It was found that both non-linearity and non-normality contribute to the transient growth. Two types of non-linear optimal initial states were found. The first had strong energy growth during the first period of fundamental mode but lost energy thereafter. The second initial state caused weak energy growth in the first period and retained high energy thereafter for a longer time. Thus, the second initial state causes triggering

from low energy to high energy in self-sustained oscillations. An experimental validation of this theoretical work can be found in Mukherjee et al. (2015), where they studied non-linear dynamics of a ducted V-flame in a laminar combustor. It was observed through non-linear time series analysis [Abarbanel et al. (1993), Cao (1997)] that due to the change of flame location within the combustor, a low amplitude limit cycle can be triggered to a high amplitude limit cycle. The high-speed flame images captured, provided substantial evidence of contorting and stretching of the flame surface during this transition from the low to high amplitude limit cycle, indicating an increase of heat release rate of the flame during high amplitude limit cycle. In an earlier work, Zhao Dan (2012) predicted the transient growth of flow disturbances in triggering Rijke tube combustion instability. The effect of the interaction index (n) of the $n - \tau$ law on maximum acoustic energy growth rate was highlighted. From this observation, the maximum growth rate is greater than 1 for an interaction index of 1.5, and the maximum growth rate is infinite for an interaction index of 7.5.

1.2.3. Instability features of different flame shapes used in gas turbine combustors and other applications

We have mentioned in the § 2.1, that there are two basic types of flames: diffusion and premixed. In addition to this, different flame shapes, allow flames to be further classified into various categories, i.e. conical flame, V-flame, flat flame, and M-flame. Some comparative studies have also been made to examine their performance.

1.2.3.1. Conical flame vs. V flame

Conical and V-flames are the most widely used flame shapes in the industrial combustors. A comprehensive study on these two flame shapes can be found from the literature.

Schuller et al. (2003) developed a unified model to predict the laminar flame transfer functions and compared the dynamics of a conical and a V-flame. This model is based on the linearization of the G-equation for an inclined flame, including the convective effect of the flow modulations propagating upstream of the flame. It has been shown that the flame dynamics are governed by two parameters, a reduced frequency and the ratio of flame burning velocity to the mean velocity. It has also been observed that a V-flame behaves as an amplifier in a certain range of frequencies. Such flames are more susceptible to combustion instabilities than conical flames.

The research of Durox et al. (2005-2009) also focuses on V-flames. Durox et al. (2005) performed analysis on an inverted conical flame, anchored on a rod at the exit of an unconfined burner. Transfer function measurement identified that these flames are sensitive to low-frequency acoustic excitations and behave like amplifiers over the broad frequency range. They also observed that the flame wrinkling, caused due to vortex structures developing in the shear layer between the jet and surrounding medium, led to strong rolling up of the flame and mutual annihilation of neighbouring reactive elements. These processes resulted in rapid variations in the flame surface area. Recently, Durox et al. (2009a) performed an experimental investigation of nonlinear flame transfer functions for different geometries. They identified that the gain of a V-flame transfer function reaches a value of 3.5 within a range of

frequencies. Whereas the gain, for conical flames, does not exceed 1 and does not exceed 2 for M flames.

In an earlier experimental work of Blackshear (1952) on conical flames in a Rijke tube, it was suggested that the flame speed has a strong impact on the phase lag between heat release and velocity perturbation, and thus on the damping characteristics of the flame dynamics. The other forms of flame are flat flame and unconfined flame. We mention a few works concerned with these flame types.

Markstein (1964) performed perturbation analysis of flat flames. In this work, the acceleration of the fluid column around the wrinkled flame was modeled as a second order oscillator, which forced the flame to respond at a sub-harmonic frequency. Sub-harmonic frequencies like this were explained by Saunders et al. (1999) for a Rijke tube. In the work on flat flames by Markstein (1952) showed that it is impossible to realize a truly flat flame sheet because of the non-uniformity of the mean flow. An oscillation in velocity field, in which the flame is anchored, would fluctuate the flame surface. The stretching and contorting of the flame sheet alters the flame propagation speed, which is directly related to the rate of combustion and therefore the heat release. This surface area variation, due to local velocity perturbations, can provide a mechanism for self-sustained thermo-acoustic oscillations. Peerlings et al. (2013) studied whether the chemi-ionisation process, present in flames, can be used as an indicator of the thermo-acoustic response of flames. The thermo-acoustic response of flat and Bunsen-type flames was determined at equivalence ratios ranging from lean to rich, as well as at various flow velocities. The maximum value of the gain of the transfer function was observed to be 3 for flat flames and 1.3 for Bunsen-type flames. There was also an effort to analyze thermo-acoustic oscillations of unconfined flames. For example, Durox et al. (2009b) verified the Rayleigh criteria for self-sustained

thermo-acoustic oscillations of unconfined flames. An acoustic energy balance was approximately obtained, in which the Rayleigh source term subtracted by damping losses determined the far field acoustic radiation level. Moreover, it was found that the pressure perturbations inside the burner, just upstream of the flame region, are nearly in phase with the flame heat release rate perturbations, an observation that might not be valid for confined flames all the time. In a different work, an experimental study on collapsing cylindrical flames was performed by Durox et al. (2001).

1.2.4. Computational and experimental work in thermo-acoustics

There is an extensive literature on computational and experimental works in the field of thermo-acoustic oscillations. We list the key ones.

Truffin et al. (2002) performed acoustic analysis to evaluate the transfer matrix of the burner. The interaction index (n) and time lag (τ) in the $n - \tau$ flame modeling have been evaluated by Large Eddy Simulation and these results were compared with the experimental results. Large Eddy simulation (LES) is a high-fidelity numerical method for turbulence, capable of predicting combustion processes. The simulation of turbulent flows can be accurately performed for all length and time scales by Direct Numerical Solution (DNS) of the Navier-Stokes equation. DNS, however, is a computationally expensive method. LES, on the other hand, is performed by the low-pass filtering of the Navier-Stokes equation and thus eliminating the computationally expensive small length scale components. In addition to this, there is the Reynolds Averaged Navier-Stokes equation (RANS), which is a time-averaged equation for the motion of the fluid flow. However, RANS simulations could be more sensitive to the choice of turbulent models than LES. Poinsot and Selle (document link is provided in the reference) focussed on the importance of LES and acoustic codes to predict

coupled acoustic fields in gas turbine combustors, as compared to a classical RANS technique. They analyzed two swirl-stabilized combustor models for both reacting and non-reacting flow cases. With the LES technique, it was identified that a strong precessing vortex core developed for non-reacting flow, which disappeared with the advent of combustion. Different works on LES can be listed in this context as well.

Martin et al. (2004) analyzed self-excited combustion instability in a lab-scale, swirl-stabilized, turbulent combustor, using a full compressible LES, Helmholtz analysis and budget of acoustic energy. Helmholtz analysis exactly identified the modes appearing during the instability. On the other hand, the budget acoustic energy explained that the Rayleigh criterion is not the only or even largest term in the acoustic energy equation. Acoustic energy losses at combustor outlet are equally as important as its amplitude, in the identification of oscillation frequency. Previously, Varoquie et al. (2002) performed experimental analysis and large eddy simulation to determine the response of non-premixed flames subjected to acoustic forcing. They identified that complete simulations were impossible on combustion instabilities since it involves acoustic waves through the whole system. Therefore, large eddy simulations were used to identify the parameter values in a $n - \tau$ model. These parameters were incorporated in a global acoustic model of the system, to check the possibility of impending combustion instability. In another work, Roux et al. (2008) performed LES to simulate the reacting flow field in a ramjet-like combustor. The predictions made were in good agreement with experiments.

On the experimental front, Matveev (2003) performed experiments with an electrically heated Rijke tube, with the mean flow provided by a blower, to identify transition to instability and excited regimes. He developed a mathematical model, incorporating the heat transfer effect, to calculate stability boundaries, limit cycles,

and history dependent effects. On a different note, efforts have been made to understand the non-linear dynamics of ducted flames. Some of them can be listed here. Karimi et al. (2007) determined experimentally the transfer function of a ducted laminar premixed flame, by measuring the heat release modulation. They also calculated the velocity perturbations at the tip of the flame holder. In addition, Karimi et al. (2009) performed the experimental study of the dynamics of a conical, ducted, laminar, premixed flame, subjected to acoustic excitation of various amplitudes. The flame transfer function was measured over a range of forcing frequencies and equivalence ratios. Kabiraj et al. (2012a) [also, Kabiraj (2012)] identified a quasi-periodic route to chaos for combustion instability in a ducted, laminar, premixed, conical flame. Following this, Vishnu (2013) made an experimental study on combustion instability on a lab-scale model of a ducted, laminar, premixed, V-flame combustor. The thermo-acoustic system was found to bifurcate from a stable state to an unstable regime, characterized by interesting dynamical states. The dynamical states observed in the experiments are, Steady state→Frequency locked→quasi-periodic→Period 3→Chaos. Kabiraj (2012b) also explained intermittency and a route to chaos in thermo-acoustic oscillations.

1.3.   Intrinsic flame instability in the context of thermo-acoustics

So far, we have explained thermo-acoustic instabilities caused by three-way coupling between combustor acoustics, flow perturbation, and flame heat release perturbation. However, recently, a major shortcoming of the established paradigm has been identified by Hoeijmakers et al. (2014), Hoeijmakers (2014) and Bomberg et al. (2015). Hoeijmakers et al. (2014) suggested that the flame subsystem in a combustor can give rise to a completely new family of modes, which are often referred to as the *flame intrinsic thermo-acoustic modes*. Although, it would be more appropriate to call

them intrinsic thermo-acoustic modes of the flame and its nearby environment. For brevity, throughout the paper, we will just call them *intrinsic modes*. Thus, a set of intrinsic modes (which might be unstable) can exist in a combustor, apart from the conventional acoustic modes. This is further illustrated in figure 7, which depicts that there is no acoustic reflection coming from the ends of the tube, when a flame subsystem (flame + air/fuel supply line) is kept in a theoretically infinite tube. However, as the aforementioned literature indicates, even in this kind of environment, the flame subsystem can give birth to a set of modes devoid of acoustic effects.
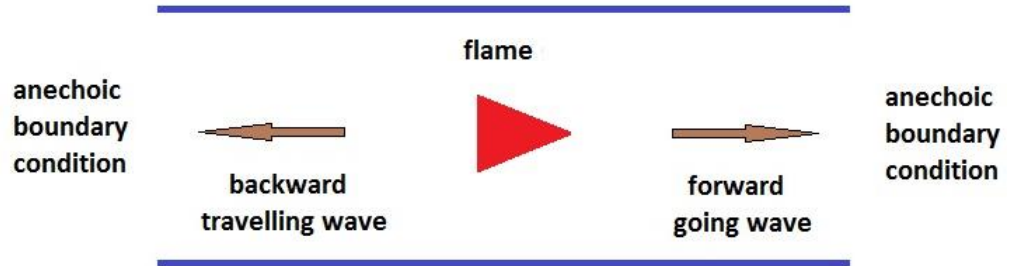
Figure 1.7: Schematic of a tube, with a flame under the anechoic boundary conditions inside it. As per Hoeijmakers et al. (2014) flame subsystem (flame + air/fuel supply line) in this environment can become unstable too, even though the contribution from tube acoustics is absent. Note that the complete flame subsystem is not depicted in this figure, but can be referred from figure 4.

Hoeijmakers et al. (2014) considered an $n-\tau$ resonator model with different degrees of transparency at the ends and numerically evaluated intrinsic mode frequencies. Their analytical analysis was confined to an infinite system: the implicit dispersion relation for the flame in an infinite system was found to be, $\varepsilon+1+\theta F(\omega)=0$, where, $F(\omega)$ is the flame transfer function, ε is the jump in specific acoustic impedance and θ is the jump in temperature across the flame. The real parts of the intrinsic mode frequencies for an infinite system were found to be $(\pi \pm 2k\pi)/\tau$, where τ is the time lag and k is an integer. The threshold of instability was found in

terms of the temperature jump. The analytical results were complemented by numerical analysis of a single intrinsic mode in a resonator. A possible physical explanation for the origin of flame intrinsic modes, was suggested to be the flame reaction on the acoustic velocity fluctuations, created by its own heat release fluctuation. In other words, the flame and its adjacent environment might create its own local, potentially unstable, feedback loop.

Independently, Bomberg et al. (2015) demonstrated the existence of the intrinsic mode, both experimentally and theoretically. In the theoretical work, the presence of these intrinsic modes was found by analyzing the system stability, using the flame transfer matrix. In the experiments, two different setups were used: laminar flame holder-stabilized and turbulent swirl-stabilized burner. The experimentally observed thermo-acoustic instability frequency closely matched the calculated frequency of the flame intrinsic modes. Thus, it was concluded that the common assumption made in thermo-acoustic instabilities: that the flame heat release always locks onto one of the acoustic modes, needs to be critically reconsidered on a case-by-case basis.

In a parallel study by Emmert et al (2015), the stability of intrinsic modes is investigated from the viewpoint of a balance of the acoustic energy across the flame. The experiments by Bomberg et al. (2015), along with direct numerical simulations (DNS) by Courtine et al. (2014), Courtine et al. (2015) and Silva et al. (2015), where a flame placed in an acoustically anechoic environment, have confirmed that the intrinsic thermo-acoustic feedback is a genuine physical phenomenon, and not just a spurious by-product of simplistic models. Courtine et al. (2015) pointed out that the theoretical predictions of the stability and the frequency of intrinsic modes strongly rely on the determination of the Flame Transfer Function. Instability frequencies and spatial structures of the modes predicted theoretically, were captured by DNS with

good accuracy when flames with sufficient confinement (small cross-section ratio between the injection duct and combustion chamber) were considered. It was further confirmed that intrinsic thermo-acoustic modes are more unstable in confined combustion chambers. A recent study by Emmert et al. (2015) has shown that a sum of acoustic and intrinsic thermo-acoustic modes constitutes the complete set of eigen-modes of a combustor. A numerical procedure has been developed to compute the acoustic and intrinsic eigen-modes of a combustor. It was noted that it is sometimes difficult to distinguish the intrinsic and acoustic modes, solely, by comparing their mode shapes. It has also been found that increased acoustic losses at the end of the combustor may destabilize the combustion system, due to intrinsic flame instability. A similar observation has been made by Hoeijmakers et al. (2016) from an experimental study, which shows that intrinsic mode instabilities could be present in combustion systems, despite significant acoustic losses. This finding also highlights that the effectiveness of passive thermo-acoustic damping devices will be restricted by intrinsic stability properties of the flame.

1.4.   State-of-the-art and scope of present work

The literature review in the previous section identifies and firmly establishes the presence of flame intrinsic modes within combustors. These modes have been neglected for decades in the study of thermo-acoustic instability. Despite this, the study of the literature is predominantly confined to the computational and experimental domain. The only analytical study performed in the field so far, considers an anechoic chamber. It has also been speculated that the derivation of analytical expression of intrinsic modes needs the anechoic boundary condition [Emmert et al. (2015)]. Due to this, the literature does not shed any light as to how the

intrinsic modes exist within a combustor under application (that is when we consider acoustic reflections from the ends of the combustor) and how many potential intrinsic modes are present in the system. For an anechoic boundary condition, it has been shown [Hoeijmakers et al. (2014)] that intrinsic modes can become unstable for certain flame parameters. Whether the criterion is the same for a practical combustor, is an unanswered question, requiring investigation. Courtine et al. (2015) mention that acoustic reflection from the ends of the combustor can further facilitate the instability. But the analytical criterion for which this phenomenon occurs is still unknown. The intrinsic modes (whenever they might exist) definitely coexist with an infinite number of acoustic modes within a combustor. However, how this coexistence takes place and whether under some conditions these modes can couple with each other, are important unanswered questions in the context of thermo-acoustic instability. All of these unanswered questions call for the development of a comprehensive analytical model, to describe the presence of intrinsic modes and their relation to classical acoustic modes within a combustor, as well as the instability criterion for the intrinsic modes.

Once the reality of the intrinsic modes has been established beyond any doubt, naturally, the following questions come to the fore. It would be highly desirable to have an analytical criterion for the appearance of unstable intrinsic modes in a combustor and to also know the boundaries and topology of the instability domain in the multidimensional parameter space of a combustor. Besides, the effects of the combustor properties (e.g., flame location, boundary conditions at the ends, and parameters of the cross-section and temperature jumps) on the flame intrinsic mode growth rates and positions must be studied. To grasp the stability behavior of intrinsic modes in a multidimensional parameter space, via numerics, might be extremely

time-consuming, if not impossible. It is also a matter of fundamental importance to find how these intrinsic modes live together with the conventional acoustic modes. A comprehensive picture of all forms of instability, due to acoustic and intrinsic modes, is needed for better understanding of combustion instability. The present work addresses all these aspects.

Here we consider a standard 1-D acoustic model of a combustor with closed-open and open-open end conditions with a heat source inside. The heat release rate is modeled by the linear $n - \tau$ law [Croco and Cheng (1956)]. Within the framework of this simplified model, we provide an overall picture of the intrinsic modes and explicit analytical expressions for the parameters of the intrinsic modes (growth rates, neutral curves, frequencies of unstable modes) for the whole range of the system parameters. We also show that whatever the properties of the 1-D combustor, including the end conditions, there is always an infinite number of intrinsic modes present. For small n, we derive explicit universal dispersion relation for intrinsic modes. These modes strongly decay for small n, which makes them practically impossible to observe. In closed-open combustors these modes can become unstable with increase of n. The main discovery is that on the neutral curve the transcendental dispersion relation can be factorized for ideal closed-open and open-open combustors. We call this phenomenon *decoupling*. Factorization means that the intrinsic modes become completely decoupled from the environment, i.e. it does not feel the properties of the combustor. This allows us to treat this problem analytically and to derive all the characteristics of intrinsic mode instabilities. The instability domain geometry proved to be so complicated that it would have been close to impossible to retrieve it numerically. For the situations where the intrinsic mode frequencies are very close to those of the acoustic modes, we show that strong coupling is possible. We consider

this scenario thoroughly. The effect of different boundary conditions, like non-ideal, closed-open, or open-open, on the intrinsic flame instability is also considered.

The structure of the thesis: The thesis is organized as follows: In **chapter 2**, we develop a mathematical model to describe the intrinsic flame instability of a 1-D combustor with closed-open end conditions, assuming a linear $n - \tau$ flame model and considering the cross-section and temperature jump across the flame. We find the analytical solutions for the principle parameters describing combustion instability, which are the instability frequency and growth rate. At the same time, we offer a comprehensive intrinsic instability diagram considering multiple intrinsic modes. We reiterate that at present all known analytical results for intrinsic modes are confined to anechoic environment only. In **chapter 3**, we describe a new form of instability that arises due to the coupling of intrinsic flame modes and conventional acoustic modes, and thus we provide an overall picture of thermo-acoustic instability that is subdivided into three categories: acoustic mode instability, intrinsic mode instability and instability due to the coupling of intrinsic and acoustic modes. In **chapter 4**, we extend the analysis developed in chapter 2 for a combustor with open-open end conditions and identify the salient difference between the intrinsic flame instability of a closed-open and an open-open combustor. In **chapter 5**, we consider cases where the end conditions of the combustors are imperfect (not perfectly closed or open) and show that the analytical solutions of chapter 2 and 4 are robust. In **chapter 6**, we summarize the main results and identify a few domains where the current work could be extended into.

Throughout this thesis, we use the following convention while referring to equations, figures, and sections.

(a) If a section is numbered as section (X.Y) where X is the chapter number and Y is the section number, we refer to it as Y within the same chapter, whereas, otherwise we refer to it as section Y of chapter X.

(b) If an equation or figure is numbered as (X.Y), where X is the chapter number and Y is the equation or figure number, we refer it as equation (Y) or figure (Y) within the same chapter, whereas, otherwise we refer to it as equation (X.Y) or figure (X.Y).

Chapter 2

Intrinsic flame instabilities in combustors: analytic description of a 1-D closed-open combustor model

2.1.   Introduction

Combustion instabilities can be observed in many systems such as liquid and solid propellant rockets, jet engines, ramjets, and industrial power plants. Combustion instability comes to the fore if the gain mechanisms associated with the non-steady combustion process are larger than the various loss mechanisms, due to viscous effects, heat transfer, particle relaxation and radiation damping [Poinsot et al. (1986)]. The prediction of gain processes driving combustion instability are, in general, diverse and complex as multiple phenomena should be taken into consideration: (i) the interaction between the flame and the turbulent length scales of the reacting and burnt gases, (ii) the interaction between the flame and the acoustics of the combustion chamber, (iii) the possible coupling between entropy waves caused by the hot spots generated by the flame and the acoustic waves produced by the non-homogeneities in the mean flow [Silva et al. (2014)]. It has been common to assume that thermo-acoustic instabilities are triggered by the coupling of flame heat release and one of the acoustic modes. The acoustic modes exist even in the absence of the flame. Thus, the

overwhelming majority of studies of combustor instabilities in the last few decades has focused on the understanding of the acoustic modes, e.g. Lieuwen and Yang (2005), Poinsot and Veynante (2011), Schuller et al. (2012) and Dowling et al. (1995, 2003).

However, recently, a major limitation of the existing notion has been reported by Hoeijmakers et al. (2014) as mentioned in § 3 of chapter 1. Hoeijmakers et al. (2014) reported that the flame subsystem (Flame and air/fuel supply line) in a combustor can give rise to a completely new family of modes, which are often referred to as the *flame intrinsic modes*. Thus, a set of intrinsic flame modes (having the potential to become unstable) can exist in a combustor, apart from the conventional acoustic modes. The analytical analysis of Hoeijmakers et al. (2014) was confined to a system with non-reflecting end conditions. The governing dispersion relation for the flame in a non-reflecting acoustic environment was found to be, $\varepsilon + 1 + \theta F(\omega) = 0$, where $F(\omega)$ is flame transfer function, ε is the ratio of specific acoustic impedance and θ is the jump in temperature across the flame. The real parts of the intrinsic mode frequencies for an infinite system were found to be $(\pi \pm 2k\pi)/\tau$, where τ is the time lag and k is an integer. Independently, Bomberg et al. (2015) identified the existence of the intrinsic mode in two different experimental setups: laminar flame holder-stabilized and turbulent swirl-stabilized burner. The experiments by Bomberg et al. (2015), along with direct numerical simulations (DNS) by Courtine et al. (2014), Courtine et al. (2015) and Silva et al. (2015), where a flame is placed in an acoustically non-reflecting environment, have confirmed that the intrinsic thermo-acoustic feedback is a genuine physical phenomenon, and not just a spurious by-product of simplistic models. Thus, the standard notion that in thermo-acoustic

instabilities the flame heat release always locks onto one of the acoustic modes, needs to be critically reconsidered on a case-by-case basis.

Once the reality of the intrinsic modes has been established beyond any doubt, the following natural questions come into the picture. It would be highly desirable to have an analytical criterion on the appearance of unstable intrinsic modes in a combustor and to also know the boundaries and topology of the instability domain in the multidimensional parameter space of a combustor. Besides, the effects of the combustor properties (e.g., flame location, boundary conditions at the ends, and parameters of the cross-section and temperature jumps) on the intrinsic mode growth rates and positions must be studied. To grasp the stability behavior of intrinsic modes in a multidimensional parameter space, via numerics, might be extremely time-consuming, if not impossible. Overall, an integrated picture of the instabilities of acoustic and intrinsic modes is needed. The present work addresses this need by focusing on the intrinsic mode part of the picture.

Here we consider a standard 1-D acoustic model of a closed-open combustor with a heat source. The heat release rate is modeled by the linear $n - \tau$ law [Crocco and Cheng (1956)]. A closed-open assumption for acoustic ends of the combustor is suitable for analytical study purpose. The closed upstream of the combustor implies choked inlet nozzle for low Mach number [Lamarque and Poinsot (2008)]. Whereas, open downstream of the combustor implies that the flow goes into the open atmosphere, the reflection coefficient of which can be found from Munjal et al. (1987). However, in practical gas turbine assembly, there is a compressor assembly in the upstream and turbine assembly in the downstream of the combustor, imposing certain limitations on the perfectly closed or perfectly open assumption of acoustic ends. A detailed analysis on impedances at acoustic boundaries can be found from

Lamarque and Poinsot (2008), Silva et al. (2014), and Marble and Candel (1977). However, in the present context, within the framework of this simplified closed-open combustor model, we can provide an overall picture of the intrinsic modes and explicit analytical expressions for the parameters of the intrinsic modes (growth rates, neutral curves, frequencies of unstable modes) for the whole range of the system parameters.

The chapter is organized as follows. In **§ 2** we introduce our model of a closed-open combustor with the $n - \tau$ law of heat release and derive a dispersion relation for small amplitude oscillations. The dispersion relation considers the effects of the cross-section and temperature jumps across the flame. It forms the basis of the subsequent analysis. In **§ 3**, we derive an analytical expression for the intrinsic modes in the limit of a small interaction index, *n*. In this limit, the intrinsic modes are heavily damped. Their frequencies are described by the same analytical expression as for the case of an infinite tube found by Hoeijmakers et al. (2014). The distinctive features of acoustic and intrinsic modes are also highlighted and discussed using numerical results. In **§ 4** we describe decoupling of the intrinsic modes from their environment on the neutral curve and exploit it to derive explicit analytical expressions for the exact intrinsic mode neutral curve, separating stability/instability domains on the $n - \tau$ plane and the growth rate near the neutral curve. We also find the exact intrinsic mode frequencies on the neutral curve. The analytical results are then compared with numerical simulations within the framework of the dispersion relation obtained in § 2 and a very good agreement is demonstrated. In **§ 5** we examine the dependence on parameters (location of the flame, the cross-section and temperature jump) of the intrinsic modes. Finally, in **§ 6**, we summarize our advance

in the understanding of intrinsic modes in a combustor and outline the outstanding questions.

2.2. 1-D mathematical model of a closed-open combustor

Throughout this chapter, we will focus on the analytical study of flame intrinsic modes in a common 1-D model of the acoustic closed-open combustor. The previous analytical studies by Hoeijmakers et al. (2014) were performed for a tube with anechoic boundary condition. The results of the only analytical study of intrinsic flame modes by Mukherjee et al. (2016) will be presented in the next section. The acoustic modes in a combustor were extensively studied [see e.g., Lieuwen T., and Yang V. (2005)]. Here we adopt the basic acoustic model from Schuller et al. (2012). The analytical approach we put forward here can also be extended to more complicated combustor setups. However, for simplicity, we will restrict the current analysis to the simplest case of a closed-open combustor. The 1-D analytical formulation based upon the $n - \tau$ model provides an efficient versatile tool, enabling us to analyze the combustor modes and provides a valuable insight into the stability behavior of these modes in multi-dimensional parameter space.

Figure 1 provides a schematic sketch of a closed-open combustor with a compact heat source at $x = x_q$, with x being the longitudinal coordinate, with the origin at the closed end of the combustor. $A_1, A_2 / B_1, B_2$ are the pressure amplitudes for the forward/backward travelling waves in the upstream and downstream region, respectively. The cross-sectional area jumps across the flame, from S_1 to S_2. The mathematical model is based on the following assumptions:

(i)   We assume a 1-D acoustic model and thus the wave is assumed to propagate only in the axial direction (x). Any wave propagation in the transverse direction (y and z) is neglected in the model.

(ii)   The end conditions of the combustor are assumed to be ideal, i.e. one end is ideal-closed and another end is ideal-open.

(iii)   The flame is assumed to lie on a single hypothetical axial plane. Any distribution of the flame (heat release) in the axial direction is not considered for the time being.

(iv)   The flame heat release rate is modeled by the linear $n - \tau$ law [Crocco and Cheng (1956)]

(v)   Effect of mean flow and the subsequent hydrodynamic instabilities are ignored in this model. We also neglect the effect of turbulence in the model.

(vi)   In actual combustors, there is a distribution in temperature across the length of the combustor. To simplify our analytical model, we ignore this distribution of temperature and assume the mean temperature to jump from T_1 to T_2 across the flame.
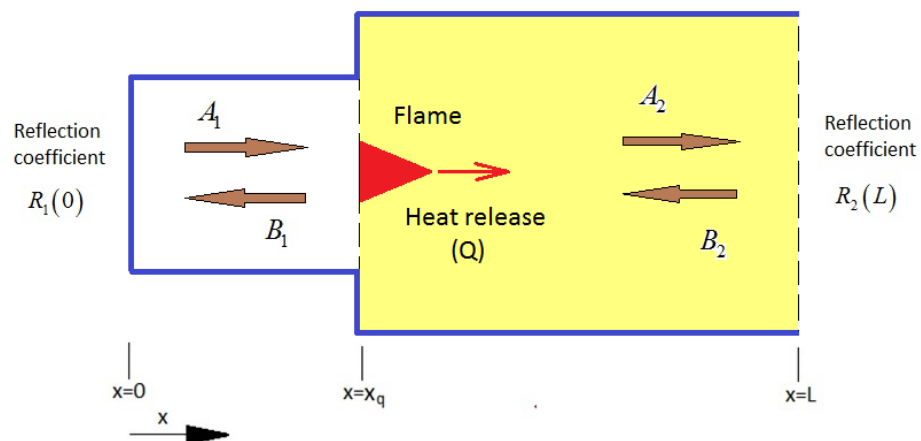
Figure 2.1: Schematic sketch of a combustor with closed-open end conditions. The combustor has a cross-sectional area jump at the flame location $x = x_q$. Thick brown arrows symbolize the forward/ backward traveling waves upstream/downstream of the flame. Yellow region marks the domain of higher temperature after the temperature jump across the flame.

The acoustic pressure and particle velocity at the upstream region and at the downstream region of the combustor can be written as harmonic functions in the space and time domain [e.g., Kinsler et al. (2000)]:

$$\tilde{p}_1(x,t) = \left[A_1 e^{ik_1 x} + B_1 e^{-ik_1 x} \right] e^{-i\omega t}, \quad \tilde{u}_1(x,t) = \left(\frac{1}{\rho_1 c_1} \right) \left[A_1 e^{ik_1 x} - B_1 e^{-ik_1 x} \right] e^{-i\omega t}, \text{ and}$$

(2.1)

$$\tilde{p}_2(x,t) = \left[A_2 e^{ik_2 x} + B_2 e^{-ik_2 x} \right] e^{-i\omega t}, \quad \tilde{u}_2(x,t) = \left(\frac{1}{\rho_2 c_2} \right) \left[A_2 e^{ik_2 x} - B_2 e^{-ik_2 x} \right] e^{-i\omega t}.$$

(2.2)

The wave numbers k_i ($i=1,2$) upstream and downstream of the flame can be presented as $k_1 = \omega/c_1$ and $k_2 = \omega/c_2$, where ω is the complex frequency, c_1, c_2 represents the speed of sound and ρ_1, ρ_2 are the mean densities upstream and downstream of the flame respectively. We assume ideal boundary conditions at the two ends,

$$\text{at } x = 0, \; A_1/B_1 = R_1(0) = 1, \text{ and,}$$

$$\text{at } x = L \; B_2 e^{-ikL}/A_2 e^{ikL} = R_2(L) = -1.$$

(2.3, 2.4)

When the mean flow is neglected, the 1-D continuity equation, momentum equation, and entropy equation, can be written as follows

Continuity equation: $\qquad \dfrac{\partial \tilde{\rho}}{\partial t} + \rho \dfrac{\partial \tilde{u}}{\partial x} = 0,$ (2.5)

Momentum equation: $\qquad \dfrac{\partial \tilde{u}}{\partial t} + \dfrac{1}{\rho} \dfrac{\partial \tilde{p}}{\partial x} = 0,$ (2.6)

Entropy equation: $\qquad T \dfrac{\partial \tilde{s}}{\partial t} = \tilde{q}.$ (2.7)

$\tilde{q}(x,t)$ is the heat release rate perturbation per unit mass, ρ and T are the mean density and mean temperature respectively.

By definition, change of entropy can be written as, $ds_t = \dfrac{dq_t}{T_t}$ [Sonntag et al. (2002)],

where the subscript 't' represents the total value (i.e. mean + perturbed value) of the thermodynamic state variables. From the first law of thermodynamics we know, $dq_t = du_t + p_t dv_t$, where v_t is the total specific volume (i.e. volume per unit mass) and the change of specific internal energy (i.e. internal energy per unit mass) is given as, $du_t = c_v dT_t$. Making use of these equations, we can rewrite $ds_t = \dfrac{dq_t}{T_t}$ as,

$$ds_t = c_v \frac{dT_t}{T_t} + \frac{R}{v_t} dv_t.$$

Integrating both sides of this expression we arrive at an equation for total entropy, $s_t = c_v \ln(T_t) + R \ln(v_t)$. Further, by making use of ideal gas equation, $p_t v_t = RT_t$ or $p_t = \rho_t RT_t$, we can derive the final expression for entropy in terms of thermodynamic state variables p_t and ρ_t,

$$s_t = c_v \ln\left(\frac{p_t}{\rho_t^{\gamma}}\right).$$

As mentioned previously, the total values of these thermodynamic state variables comprise both mean and perturbed values. Differentiating both sides of the total entropy equation $s_t = c_v \ln\left(\dfrac{p_t}{\rho_t^{\gamma}}\right)$ with respect to time, 't' and assuming that the mean values of all the thermodynamic state variables are constant with respect to time, we obtain,

$$\frac{\partial \tilde{s}}{\partial t} = c_v \left[\frac{1}{p}\frac{\partial \tilde{p}}{\partial t} - \frac{\gamma}{\rho}\frac{\partial \tilde{\rho}}{\partial t}\right]. \tag{2.8}$$

Making use of (8), equation (7) yields,

$$\frac{\partial \tilde{\rho}}{\partial t} = \frac{\rho}{c_p T} \left[c_v \frac{T}{p} \frac{\partial \tilde{p}}{\partial t} - \tilde{q} \right].$$

Differentiating both sides of this equation with respect to time, 't' provides us the following,

$$\frac{\partial^2 \tilde{\rho}}{\partial t^2} = \frac{\rho}{c_p T} \left[c_v \frac{T}{p} \frac{\partial^2 \tilde{p}}{\partial t^2} - \frac{\partial \tilde{q}}{\partial t} \right]. \tag{2.9}$$

Further, differentiating equation (5) with respect to 't' and equation (6) with respect to 'x', and thereafter subtracting one equation from the other leads us to,

$$\frac{\partial^2 \tilde{\rho}}{\partial t^2} = \frac{\partial^2 \tilde{p}}{\partial x^2}. \tag{2.10}$$

Using equation (9) in equation (10) and making use of $c_p = \gamma R / (\gamma - 1)$, or, $c_p T = c^2 / (\gamma - 1)$, we arrive at the final simplified form of the wave equation for a combustor with the flame heat release rate perturbation,

$$\frac{1}{c^2} \frac{\partial^2 \tilde{p}}{\partial t^2} - \frac{\partial^2 \tilde{p}}{\partial x^2} = \frac{(\gamma - 1)\rho}{c^2} \frac{\partial \tilde{q}}{\partial t}. \tag{2.11}$$

Equations (6) and (11) can be simplified assuming $e^{-i\omega t}$ dependence of $\tilde{p}$, $\tilde{u}$ and $\tilde{q}$ for a thin flame configuration depicted here in figure 1 (recall that we assume the flame to lie on single axial hypothetical plane in our model. In other words, the flame can be treated as infinitely thin). Equation (6) when integrated across the flame thickness Δx provides the following,

$$\int_{x_q}^{x_q + \Delta x} \left(-i\omega \tilde{u} + \frac{1}{\rho} \frac{\partial \tilde{p}}{\partial x} \right) dx = 0,$$

which can be simplified as,

$$-i\omega\tilde{u}\left(\Delta x\right)+\frac{1}{\rho}\left(\tilde{p}_2-\tilde{p}_1\right)=0. \tag{2.12}$$

For an infinitely thin flame $\Delta x \to 0$, hence, equation (12) reduces to the following,

$$\tilde{p}_1 = \tilde{p}_2. \tag{2.13}$$

This offers us a continuity of acoustic pressure across the thin flame configuration.

Moreover, using equation (6), equation (11) can be restructured as,

$$\frac{1}{c^2}\frac{\partial^2 \tilde{p}}{\partial t^2}+\rho\frac{\partial^2 \tilde{u}}{\partial x \partial t}=\frac{(\gamma-1)\rho}{c^2}\frac{\partial \tilde{q}}{\partial t}. \tag{2.14}$$

Equation (14) when integrated across the flame thickness Δx provides us another jump condition across the flame in the harmonic domain. To this end, we assume the form $\tilde{q}=\tilde{Q}\delta\left(x-x_q\right)/\rho S$, $\tilde{Q}$ is the heat release rate perturbation (recall that $\tilde{q}$ is the heat release rate perturbation per unit mass). This leads us to the following,

$$\int_{x_q}^{x_q+\Delta x} S\left[\frac{1}{c^2}\left(-\omega^2\tilde{p}\right)+\left(-i\omega\right)\frac{\partial \tilde{u}}{\partial x}\right]dx = \int_{x_q}^{x_q+\Delta x} \frac{(\gamma-1)}{\rho c^2}\left(-i\omega\tilde{Q}\left(x-x_q\right)\right)dx,$$

which can further be simplified to,

$$\left(\frac{S_2}{\rho_2 c_2^2}-\frac{S_1}{\rho_1 c_1^2}\right)\left(-\omega^2\tilde{p}\right)\Delta x+\left(-i\omega\right)\left(S_2\tilde{u}_2-S_1\tilde{u}_1\right)=\frac{(\gamma-1)}{\rho_1 c_1^2}\left(-i\omega\tilde{Q}\right). \tag{2.15}$$

For infinitely thin flame $\Delta x \to 0$, and thus equation (15) reduces to the following jump condition of flow velocity across the flame,

$$S_1\tilde{u}_1+\frac{(\gamma-1)}{\rho_1 c_1^2}\tilde{Q}=S_2\tilde{u}_2. \tag{2.16}$$

The pressure and flow rate balance at the flame location, $x=x_q$, thus, can be obtained from (13) and (16) [see Dowling et al. (1995), Bauerheim et al. (2015) for further details].

Here, $\tilde{Q}(t)$ is the heat release rate perturbation at $x = x_q$ and γ represents the ratio of specific heats of air (c_p/c_v) [Sonntag et al. (2002)]. It is assumed that the heat source acts like a monopole with a volume outflow $(\gamma-1)(\tilde{Q}/\rho_1 c_1^2)$ [Dowling et al. (1995), and also shown in equation (16)]. The linear heat release law can be assumed to be of the form, [see e.g., Truffin et al. (2002); Truffin and Poinsot (2005)]

$$\tilde{Q}(t) = \left(\rho_1 S_1 c_1^2/(\gamma-1)\right) n \tilde{u}_1(t-\tau). \tag{2.17}$$

Here, n and τ are the interaction index and time lag respectively. The rate of heat release fluctuations, $\tilde{Q}$, is assumed to be proportional to the local velocity upstream of the flame, $\tilde{u}_1$, with a time lag, τ. In the frequency domain, this can be written as [Truffin and Poinsot (2005)],

$$\tilde{Q}(\omega) = \left(\rho_1 S_1 c_1^2/(\gamma-1)\right) n e^{i\omega\tau} \tilde{u}_1(\omega). \tag{2.18}$$

In the normalized form (i.e. heat release rate perturbation and velocity perturbation both normalized by the mean quantities), equation (18) yields an expression of the flame transfer function, as explained in § 2.2.1 of chapter 1, $FTF(\omega) = n e^{i\omega\tau}$. Thus, n and τ provide information on the gain and the phase of the flame transfer function respectively. The set of homogeneous equations for A_1, B_1, A_2 and B_2, (3), (4), (13) and (16) is usually presented in the matrix form [e.g., Schuller et al. (2012); Munjal and Mukherjee (2010, 2011)]

$$
\begin{bmatrix}
1 & -1 & 0 & 0 \\
e^{ik_1 x_q} & e^{-ik_1 x_q} & -e^{ik_2 x_q} & -e^{-ik_2 x_q} \\
\left(1+ne^{i\omega\tau}\right)e^{ik_1 x_q} & \left(\begin{array}{c}-1\\-ne^{i\omega\tau}\end{array}\right)e^{-ik_1 x_q} & -\left(\dfrac{S_2}{S_1}\right)\left(\dfrac{\rho_1 c_1}{\rho_2 c_2}\right)e^{ik_2 x_q} & \left(\dfrac{S_2}{S_1}\right)\left(\dfrac{\rho_1 c_1}{\rho_2 c_2}\right)e^{-ik_2 x_q} \\
0 & 0 & -e^{ik_2 L} & -e^{-ik_2 L}
\end{bmatrix}
\begin{Bmatrix} A_1 \\ B_1 \\ A_2 \\ B_2 \end{Bmatrix} =
\begin{Bmatrix} 0 \\ 0 \\ 0 \\ 0 \end{Bmatrix}
$$

$$. \tag{2.19}$$

However, here it becomes essential to use a compact dispersion relation. The compact form of dispersion relation provides the basis of all analytical derivations in the subsequent sections. For a nontrivial solution of the eigen-value problem (19) to exist, the determinant of the 4×4 matrix in (19) has to be zero, which yields

$$\left[(S_2/S_1)(\rho_1/\rho_2)(c_1/c_2)+1\right]\cos\left((k_2-k_1)x_q-k_2L\right)+$$
$$\left[(S_2/S_1)(\rho_1/\rho_2)(c_1/c_2)-1\right]\cos\left(k_2L-(k_1+k_2)x_q\right)+2ne^{i\omega\tau}\sin k_1x_q\sin k_2\left(x_q-L\right)=0.$$

$$(2.20)$$

We denote the function on the left-hand side of transcendental equation (20) as $f(\omega)$. Further, for brevity, we will refer to $f(\omega)$ as 'detuning'. Thus, dispersion relation (20) can be re-written compactly as,

$$f(\omega)=0.\tag{2.21}$$

The dispersion relation can be simplified for special cases worth considering in detail. When there is no cross-section and temperature jump across the flame, that is $S_1=S_2$ and $T_1=T_2$, and thus $c_1=c_2$, $\rho_1=\rho_2$ and $k_1=k_2=k$, the dispersion relation (20) reduces to

$$\cos kL+ne^{i\omega\tau}\sin kx_q\sin k\left(x_q-L\right)=0.\tag{2.22}$$

The dispersion relation (22) can be further simplified, when the flame is located exactly in the center of the combustor, i.e. at $x_q=L/2$,

$$\cos kL=ne^{i\omega\tau}/\left(2+ne^{i\omega\tau}\right).\tag{2.23}$$

The dispersion relation (20), (22) and (23) prescribes the eigen-frequencies ω of the system in implicit form. Equation (20) describes the most general case (a closed-open combustor with a cross-section and temperature jump across the flame), while

44

equations (22) and (23) are the reduced versions of (20) for special cases. The real part of ω is the frequency and the imaginary part is the growth/decay rate. Since the dispersion relation in the form (20) is more amenable for analytical study than the commonly used matrix formulation (19), we employ it as the starting point for our subsequent analysis. For an insight into the physics of flame intrinsic modes, the particular simplifications of the dispersion relation (22), (23) will be also used. There is no general method enabling one to solve transcendental equations of this type [Kreyszig (2011)]. However, as we show in **§** 4, the dispersion relation can be factorized on the neutral curves, which allows us to find the neutral curve exactly and approximate solutions in its vicinity.

2.3. The place of intrinsic modes in the general picture of the combustor modes

In this section, we derive analytical expressions for the intrinsic mode frequency and decay rate in the limit of small n, for a closed-open combustor and numerically validate the formula [Also presented in the work of Mukherjee et al. (2016)].

2.3.1. Analytical expression for intrinsic modes in the limit of small n

To introduce this idea, we start with the simplest form of the dispersion relation, namely, (23), which provides an implicit expression for all the modes present in the combustor. The presence of flame intrinsic modes different from the conventional acoustic modes, has been established recently [Hoeijmakers et al (2014)]. The intrinsic modes observed in experiments and simulations, see e.g. [Bomberg et al. (2015), Courtine et al. (2015), Silva et al. (2015)], were both stable and unstable modes. These modes seemingly appear out of nowhere. To understand better the place of intrinsic modes in the big picture, it is desirable to know whether these

modes exist when they are not unstable, and if this is the case, where in the complex plane are their frequencies. In this section, we address these questions for the case of a closed-open combustor in the limit of a weak flame. From the simplified dispersion relation (23) it is easy to see that for $n \to 0$ there are only two sets of roots:

(i)   the conventional acoustic modes specified by the condition $\cos kL = 0$, and,

(ii)   a new set of roots with large negative imaginary part (this is, $|e^{i\omega\tau}| \gg 1$, or, in other words, the strongly damped modes). This can be explained as follows. For nonzero $\cos kL$, there is only one possibility for equation (23) to have solutions, that is the numerator must be $O(1)$. This implies that when n is small, $e^{i\omega\tau}$ has to be large ($O(1/n)$). We now apply the same reasoning to the general case.

To find the roots of the full dispersion relation (20) in the limit of small n, we simplify the trigonometric expressions in (20) using Euler's formula, that is $\cos\alpha = (e^{i\alpha} + e^{-i\alpha})/2$, and $\sin\alpha = (e^{i\alpha} - e^{-i\alpha})/2i$, and divide both sides of the resulting equation by $e^{i((k_1 - k_2)x_q + k_2 L)}$. This leads to the following expression,

$$\left[\left(\frac{S_2}{S_1}\right)\left(\frac{\rho_1 c_1}{\rho_2 c_2}\right) + 1\right]\left(e^{2i(k_2(x_q - L) - k_1 x_q)} + 1\right) + \left[\left(\frac{S_2}{S_1}\right)\left(\frac{\rho_1 c_1}{\rho_2 c_2}\right) - 1\right]\left(e^{-2ik_1 x_q} + e^{2ik_2(x_q - L)}\right)$$
$$-ne^{i\omega\tau}\left(e^{2ik_2(x_q - L)} - 1 - e^{2i(k_2(x_q - L) - k_1 x_q)} + e^{-2ik_1 x_q}\right) = 0 \quad .$$

(2.24)

By the same reasoning (as for the simplified dispersion relation considered above), the new set of roots (intrinsic modes) for the full dispersion relation (20), must have a large negative imaginary part. Thus, for these new roots, all the exponents in (24), (that is $2i(k_2(x_q - L) - k_1 x_q)$, $-2ik_1 x_q$ and $2ik_2(x_q - L)$) are highly negative as well.

Hence, for small n, $e^{-2ik_1 x_q} \to 0$, $e^{2ik_2(x_q - L)} \to 0$, $e^{2i\left(k_2(x_q - L) - k_1 x_q\right)} \to 0$. Then

dispersion relation (24) assumes the simplified form,

$$\left[(S_2/S_1)(\rho_1/\rho_2)(c_1/c_2) + 1\right] + ne^{i\omega\tau} = 0 . \tag{2.25}$$

The general solution of equation (25) is

$$i\omega\tau = \left(2m^i + 1\right)i\pi + \ln\left(\left[(S_2/S_1)(\rho_1/\rho_2)(c_1/c_2) + 1\right]/n\right),$$

Which instantly provides us with an explicit expression for the modal frequency, in

the asymptotic limit of small n,

$$\begin{aligned} \omega &= \left(2m^i + 1\right)(\pi/\tau) - (i/\tau)\ln\left(\left[(S_2/S_1)(\rho_1/\rho_2)(c_1/c_2) + 1\right]/n\right) \\ &\approx \left(2m^i + 1\right)(\pi/\tau) + (i/\tau)\ln(n) \end{aligned} . \tag{2.26a,b}$$

where m^i is the mode number of the flame intrinsic modes. This expression (26a) is

identical to the result found by Hoeijmakers et al. (2014) for an infinite tube with a

flame inside. Thus, in the limit of small n, intrinsic modes for 1-D closed-open

combustor have the same frequencies as those in the infinite tube. We stress that the

frequencies given by (26a) do not depend on any parameters of the combustor,

including the end conditions. Note that the intrinsic modes have their own mode

numbers, completely independent of the mode numbers of the acoustic modes.

From equation (26b) it is also easy to see that in the limit of small n, there is always

an infinite number of intrinsic modes present in the system for any n and τ. The real

part of the flame intrinsic mode frequency depends only on the time lag alone and is

given by the expression, $\left(2m^i + 1\right)(\pi/\tau)$. The decay rates, however, do not depend on

the mode number (m^i). Decay rates are inversely proportional to τ and

logarithmically dependent upon n, the temperature jump and cross-section jump of

the combustor. In the asymptotic limit of small n, the flame intrinsic modes are

strongly damped and independent of the characteristics of the combustor and flame position. Since the decay rate is high, the intrinsic modes to leading order in $e^{-ik_1 L}$, do not feel the combustor boundaries. This explains why the result coincides with those for the infinite tube. The practical implication of strong damping of the intrinsic modes in combustors with weak flames, is that this feature makes it practically impossible to observe their manifestations in such regimes.

Thus, for small but non-zero n, there is always an infinite number of flame intrinsic modes present in a combustor, just as there is an infinite number of acoustic modes present in a combustor. However, in contrast to nearly neutral acoustic modes, for small n, all these modes are strongly damped. They cease to exist for $n = 0$, while acoustic modes do not. We have established that in the limit of small n these modes are equally spaced and their frequencies are determined only by the time lag τ and, correspondingly, do not depend at all on other characteristics of the system. We will show below that the intrinsic modes become unstable only once the value of n exceeds a certain threshold. Their behavior near the neutral curve will be studied in § 4. In of itself, the dispersion relation behavior in the limit of small n is only important in the context of outlining the general picture of intrinsic modes. But its significance becomes apparent in § 4 since the frequencies of intrinsic modes on the neutral curve prove to coincide exactly with the real parts of the eigen-values found in the small n limit.

2.3.2.   Understanding the stability behavior of intrinsic modes

Here we examine the features of the full dispersion relation (20) numerically. As an example, we consider a combustor with the parameters of the test rig at IIT Madras [Vishnu et al. (2015)]: the length L is 0.75 m, the cross-section S is 0.0016 m^2, the

temperature T is constant throughout the duct and equal to 297 K when there is no flame.
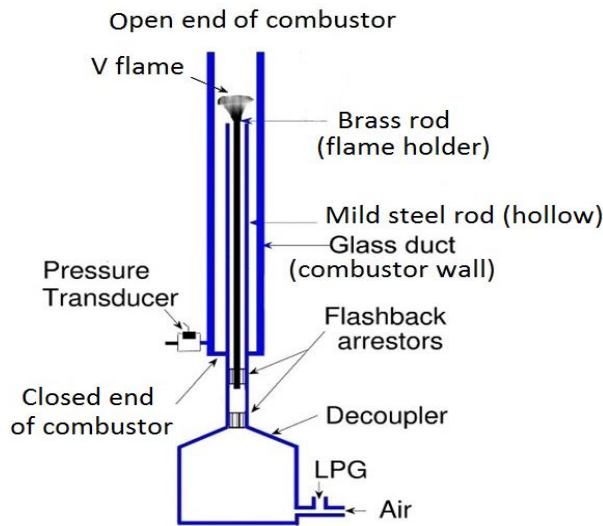
Figure 2.2: Sketch of the experimental setup [Vishnu et al. (2015) and Mukherjee et al. (2015)]. The glass duct, marked by thick blue line shows combustor wall. The upper end of the glass duct is open and the lower end is flanged (closed). The flame sits on the tip of a brass rod (shown by thick black line), concentric to the glass duct. There is a hollow mild steel rod (shown by thin blue line) concentric to this glass duct. Supply of air-fuel mixture comes via this mild steel rod. The flame can be traversed across the glass duct using a traversing mechanism (not shown in the figure). The figure is not to scale.

Figure 2 provides a sketch of the setup. The actual setup consists of a glass duct (shown by thick blue line) with the top end open and the bottom end closed. Concentric to the duct there is a thin brass rod (shown by the black line), at the tip of which the flame sits. There is a hollow mild steel rod (shown by thin blue line) concentric to this brass rod, through which air/fuel mixture comes in. In the actual setup, there is a substantial temperature jump across the flame. However, for simplicity, we ignore this temperature jump in most of our numerical and analytical study, except in § 5, where we focus on the effect of the temperature jump across the flame on intrinsic flame instability. The flame in the setup can be traversed across the length of the glass duct. For most of our analysis, we assume the flame to be located at $x_q = L/2$. However, we stress that the specific parameters of the combustor are

49

immaterial for our study and they are used for illustration only. If the 1-D model idealization and the ideal end conditions assumptions remain valid, our analytical model is independent of the combustor specific properties and dimensions.

A valuable insight into the nature of the intrinsic modes can be gained through a set of contour plots of the absolute value of function $f(\omega)$, prescribed in the full dispersion relation (20, 21). On the complex ω plane, these plots show the topology of $f(\omega)$ with both the frequencies and the growth/decay rates of the modes at the same time. They also facilitate a comparative study of acoustic and intrinsic modes. In figures 3-5, acoustic modes are marked with diamonds, while intrinsic modes are shown by triangles. The acoustic mode frequencies are $(2m^a + 1)(\pi c/2L)$ (for $m^a = 0, 1, 2...$) [Kinsler et al. (2000)] and have zero growth rates in figure 3. The instability domain is marked in yellow. The iso-lines in the figures 3-5 present the mapping of the absolute value of detuning function $f(\omega)$ onto the complex ω plane. The innermost closed loops of the iso-lines represent the solution region for modal frequency ω. The number of frequencies in the system far exceeds the number of acoustic modes, as was also noted by Emmert et al. (2016) in their analysis of a premixed combustor.

To show in the same figure the iso-lines of detuning $|f(\omega)|$ for both acoustic and intrinsic modes with a huge difference in the decay rates, we split figure 3 into two panels: for small interaction index n ($n = 0.025$) and time lag, τ, equal to 3 ms. In the chosen frequency range, there are three intrinsic modes with strong decay rates, as shown in the bottom panel. These modes are equally spaced and the frequencies of these modes are well predicted by (26a). The upper panel shows acoustic modes,

which are neutral for the chosen n and τ. When, in figure 4, n is increased from 0.025 to 1.0, the decay rates of the intrinsic modes significantly decrease.
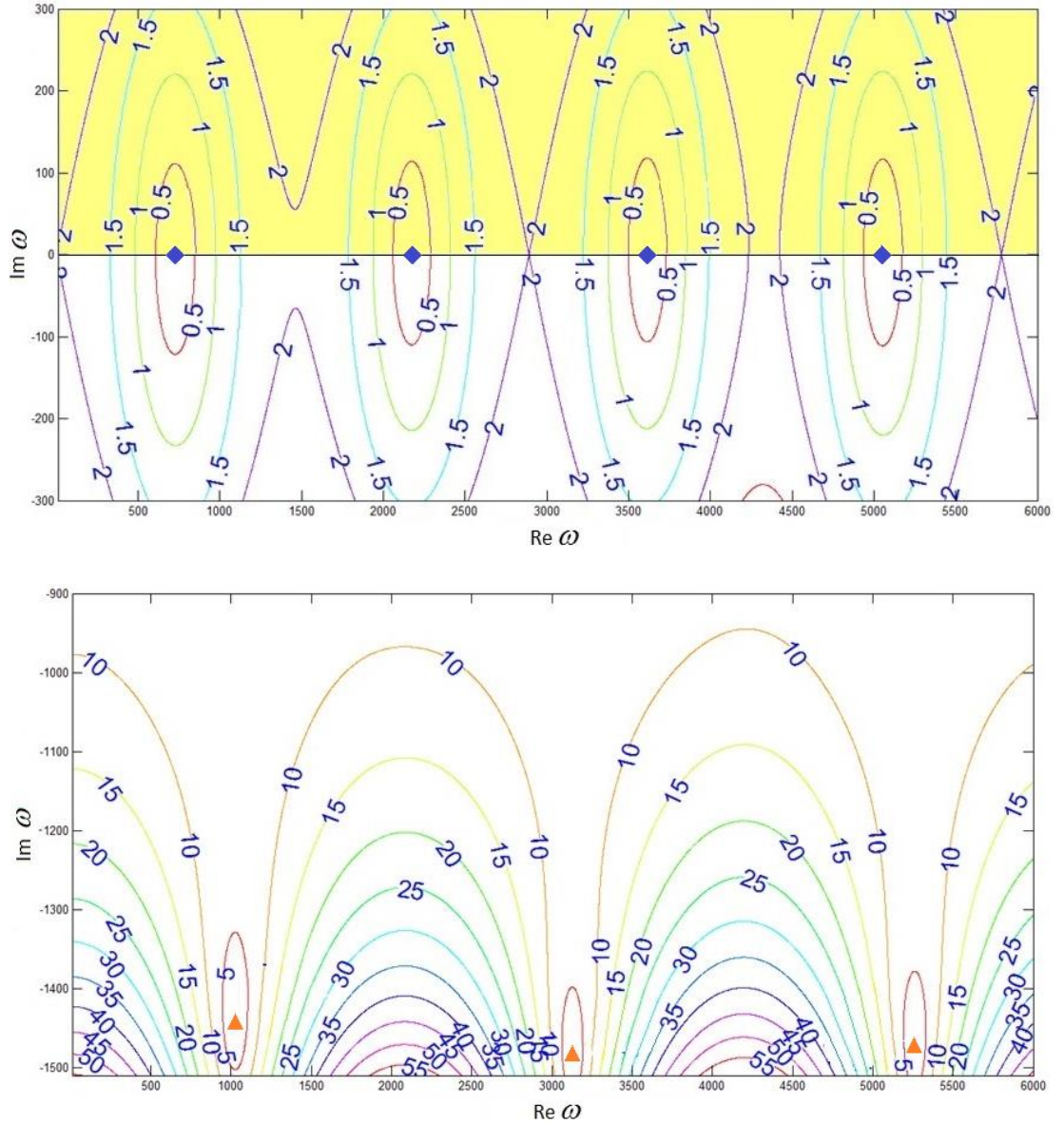
Figure 2.3: Contour plot of detuning $|f(\omega)|$ for $n = 0.025$ and $\tau = 3.0$ ms. The parameters used for this plot are: the length L is 0.75 m, the cross-section S is 0.0016 m², the temperature T is assumed constant throughout the duct and equal 297 K. The flame is located at $x_q = L/2$, $c_1 = c_2 = 345$ m/s. The two sections are parts of the same contour plot. The domain of instability is marked in yellow. Blue diamonds and orange triangles represent the acoustic and intrinsic modes respectively.
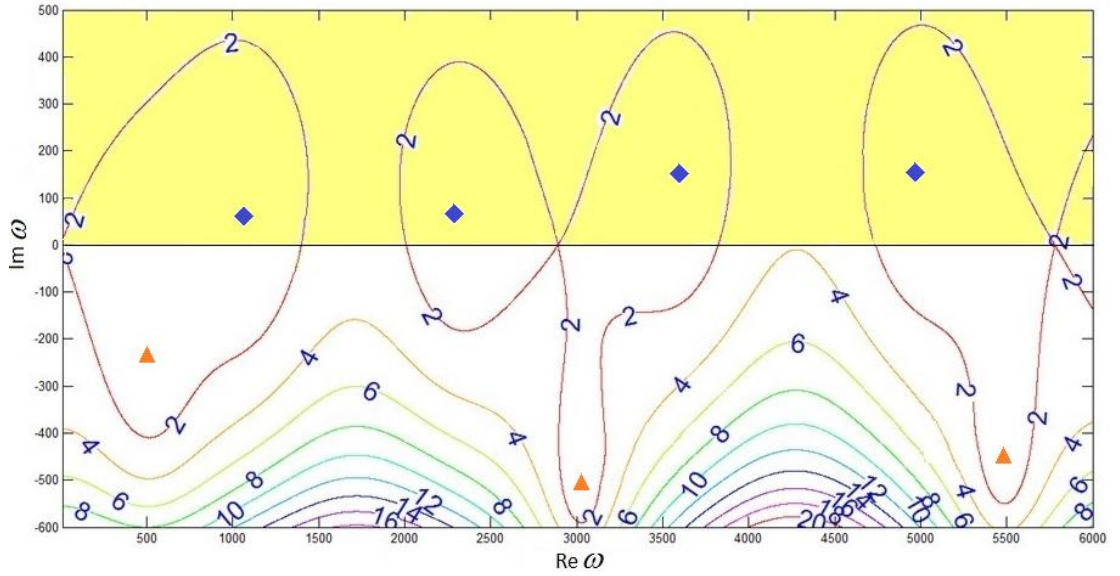
Figure 2.4: Contour plot of $|f(\omega)|$ for $n = 1.0$, $\tau = 3.0$ ms. Notation and other parameters are the same as in Fig 3.
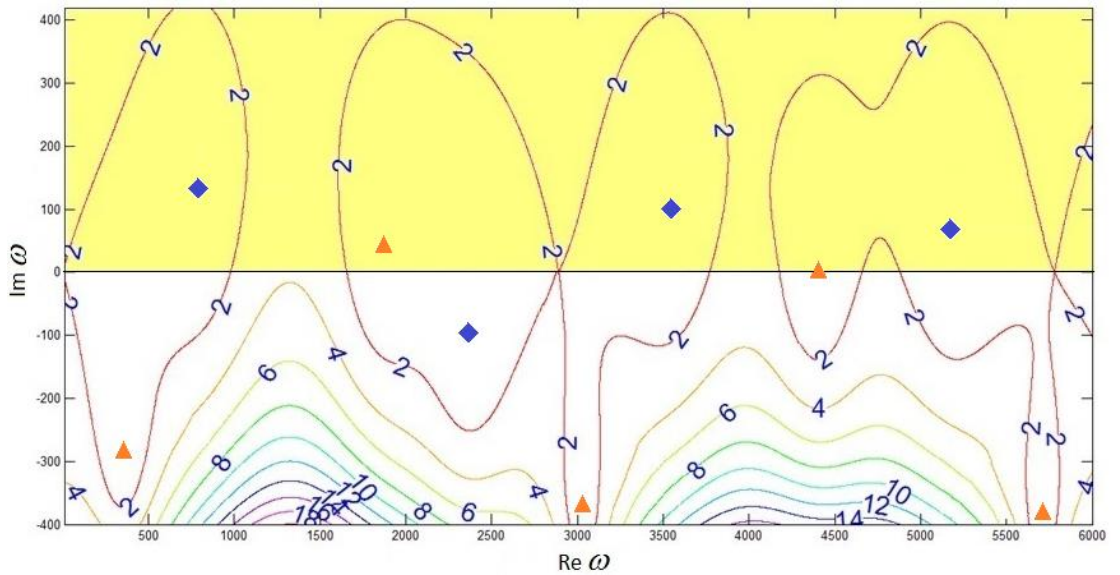
Figure 2.5: Contour plot of $|f(\omega)|$ for $\tau = 5.0$ ms and $n = 1.0$. Notation and other parameters are the same as in Fig.3.

Comparison of figures 4 and 5 shows that increasing τ from 3 ms to 5 ms reduces the intrinsic mode frequency. At some threshold value of n, these intrinsic modes become unstable. For example, the fourth intrinsic mode at 4398 rad/s becomes unstable when n is 1.0. Further numerical simulations (not shown here) indicate that

all intrinsic modes become unstable upon exceeding a certain n-threshold that will be predicted analytically in § 4.2.

To summarise, we can say that the intrinsic modes are strongly damped in the limit of small n and in this range, are easily distinguishable from acoustic modes. On the complex ω plane, the modes could be always distinguished by tracing their position by varying n. The frequency of the intrinsic modes depends primarily on τ and does not depend on any parameters of the combustor. We stress that the frequency depends on n very weakly (except for intrinsic-acoustic mode coupling scenario, which will be discussed, in detail, in chapter 3). In contrast, the intrinsic mode stability is strongly dependent on n. These modes become unstable upon exceeding a certain threshold value of n.

2.3.3.   Maps of acoustic and intrinsic modes on the $n-\tau$ plane

The similarities and the differences between acoustic and intrinsic modes can also be elucidated by a set of maps on the $n-\tau$ plane. These maps offer us a lucid picture of the evolution of intrinsic modes in the parameter space, also serving as a validation tool for our analytical results of § 3.1. Figures 6 and 7 give examples of such kinds of maps for acoustic and intrinsic modes. The acoustic modes are indicated by diamonds and intrinsic modes by circles. These modal frequencies are tracked down manually on the complex frequency plane (as shown in contour plots 3-5) by changing parameters n and τ.
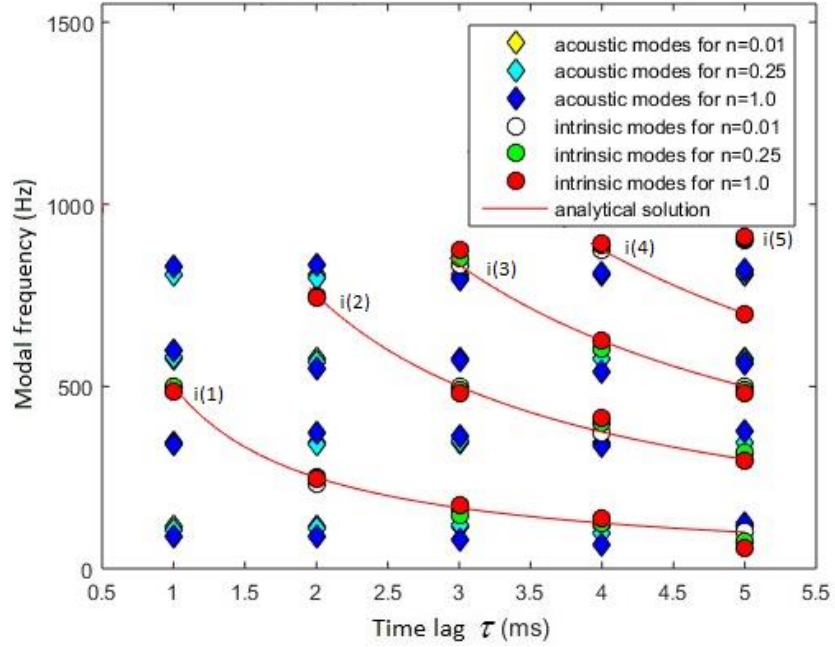
Figure 2.6: Map of acoustic (diamonds) and intrinsic (circles) modes: modal frequency vs. time lag τ for n =0.01, 0.25, 1.0. Solid lines i(1), i(2), i(3), i(4) and i(5) show the analytical solution (26a) for the first, second, third, fourth and fifth intrinsic modes, respectively, for small n. Other parameters are the same as in Fig.3.
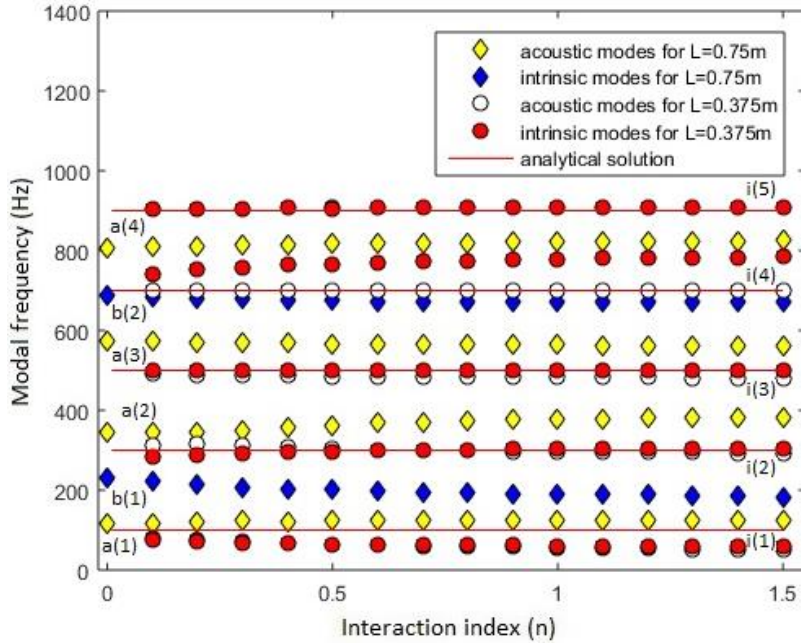
Figure 2.7: Maps of acoustic (diamonds) and intrinsic modes (circles): modal frequency vs. interaction index n. Solid lines i(1), i(2), i(3), i(4) and i(5) show the analytical solution (26a) for the first, second, third, fourth and fifth intrinsic modes, respectively, for small n. The plot is for: τ =5 ms and two different combustor lengths: L = 0.75m, 0.375m. The numerical solutions for the first, second, third and fourth acoustic modes are represented by a(1), a(2), a(3) and a(4), respectively, for L = 0.75m, whereas, the numerical solutions for the first and second acoustic modes are represented by b(1) and b(2), respectively, for L = 0.375m. Other parameters are the same as in Fig.3.

In figure 6, the time lag, τ, varies from 1 ms to 5 ms. Three different values of n are considered: $n = 0.01$, 0.25 and 1.0 and the corresponding modal frequencies are obtained using contour plots. The numerical results are compared with the analytical solution (26a). The flame intrinsic mode frequencies have a $(1/\tau)$ dependence well outside the limit of small n, which is shown by solid line hyperbolae. For this case, the key numerical observation is that a substantial variation of n hardly alters the intrinsic mode frequencies.

In figure 7, τ is fixed at 5 ms and n is varied from 0 to 1.5. The corresponding modal frequencies are obtained from the contour plots, similar to figures 3-5. When the flame is not present in the system, (that is, $n = 0$), the intrinsic modes are absent, while the frequencies of the acoustic modes are $(2m^a + 1)(\pi c/2L)$ (for $m^a = 0, 1, 2\ldots$) for a closed-open combustor. As we increase n, the flame intrinsic modes emerge. The intrinsic mode frequencies are weakly dependent on n [when there is no coupling with the acoustic modes]. In the range of n considered here, the overall change of the intrinsic mode frequency is less than 5%. To illustrate the weak dependence of intrinsic mode frequencies on the combustor length, figure 7 presents results for two different combustor lengths.

Thus, we can confirm that the evolution of intrinsic modes on the $n - \tau$ plane is indeed completely independent of the acoustic modes in the range of small n. Crucially, the analytical prediction of the intrinsic mode frequencies (26a), obtained in the asymptotic limit of small n, is found to be a very good approximation for a wide range of n.

2.4.   Intrinsic mode instability: neutral curves and growth rates

Hoeijmakers et al. (2014) found intrinsic modes to be unstable for some values of n and τ. Small n limit of the dispersion relation (26b) also suggests that the decay rate of intrinsic modes is logarithmically dependent on n. As n increases, the decay rate decreases and at some threshold value of n, the decay rate crosses zero, making the intrinsic mode unstable. Here, in § 4.1, we will derive an exact analytical expression for the intrinsic mode frequency at the neutral curve. Then, in § 4.2, we will find the exact threshold value of n for intrinsic mode instability, that is, we will find the neutral curve in the $n-\tau$ parameter space. In § 4.3 we derive the growth/decay rates near the neutral curve. The geometry of instability domains for each mode proved to be quite complicated. Hence, to simplify handling of an infinite number of modes, we introduce bounds for the stability domain in § 4.4 and derive a simple estimate for the largest growth rate in § 4.5.

2.4.1.   The frequency of the intrinsic modes at the neutral curve

In the previous section, we have found the intrinsic mode frequency in the limit of small n. Here we derive the exact frequency at the neutral curve on the $n-\tau$ plane.

2.4.1.1.   Decoupling on the neutral curve

The intrinsic modes found analytically for small n, can be traced numerically for arbitrary n. At first, we denote ω_c^i as the discrepancy between the eigen-frequency ω^i and ω_0^i, the small n prediction given by a real part of (26a). However, we stress that we do not *a priori* assume ω_c^i / ω_0^i to be small in our analysis. Thus, for any n, $Re(\omega^i) = \omega_0^i + \omega_c^i$, where superscript i denotes the intrinsic modes. For any value of n, the intrinsic mode frequency, ω, can be written as, $\omega^i = Re(\omega^i) + iIm(\omega^i)$, or

$\omega^i = \left(\omega_0^i + \omega_c^i\right) + iIm\left(\omega^i\right)$. On substituting this presentation of ω^i into the full dispersion relation (20), we can re-write it as,

$$(\alpha+1)\cos\left\{\left(\omega_0^i + \omega_c^i + iIm\left(\omega^i\right)\right)\beta_1\right\} + (\alpha-1)\cos\left\{\left(\omega_0^i + \omega_c^i + iIm\left(\omega^i\right)\right)\beta_2\right\}$$
$$+2ne^{i\left(\omega_0^i + \omega_c^i + iIm\left(\omega^i\right)\right)\tau}\sin\left\{\left(\omega_0^i + \omega_c^i + iIm\left(\omega^i\right)\right)x_q/c_1\right\}$$
$$\sin\left\{\left(\omega_0^i + \omega_c^i + iIm\left(\omega^i\right)\right)(x_q - L)/c_2\right\} = 0 \qquad , \qquad (2.27)$$

where α, β_1 and β_2 are,

$$\alpha = \left(\frac{S_2}{S_1}\right)\left(\frac{\rho_1 c_1}{\rho_2 c_2}\right), \quad \beta_1 = x_q\left(\frac{1}{c_2} - \frac{1}{c_1}\right) - \frac{L}{c_2} \quad \text{and} \quad \beta_2 = \frac{L}{c_2} - x_q\left(\frac{1}{c_1} + \frac{1}{c_2}\right). \qquad (2.28)$$

By virtue of the real part of (26a), we have, $e^{i\omega_0^i \tau} = -1$. Substitution of this identity into (27) simplifies it further. By definition, $Im\left(\omega^i\right)$ is equal to zero for the threshold value of n, i.e. $Im\left(\omega^i\right) = 0$ at $n = n_{th}^i$. This specifies the neutral curve. Thus, on the neutral curve, the imaginary part of (27) reduces to,

$$2in_{th}^i \sin\left(\omega_c^i \tau\right)\sin\left(k_1 x_q\right)\sin\left(k_2\left(x_q - L\right)\right) = 0. \qquad (2.29)$$

It is easy to see that this equation is factorized. It is satisfied when just one multiplier containing ω_c^i vanishes, that is,

$$\sin\left(\omega_c^i \tau\right) = 0. \qquad (2.30)$$

This gives us an explicit expression for ω_c^i,

$$\omega_c^i = m\pi/\tau, \qquad (2.31)$$

where m is an integer (not to be confused with the intrinsic mode number m^i). Once ω_c^i is obtained via (31), the frequency for the neutral intrinsic mode can be calculated

using its definition $Re(\omega^i) = \omega^i_0 + \omega^i_c$, which yields (on the neutral curve $\omega^i = Re(\omega^i)$),

$$\omega^i = (2m^i + 1)(\pi/\tau) + (m\pi/\tau). \qquad (2.32)$$

Because of extensive (but not comprehensive) numerical analysis of the full dispersion relation (20), we hypothesize that the modulus of integer m in (31) does not exceed unity, since $|m| > 1$ would imply $\omega^i_c \tau \geq 2\pi$. Recall, that according to (26b), the real parts of the frequencies of two neighbouring intrinsic modes, in the limit of small n, are separated by a factor of $\pm 2\pi/\tau$. Hence, any discrepancy exceeding $|\pm 2\pi/\tau|$, will imply the change of the mode number. For example, if the third intrinsic mode has the frequency discrepancy exceeding $-2\pi/\tau$, it would have become the second intrinsic mode, while the second intrinsic mode would have become third intrinsic mode. Thus, these modes will exchange their identities. So far, in numerics, we have not seen a single instance of such an exchange. Therefore, we assume ω^i_c to be restricted by the condition prohibiting such an exchange of identities, $-2\pi/\tau < \omega^i_c < 2\pi/\tau$.

According to (31), on the $m=0$ part of the neutral curve in the $n-\tau$ plane, $\omega^i_c = 0$, that is, the frequency exactly equals the value predicted in the limit of small n. This remarkable coincidence will be discussed in the next section. Apart from the $m=0$ option, the assumption prohibiting the exchange of identities condensed into condition $-2\pi/\tau < \omega^i_c < 2\pi/\tau$ leaves only two other possibilities: $m = \pm 1$. This corresponds to an intrinsic mode frequency shift by a factor π/τ on either side of ω^i_0

.

2.4.1.2. Why is the instability frequency independent of the combustor parameters on the neutral curve?

We have found an unexpected remarkable exact result. On the neutral curve, the instability frequency is completely independent of all the parameters of the combustor we consider in our model (the length, the flame location, the cross-section jump and the temperature jump) except for the time lag τ. Here we briefly discuss possible mathematical and physical reasons for such unusual behavior.

It is easy to see from (29) that at the neutral curve the intrinsic mode deviation, ω_c^i, from ω_0^i, i.e. its frequency in the asymptotic limit of $n \to 0$, is completely decoupled from the flame location and temperature jump, because of the equation factorization. Note also that the effect of cross-section jump does not even feature in this equation. This makes the intrinsic mode frequency completely independent of the environment on the neutral curve. In the segment of the neutral curve corresponding to $\omega_c^i \tau = 0$, the eigen-frequency is exactly equal to ω_0^i and in the segments corresponding to $\omega_c^i \tau = \pi$ and $\omega_c^i \tau = -\pi$, there is a frequency deviation of π/τ and $-\pi/\tau$ respectively, when compared to ω_0^i. There is, however, a qualitative difference between the eigen-frequencies in the asymptotic limit of small n and the eigen-frequencies on the neutral curve. In the limit of small n, the intrinsic modes are so strongly damped that they do not feel the combustor end conditions. Hence, they also do not feel the length of the combustor, as well as the position of the flame. We stress that as per (26b), neither the real part of ω^i, nor its imaginary part feels the parameters of the combustor (except τ) in the limit of small n. It can be seen from the contour plots in figures 3-5, that as n is increasing, the real part of the eigen-

59

frequency, $\mathrm{Re}\,\omega^i$, for a given combustor, is hardly changing. Hence, the real part remains insensitive to all parameters of the combustor (except τ), while the decay rate depends on all the characteristics of the chosen combustor. When on the complex ω^i plane, as we approach the neutral curve (from either side), the intrinsic modes growth/decay rate, by definition, tends to zero. Hence, given that on the neutral curve even the weak dependence of $\mathrm{Re}\,\omega^i$ vanishes, the dependence of ω^i on the flame location, cross-section and temperature jump also vanishes. To explain why the dependence of $\mathrm{Re}\,\omega^i$ on all parameters but τ vanishes on the neutral curve, consider our simplified dispersion relation (23) which we repeat for convenience $\cos kL = ne^{i\omega\tau}\big/\big(2 + ne^{i\omega\tau}\big)$. By definition, on the neutral curve, the eigen-frequency $,\omega$, is real. Since $k = \omega/c$ and the speed of sound c is also real, this requires $\cos kL$ to be real as well. This is possible only if $e^{i\omega\tau}$ is real, which implies $\sin(\omega\tau) = 0$, resulting in the solution, $\omega_c^i = m\pi/\tau$, where m is an integer. The same type of reasoning applies to the general form of the dispersion relation (20).

The decoupling phenomenon is not confined to the specific closed-open combustor we were examining. It can be shown that the decoupling (or the factorization) holds for other types of combustors of arbitrary length, cross-section and temperature jump with perfectly closed or perfectly open end conditions.

2.4.2. Instability threshold for the intrinsic modes

Here we derive an explicit expression for n as a function of τ, where the intrinsic mode becomes unstable. We will refer to this specific function as n_{th}^i. On this basis, for each intrinsic mode, we will draw a set of neutral curves, i.e. the boundaries of stability domains in the $n - \tau$ plane. These neutral curves will be analyzed below, to provide an insight into the stability behavior of intrinsic modes.

2.4.2.1. The neutral curve: Exact solution

Making use of $e^{i\omega_0^i \tau} = -1$, the real part of (27) on the neutral curve can be written as,

$$(\alpha+1)\cos\left\{\left(\omega_0^i+\omega_c^i\right)\beta_1\right\}+(\alpha-1)\cos\left\{\left(\omega_0^i+\omega_c^i\right)\beta_2\right\}-$$
$$2n_{th}^i \cos\left(\omega_c^i \tau\right)\sin\left(k_1 x_q\right)\sin\left\{k_2\left(x_q-L\right)\right\}=0 \quad ,$$

which directly yields the threshold n_{th}^i,

$$n_{th}^i = \frac{(\alpha+1)\cos\left\{\left(\omega_0^i+\omega_c^i\right)\beta_1\right\}+(\alpha-1)\cos\left\{\left(\omega_0^i+\omega_c^i\right)\beta_2\right\}}{2\cos\left(\omega_c^i \tau\right)\sin\left(k_1 x_q\right)\sin\left\{k_2\left(x_q-L\right)\right\}}, \qquad (2.33)$$

where α, β_1 and β_2 are provided by (28). Primarily, we examine a special case of

$x_q = L/2$. In this case, expression (33) can be significantly simplified. For the

segments of the neutral curve corresponding to $\omega_c^i \tau = 0$, $\omega_c^i \tau = \pi$ and $\omega_c^i \tau = -\pi$,

we find

$$n_{th}^i = 2\cos\left(\left(2m^i+1+m\right)\frac{\pi L}{\tau c}\right)\bigg/\left[\cos\left(\omega_c^i \tau\right)\left\{\cos\left(\left(2m^i+1+m\right)\frac{\pi L}{\tau c}\right)-1\right\}\right]. \qquad (2.34)$$

Where m is 0, +1 and -1 for the neutral curve segments $\omega_c^i \tau = 0$, $\omega_c^i \tau = \pi$ and

$\omega_c^i \tau = -\pi$ respectively. The neutral curve for the second intrinsic mode ($m^i = 1$) is

shown in figure 8 (a) as a typical example. Figure 8 (a) has two notable features.

There is a narrow island of instability shown to the left and a large instability domain

confined by neutral curve loop on the right-hand side, hereinafter referred to as

'neutral loop' or just 'loop' for brevity. The right-hand side loop has three distinct

segments. They correspond to the branches, $\omega_c^i \tau = 0$, $\omega_c^i \tau = \pi$ and $\omega_c^i \tau = -\pi$ (blue,

red and green respectively).
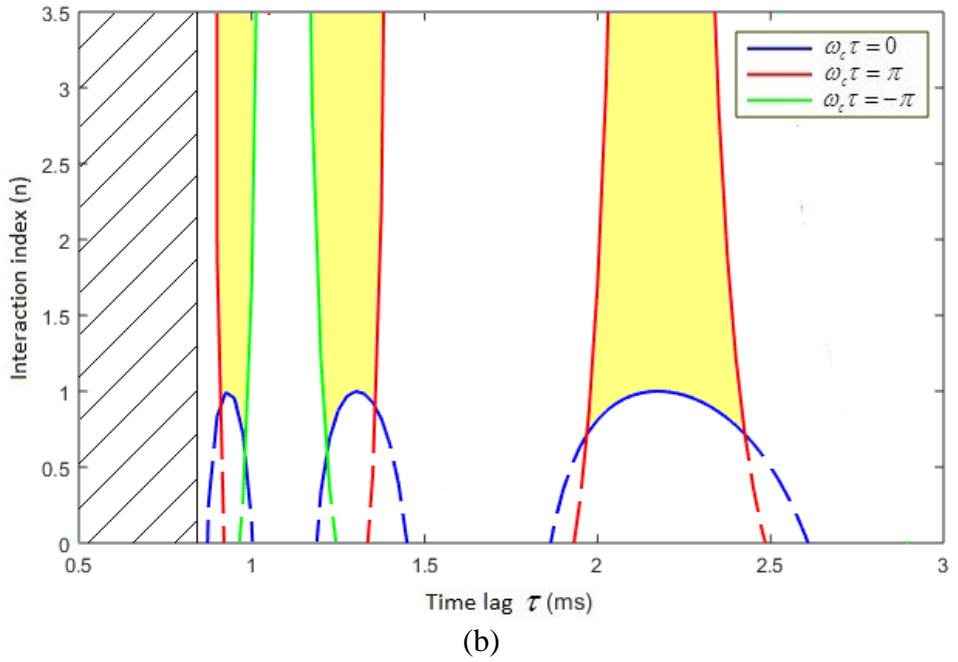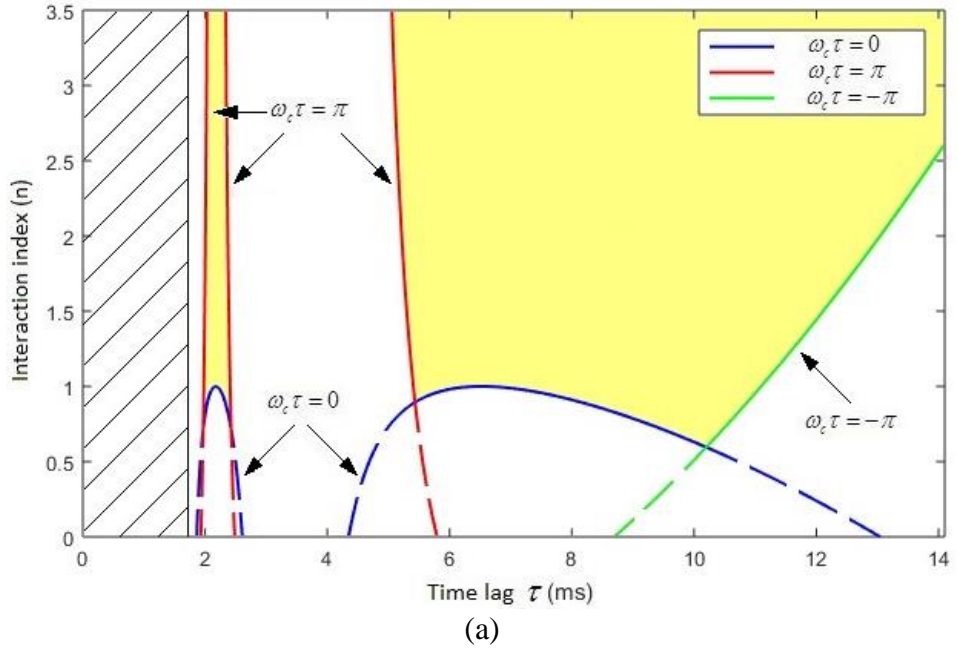
Figure 2.8: Neutral curve and stability domain on the $n - \tau$ plane for the second intrinsic mode ($m^i = 1$). Both figures are the same but on a different scale. In figure (b), the interval in τ is different, showing domains for the smaller time lag. The instability domain is marked in yellow. The segments $\omega_c^i \tau = 0$, $\omega_c^i \tau = \pi$ and $\omega_c^i \tau = -\pi$ of the neutral curve are indicated by arrows (blue, red and green respectively). The solid lines show segments of the neutral curve for the second intrinsic mode and the dashed lines show their continuations, which are also exact solutions of (34). We interpret them as neutral curves for acoustic modes coupled to the intrinsic mode. The hatched area indicates the domain with multiple instability islands, narrowing as τ decreases. These islands are difficult to plot so they are not shown. The parameters are the same as in figure 3.

Feature–wise, the pattern of the instability island on the left is the same as the larger loop on the right. Moreover, this pattern is repetitive (with diminishing width) towards the left (this is evident from figure 8 (b) drawn for smaller time lags). To avoid cluttering the figure, we hid these patterns under hatched lines. As these loops become thinner, they still manifest themselves as a combination of $\omega_c^i \tau = 0$, $\omega_c^i \tau = \pi$ and $\omega_c^i \tau = -\pi$ segments of the neutral curve. The 'instability domain' is marked in yellow. Each neutral loop composed of the neutral curve segments $\omega_c^i \tau = 0$, $\omega_c^i \tau = \pi$ and $\omega_c^i \tau = -\pi$ confines the instability domain from below.

For any specific loop, the solid lines represent the neutral curve for intrinsic modes and the dashed lines show their continuations. These continuations are due to the neutral curves for acoustic modes being coupled to intrinsic modes, as these dashed lines correspond to exact neutral solutions of the full dispersion relation (20), deeply embedded into the intrinsic mode stability domain. This interpretation is supported by numerical observations, discussed below in § 4.2.2. Detailed analysis as to how intrinsic and acoustic mode live together in a combustor will be discussed in chapter 3. The neutral curves segments, corresponding to $\omega_c^i \tau = \pi$ and $\omega_c^i \tau = -\pi$, yield higher values of n_{th}^i when compared to the $\omega_c^i \tau = 0$ segment. The islands of instability in the left-hand corner of figure 8 (a) (and of 8 (b)) manifest a strong coupling between acoustic and intrinsic modes. While discussing figure 8, we should mention that there also are nearly vertical, isolated segments of the neutral curve that we have opted not to show in the figure (but will be discussed in chapter 3). These segments correspond to $\omega_c^i \tau = \pi$ and $\omega_c^i \tau = -\pi$ segments, located between the large loop on the right and

the first small loop on the left of the figure and are due to acoustic modes being coupled with intrinsic modes.
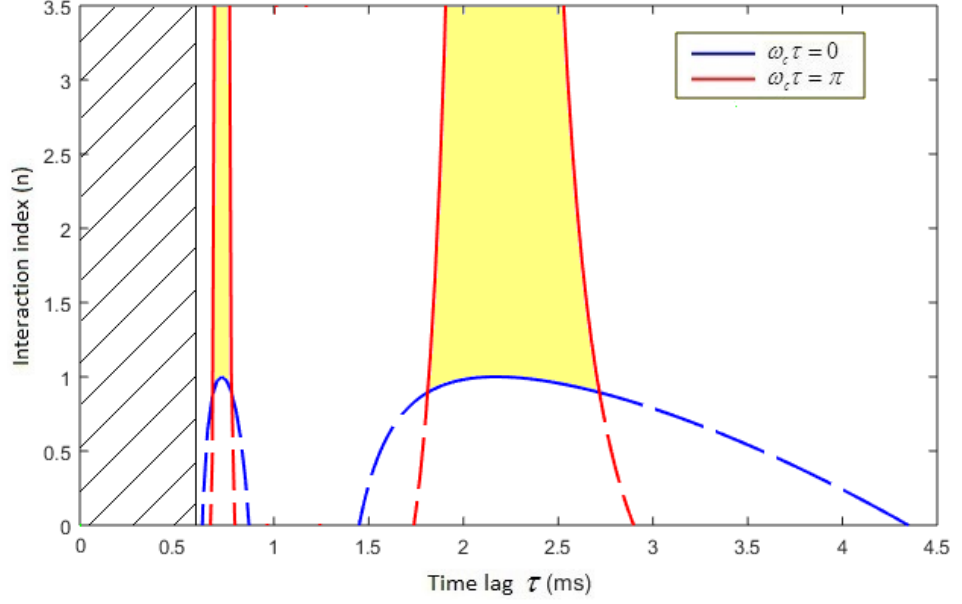
Figure 2.9: Neutral curve and stability domain on the $n - \tau$ plane for the first intrinsic mode (m^i =0). Notations and other parameters are the same as in figure 8. The neutral segment corresponding to $\omega_c^i \tau = -\pi$ does not feature here.

Note that for the first intrinsic mode (m^i =0), the neutral curve segment $\omega_c^i \tau = -\pi$ is very peculiar. According to (34), n_{th}^i is infinite, while (26a) predicts zero frequency.

The first intrinsic mode, nonetheless, has neutral loop segments $\omega_c^i \tau = 0$ and $\omega_c^i \tau = \pi$, which confine the instability region that overlaps with the small neutral loops on the left for second intrinsic mode, as can be seen from figure 9.

According to (33), (34), n_{th}^i can be either positive or negative. Of course, only positive n_{th}^i have physical sense. Correspondingly, figure 8 is plotted showing only positive n_{th}^i. However, a helpful insight can be gained by looking at the neutral curve continuation behavior in the unphysical domain. Figure 10 pictures the same

instability domain on the "extended" $n - \tau$ plane, i.e. with negative n_{th}^{i} included.

The neutral curve segments ($\omega_c^i \tau = 0$, $\omega_c^i \tau = \pi$ and $\omega_c^i \tau = -\pi$) extend into the negative n-region and intersect with each other. These intersections are calculated numerically (refer to Appendix I, § AI.1). Thus, a positive n_{th}^{i} exists only in certain bands of τ (see Appendix II, § AII.1 for details). The figure shows links between the seemingly disjointed neutral curve segments presented in Figure 8.
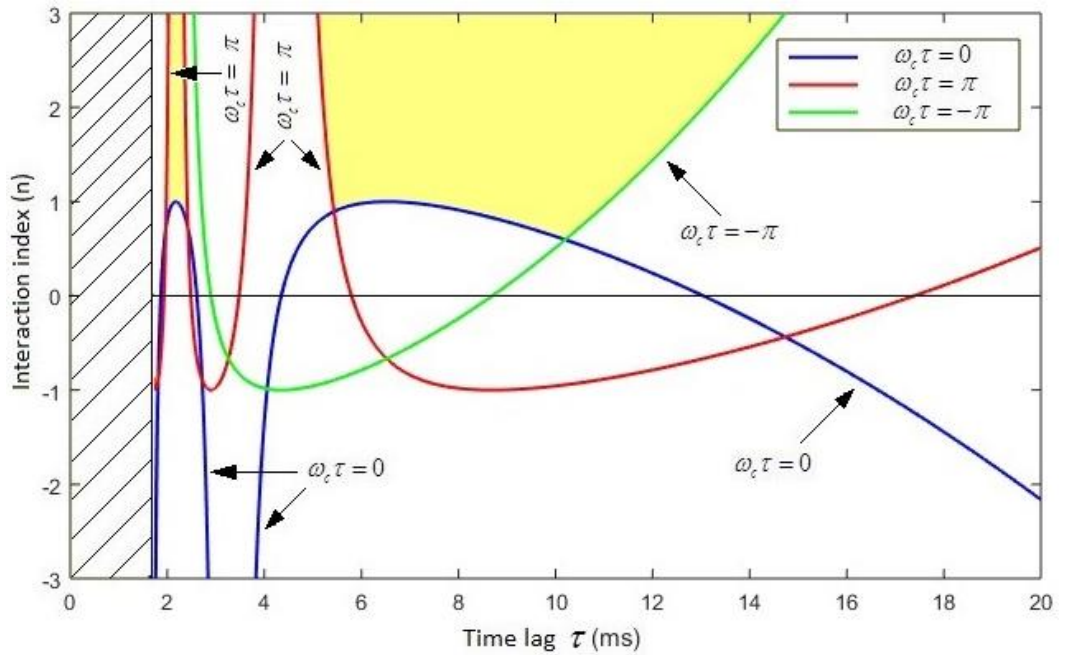
Figure 2.10: Neutral curve and stability domain for the second intrinsic mode ($m^i = 1$) on the "extended" $n - \tau$ plane. Notations and parameters are the same as in figure 8.

To give a better overall idea of the geometry of the instability domain with more than one mode, we first consider just the first three modes (that is for $m^i = 0$, $m^i = 1$ and $m^i = 2$) simultaneously. Figure 11 illustrates the general tendencies: (i) as the mode number m^i increases, the neutral curve loop shifts to the right; (ii) the span of the

islands of instability on the left also increases; (iii) the segments corresponding to $\omega_c^i \tau = \pi$ and $\omega_c^i \tau = -\pi$ become less steep for higher modes.
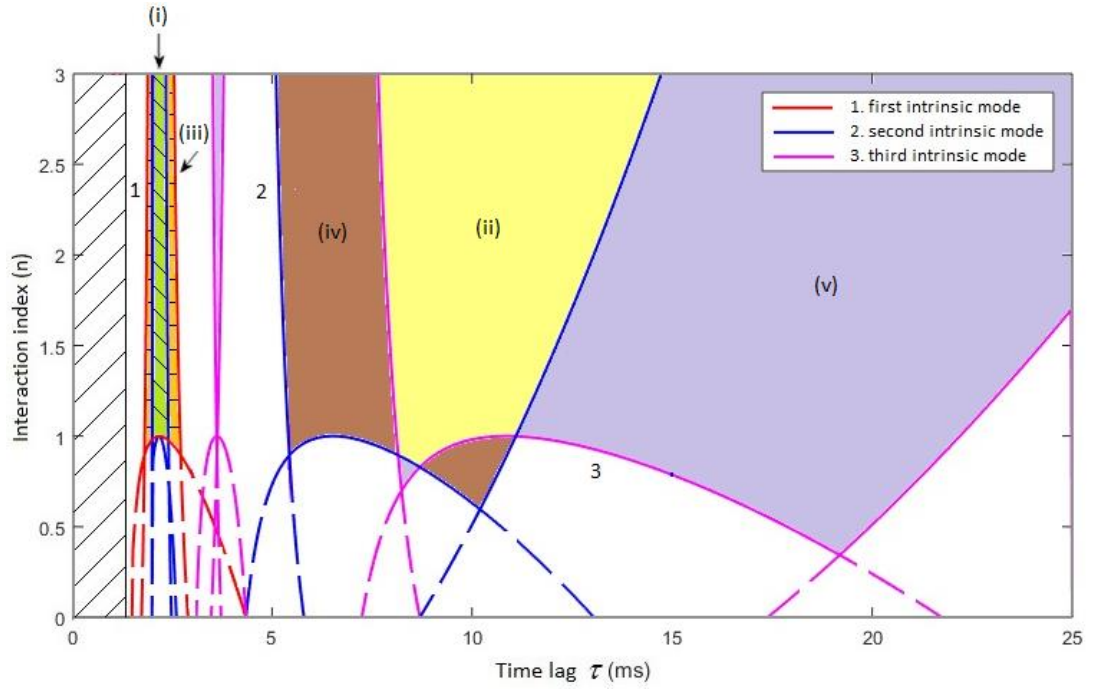
Figure 2.11: The neutral curves and stability domain on the $n - \tau$ plane for the first (m^i =0), second (m^i =1) and third (m^i =2) intrinsic modes, shown by numbers 1, 2 and 3 (Red, blue and magenta respectively). The common domain of instability for the first and second modes is marked in lime in right hatching and indicated by (i) (lime) and for the second and third intrinsic modes it is yellow and indicated by (ii). Horizontal hatching indicated by (iii) (gold), brown domain indicated by (iv) and lavender indicated by (v) correspond to the non-overlapping domains of instability for the first, second and third intrinsic modes respectively. The parameters are the same as in figure 8.

Note that the characteristic values of n_{th}^i are smaller, when compared to the threshold values of n for an infinite tube [Hoeijmakers et al. (2014)]. For an infinite tube, according to equation (26a), $n_{th}^i = (S_2/S_1)(\rho_1/\rho_2)(c_1/c_2) + 1$, which yields $n_{th}^i = 2$ for a uniform tube, i.e., if we assume, for simplicity, $S_2/S_1 = 1$, $\rho_1/\rho_2 = 1$ and $c_1/c_2 = 1$. For a combustor, n_{th}^i can be substantially smaller. The values for n_{th}^i for a

closed-open combustor, as shown in figures 8, 9 and 11, lies in the range of 0.4 to 1. The observation that, in a combustor, the intrinsic modes can become unstable at a much lower value of n, might have major practical implications.

2.4.2.2. Numerical validation of the analytical predictions for the neutral curve

Here we will corroborate the numerical and analytical results of § 4.2.1 for n_{th}^i, focusing on the accuracy of the analytical predictions for the examples considered in figures 8 and 11. Figure 12 shows a sample comparison of the analytical prediction of n_{th}^i given by (34) with that of the exact numerical solution of (20) for $m^i = 1$. The plot demonstrates that the numerical solution corroborates very well with the analytical prediction. At present, to plot the exact numerical solution, we manually track the loci of acoustic and intrinsic modes on the $n - \tau$ plane, by gradually increasing n. In this way, we ascribe identities to the modes, labelling them as intrinsic or acoustic.
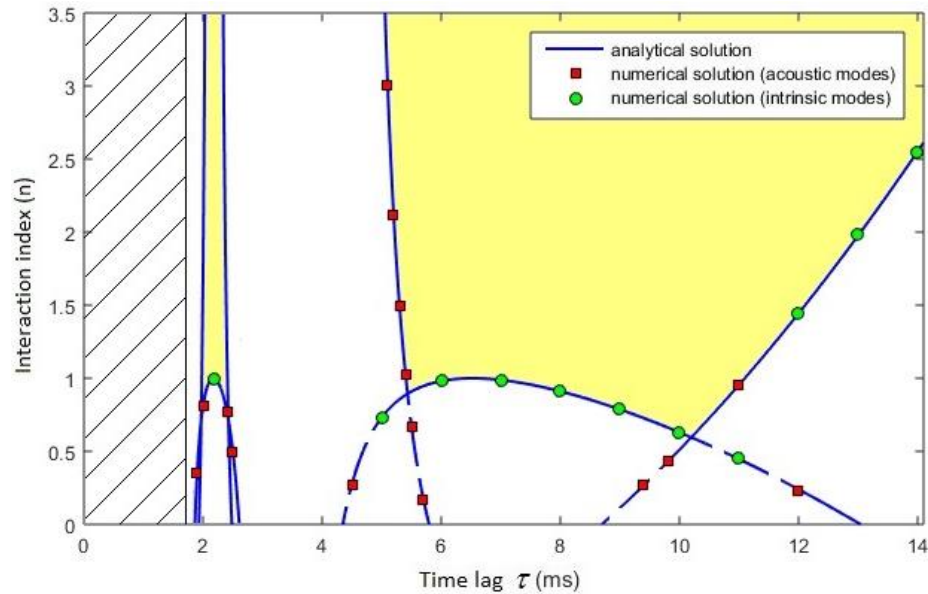
Figure 2.12: Neutral curve: comparison of analytical and numerical results for $m^i = 1$. Solid and dashed lines show the analytical solutions for intrinsic and acoustic modes respectively. Numerical solutions are shown by green circles and red squares. The parameters are the same as in figure 8.

Figure 12 also confirms the overall analytical picture. The instability domain has two distinctly different regions on the $n - \tau$ plane: the narrow islands of instability on the left and the main instability domain on the right. For the neutral curve on the right of figure 12, the analytical prediction of n^i_{th}, for the intrinsic modes, exactly coincides with the numerical solution. As mentioned in § 4.2.1, the combination of neutral curves $\omega^i_c \tau = 0$, $\omega^i_c \tau = \pi$ and $\omega^i_c \tau = -\pi$, is a repetitive pattern for any mode. Even though the numerical solution exactly matches the analytical prediction, on the left side region of the $n - \tau$ plane, it is difficult to identify the nature of these modes without extra analysis. A simple technique to identify the nature of the modes will be explained in § 6 of chapter 3.

Thus, here we have derived an explicit exact analytical expression (33) for the neutral curves on the $n - \tau$ plane. A set of neutral curves has been drawn for each mode. Figures 8, 9 and 11 give a good idea of the geometry of the instability domains. The neutral curves have, qualitatively, two different regions. A region on the left, i.e. towards smaller values of τ, comprises of loops with diminishing τ widths, made of strongly coupled acoustic-intrinsic modes. On the other hand, the region on the right exhibits a single large loop. The neutral curve has three distinct segments corresponding to $\omega^i_c \tau = 0$, $\omega^i_c \tau = \pi$ and $\omega^i_c \tau = -\pi$ in $n - \tau$ space. The $\omega^i_c \tau = \pi$ and $\omega^i_c \tau = -\pi$ segments predict higher values of n^i_{th} compared to $\omega^i_c \tau = 0$ segments. These segments are initially steep, becoming less steep as the mode number, m^i, increases. For higher values of m^i, the span of the neutral curve segment $\omega^i_c \tau = 0$ becomes wider, moving further to the right in $n - \tau$ space. Analytically, we can find the loci of the intersection points of the neutral curve segments $\pm\omega^i_c \tau = \pi$ and $\omega^i_c \tau = 0$

. The analysis is, however, cumbersome and does not result in an easy to use formula. To get tractable formulae we look for asymptotic behavior for large and small τ.

2.4.2.3. Neutral curve asymptotics for small and large τ

Here we examine the neutral curve behavior for large and small τ, which will provide us with compact formulae for n_{th}^i at the intersection points of neutral curve segments $\pm \omega_c^i \tau = \pi$, and $\omega_c^i \tau = 0$, in the limit of large and small τ.

(a) Asymptotics for small τ

It can be seen from figures 8 and 11 that the instability islands on the left-hand side are quite narrow and the boundaries corresponding to $\omega_c^i \tau = \pm\pi$ are almost vertical. This trend continues further to the left, as this pattern of neutral curves is repetitive. As these islands of instability become increasingly narrow, it becomes more difficult to accurately resolve them numerically. In this section, we make use of this narrowness of neutral curve loops and derive an approximate expression for the width of the instability domains bounded by these loops.

It can be shown (see Appendix II, § AII.1), that the maximum value of n_{th}^i for the $\omega_c^i \tau = 0$ segments of the neutral curve is 1 (when, $S_2/S_1 = 1$, $c_1/c_2 = 1$, $\rho_1/\rho_2 = 1$ and $x_q = L/2$). We will use this to find τ that correspond to maximum n_{th}^i for $\omega_c^i \tau = 0$. Moreover, we can find the half width of the neutral loop for the small τ regime, by estimating the distance (in terms of τ) between the position of the local maximum of n_{th}^i and the intersection points of $\omega_c^i \tau = 0$ and $\omega_c^i \tau = \pm\pi$. Here we will not seek exact analytical expressions for the intersection points of the segments $\omega_c^i \tau = 0$ and

$\omega_c^i \tau = \pm\pi$. Instead, assuming the neutral curve segments $\omega_c^i \tau = \pm\pi$ to be vertical, and the intersection point of $\omega_c^i \tau = 0$ and $\omega_c^i \tau = \pm\pi$ to correspond to $n_{th}^i = 1$, we can derive an analytical estimate for the half width of the neutral loop. Since the neutral curve segments $\omega_c^i \tau = \pm\pi$ are assumed to be vertical, the neutral curve loop width is independent of the n_{th}^i on $\omega_c^i \tau = \pm\pi$ segments.

First, we find the location of τ corresponding to $n_{th}^i = 1$ on the neutral curve segment $\omega_c^i \tau = 0$. Let us call it τ_1. Requiring $n_{th}^i = 1$, we immediately get from equation (34)

$$\cos\lambda = -1, \tag{2.35}$$

where $\lambda = \left(2m^i + 1\right)\pi L \big/ \tau_1 c$. The solution of (35) is

$$\lambda = \left(2m + 1\right)\pi, \quad m = 0,1,2,\ldots \tag{2.36}$$

where m is the loop number of the neutral curve segment $\omega_c^i \tau = 0$, with $m = 0$ being the rightmost loop. As we show in Appendix II, m must be restricted to odd integers only, i.e., $m = 2j + 1$, because only for these loops is n_{th}^i positive, whereas for the loops corresponding to even integers $m = 2j$, n_{th}^i is negative. Therefore, these intersection points should not be considered. Making use of (36), we arrive at a simple expression for τ_1, corresponding to the local maximum of n_{th}^i on $\omega_c^i \tau = 0$,

$$\tau_1 = \left\{\left(2m^i + 1\right) \big/ \left(2m + 1\right)\right\}\left(L/c\right). \tag{2.37}$$

We introduce $\tau_{2(+\pi)}$ and $\tau_{2(-\pi)}$ as the values of τ at the intersections of $n_{th}^i = 1$ with the $\omega_c^i \tau = \pm\pi$ segments of the neutral curve. From (34) we find,

$$\cos\lambda = 1/3. \tag{2.38}$$

Solving (38) yields,

$$\lambda = (2m + 0.392)\pi.$$ (2.39)

Then for $\omega_c^i \tau = \pi$ and $\omega_c^i \tau = -\pi$, we have $\lambda_{(+\pi)} = (2m^i + 2)\pi L / \tau_{2(+\pi)} c$ and

$\lambda_{(-\pi)} = (2m^i)\pi L / \tau_{2(-\pi)} c$. Using (39) we find the points of the segment

intersections, $\tau_{2(+\pi)}$ and $\tau_{2(-\pi)}$

$$\tau_{2(+\pi)} = (L/c)\{(2m^i + 2)/(2m + 0.392)\} \text{ and}$$

$$\tau_{2(-\pi)} = (L/c)\{2m^i/(2m + 0.392)\}.$$ (2.40 a, b)

The distance between τ_1, specified by (37), and τ_2, given by (40 a, b), is the half

width of the neutral loop in the asymptotic limit of small τ, $\Delta\tau_{(\pm\pi)} = |\tau_{2(\pm\pi)} - \tau_1|$.

On making use of (40a) and (40b) the solution for $\Delta\tau_{(\pm\pi)}$ reads,

$$\Delta\tau_{(+\pi)} = \frac{L}{c}\left|\frac{(2m + 1.216m^i + 1.608)}{(2m+1)(2m+0.392)}\right| \text{ and}$$

$$\Delta\tau_{(-\pi)} = \frac{L}{c}\left|\frac{(2m - 1.216m^i + 0.392)}{(2m+1)(2m+0.392)}\right|.$$ (2.41 a,b)

This expression can be further simplified for higher values of m:

$\Delta\tau_{(\pm\pi)} \approx (L/c)(1/2m)$. This gives us the half width of the neutral loop for small τ

and large m. Recall, that the central point of the neutral loop is given by (47).

Thus, we derived a simple expression for the neutral loop width, valid for large m

and small τ. The loop width is independent of the mode number of the intrinsic

mode and is inversely proportional to the loop number m. This quantifies how the

instability island width tends to zero as $\tau \to 0$. Since, as $\tau \to 0$, the density of the

loops increases, it would be almost impossible to correctly capture this behavior numerically.

(b)   Asymptotics for large τ

As figure 11 suggests, the largest neutral curve loop shifts towards larger values of τ, with an increase of the mode number. In this section, we will find asymptotics of n^i_{th} for large time lag τ, that is $\tau >> \pi L/c$. The large τ assumption provides a way to explicitly find the intersection points for the neutral curve segments $\omega^i_c \tau = 0$ and $\omega^i_c \tau = \pm \pi$ belonging to the largest loop, as shown in figure 8. At the intersection, n^i_{th} simultaneously satisfies equations for the neutral curve segments $\omega^i_c \tau = 0$ and $\omega^i_c \tau = \pm \pi$ given by (44).

Although the range of τ, for which this large τ analysis is valid, might be too high from a practical combustor perspective, it is important to have an overall picture of the stability domain. The analysis addresses this need. The part of the domain which has a large τ is also interesting, because the lowest threshold and the highest growth rates occur there, which might serve as upper bounds for key characteristics of practical combustors. We also mention that, as we show below, simple formulae, obtained using large τ asymptotics, work remarkably well, far beyond the domain their formal applicability.

The analysis (carried out in Appendix III, § AIII.1) yields an explicit expression for the normalized time lag, $\tau_n (\tau_n = \tau c / \pi L)$, written as $\tau_{n(+\pi,0)}$, to stress the fact that it corresponds to the intersection point of $\omega^i_c \tau = 0$ and $\omega^i_c \tau = \pi$, valid for large τ,

$$\tau_{n(+\pi,0)} = \left(4m^i + 3\right) \Big/ \left\{\left(2m_{(+\pi,0)} + 1\right)\pi\right\}. \tag{2.42}$$

Here, $m_{(+\pi,0)} = 0,1,2,\ldots$, where $m_{(+\pi,0)}$ is the intersection point number of the neutral curve segments $\omega_c^i \tau = 0$ and $\omega_c^i \tau = \pi$, with $m_{(+\pi,0)} = 0$ being the rightmost intersection point, while m^i is the mode number. Similar consideration of the intersections of the neutral curve segments $\omega_c^i \tau = 0$ and $\omega_c^i \tau = -\pi$ yields,

$$\tau_{n(-\pi,0)} = \left(4m^i + 1\right) \Big/ \left\{\left(2m_{(-\pi,0)} + 1\right)\pi\right\}. \tag{2.43}$$

Here $m_{(-\pi,0)}$ is an integer, indicating the intersection point number of the neutral curve segments $\omega_c^i \tau = 0$ and $\omega_c^i \tau = -\pi$, with $m_{(-\pi,0)} = 0$ being the rightmost intersection point, while m^i is the mode number. The n_{th}^i corresponding to (42) and (43) can be given as,

$$n_{th(+\pi,0)}^i = 2\sin\left(3\pi/8m^i\right) \Big/ \left[\sin\left(3\pi/8m^i\right) + 1\right],$$

$$n_{th(-\pi,0)}^i = 2\sin\left(\pi/8m^i\right) \Big/ \left[\sin\left(\pi/8m^i\right) + 1\right]. \tag{2.44, 2.45}$$

This expression quantifies how $n_{th(+\pi,0)}^i$ and $n_{th(-\pi,0)}^i$ tend to zero as m^i increases. A comparison of (44) and (45) shows that $n_{th(-\pi,0)}^i < n_{th(+\pi,0)}^i$. Thus, the intersection points of neutral curve segments $\omega_c^i \tau = 0$ and $\omega_c^i \tau = -\pi$, correspond to a lower value of n_{th}^i when compared to the intersection of neutral segments $\omega_c^i \tau = 0$ and $\omega_c^i \tau = \pi$.

Thus, to avoid dealing with large $m_{(+\pi,0)}$, $m_{(-\pi,0)}$ and large τ regimes head on, we found a simple analytical description of the points of intersection of the segments of neutral curves $\omega_c^i \tau = 0$ and $\omega_c^i \tau = \pi$, as well as $\omega_c^i \tau = 0$ and $\omega_c^i \tau = -\pi$, assuming large τ. At the intersection of neutral curve segments, n_{th}^i decreases with the increase of mode number. n_{th}^i at the intersection of $\omega_c^i \tau = 0$ and $\omega_c^i \tau = \pi$ is always larger than n_{th}^i at the intersection of $\omega_c^i \tau = 0$ and $\omega_c^i \tau = -\pi$. The extreme right intersection point of $\omega_c^i \tau = 0$ and $\omega_c^i \tau = -\pi$ (that is, the intersection of the large loop with $m_{(-\pi,0)} = 0$, as given by (43)) corresponds to the lowest value of n_{th}^i for any fixed mode number. These asymptotics proves to be extremely useful for finding the bounds of the instability domain in § 4.4 and in estimating the maximal growth rate in § 4.5.

2.4.3. The growth/decay rates near the neutral curve

In the context of intrinsic mode instability, the growth rate is of prime interest. The derivation of growth/decay rate directly from the original dispersion relation (20) for all values of n on the $n - \tau$ plane, is very challenging and hardly a priority. For large deviations from the neutral curve, the mode in question is either strongly decaying, therefore playing little role in the dynamics of the system, or has too high growth rates, implying that the linear theory we adopted quickly ceases to be applicable. Thus, only the growth/decay rates near the neutral curve are of true interest.

2.4.3.1. Analytical expression for the growth rate

Thanks to the discovered phenomenon of decoupling on the neutral curve, in the previous section we established the exact location of the neutral curve on the $n - \tau$

plane. Here, exploiting the decoupling and proximity to the neutral curve, we will find, analytically, the growth/decay rate in the curve vicinity. To this end, consider a point (n, τ) on the $n - \tau$ plane, near the neutral curve, for a particular mode m^i, denoting the deviation from the curve as n_1^i, i.e. $n - n_{th}^i = n_1^i \ll n_{th}^i$. The eigen-frequency at the chosen point (n, τ) differs from its value on the neutral curve ω_0^i for the same τ. We denote this deviation as ω_1^i. Assume that the real part of ω_1^i is small and of little interest near the neutral curve. This implies that ω_1^i represents the growth/decay rate. *A priori* this assumption is difficult to justify rigorously. However, the fact that the real part of eigen-frequency on the $\omega_c^i \tau = 0$ segments of the neutral curve is identical to case for the limit of small n, suggests that ω_1^i has a negligibly small real part. This assumption, as we show below, is also supported by numerics. Hence, $n = n_{th}^i + n_1^i$, $\omega = \omega_0^i + \omega_1^i$. Substituting this expansion of n and ω into the original dispersion relation (20) and neglecting higher order terms in ω_1^i in sin and cos function expansion, we obtain,

$$(\alpha + 1)\left\{\cos\left(\omega_0^i \beta_1\right) - \omega_1^i \beta_1 \sin\left(\omega_0^i \beta_1\right)\right\} + (\alpha - 1)\left\{\cos\left(\omega_0^i \beta_2\right) - \omega_1^i \beta_2 \sin\left(\omega_0^i \beta_2\right)\right\}$$

$$+ 2\left(n_{th}^i + n_1^i\right)\left(1 + i\omega_1^i \tau\right)e^{i\omega_0^i \tau}\left\{\sin\left(\omega_0^i x_q/c_1\right) + \omega_1^i\left(x_q/c_1\right)\cos\left(\omega_0^i x_q/c_1\right)\right\}$$

$$\left\{\sin\left(\omega_0^i\left(x_q - L\right)/c_2\right) + \omega_1^i\left(\left(x_q - L\right)/c_2\right)\cos\left(\omega_0^i\left(x_q - L\right)/c_2\right)\right\} = 0$$

. (2.46)

Subtracting the original dispersion relation (20) for $\omega = \omega_0^i$ from this form (46), we obtain a perturbed form of the dispersion relation (20), which yields an explicit analytical expression for the growth/decay rate ω_1^i,

$$\omega_1^i = \frac{2n_1^i e^{i\omega_0^i \tau} \sin\left(\omega_0^i x_q/c_1\right) \sin\left(\omega_0^i \left(x_q - L\right)/c_2\right)}{\left[(\alpha+1)\beta_1 \sin\left(\omega_0^i \beta_1\right) + (\alpha-1)\beta_2 \sin\left(\omega_0^i \beta_2\right) - \Sigma\right]}.$$ (2.47)

where,

$$\Sigma = 2n_{th}^i e^{i\omega_0^i \tau} \left\{ \begin{array}{l} i\tau \sin\left(\omega_0^i x_q/c_1\right) \sin\left(\omega_0^i \left(x_q - L\right)/c_2\right) \\ + \left(x_q/c_1\right) \cos\left(\omega_0^i x_q/c_1\right) \sin\left(\omega_0^i \left(x_q - L\right)/c_2\right) \\ + \left(\left(x_q - L\right)/c_2\right) \sin\left(\omega_0^i x_q/c_1\right) \cos\left(\omega_0^i \left(x_q - L\right)/c_2\right) \end{array} \right\}.$$

while α, β_1 and β_2 are given by (28). It can be verified by direct calculation of ω_1^i, that its real part is, indeed, insignificant, as was assumed. Thus, $\omega_1^i \approx Im\left(\omega_1^i\right)$ and will be treated as the growth/decay rate. We stress that, in contrast to the frequencies on the neutral curve, according to (47), ω_1^i depends on all combustor parameters. Equation (47) is valid for the neutral segment $\omega_c^i \tau = 0$. A similar exercise can be carried out for other neutral segments $\omega_c^i \tau = \pm\pi$ as well.

Thus, we have derived an explicit expression for the intrinsic mode growth/decay rates near the neutral curve on the $n - \tau$ plane. For simplicity, only the first order term in n_1^i has been presented. Higher order corrections in n_1^i could be found in a similar fashion. The justification of our *a priori* assumption and the accuracy of the analytical results will be demonstrated by comparison with the numerical solution in § 4.3.2. The formula above gives the growth/decay rates for each intrinsic mode. In principle, by considering all the modes, we can find the absolute maximum growth rate or the minimum decay rate for any point (n, τ) on the $n - \tau$ plane. In practice, it might be difficult to deal with an infinite number of modes so alternatives are needed.

2.4.3.2. Numerical validation of analytical expression

Here we validate the analytical growth rate given by (47) with the numerical solution of (20). The comparison will also give us an idea of the range of applicability and accuracy of our analytical approach.

Figure 13 shows a comparison of the analytical prediction of the growth rates given by (47) with that of the numerical results for $m^i = 1$ and $\tau = 6$ ms. Near n^i_{th} (0.98 for this case), analytical and numerical predictions agree quite well. However, as we move away from n^i_{th}, the analytical prediction starts to deviate from the numerical results. We can therefore conclude that the analytical prediction for the growth rate is in good agreement with the numerical solution near n^i_{th}, where it is of most interest.

Expectedly, as we move away from the vicinity of n^i_{th}, the accuracy of approximate solution (47) decreases. However, we stress that a massive twenty percent deviation from n^i_{th} results only in smaller than two percent discrepancy of the growth/decay rate. Recall also that our approximate solution (47) is a just the leading order term of expansion in n^i_1 (the departure of n from n^i_{th}). Taking into account the next terms of the expansion would have further improved the accuracy. However, we do not pursue this line here.
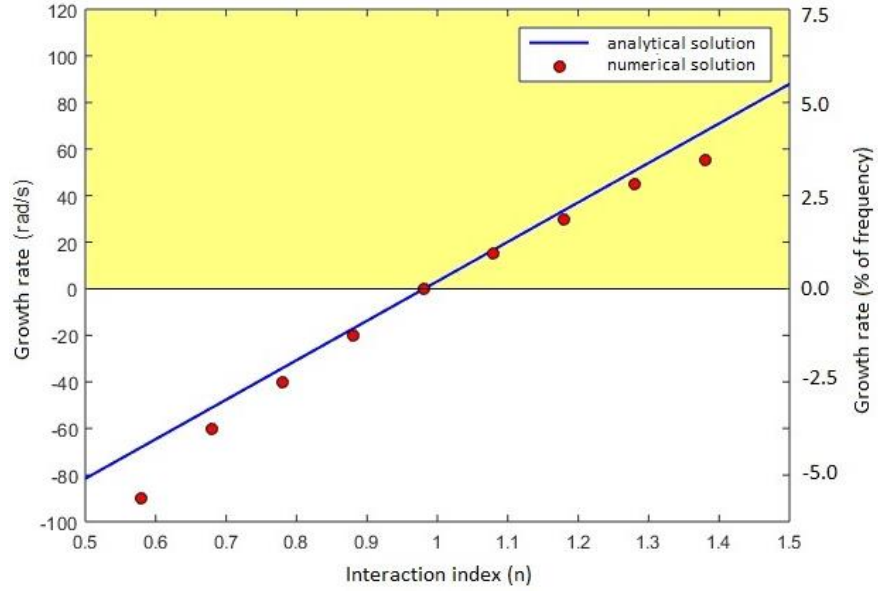
Figure 2.13: Growth rate for $m^i = 1$ at $\tau = 6$ ms: comparison of the analytical result (47) and numerical solution of the original dispersion relation (20). A solid blue line and red circles show the analytical and numerical solutions respectively. The instability domain is marked in yellow. The parameters are the same as in Fig.8.

It has been thoroughly checked that the analytical prediction of the growth rate (47) works very well for all τ, including near intersections of different segments of the neutral curve. A couple of such examples are depicted by figures 14 (a) and (b), which are applicable for $m^i = 1$ at (a) $\tau = 5.435$ ms (the intersection point of neutral loop segment $\omega^i_c \tau = 0$ and $\omega^i_c \tau = \pi$ for the extreme right neutral loop) and (b) $\tau = 10.2$ ms (the intersection point of the neutral loop segment $\omega^i_c \tau = 0$ and $\omega^i_c \tau = -\pi$ for the extreme right neutral loop). The numerical results for growth rate agree quite well for both intrinsic and coupled acoustic mode (details of coupling will be in chapter 3) near the n^i_{th} (0.89 and 0.6 respectively for figures 14 (a) and (b)).
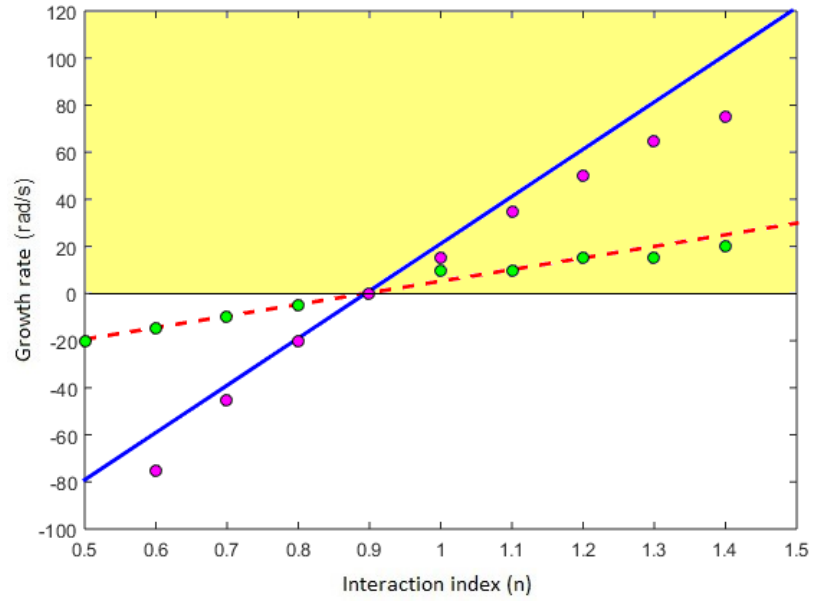
(a)
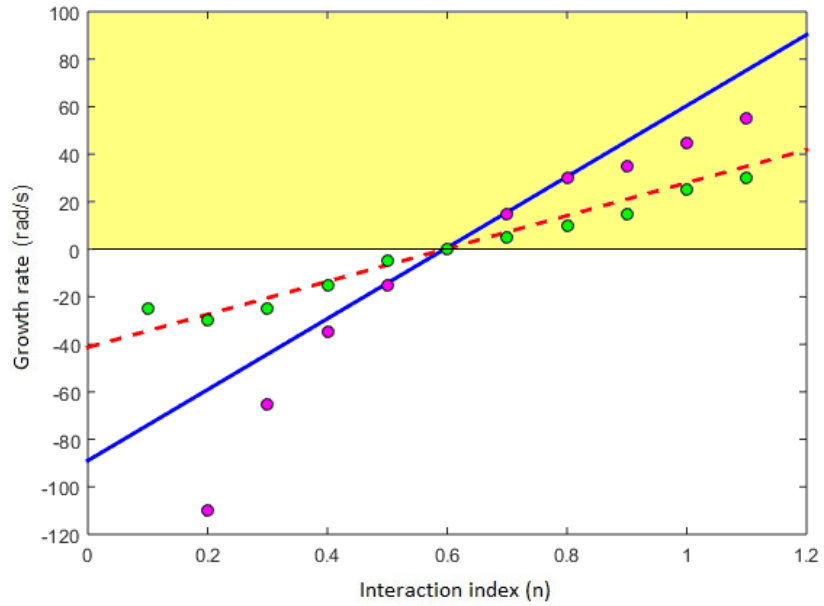
(b)

Figure 2.14: Growth rate for $m^i = 1$ at (a) $\tau = 5.435$ ms (the intersection point of neutral loop segment $\omega^i_c \tau = 0$ and $\omega^i_c \tau = \pi$ for the extreme right neutral loop) and (b) $\tau = 10.2$ ms (the intersection point of neutral loop segment $\omega^i_c \tau = 0$ and $\omega^i_c \tau = -\pi$ for the extreme right neutral loop): comparison of analytical result (47) and numerical solution of the original dispersion relation (20). Blue continuous and red dotted lines are analytical solutions for intrinsic and coupled acoustic modes respectively. Magenta and green circular dots are their numerical counterparts. The instability domain is marked in yellow. The parameters of the system are the same as in Fig.8.

2.4.4.   Bounds on the stability domain

In § 4.3 we mentioned a potential difficulty in finding the boundary of stability domain and growth/decay rates for any point on the $n - \tau$ plane, when all the modes are considered. The small loops, on the left of the neutral curves for higher modes, overlap with the large loop of the neutral curves for lower modes, creating an extremely intricate picture of overlapping loops of different, often incomparable, widths for various modes. So, here we suggest an alternative, a "short-cut". Instead of dealing with intricately curved stability domain specified by contributions of an infinite number of modes, we coarse-grain the stability behavior of all the intrinsic modes and develop an "integral" stability map. This provides an upper and lower bound of the stability domain on the $n - \tau$ plane. Figure 15 introduces the concept of a stability envelope for the intrinsic modes. For the sake of simplicity, only the intrinsic modes one to six are shown in the figure. Only the outermost stability loops for each mode are plotted; as, discussed in the previous section, the outermost stability loops correspond to the minimum value of n_{th}^i. The dash-dotted black line indicates the upper bound of the stability envelope and the dashed black line shows the lower bound of the stability envelope. The short thin dashed pink line shows the analytical prediction (45) of the lower bound. Thus, there exist three distinctly different regions of the coarse-grain stability:

i. For any point on the $n - \tau$ plane below the lower bound of the stability envelope, all the intrinsic modes are linearly stable.

ii. For any point on the $n - \tau$ plane above the upper bound of the stability envelope, all the intrinsic modes are linearly unstable.

iii. For any point on the $n - \tau$ plane in between the upper and lower bound of the stability envelope, the intrinsic modes can be linearly stable (for $n - \tau$ values falling

into the white region) or unstable (for $n - \tau$ values corresponding to the yellow region). For the points lying in the yellow region within the stability envelope, the maximum growth rate is roughly proportional to the vertical distance of the point from the lower bound of the stability envelope (this distance can be interpreted as n_1^i in (46)). Similarly, for the points lying in the white region above the lower stability envelope, the maximum decay rate is proportional to the vertical distance of the point from the upper bound of the stability envelope. This domain needs extra analysis, which is carried out in the next section.
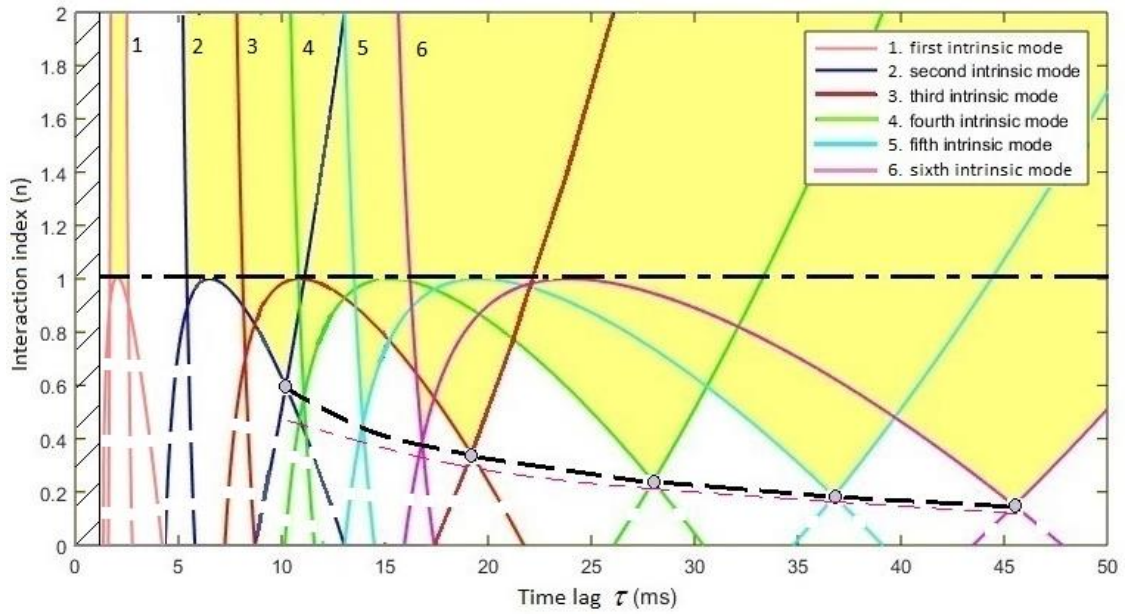
Figure 2.15: Neutral curve and stability domain on the $n - \tau$ plane for the first six intrinsic modes. The instability domain is marked in yellow. The black dashed line that connects the intersections, indicated by circles, shows the instability domain lower envelope, which is the locus of the lowest threshold of instability for each mode. Below this envelope, all points on the $n - \tau$ plane are guaranteed to be stable. A short dashed thin pink line shows the analytical prediction (45) of the lower bound. The black dash-dotted line is the locus of the maximal threshold of instability for each mode. Above this line, all points on the $n - \tau$ plane are unstable. Between the dash-dotted and the dashed line, there is a conditional instability domain. Stability at any point (n, τ) lying between these two lines depends on whether the point is in the white or the yellow region. Hatched area indicates the domain with multiple instability islands of decreasing scale, which are not shown. Also not shown, are the narrow loops due to higher modes. For simplicity, only the big right loop of the neutral curves for each mode was plotted, since these loops provide the minima of n_{th}^i. The parameters used are the same as in Fig.8.

The point we want to reiterate here, is that the large τ asymptotics formulae (43, 45), for the lower bound of the stability envelope, provides a good accuracy even far beyond the range of its formal validity.

2.4.5. Estimates of the maximal growth rates

In of itself, the distance to the bounds of the stability envelope can provide only qualitative tendencies of the intrinsic mode growth/decay rates as a function of the parameters of the system. To quantify the growth/decay rates, we need to know the mode number of the dominant mode. To this end, we can employ the large τ asymptotics (42-45), which were found to work surprisingly well for the whole range of τ, exceeding $\tau = \pi L/c$. Thus, for example, for a given τ, the lower bound of the stability domain will be determined by the mode m^i specified (approximately) by (43). In the generic case, any given τ specifies the two nearest mode numbers (see Fig AIII.1a and the follow-up discussion). As can be seen from figures 11 and 15, all modes with numbers below those of these two modes are stable (for large n) for this τ and thus, their growth rates need not be considered. As a result, the maximal growth rate can be easily estimated using (47), by applying it to just these two modes. It can be shown that all the higher modes have smaller growth rates and, therefore, can be ignored.

We further elaborate on this point with the use of figure 16. Let us consider stability at a sample point on the $n - \tau$ plane, choosing, say, n =0.9 and τ =16.5 ms (the point is indicated by the diamond). On the $n - \tau$ plane, according to our large τ asymptotics (43), the chosen value of τ, τ =16.5 ms falls somewhere in between the values of τ that correspond to the minima of n_{th}^i for the second and third modes.

Hence, figure 16 depicts just these two intrinsic modes in the form of their large loops of the neutral curve. As has been found in § 4.2.3 (b), n_{th}^i is minimal for the extreme right intersection point of $\omega_c^i \tau = 0$ and $\omega_c^i \tau = -\pi$. Thus, the large neutral curve loop on the right corresponds to the dominant intrinsic mode instability. Any instability corresponding to the smaller loops of overlapping higher order modes will be weaker. Hence, the maximum growth rate will be determined by proximity to the large neutral curve loop on the right. This will form the basis of our maximum growth rate estimate at a particular point on the $n - \tau$ plane. The dashed vertical purple line represents the formal (optimistically interpreted) threshold of applicability of the large τ asymptotics, $\tau = \pi L / c$. As showed in Appendix III, the large τ asymptotics can be used with high confidence for all τ exceeding this threshold. For the particular example indicated by the diamond ($n = 0.9$, $\tau = 16.5$ ms), the second intrinsic mode according to (47) has a negative growth rate, while the actual growth rate of the third intrinsic mode is 23 rad/s. Thus, for any τ exceeding $\tau = \pi L / c$, we can pinpoint the particular mode which has the greatest growth rate and find it using the explicit expression (47). It has been checked by direct calculation that all higher intrinsic modes either have smaller growth rates than the third intrinsic mode or remain stable. Note that had we taken the distance (along the vertical) between the diamond and the dashed green line in figure 16 as an estimate of n_1^i, the maximum growth rate would have been 69 rad/s (assuming $n_{th}^i \approx 0.4$ in (47)).

Thus, the coarse-grained stability diagram is helpful for a rough instant stable/unstable answer. For a realistic estimate of the maximal growth rate or minimal decay rate, one must first identify the most unstable mode, using either (43) or figure (AIII.1a).
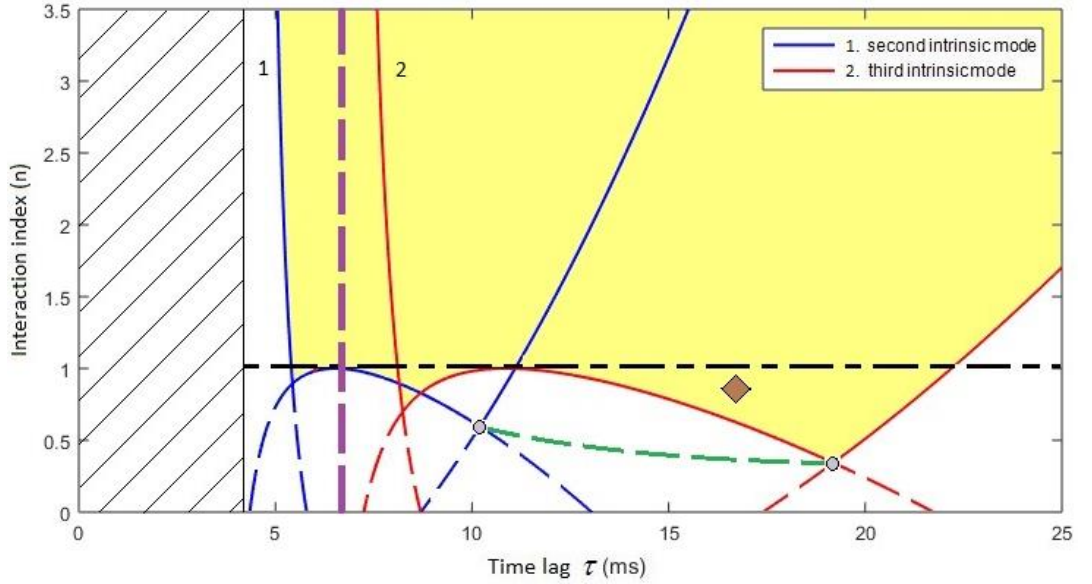
Figure 2.16: Neutral curve and stability domain on the $n - \tau$ plane for two intrinsic modes m^i =1, 2. This figure shows a subset of curves from figure 15. Note that the lower bound of instability is shown by a dashed green line. The diamond indicates the chosen sample point n =0.9 and τ =16.5 ms on the $n - \tau$ plane. The dashed vertical purple line, $\tau = \pi L/c$, is the threshold in τ above which the large τ assumption applies.

2.5.　Dependence of intrinsic mode stability on the cross-section/temperature jumps and flame location

Equation (26a) describes how the dispersion relation for strongly decaying intrinsic modes depends on the cross-section jump and temperature jump in the range of small n. In this section, we will find how n^i_{th} and the growth rate depend on the main parameters of our combustor model: (i) cross-section jump, (ii) temperature jump and (iii) flame location.

Figure 17 (a) illustrates the dependence of the neutral curve main loop on cross-section jump, plotted on the basis of (33). It presents two different cases of cross-section jump: $S_2/S_1 =1$ and $S_2/S_1 =2$. Brown and lavender mark the instability

domains for each case, with the common domain being marked in yellow. In all subsequent figures, the common instability domain is also marked in yellow. It can be seen, from figure 17 (a), that the span of the largest instability domain on the right is wider for lower values of cross section jump, whereas the peak n_{th}^i remains the same.

Figure 17 (b), generated for two different time lags of 7 and 9 ms for $m^i = 1$, shows that the n_{th}^i reduces with respect to cross-section jump, when the time lag is 9 ms, whereas n_{th}^i attains a constant value with respect to cross-section jump, when the time lag is 7 ms. Hence, cross-section jump might reduce n_{th}^i or keep n_{th}^i constant dependent upon the circumstances.
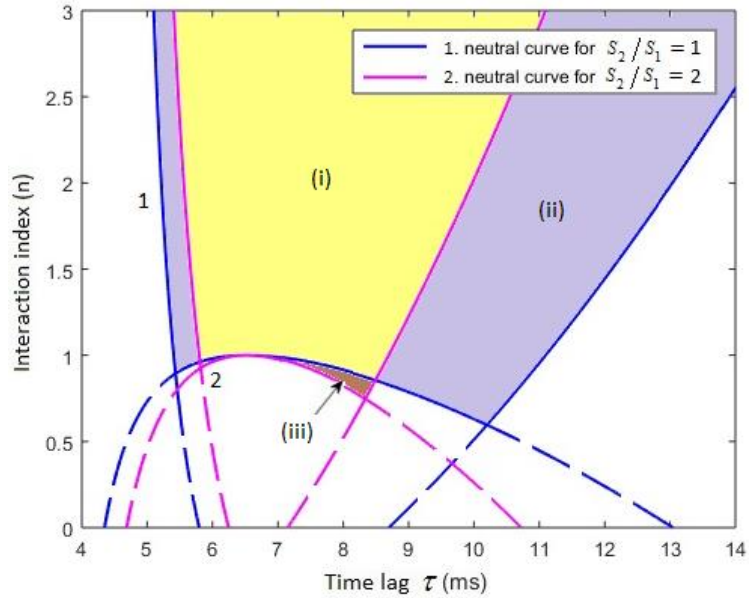
Figure 2.17 (a): Effect of cross-section jump on the stability domain for $m^i = 1$. The plot is based on (33) and shows no jump (S_2/S_1 =1) and (S_2/S_1 =2) cross section jump configurations. The instability domains for the cases S_2/S_1 =1 and S_2/S_1 =2 are indicated by lavender (ii) and brown (iii) respectively. The common instability domain for these two cases is marked in yellow and indicated by (i). Other parameters and notations are the same as in Fig.8.
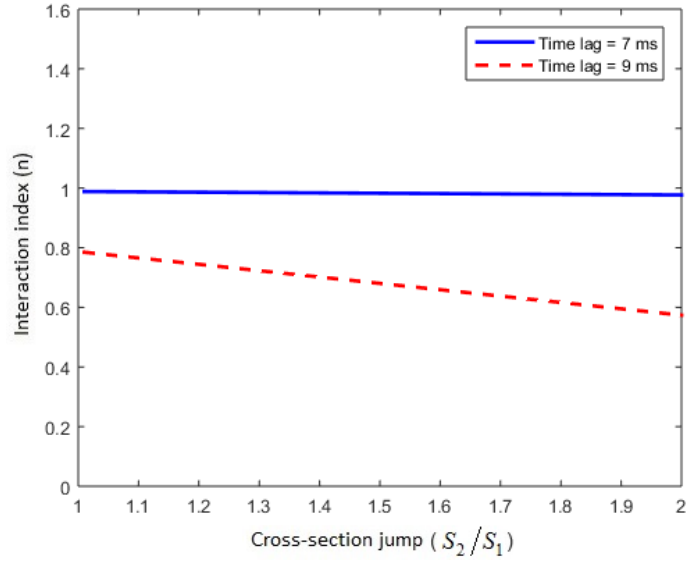
Figure 2.17 (b): Effect of cross-section jump (S_2/S_1) on n_{th}^i, for $m^i=1$. The blue continuous line and the red dotted line represent two different time lags of 7 and 9 ms. Other parameters are the same as in Fig.8.

The effect of temperature jump on $n_{th}^i(\tau)$ is slightly different. Figure 18 (a) and (b), plotted on the basis of (33), compares two different cases of temperature jump: for $T_2/T_1=1$ (or, $c_2/c_1=1$) and $T_2/T_1=4$ (or, $c_2/c_1=2$). These two different cases are shown for the flame locations (a) $x_q = L/2$ (=0.375m) and (b) $x_q = L/3$ (0.25m), respectively. Figure 18 (a) shows that temperature jump stretches the neutral curve main loop slightly to the left but, at the same time, the span reduces on the right-hand side. The peak of neutral curve segment $\omega_c^i \tau = 0$ attains higher value. Thus, for this case, the n_{th}^i increases with respect to temperature jump in the low time lag region of the neutral curve.
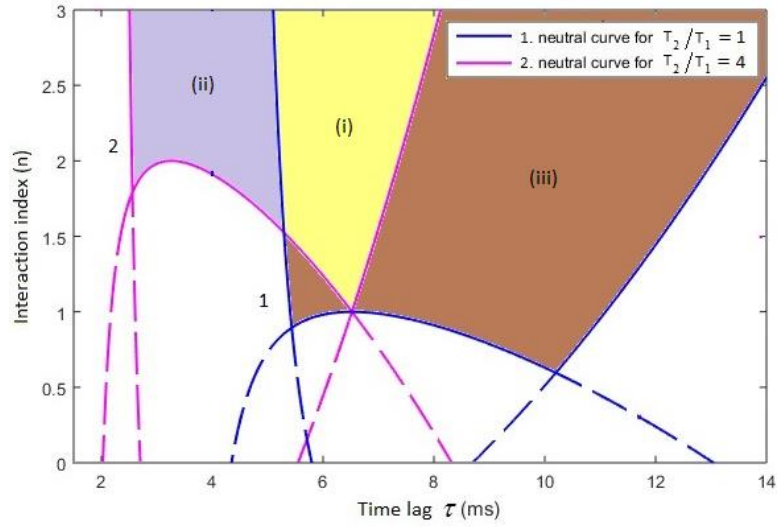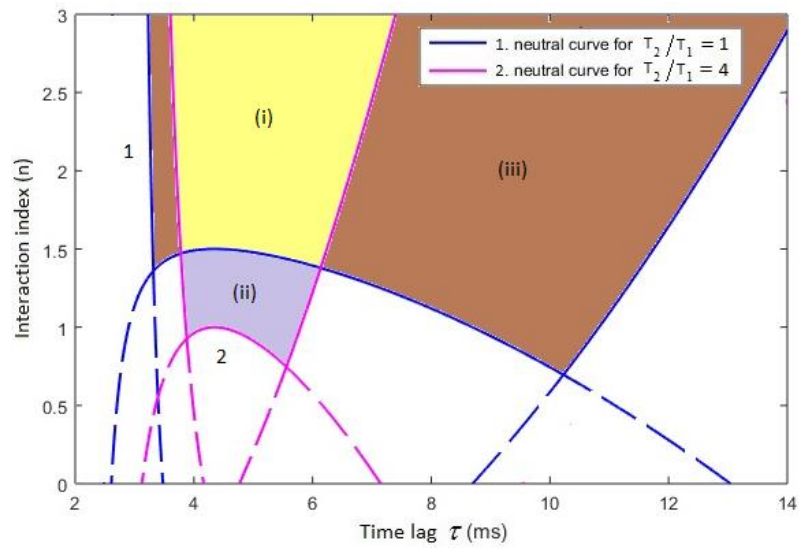
Figure 2.18 (a, b): Effect of temperature jump on stability domain for $m^i = 1$. The plot is based on (33) and shows configurations with no jump, i.e. $T_2/T_1 = 1$ (or, $c_2/c_1 = 1$)) and with $T_2/T_1 = 4$ (or, $c_2/c_1 = 2$)) temperature jump. Figures (a) and (b) are for two flame locations $x_q = L/2$ and $x_q = L/3$. The instability domains for the cases $c_2/c_1 = 1$ and $c_2/c_1 = 2$ are indicated by brown (iii) and lavender (ii) respectively. The common instability domain for these two cases is marked in yellow and indicated by (i). Other parameters and notations are the same as in Fig.8.
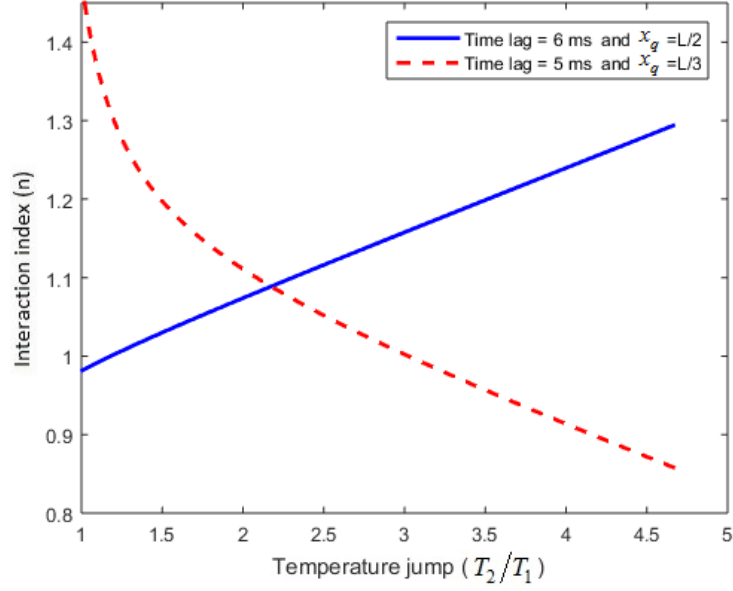
Figure 2.18 (c): Effect of temperature jump (T_2/T_1) on n_{th}^i, for $m^i = 1$. The blue continuous line and the red dotted line represent two different time lags of 6 and 5 ms, at flame locations $x_q = L/2$ and $x_q = L/3$ respectively. Other parameters are the same as in Fig.8.

The observations are slightly different for a different flame location, as shown in figure 18 (b). The figure shows that the temperature jump reduces the span of the neutral loop on either side and shifts the peak of the neutral loop down at the same time. This means that for this case the n_{th}^i decreases with respect to temperature jump for all time lags shown in the figure. The fact that temperature jump in figure 18 (a) moves the intrinsic instability domain to the lower time lag region, makes it an important aspect. In most of the practical combustor applications, time lag is small, meaning, as per figure 18 (a), at elevated temperature, not only the small neutral loops on the left, but also the large neutral loop on the right could play a crucial role in defining intrinsic instability of practical combustors. Figure 18 (c) depicts two cases of different time lags of 6 and 5 ms at flame locations $x_q = L/2$ and $x_q = L/3$ respectively, for $m^i = 1$. n_{th}^i increases with respect to temperature jump, when the

time lag is 6 ms at $x_q = L/2$. However, n_{th}^i reduces with respect to temperature jump when the time lag is 5 ms at $x_q = L/3$. Hence, the temperature jump has the potential to increase or decrease n_{th}^i.

Figure 19 (a), plotted on the basis of (33), demonstrates the effect of flame location on $n_{th}^i(\tau)$. The figure is drawn for two different flame locations, x_q =0.375m and 0.25m. Figure 19 (a) shows that as the flame location shifts away from the middle of the combustor (that is $x_q = 0.375$m), the neutral curve stretches to the left and the n_{th}^i increases for all time lags shown in the figure. Moreover, it can be shown (refer to Appendix IV, § AIV.I), that in the absence of cross-section and temperature jump, the flame location yielding the minimal n_{th}^i, is at the middle of the combustor. The minimal n_{th}^i flame location is independent of cross section jump and depends only on the temperature jump across the flame (refer to Appendix IV). In this context, note that the function on the right-hand side of equation (33) is symmetric with respect to $x_q = L/2$. Thus, we can only focus on one-half of the combustor for the analysis of the effect of the flame location. Figure 19 (b), drawn for two different time lags of 7 and 9 ms for $m^i = 1$, further validates the observations made from figure 19 (a). Figure 19 (b) shows that the minima of n_{th}^i, with respect to the flame location, for both time lags lie at $x_q = L/2$ (=0.375m for this case). The time lag of 9 ms lowers the n_{th}^i further, compared to the time lag of 7 ms.
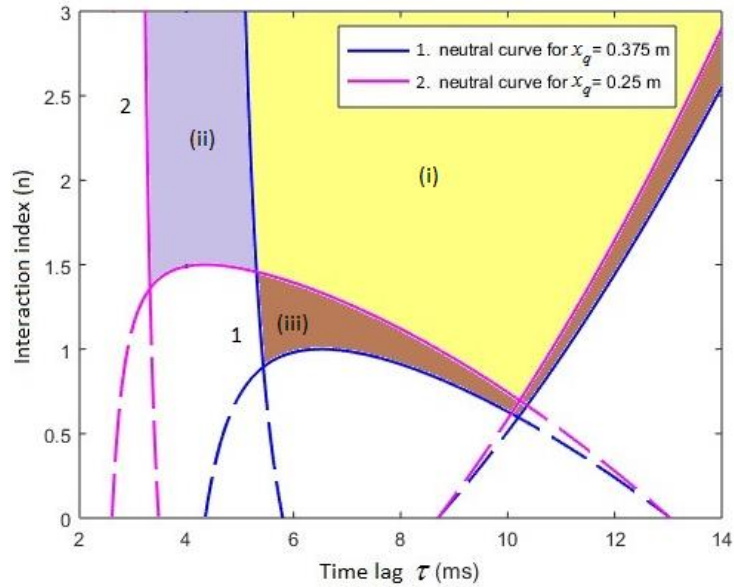
Figure 2.19 (a): Effect of the flame location on the stability domain for $m^i = 1$. The plot is based on (33) and shows two flame locations: x_q =0.375m and 0.25m. The instability domains for the cases x_q =0.375m and x_q =0.25m are indicated by brown (iii) and lavender (ii) respectively. The common instability domain for these two cases is marked in yellow and indicated by (i). Other parameters and notation are the same as in Fig.8.
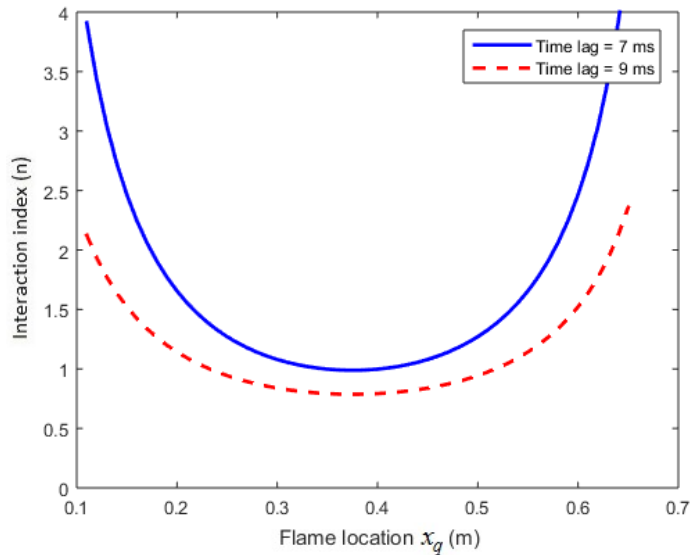

Figure 2.19 (b): Effect of flame location (x_q) on n^i_{th}, for $m^i = 1$. The blue continuous and the red dotted lines are for two different time lags of 7 and 9 ms. Other parameters are the same as in Fig.8.

A similar analysis can be performed for the growth rates as well. Figures 20 (a), (b) and (c) show the effect that cross-section jump, temperature jump, and flame location

respectively, have on the growth rate. Growth rates are calculated using the analytical result (47). Figure 20 (a) shows two different cases for time lag, 7ms, and 9ms (the flame is at x_q =0.375m), where, cross-section jumps of S_2/S_1 =1 and S_2/S_1 =2 are introduced for each case. The growth rate hardly depends on cross section jump for the time lag of 7 ms but becomes more dependent with the increase of the cross-section for the time lag of 9 ms. Figure 20 (b) shows two different cases for time lag, 6 ms (the flame is at x_q =0.375m) and 5 ms (the flame is at x_q =0.25m), where, temperature jumps of T_2/T_1 =1 (or, c_2/c_1 =1) and T_2/T_1 =4 (or, c_2/c_1 =2), are introduced for each case. The account of temperature jump reduces the growth rate for a time lag of 6 ms and increases it significantly for a time lag of 5 ms. Figure 20 (c) shows two different cases of flame locations: x_q =0.375m and x_q =0.30m at time lag = 6 ms. Shifting the flame location from x_q =0.375m (or $x_q = L/2$) to x_q =0.30m, reduces the growth rate. This is a general trend, as it has been mentioned in this section already, that the critical location from the intrinsic instability perspective is the middle of the closed-open combustor, in the absence of temperature jump.

Thus, by manipulating the system parameters, such as cross section jump, temperature jump, and flame location, one can increase/decrease the n_{th}^{i} and decrease/increase the growth rate, and hence dampen/instigate the intrinsic mode instability.
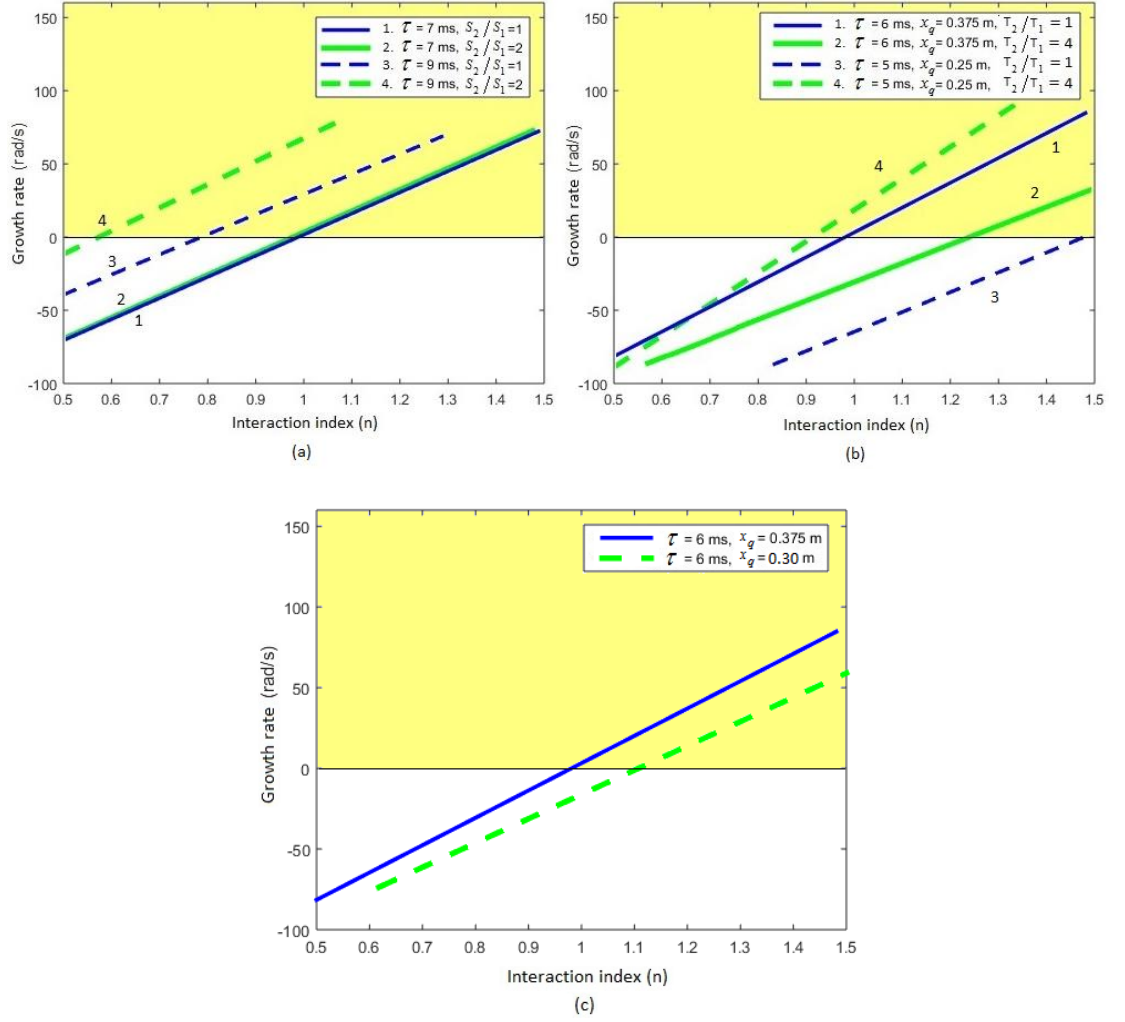
Figure 2.20: Effect of cross-section expansion and temperature jump on growth rates for $m^i = 1$ (based on (47)). (a) Two different time lags (7 and 9 ms) are indicated by solid and dashed lines. Two values of the cross section jump (S_2/S_1 =1 and S_2/S_1 =2) are marked blue and green. (b) Two different time lags at different flame locations (6 ms at x_q =0.375m and 5 ms at x_q =0.25m) are plotted by solid and dashed lines. The growth/decay rate dependence on n, for two values of temperature jumps T_2/T_1 =1 (or, c_2/c_1 =1) and T_2/T_1 =4 (or, c_2/c_1 =2) are marked in blue and green. (c) Two values of flame locations x_q =0.375m and x_q =0.30m at time lag = 6 ms are marked in blue and green. Other parameters and notation are the same as in Fig.8. The domain of instability is marked in yellow.

2.6.   Concluding remarks

In the present work, we have analytically examined flame intrinsic modes, within the framework of the simplest 1-D acoustic model of a combustor with $n - \tau$ heat

92

release. In this case, we considered a closed-open combustor, despite our approach being applicable to other configurations of combustors as well The main results can be summarized as follows:

(i)   We answered an outstanding question as to where unstable intrinsic flame modes come from. Our analysis shows that for any nonzero n and τ, there are always an infinite number of intrinsic modes present in a closed-open combustor. This should also hold for any combustor. For small values of n, a simple explicit dispersion relation (26a) describes a set of strongly damped modes. To leading order, the real parts of the frequencies $\mathrm{Re}\left(\omega^i\right) = \left(2m^i + 1\right)\left(\pi/\tau\right)$, where m^i is the mode number, do not depend on the characteristics of the combustor and the flame position. This is in contrast with the acoustic modes, whose frequencies are primarily determined by the combustor length, L ($\omega^a = (2m^a + 1)\left(\pi c/2L\right)$ (for $m^a = 0, 1, 2\ldots$) for a closed-open combustor). For small n, the decay rate of the intrinsic modes does not depend on the mode number and is inversely proportional to τ. The decay rate logarithmically depends on n. For the weak flame regime, characterized by small n, the heavily damped nature of these modes makes it practically impossible to detect them in combustion systems. The strong decay also makes these modes insensitive to the flame location and the specific properties of the combustor boundaries. Hence, to leading order, the modes in any combustor coincide with the intrinsic modes in the infinite tube with anechoic boundary conditions as described by Hoeijmakers et al. (2014). With the increase of n, the real part of the frequency shifts only very slightly (when there is no coupling with acoustic modes), thus remaining insensitive to all parameters of the system but τ. In contrast to this, the imaginary part depends on all parameters of the combustor and varies significantly.

(ii)   For each intrinsic mode for any τ, there is a threshold value of n above which the mode becomes unstable. The threshold depends on the characteristics of the combustor and the flame position, as explicitly given by expression (33). For each intrinsic mode, the convoluted neutral curve, separating stability and instability domains, is made of segments of three types, specified by the equations $\omega_c^i \tau = 0$, $\omega_c^i \tau = \pi$ and $\omega_c^i \tau = -\pi$, where ω_c^i is the discrepancy between the real part of the frequency on the neutral curve and the real part of the frequency in the limit of small n. The intricate shape of the instability domain, composed of an infinite number of loops of various scales, has been revealed. Remarkably, on the long stretches of the neutral curve, with the lowest threshold in n, the frequency exactly equals the real part of the frequency in the limit of small n. On the neutral curve, the instability frequency is independent of the flame location and the combustor parameters (except τ) and the mode completely decouples from the environment. This astonishing analytical result has been validated numerically. The fact that the frequencies of marginally unstable intrinsic modes are determined solely by τ, suggests that there are natural oscillations in the subsystem fuel injector-flame, determined by the ratio of the distance from the fuel injector to flame front and the flow velocity.

(iii)   Crucially, the threshold value of n is much smaller for a closed-open combustor when compared to the case with the anechoic boundary condition [Hoeijmakers et al. (2014)]. Thus, in a combustor, intrinsic modes can become unstable at a much lower value of n on the $n - \tau$ plane. The analytical results for the neutral curve are exact and could be used as a test case for complex software packages.

(iv)   The growth/decay rates near the neutral curve have been found analytically and validated numerically. A stability envelope has been introduced, to provide a

coarse-grained stability diagram on the $n - \tau$ plane with all intrinsic modes taken into account. Below this stability envelope, all modes are stable; above this envelope, all modes are unstable; and within the stability envelope, we have conditional stability domain. A simple technique has been developed to estimate the maximal growth rate at any point on the $n - \tau$ plane.

(v) The dependence of the instabilities on the key parameters of the combustor (the flame location, the cross-section, and the temperature jumps across the flame) has been described analytically. On this basis, by manipulating the system parameters like cross section jump, temperature jump, and flame location, one can increase/lower the n_{th}^i and increase/decrease the growth rate, hence preventing/instigating the intrinsic mode instability.

(vi) The question regarding when acoustic modes and when intrinsic modes dominate combustion instability remains unanswered. Both scenarios are possible. Obviously, the intrinsic modes are dominant when all acoustic modes are decaying. Such a possibility is illustrated in figure 21. A sample contour plot of detuning $\left| f\left(\omega\right) \right|$ is drawn for $\tau = 2.2$ ms, $n = 1.1$ for the combustor parameters, specified in figure 3. The first and second intrinsic mode (marked by triangles) are unstable in this parameter range, whereas all the acoustic modes (marked by diamonds) decay simultaneously, making the intrinsic mode the main factor in combustion instability.
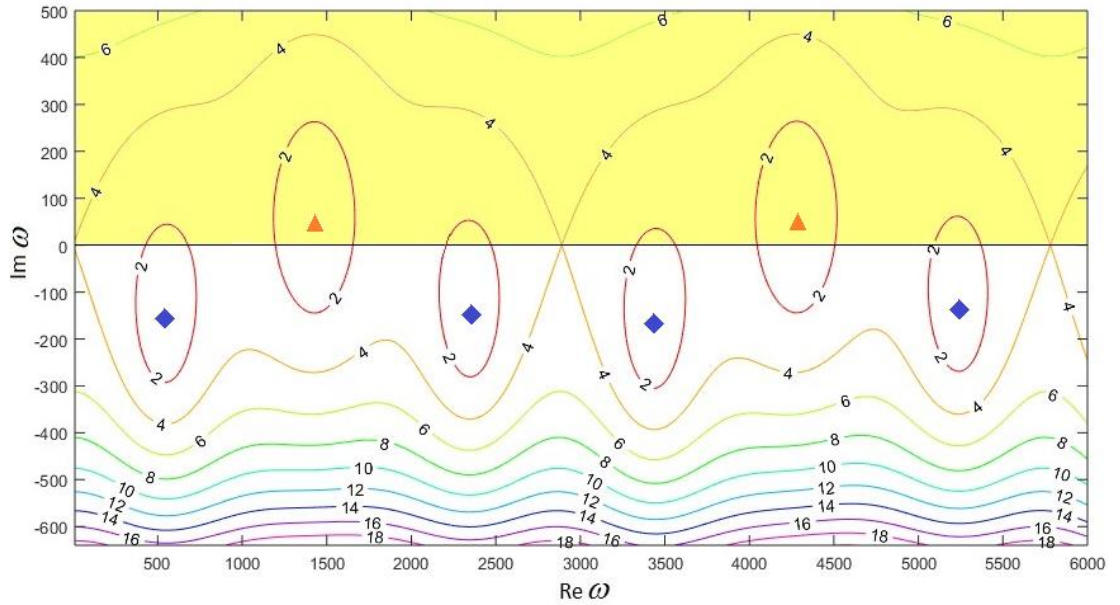
Figure 2.21: Contour plot of detuning $\left| f\left(\omega\right) \right|$ for $\tau = 2.2$ ms and $n = 1.1$. The domain of instability is marked in yellow. Blue diamonds and orange triangles represent the acoustic and intrinsic modes respectively. Other parameters are the same as in Fig.3.

The present chapter was confined to the analytic study of linear intrinsic flame modes *per se*, within the framework of the simplest $n - \tau$ model of a combustor and from our perspective, it answered all the questions we aimed at within the framework of this setting. Once the clarity within the framework of linear models is achieved, a study of nonlinear dynamics of intrinsic modes and their nonlinear interactions with acoustic modes will be a natural next step opening a vast new field.

Chapter 3

Coupling of acoustic and intrinsic modes in a 1-D combustor model: a new mechanism of the thermo-acoustic instability

3.1. Introduction

In chapter 2 we have found the main features and stability pattern of flame intrinsic modes, within the framework of a generic linear $n - \tau$ model of a closed-open 1-D combustor. The consideration was based on the key assumption that the intrinsic modes and acoustic modes do not couple with each other. This assumption is too restrictive. It is obvious that in a practical combustion system, under certain conditions, the intrinsic modes and acoustic modes will have similar frequencies and thus, might strongly interact with each other. To our knowledge, the interaction of intrinsic and acoustic modes has not been considered in the literature. Here we study the linear coupling of these modes for the first time. In this chapter, we will consider acoustic mode-intrinsic mode interaction for the case of a 1-D closed-open combustor and show that it is important in the big picture of combustor thermo-acoustic instabilities.

Generally, in a combustor, both the acoustic and intrinsic modes can become unstable, giving rise to the following two qualitatively different scenarios of instability,

i. Acoustic mode becoming unstable at zero threshold, $n_{th}^a = 0$, with instability frequency of $\omega_0^a = \left(2m^a + 1\right)\dfrac{\pi c}{2L}$ for a closed-open combustor, (where m^a =0, 1, 2…, while superscript a denotes acoustic mode);

ii. Intrinsic mode becoming unstable at n_{th}^i, predicted by equation (2.33), with instability frequency given by equation (2.32);

The first type of instability has been studied quite widely in the literature and has been the focus of research in combustion for the past few decades. A good account of the work can be found in the text book of Lieuwen T., and Yang V. (2005) and Poinsot T. and Veynante D (2011)). Nonetheless, for consistency, a brief overview of this kind of instability will be provided in § 2. The second type of instability represents the case when an intrinsic mode is uncoupled. This case has been worked out, in detail, in chapter 2. Another important aspect is that in the first type of instability, the flame heat release rate and the acoustic pressure are in phase with each other, as shown in figure 1 (a) and 1 (b). The 'Rayleigh Index' (

$$R_a = \int\limits_{0}^{T}\int\limits_{0}^{V} p'(x,t)q'(x,t)dvdt,$$ where the acoustic pressure oscillation is p', the time

period is T, combustor volume is V (control volume) and the heat release oscillation is q') is positive for this case. When, the flame heat release rate and acoustic pressure are out of phase with each other, as illustrated in figure 1 (a) and 1 (c), the Rayleigh index is negative, which implies the acoustic mode decay and hence, the first type of instability does not occur. However, as we show below, such an acoustic mode might

become unstable due to coupling with one of the intrinsic modes in close vicinity (in the frequency domain). When the Rayleigh index is positive, the first type of instability inevitably occurs. However, when the first type of instability is not possible due to out of phase relationship between the flame heat release and acoustic pressure, the new type of instability, that is instability due to intrinsic mode-acoustic mode coupling, comes into the picture.
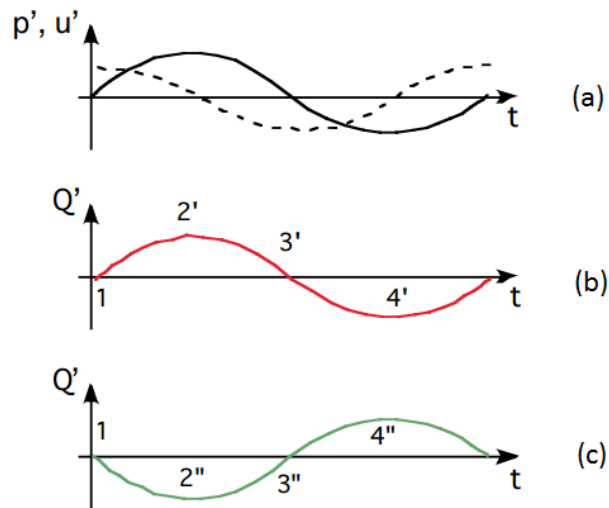
Figure 3.1: Mode shape of (a) acoustic pressure, velocity fluctuation and (b, c) flame heat release rate fluctuation [Polifke (2009)]. In (b) acoustic pressure fluctuation is in phase with the flame heat release rate fluctuation, indicating growth of acoustic mode. On the other hand, in (c) acoustic pressure fluctuation is out of phase with the flame heat release rate fluctuation, indicating decay of acoustic mode.

Our current effort will be focused on this new type of instability, where acoustic modes do interact with intrinsic modes and become unstable at a different frequency compared to the case (i). It will be shown, later in this chapter, that this scenario is difficult to track down, as the identity of such an acoustic mode is lost once it becomes unstable and it tends to behave exactly like an intrinsic mode. Coupling between modes has been a topic of interest in different research fields, as for example, in plasmas, in ocean waves, where surface waves can couple with internal gravity waves under certain circumstances (e.g. Soloviev and Lukas (2014), Craik

(1985), Watson et al. (1976), Watson (1990)). Throughout this chapter, we will restrict our analytical and numerical models to a closed-open combustor, the model of which has been introduced in Chapter 2.

The chapter is organized as follows. In **§ 2,** examples of numerical evidence of intrinsic-acoustic mode coupling are provided. Contour plots of the full dispersion relation are used to demonstrate the coupling. In **§ 3,** a comparative study of the pressure and velocity profiles of the coupled intrinsic and acoustic modes will be made, where the salient features of the mode shapes will be highlighted. In **§ 4,** the pressure and velocity profiles of the intrinsic and acoustic modes, with no coupling, are discussed. Some light will also be shed on the aspect of why mode shapes do not provide conclusive evidence on the nature of the modes. In **§ 5,** a new form of instability, due to the linear coupling of intrinsic and acoustic modes, will be introduced. This form of instability is different from the two other types of combustion instabilities studied in the literature, i.e. pure acoustic mode instability, pure intrinsic mode instability. In **§ 6,** we derive a simple mathematical model which captures the main features of the intrinsic and acoustic mode coupling. In the simplest model of coupling, the governing equation obtained, by reduction of the full dispersion, is quadratic. The four types of coupling in this system are identified. In **§ 7,** a numerical examination within the framework of the full dispersion relation is performed, to check the accuracy of the simple model developed in § 6. For better accuracy, in **§ 8,** the quadratic model developed in § 6, is improved by incorporating the higher order terms. Thus, we arrive at a quartic equation for the coupled modes, an increase in complexity compared to the quadratic equation of § 6. In **§ 9,** a further numerical examination is performed to examine the accuracy of the quartic equation model. In **§ 10,** we provide a complete picture of the coupling near the intersection

points of the neutral curve segments. The evolution of one type of coupling into another is also discussed. In **§ 11,** the domain on the neutral curve where intrinsic-acoustic mode coupling occurs is identified. In **§ 12,** we focus on the limitations of the quadratic equation for the coupling description developed in § 6 and elaborate on the scenarios when the quartic equation model of § 8 should be used, rather than the quadratic equation model of § 6. In **§ 13,** we formulate concluding remarks and outline the scope of future work.

3.2. Evidence of intrinsic-acoustic mode coupling in contour plots of dispersion relation equation detuning

In chapter 2 (fig 2.3), we have seen an example where the first intrinsic mode is largely decaying in the limit of small n and as n is increased, the first acoustic mode becomes unstable, whereas the first intrinsic mode remains stable. Further observation shows that the first acoustic mode becomes unstable at the frequency of the first intrinsic mode. In this section, we will examine this phenomenon in detail. Here we consider a situation where we gradually increase n and track down the loci of the first intrinsic mode and first acoustic mode on the complex frequency plane. To show this, figure 2 (a), (b) and (c) present contour plots of the detuning function prescribed by the full dispersion relation (2.20) for $\tau = 3$ ms, $x_q = L/2$ and neglecting the effect of cross-section and temperature jump across the flame. In figure 2, the acoustic and intrinsic modes are indicated by blue diamonds and orange triangles respectively. The instability domain is marked in yellow. Figure 2 (a) shows the case when $n = 0.25$ and the first acoustic mode decays, whereas the decay rate of the first intrinsic mode reduces (compared to an uncoupled intrinsic mode). With the increase of n, the first acoustic and the first intrinsic mode frequencies come close to

each other. In figure 2 (b), n is increased to 0.5, keeping $\tau = 3$ ms. The decay rate of the first acoustic mode increases further, whereas the decay rate of the first intrinsic mode reduces. Thus, these two modes come closer to each other in the complex frequency plane. Another important aspect is the crossover of frequency, that is, the frequencies of the first acoustic and first intrinsic modes cross each other and the first acoustic mode attains higher frequency than the first intrinsic mode. One important point, with figures 2 (a) and (b), is that the decay rate of the first intrinsic mode is always lower than the decay rate of the first acoustic mode, even if they come very close to each other on the complex frequency plane. In figure 2 (c), n is further increased to 0.8, keeping τ the same. It can be seen that the first acoustic mode comes to the neutral line and tends to become unstable at this value of n, at the same frequency of first intrinsic mode in the asymptotic limit of small n (as per figure 2.10). The decay rate of the first intrinsic mode is reduced further, but the mode does not cross the neutral line.
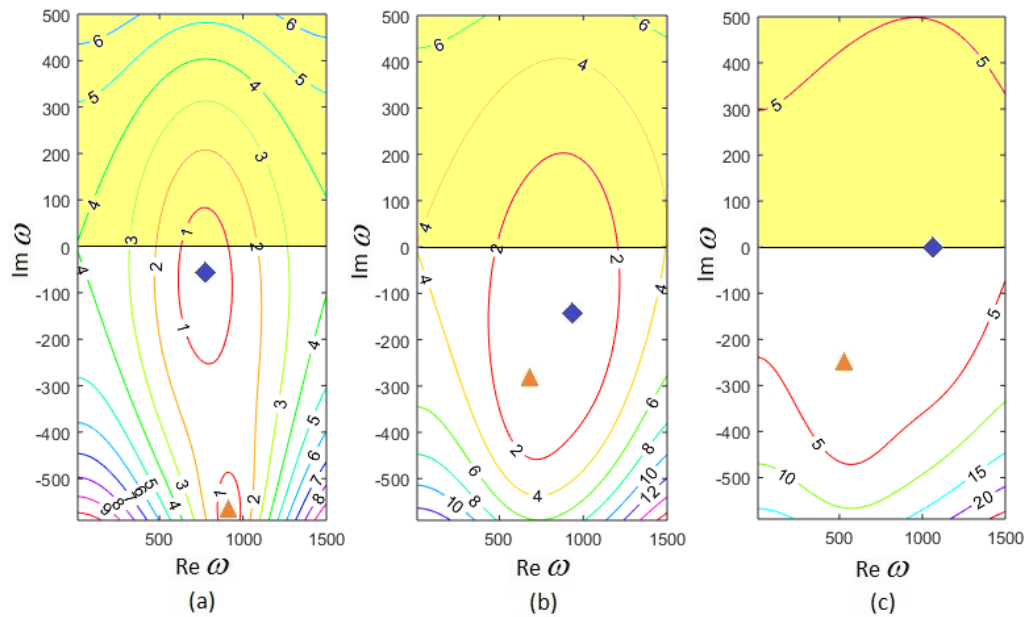
Figure 3.2: Contour plot of f for $n = 0.25$, $n = 0.5$, $n = 0.8$ at $\tau = 3.0$ ms. Other notations and parameters are the same as in Fig.2.8.

Figure 2 illustrates the basic scenario of intrinsic-acoustic mode coupling when, due to a gradual increase of n, the initially decaying acoustic mode becomes unstable at the frequency of the intrinsic mode in the limit of small n. It is not easy to establish the true identity of the mode on the neutral curve. Here, we manually track down the acoustic and intrinsic mode on the complex frequency plane, while gradually increasing n.

3.3. Pressure and velocity profiles of acoustic and intrinsic modes

As it was discussed in the previous section, the identities of the coupled modes are not straightforward to find out when these modes are close to each other. It might be possible to reveal the identity of the modes through a detailed study of their pressure and velocity profiles as the solutions "move" on the $n - \tau$ plane because of varying value of n.

From equations (2.1, 2.2), by making use of (2.3, 2.4), the pressure and velocity profiles upstream of the flame can be written as

$$p_1(x) = 2B_1 \cos(kx) \text{ and} \tag{3.1}$$

$$u_1(x) = (2i/\rho c) B_1 \sin(kx). \tag{3.2}$$

We have omitted the time dependence of pressure and velocity in equations (1, 2), as compared to the equations (2.1) and (2.2). Clearly, from (1), we find a cosinusoidal distribution of pressure and a sinusoidal distribution of velocity in the axial direction, x. The pressure distribution downstream of the flame has the following form,

$$p_2(x) = -2ie^{-ikL} B_2 \sin\{k(x-L)\}, \tag{3.3}$$

where B_2 in (3) is related to B_1 in (1) and (2) as

$$B_2 = ie^{ikL} \left[\cos(kx_q) / \sin\{k(x_q - L)\} \right] B_1. \tag{3.4}$$

103

Making use of (4), the pressure distribution downstream of the flame, as given by (3), can be restructured as,

$$p_2(x) = 2B_1 \left[\cos(kx_q)/\sin\{k(x_q - L)\} \right] \sin\{k(x-L)\}. \tag{3.5}$$

The corresponding velocity profile downstream of the flame can be shown to have the form,

$$u_2(x) = -(2/\rho c)e^{-ikL}B_2 \cos\{k(x-L)\}. \tag{3.6}$$

Again, similar to the previous case, making use of (4), equation (6) can be rearranged as,

$$u_2(x) = -(2i/\rho c)B_1 \left[\cos(kx_q)/\sin\{k(x_q - L)\} \right] \cos\{k(x-L)\}. \tag{3.7}$$

Equations (1) and (5) together, provide the acoustic pressure distribution across the length of the combustor. Similarly, (2) and (7) combined, provide the acoustic velocity distribution across the length of the combustor. Indeed, the expressions (1), (2), (5) and (7) describe complex quantities, as $k = \omega/c = (\omega_r + i\omega_{im})/c$. To support this statement, the trigonometric expressions in (1) and (2) can be written as,

$$\cos(kx) = \cos(\omega_r x/c)\cos(i\omega_{im} x/c) - \sin(\omega_r x/c)\sin(i\omega_{im} x/c),$$

$$\sin(kx) = \sin(\omega_r x/c)\cos(i\omega_{im} x/c) + \cos(\omega_r x/c)\sin(i\omega_{im} x/c). \tag{3.8}$$

$\cos(i\omega_{im} x/c)$ and $\sin(i\omega_{im} x/c)$ in equation (8) can be expanded as per Euler's formula to show the purely real and purely imaginary nature of $\cos(i\omega_{im} x/c)$ and $\sin(i\omega_{im} x/c)$, respectively,

$$\cos(i\omega_{im} x/c) = (e^{-\omega_{im} x/c} + e^{\omega_{im} x/c})/2,$$

$$\sin(i\omega_{im} x/c) = (e^{-\omega_{im} x/c} - e^{\omega_{im} x/c})/2i. \tag{3.9}$$

Making use of (8) and (9), we arrive at the following expressions of $p_1(x)$ and $u_1(x)$ as per (1) and (2), to confirm our earlier statement that indeed $p_1(x)$ and $u_1(x)$ are complex quantities, i.e. they have amplitude and phase.

$$p_1(x) = B_1 \left[\cos\left(\omega_r x/c\right)\left(e^{-\omega_{im}x/c} + e^{\omega_{im}x/c}\right) + i\sin\left(\omega_r x/c\right)\left(e^{-\omega_{im}x/c} - e^{\omega_{im}x/c}\right)\right],$$

$$u_1(x) = \frac{B_1}{\rho c}\left[\cos\left(\omega_r x/c\right)\left(e^{-\omega_{im}x/c} - e^{\omega_{im}x/c}\right) + i\sin\left(\omega_r x/c\right)\left(e^{-\omega_{im}x/c} + e^{\omega_{im}x/c}\right)\right].$$

(3.10)

Using equations (5) and (7) the same can be shown for $p_2(x)$ and $u_2(x)$. At this point, we can study the pressure and velocity profiles of intrinsic and the coupled-acoustic modes based on equations (1), (5), (2) and (7). Figures 3-9 show such pressure and sample velocity profile plots for the acoustic and intrinsic modes for the same value of τ ($\tau = 3$ ms), as shown in the example (figure 2) of § 2. The first intrinsic and first acoustic modes are coupled in this case. The red dashed and blue solid lines represent the intrinsic and acoustic modes respectively. The effects of cross-section and temperature jump across the flame are neglected here. Panels (a) and (b) show acoustic pressure and velocity amplitude respectively, whereas panels (c) and (d) represent acoustic pressure and velocity phase respectively (As per equation (10), pressure and velocity are complex quantities).

In figure 3, n is infinitesimally small, so the intrinsic mode is heavily decaying. Therefore, it does not feel the boundaries of the combustor, as can be seen from the pressure profile. The acoustic mode, in contrast, is determined by the combustor boundaries and has zero phase. As n is increased to 0.1, figure 4 shows that the intrinsic mode becomes less localized and starts feeling the combustor boundaries. However, this mode is still heavily decaying. The decay rate of the intrinsic mode

105

reduces and it comes closer to the acoustic mode. The acoustic mode keeps on being determined by the combustor boundaries. There is a jump in the velocity profile at the flame location ($x_q = L/2$), as it is an obvious effect of the flame acting as a monopole source (see equation (2.16)). As the n is increased further to 0.3 in figure 5, acoustic and intrinsic mode come closer to each other. The acoustic mode decay increases, whereas the decay rate of the intrinsic modes reduce. A hump is visible in the pressure profile of the intrinsic mode. The phase angle for the intrinsic mode pressure remains higher than that of the acoustic mode. At n=0.4, shown in figure 6, the acoustic mode and intrinsic mode attain almost equal frequency, and thus the frequencies start "crossing" each other. The intrinsic mode still maintains a higher decay rate than the acoustic mode. An apparent dip is visible in the acoustic mode pressure profile, but the pressure and velocity profiles for the acoustic and intrinsic modes look almost identical. This might serve as a strong evidence of coupling.

As n is increased to 0.5, as shown in figure 7, acoustic and intrinsic mode frequencies cross each other and, for the first time, the acoustic mode attains higher frequency than the intrinsic mode. Interestingly, the decay rate for both the intrinsic and acoustic mode reduces. The gap between the hump in the pressure profile for intrinsic mode and dip in the pressure profile of acoustic mode becomes more prominent. The intrinsic mode pressure profile maintains a higher phase angle than the acoustic mode pressure profile. The jump in velocity amplitude at the flame location is stronger for the acoustic mode compared to the intrinsic mode. Figure 8 shows that the increase of n, to 0.7, brings the acoustic mode particularly close to the neutral line, and the intrinsic mode tends to come closer to the neutral line as well. The difference between the pressure profile hump and dip for these two modes becomes more prominent. As in figure 9, the acoustic mode becomes unstable at the

frequency of the intrinsic mode in the asymptotic limit of small n, whereas the intrinsic mode comes closer to the neutral curve. The phase angle for the acoustic mode becomes zero again, whereas the intrinsic mode pressure profile manifests higher phase angles. The difference between pressure profile hump and dip for these two modes remains substantial like in figures 7 and 8. The jump in velocity amplitude at the flame location is stronger for acoustic mode, just like previous two cases. The discontinuity in the velocity profiles at the flame location is a consistent feature for all these figures.

We have thus performed a comparison of the pressure profiles of a coupled pair of an intrinsic and acoustic mode. A coupled acoustic mode decays for small n and then, both the acoustic mode and intrinsic mode approach the neutral line with the increase of n. From the point when the frequencies of the two modes cross on the complex frequency plane, the pressure and velocity profiles of acoustic and intrinsic modes appear almost identical. This is the most important observation of the pressure profile study. The difference between the pressure profiles of two modes become more prominent with an increase of n.
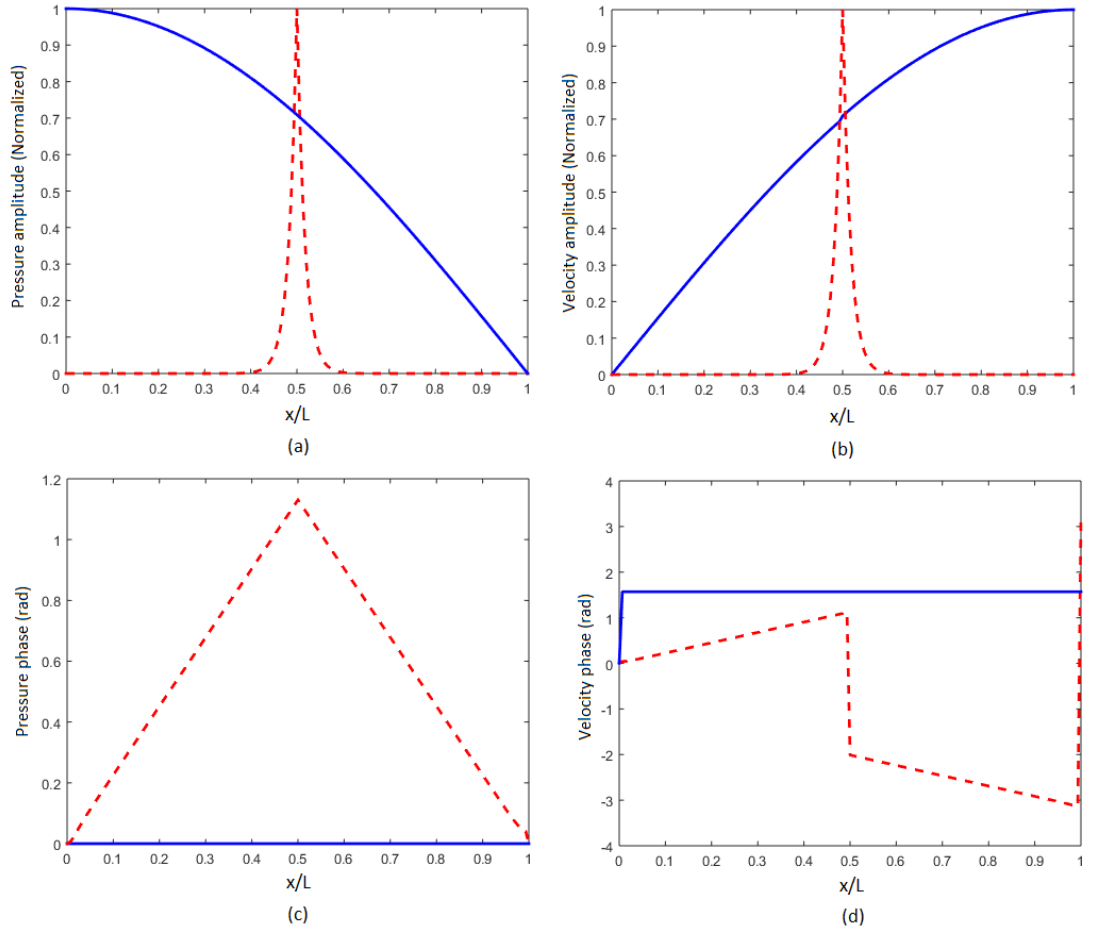
Figure 3.3: (a, b) Normalized pressure, velocity amplitude and (c, d) pressure, velocity phase, in radians, of intrinsic mode and acoustic modes, based on equations (1), (5), (2) and (7), for $x_q = L/2$, $n = 10^{-30}$, $\tau = 3$ms, $\omega^a = 720 - i*0$ rad/s, $\omega^i = 1040 - i*27000$ rad/s. The red dashed and blue solid lines represent the intrinsic and acoustic modes respectively. The pressure profile shows a strongly decaying intrinsic mode on either side of the flame and thus, the intrinsic mode does not feel the boundaries of the combustor. The same trend is also true for the velocity profile for intrinsic mode. The phase of the acoustic mode is zero. The effect of cross-section and temperature jump across the flame has been neglected here.
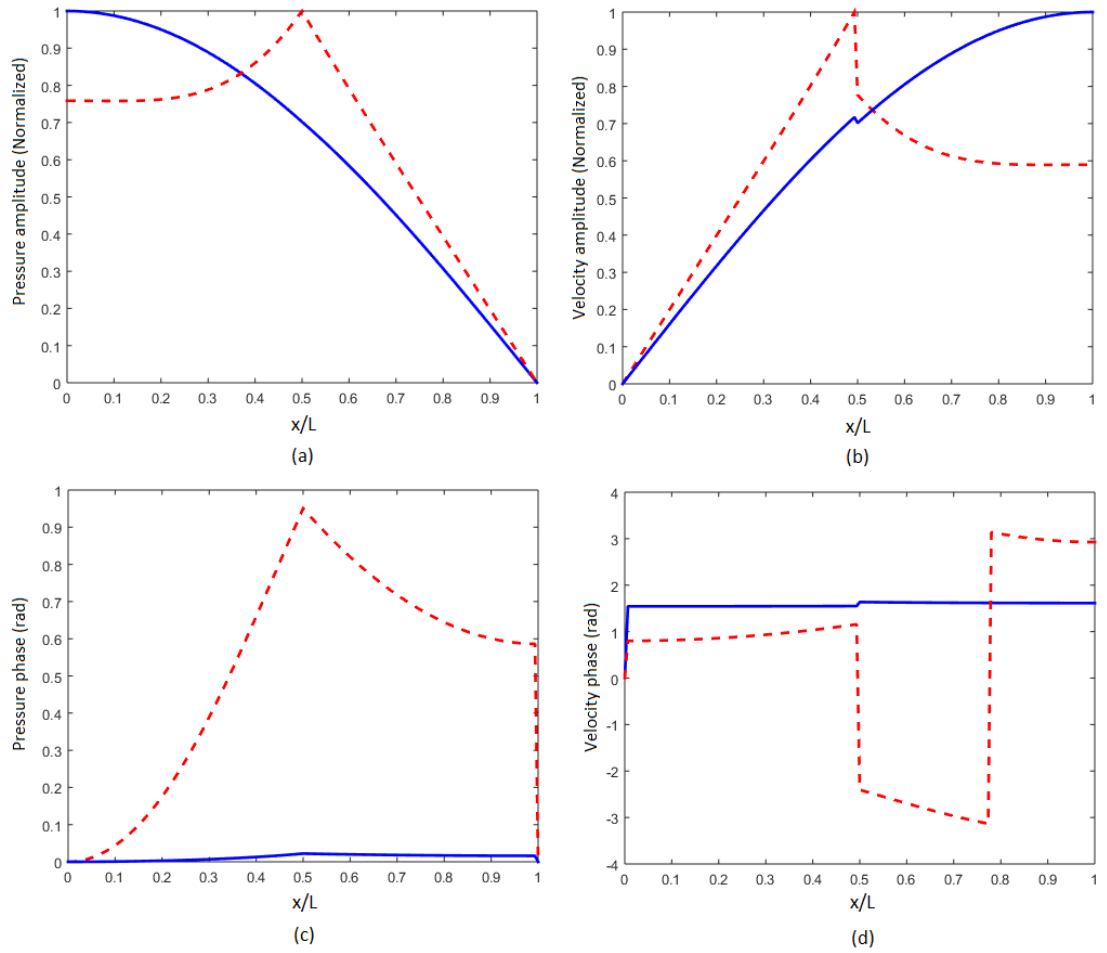
Figure 3.4: (a, b) Normalized pressure, velocity amplitude and (c, d) pressure, velocity phase, in radians, of intrinsic and acoustic modes, based on equations (1), (5), (2) and (7), for

$$x_q = L/2 \, , \ n = 0.1, \ \tau = 3\text{ms}, \ \omega^a = 730 - i *20 \text{ rad/s}, \ \omega^i = 980 - i *950 \text{ rad/s}.$$ Other

parameters and notations are the same as in figure 3. The acoustic mode feels the combustor boundary while the intrinsic mode only starts to feel combustor boundary. The intrinsic mode is still heavily decaying on either side of the flame.
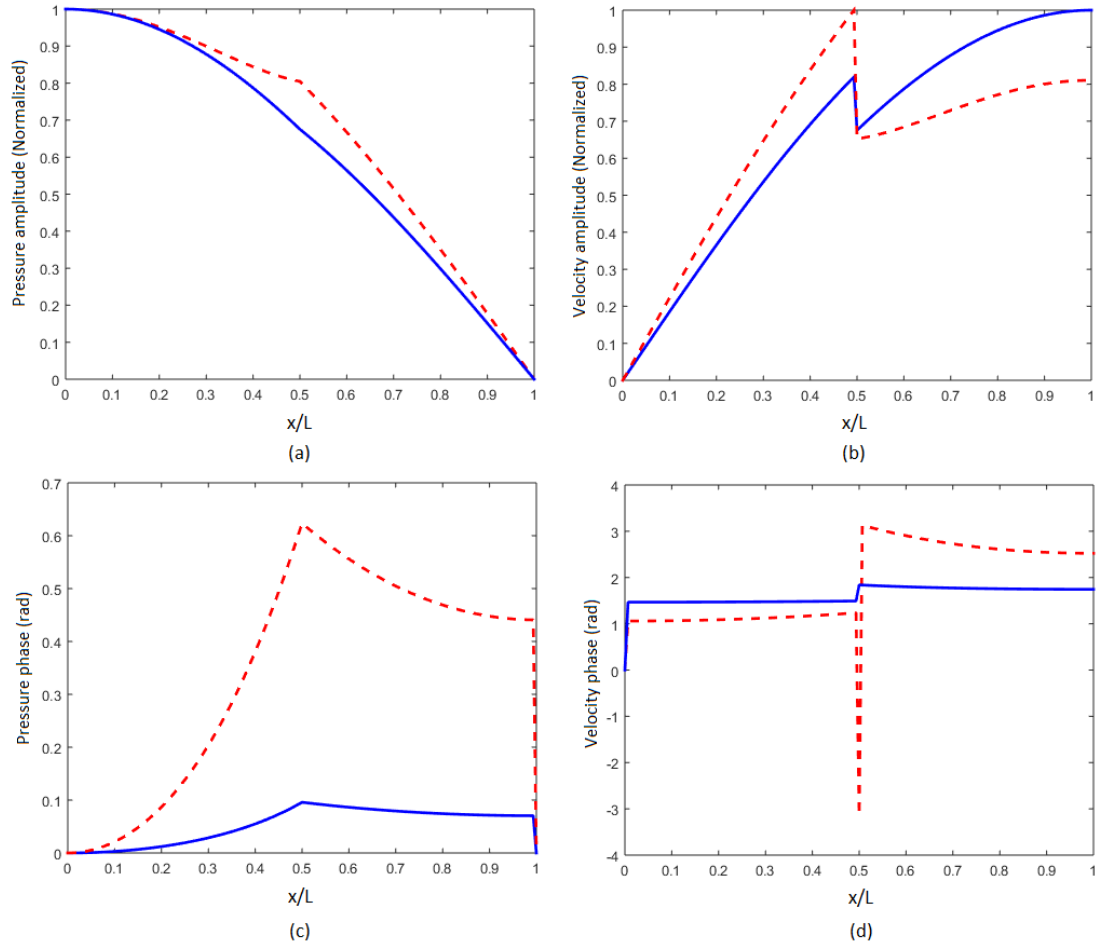
Figure 3.5: (a, b) Normalized pressure, velocity amplitude and (c, d) pressure, velocity phase, in radians, of intrinsic and acoustic modes, based on equations (1), (5), (2) and (7), for $x_q = L/2$, n =0.3, τ =3ms, ω^a =770- i *80 rad/s, ω^i =890- i *500 rad/s. Other parameters and notations are the same as in figure 3. Both the acoustic and intrinsic mode feel the combustor boundaries.
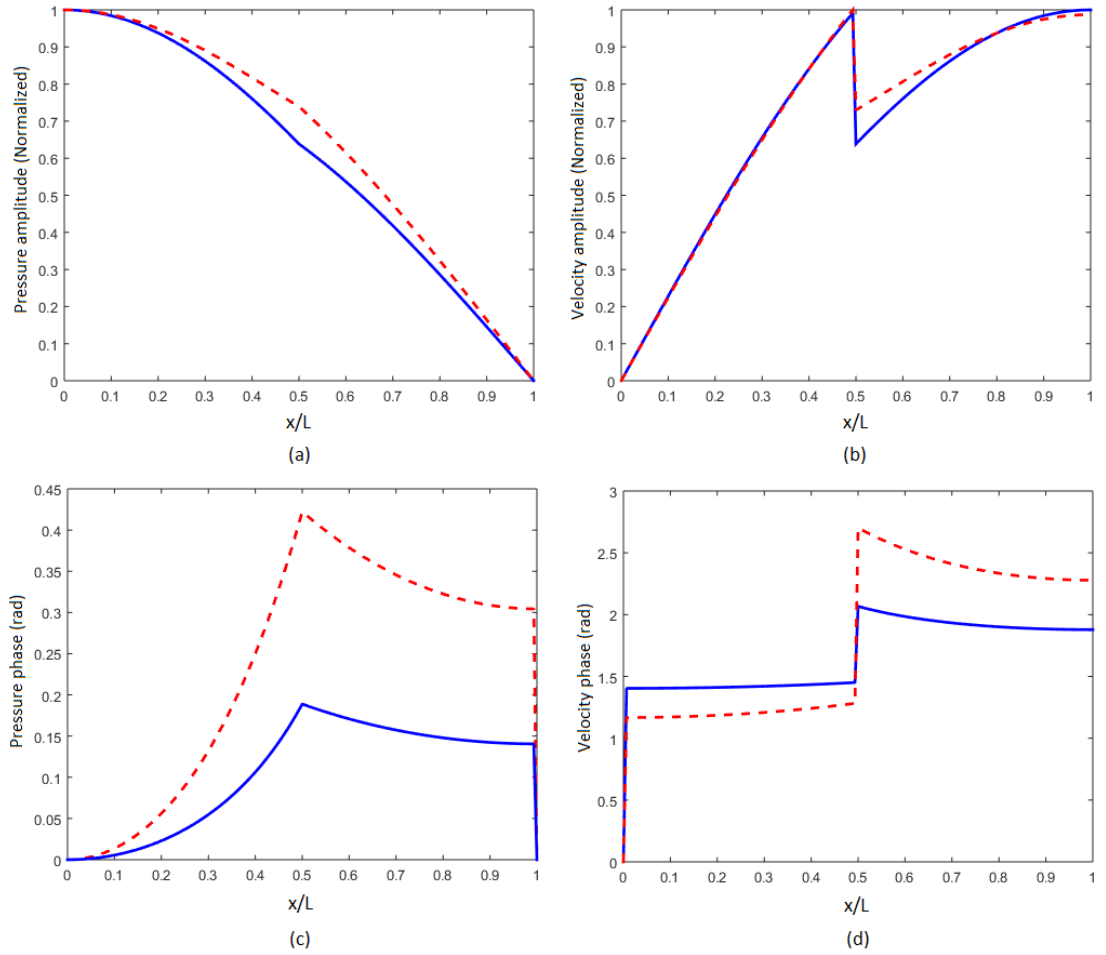
Figure 3.6: (a, b) Normalized pressure, velocity amplitude and (c, d) pressure, velocity phase, in radians, of intrinsic and acoustic modes, based on equations (1), (5), (2) and (7), for

$x_q = L/2$, n =0.4, τ =3ms, ω^a =830- i *140 rad/s, ω^i =820- i *350 rad/s. Other

parameters and notations are the same as in figure 3. The real parts of the acoustic and intrinsic mode frequencies are almost the same. The crossing of the acoustic and intrinsic modes starts at this point. The intrinsic and acoustic mode pressure and velocity profiles appear almost identical at this point.
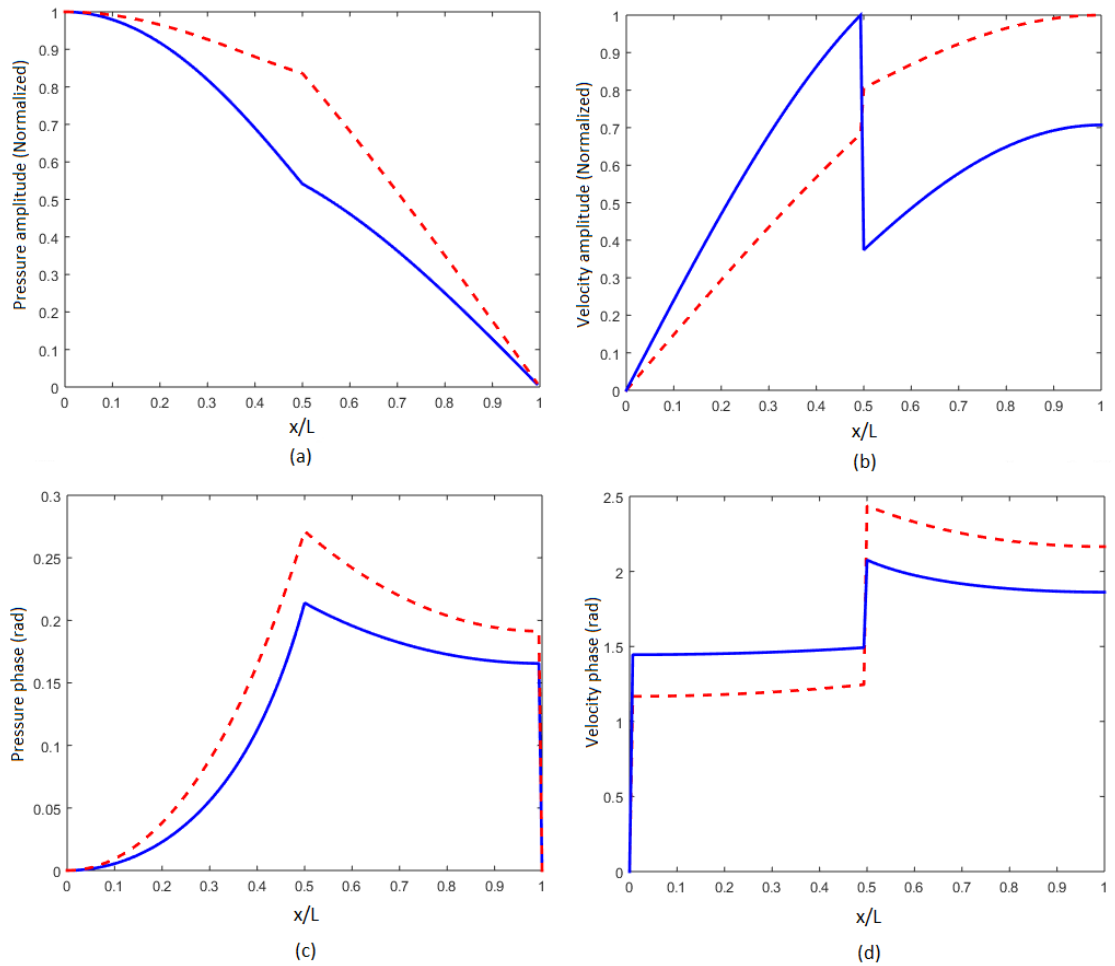
Figure 3.7: (a, b) Normalized pressure, velocity amplitude and (c, d) pressure, velocity phase, in radians, of intrinsic and acoustic modes, based on equations (1), (5), (2) and (7), for

$$x_q = L/2, \; n=0.5, \; \tau=3\text{ms}, \; \omega^a=950- i *120 \text{ rad/s}, \; \omega^i=680- i *290 \text{ rad/s}.$$ Other

parameters and notations are the same as in figure 3. The acoustic and intrinsic modes have already crossed each other at this point. The intrinsic mode however, maintains a larger decay rate than the acoustic mode. In the pressure profile of the intrinsic mode, there is a hump, whereas for the acoustic mode we find a dip at the flame location. The jump in velocity amplitude at the flame location is stronger for the acoustic mode.
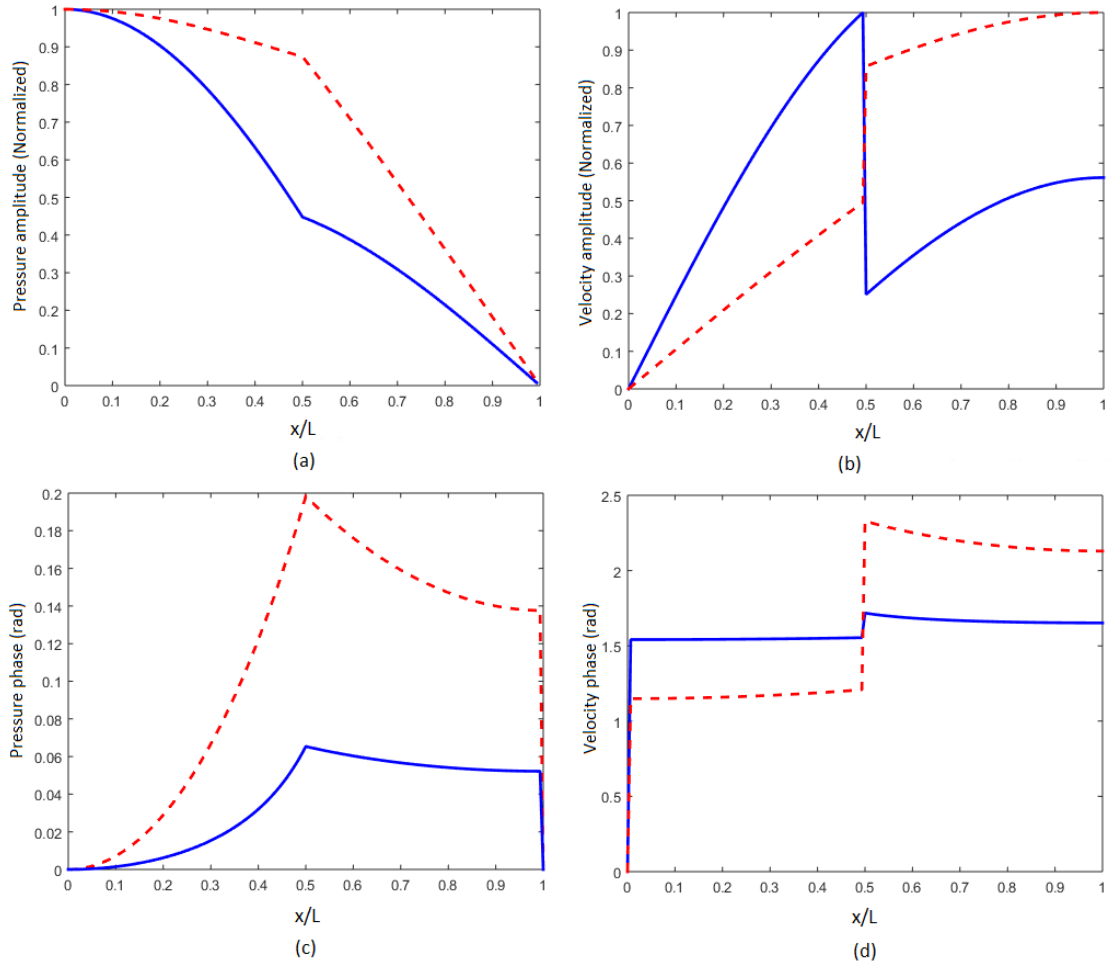
Figure 3.8: (a, b) Normalized pressure, velocity amplitude and (c, d) pressure, velocity phase, in radians, of intrinsic and acoustic modes, based on equations (1), (5), (2) and (7), for

$$x_q = L/2, \ n = 0.7, \ \tau = 3\text{ms}, \ \omega^a = 1020 - i*30 \text{ rad/s}, \ \omega^i = 580 - i*260 \text{ rad/s}.$$ Other

parameters and notations are the same as in figure 3. After crossing, the acoustic and intrinsic mode frequencies are far apart in this case. The intrinsic mode maintains a larger decay rate than the acoustic mode. The hump in the intrinsic mode and dip in the acoustic mode pressure profiles become more prominent at the flame location. The jump in velocity amplitude at the flame location is stronger for the acoustic mode.
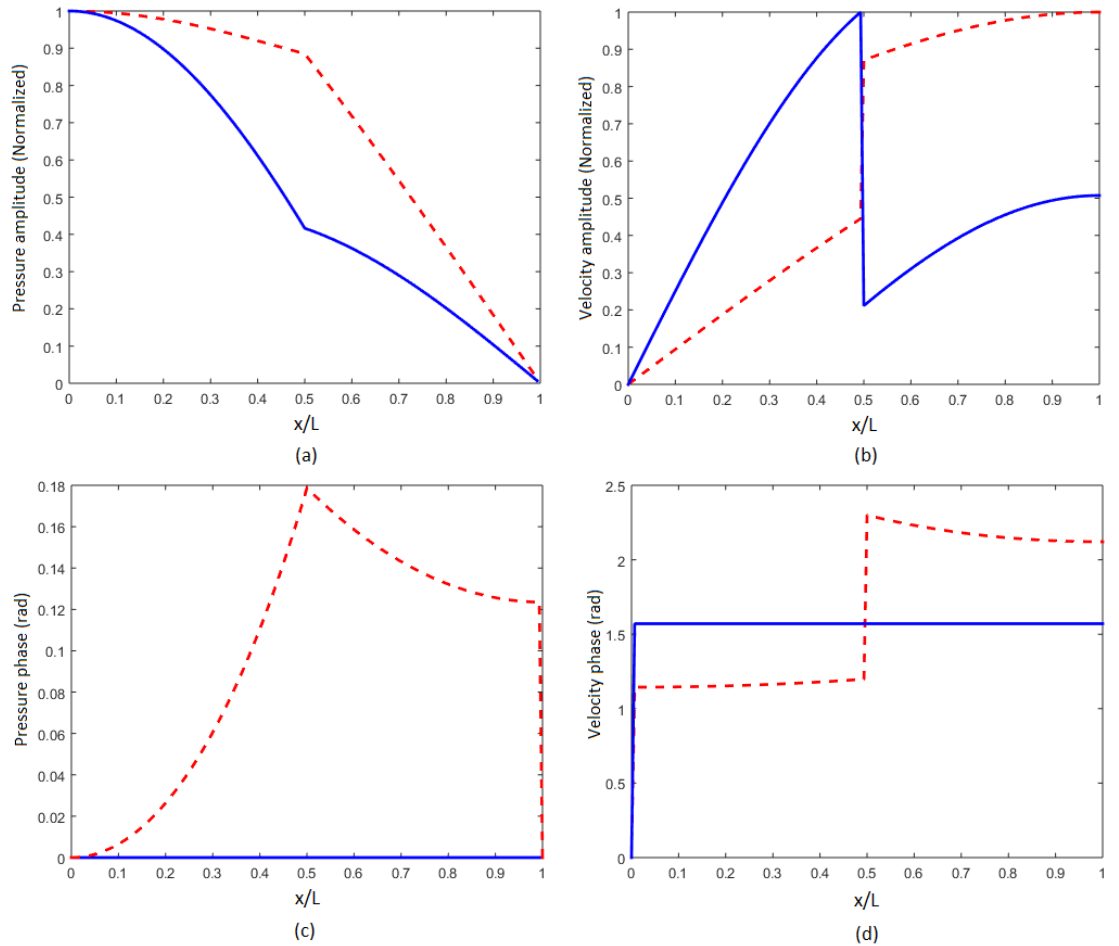
Figure 3.9: (a, b) Normalized pressure, velocity amplitude and (c, d) pressure, velocity phase, in radians, of intrinsic and acoustic modes, based on equations (1), (5), (2) and (7), for $x_q = L/2$, n =0.8, τ =3ms, ω^a =1050+ i *0 rad/s, ω^i =550- i *250 rad/s. Other parameters and notations are the same as in figure 3. The acoustic mode becomes marginally stable at this point, whereas the intrinsic mode maintains a large decay rate. In this case also, the hump in the intrinsic mode and dip in the acoustic mode pressure profiles remain prominent at the flame location. The phase angle of the acoustic mode becomes zero again. The jump in velocity amplitude at the flame location is stronger for the acoustic mode.

3.4. Close proximity of pressure profiles between acoustic and intrinsic modes during coupling

In § 3, we have noted that in the limit of small n, pressure profiles of acoustic and intrinsic modes are clearly distinguishable. However, the same may not be valid when these modes approach the neutral curve. In § 3, we have examined the nature of pressure and velocity profiles of intrinsic and acoustic modes when they couple with

each other. In this section, we first explore a slightly different scenario. We analyze the pressure and velocity profiles of acoustic and intrinsic modes when we do not have any coupling of modes, and thus we have pure acoustic and pure intrinsic instability. Later, moving forward from this point, we provide an overall explanation of why mode shapes might not distinctively reveal individual identities of acoustic and intrinsic modes.

Figures 10 and 11 illustrate a scenario of pure acoustic mode instability for a fixed time lag (τ =4.5 ms), where the first acoustic mode becomes unstable (as it satisfies the positive Rayleigh index criterion). The pressure profile of the acoustic mode behaves in a similar manner to a classical first acoustic mode of a closed-open combustor. The decaying intrinsic mode for n =0.3, as shown in figure 10, has a sharp hump (at the flame location $x_q = L/2$) in the pressure profile. The jump in the velocity amplitude is also prominent, for the intrinsic mode, at the flame location. As n is increased from 0.3 to 5.0, we cannot spot any noticeable and qualitative change in the pressure profile of the intrinsic mode. Thus, we can identify some distinction between the mode shapes of acoustic and intrinsic mode for this case, where pure acoustic mode instability prevails.
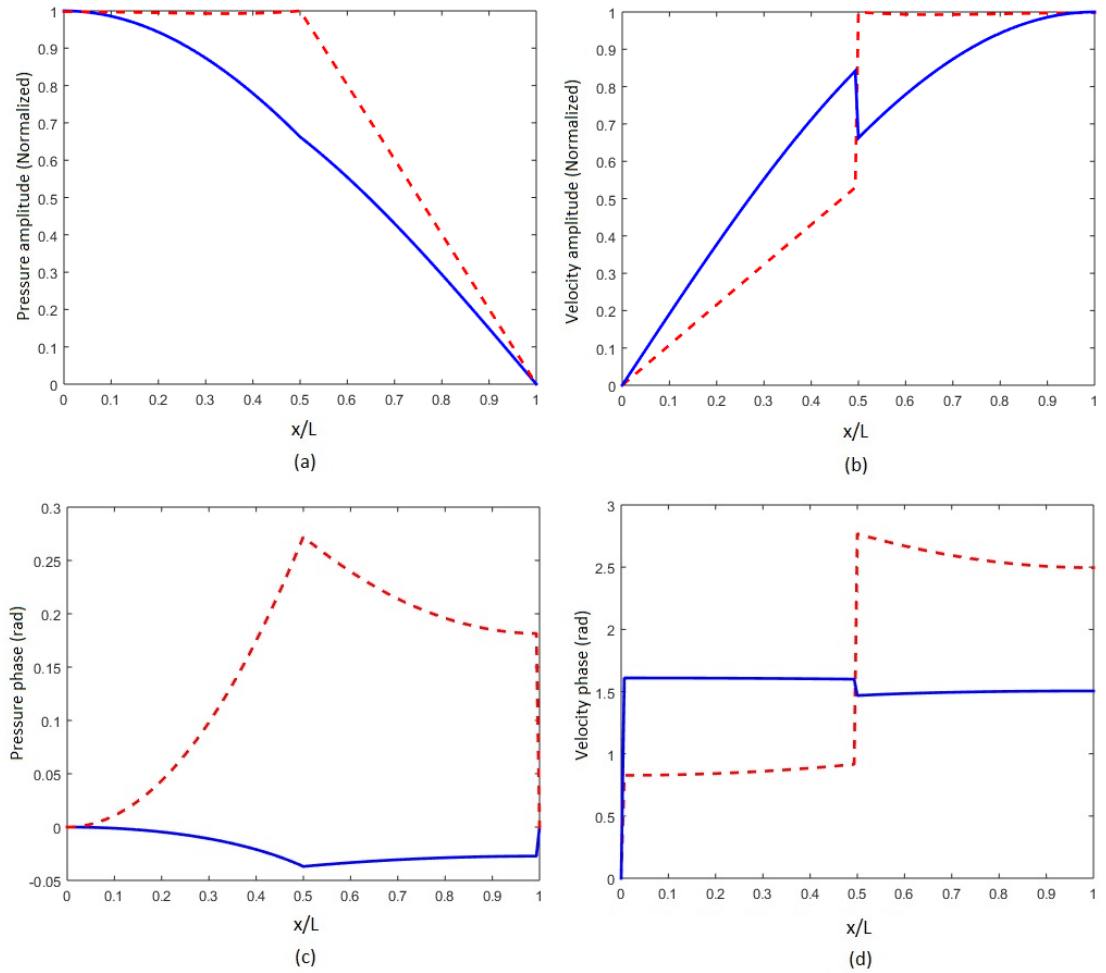
Figure 3.10: (a, b) Normalized pressure, velocity amplitude and (c, d) pressure, velocity phase, in radians, of intrinsic and acoustic modes, based on equations (1), (5), (2) and (7), for

$$x_q = L/2 \, , \, \tau = 4.5 \text{ ms}, \, n = 0.3, \, \omega^a = 780 + i*30 \text{ rad/s}, \, \omega^i = 500 - i*460 \text{ rad/s. Other}$$

parameters and notations are the same as in figure 3. For this n, the acoustic mode grows, whereas the intrinsic mode manifests large decay. This is a scenario of pure acoustic mode instability. Figures (a) and (c) demonstrate distinctive humps for the intrinsic modes, as compared to mild dips for the acoustic modes.
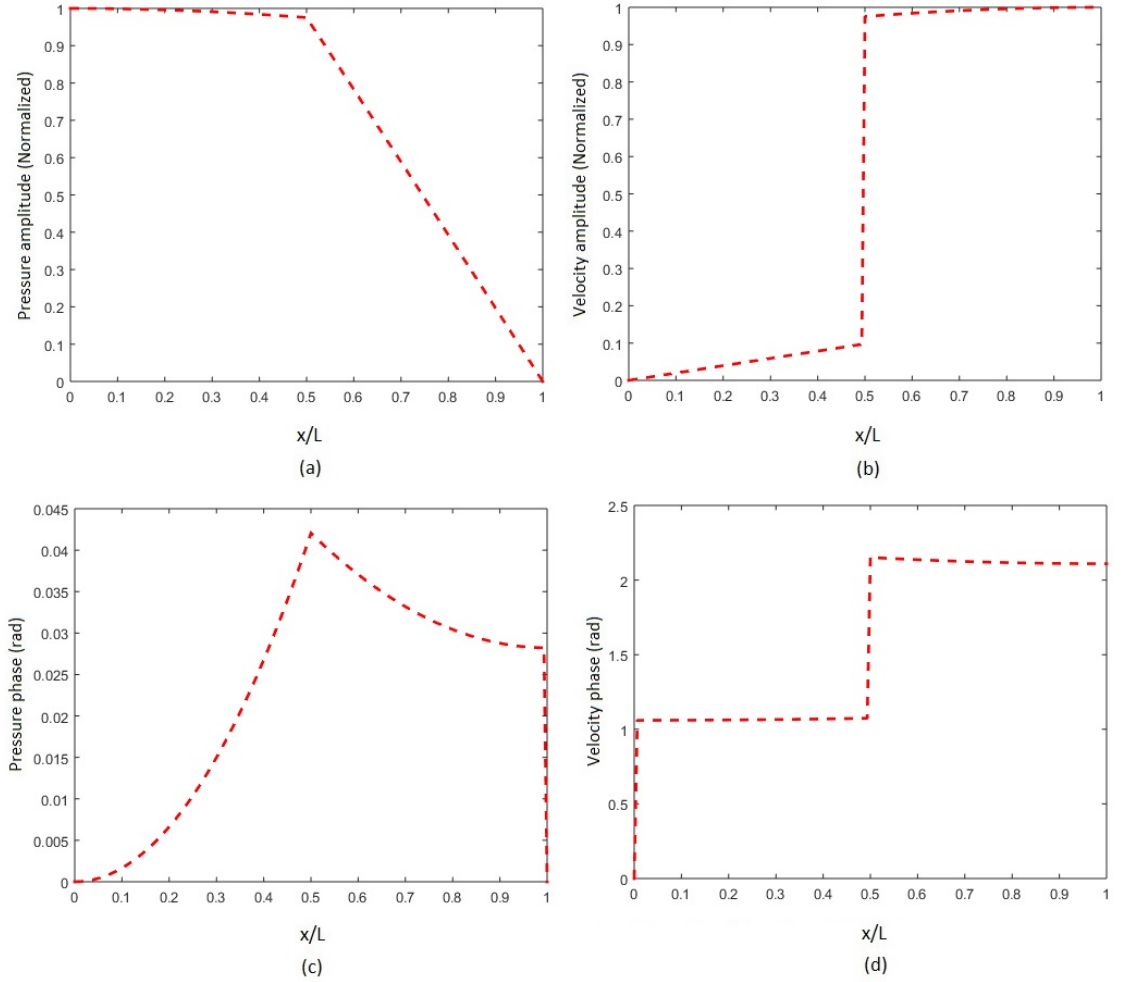
Figure 3.11: (a, b) Normalized pressure, velocity amplitude and (c, d) pressure, velocity phase, in radians, of intrinsic modes, based on equations (1), (5), (2) and (7), for $x_q = L/2$, $\tau = 4.5$ ms, $n = 5.0$, $\omega^i = 250 - i*140$ rad/s. The intrinsic mode maintains a decaying nature, similar to figure 10. However, here it comes closer to the neutral line. Compared to figure 10, the increase of n does not introduce any noticeable change in the mode shapes of the intrinsic mode. Other parameters and notations are the same as in figure 3.

Similarly, in figures 12 and 13 we observe pure intrinsic mode instability. The same case is also depicted in the concluding section of chapter 2 (fig 2.21). As per figure 12, at $\tau = 2.2$ ms, $n = 0.4$, both the acoustic and intrinsic modes decay in the complex frequency plane. The pressure profile of the acoustic mode resembles the classical first acoustic mode of a closed-open combustor, whereas for the intrinsic mode, the pressure profile manifests a prominent dip at the flame location $x_q = L/2$. The jump

in the velocity profile is also quite prominent for the decaying intrinsic mode. As we increase n to 1.1, the intrinsic mode becomes unstable, whereas, the acoustic mode decays. Figure 13 represents this case. The figure shows that the acoustic mode retains a visually identical profile of that of a classical first acoustic mode for a closed-open combustor. However the dip in the intrinsic mode pressure profile becomes more prominent. The jump in the velocity profile for the intrinsic mode at the flame location, retains its distinction. Thus, we can distinguish the mode shapes of acoustic and intrinsic modes in this scenario, where pure intrinsic mode instability exists.

This distinctive nature of the mode shapes might not exist when two modes couple in the complex frequency plane. It is expected, during coupling, that the modes come close to each other in the complex frequency plane. In other words, their frequencies are very close to each other. It is a matter of interest to find out what the patterns of the mode shapes are when two modes with closely spaced frequencies come close to each other. It is also a matter of interest to find out whether we can find any distinctive features of the mode shapes for closely spaced modes. Figure 14 is dedicated for that purpose. Figure 14 (a) and 14 (c) represent the pressure and velocity amplitudes of three marginally unstable intrinsic modes. The first two modes have smaller frequencies than the first acoustic mode frequency of a closed-open combustor, whereas the third mode has the same frequency as that of the first acoustic mode frequency of closed-open combustor without a flame and temperature jump. Visually, all three modes have similar mode shapes. Figure 14 (b) and 14 (d) represent pressure and velocity amplitudes of four marginally unstable intrinsic modes. The first three modes have smaller frequencies than the second acoustic mode frequency of closed-open combustor, whereas the fourth mode has the same

frequency as that of the second acoustic mode frequency of closed-open combustor without a flame. The shapes of the first three modes are visually similar in nature and contain a mixed behavior of both the first and second acoustic modes of a closed-open combustor. This trend continues in an identical manner, for higher frequency modes. Hence, when modes come very close to the neutral line in the complex frequency plane and close to each other, it is hard to distinguish them purely by looking at their mode shapes.
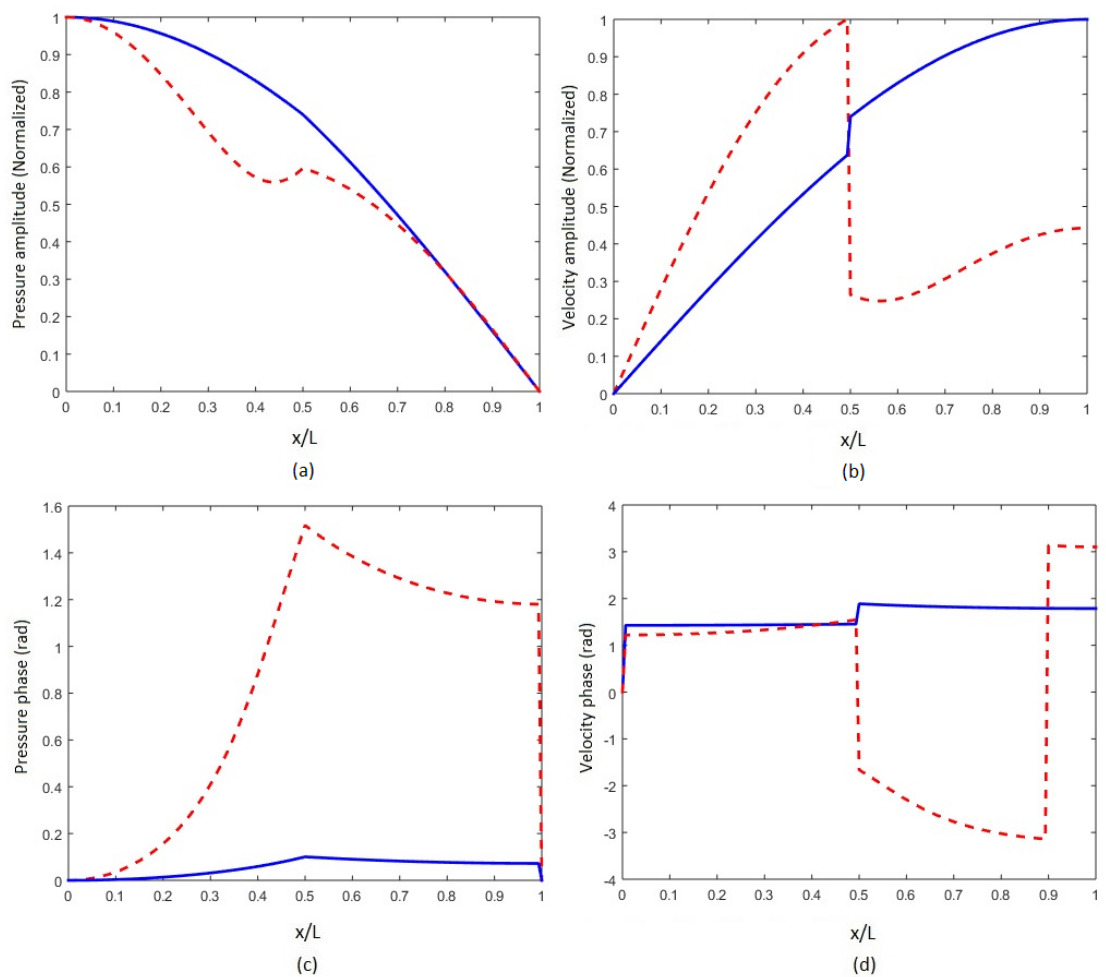
Figure 3.12: (a, b) Normalized pressure, velocity amplitude and (c, d) pressure, velocity phase, in radians, of intrinsic and acoustic modes, based on equations (1), (5), (2) and (7), for $x_q = L/2$, $\tau = 2.2$ ms, $n = 0.4$, $\omega^i = 1420 - i*520$ rad/s, $\omega^a = 690 - i*100$ rad/s. Both the acoustic and intrinsic modes decay for this value of n. Pressure amplitude and phase show a distinctive dip and hump for the intrinsic mode, compared to the acoustic mode. Other parameters and notations are the same as in figure 3.
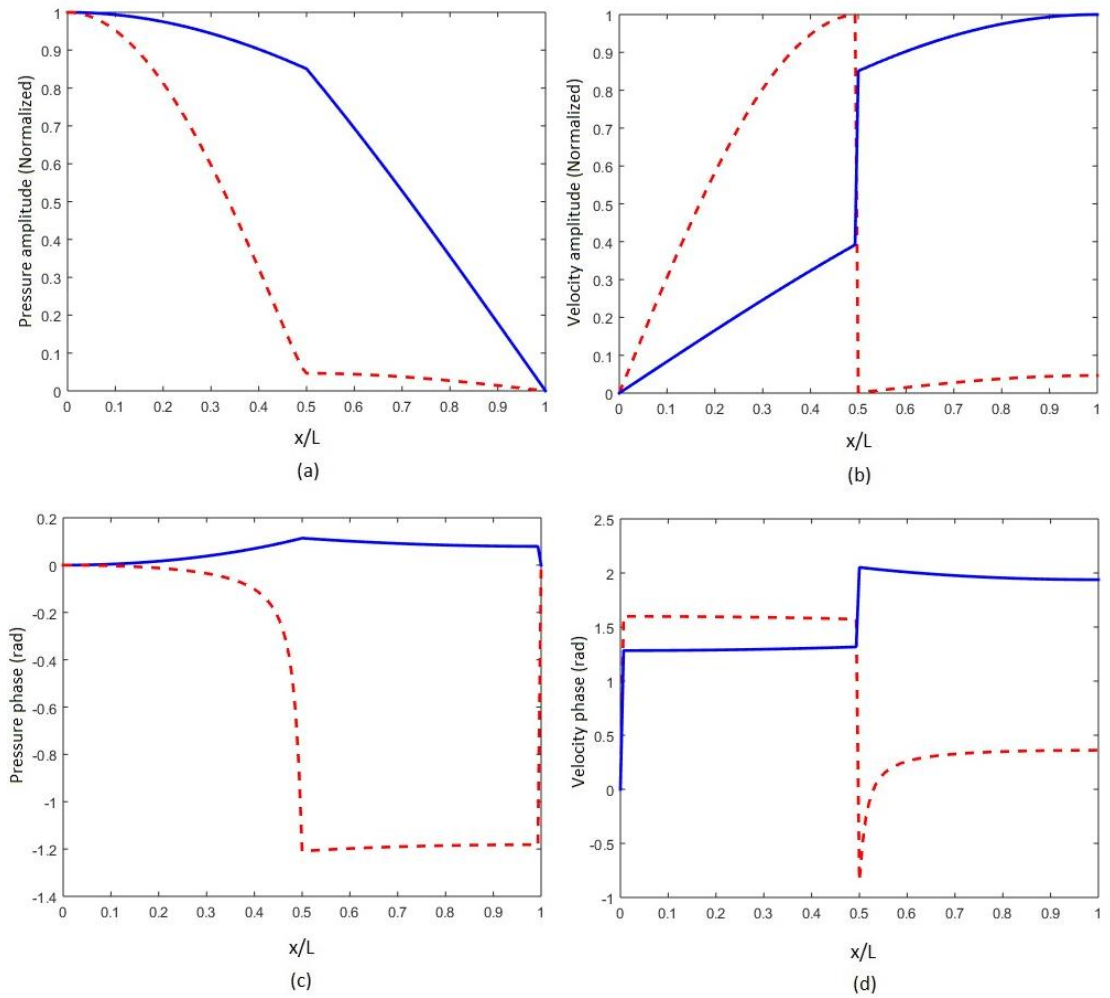
Figure 3.13: (a, b) Normalized pressure, velocity amplitude and (c, d) pressure, velocity phase, in radians, of intrinsic and acoustic modes, based on equations (1), (5), (2) and (7), $x_q = L/2$, τ =2.2 ms, n =1.1, ω^i =1430+i *40 rad/s, ω^a =540-i *160 rad/s. Compared to figure 12, an increase of n makes the intrinsic mode unstable, whereas the acoustic mode decays. This is a scenario of pure intrinsic mode instability. The pressure and velocity profiles are distinctively different for this case. Other parameters and notations are the same as in figure 3.
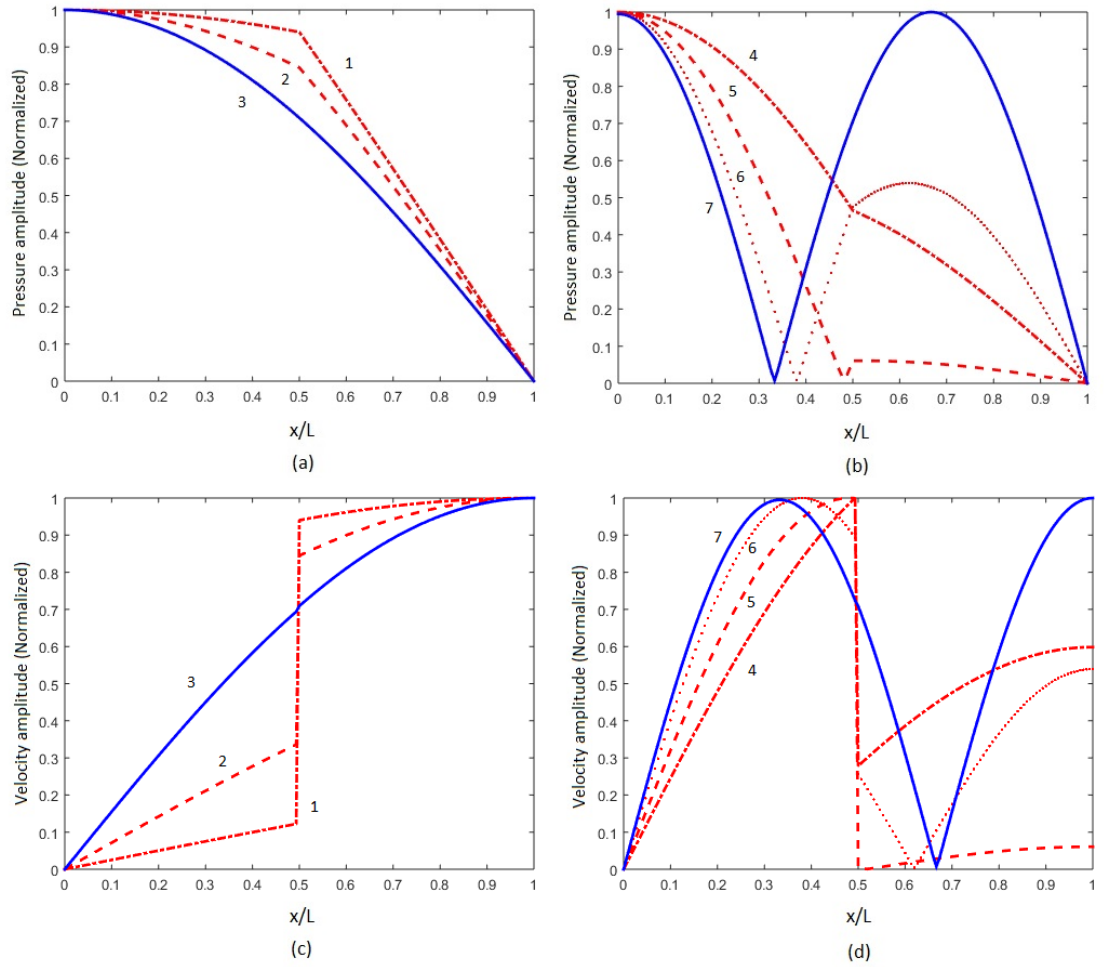
Figure 3.14: **(a)** Normalized pressure amplitude and **(c)** Normalized velocity amplitude of intrinsic modes, based on equations (1), (5), for three different frequencies (1) $\omega^i = 320 + i$ *10 rad/s, (2) $\omega^i = 520 + i$ *10 rad/s, (3) $\omega^i = 720 + i$ *10 rad/s, showed by the dashed-dotted red line, dashed red line and continuous blue line respectively. Frequency (3) is the first acoustic mode frequency of closed-open combustor and the frequencies for (1) and (2) are less than that of (3). The mode shapes for (1) and (2) are similar to that of (3).
(b) Normalized pressure phase and **(d)** Normalized velocity phase of intrinsic modes, based on equations (1), (5), for four different frequencies (4) $\omega^i = 1000 + i$ *10 rad/s, (5) $\omega^i = 1500 + i$ *10 rad/s, (6) $\omega^i = 1900 + i$ *10 rad/s, (7) $\omega^i = 2170 + i$ *10 rad/s, represented by the dashed-dotted red line, dashed red line, dotted red line and continuous blue line respectively. Frequency (7) is the second acoustic mode frequency of a closed-open combustor and frequencies for (4), (5) and (6) are less than that of (7). Mode shapes of (4), (5) and (6) have mixed behavior of both mode (3) and (7). This figure is for $x_q = L/2$.

Therefore, we have seen that the comparison of mode shapes could be a reliable

option when modes do not couple with each other and we have a pure acoustic and

pure intrinsic mode instability. However, when intrinsic and acoustic modes couple to each other and they come close to each other in the complex frequency plane, their mode shapes are often hardly distinguishable, as witnessed from figures 3-9 and explained in figure 14. An identical observation of this limitation of mode shapes to identify the acoustic and intrinsic modes has also been reported by Emmert et al. (2016).

3.5. Three types of instability in a combustor: flame-acoustic coupling; the complete picture

In the introductory section, it was mentioned that, as per the literature, in a classical combustor setup, there are two distinctly different forms of linear instability, due to the presence of a flame:

i. A *classical acoustic mode instability* occurs when one of the acoustic modes couples with flame heat release and becomes unstable. The route is well studied (e.g., Lieuwen T., and Yang V. (2005), and Poinsot T. and Veynante D (2011)) and will be very briefly discussed here for the sake of completeness.

ii. An *intrinsic flame mode instability* occurs when one of the flame intrinsic modes becomes unstable without affecting any of the acoustic modes. This form of instability has been discussed in greater detail in chapter 2 for a closed-open combustor.

Apart from these two forms of instability, here we describe a third form of instability, not reported so far in the literature to the best of our knowledge. This is a *coupled intrinsic-acoustic mode instability*, which occurs when a decaying acoustic mode (because of the negative Rayleigh index) couples with one of the intrinsic modes

(with a frequency close to the acoustic mode) and becomes unstable. This is the salient discussion point for this chapter.

The key question is when does an intrinsic mode becomes important. An intrinsic mode matters in two different types of situations: when the intrinsic modes grow, while the acoustic modes decay (an example of which is provided in the concluding section of chapter 2, Fig. 2.21) and when acoustic and intrinsic modes are strongly coupled in such a way that the intrinsic mode triggers instability of an acoustic mode, which otherwise, according to the Rayleigh instability criterion, should be decaying. In the following sections, we give a brief overview of these three types of combustor instabilities.

3.5.1. Instability of acoustic modes uncoupled from the intrinsic modes – the instability of the first type

First, we provide a brief overview of the classical acoustic mode instability. This kind of instability occurs when acoustic pressure is in phase with flame heat release and a detailed discussion of it is can be found in [Lieuwen T., and Yang V. (2005), and Poinsot T. and Veynante D (2011)]. However, for the sake of completeness, we briefly review this type of instability. We are interested in a simple expression for the growth rate of acoustic mode when it becomes unstable at $n_{th}^{a} = 0$ (where superscript a represents acoustic modes). For simplicity, we are going to start with the dispersion relation (2.23) for $x_q = L/2$, instead of the general equation (2.20), in §2.2.

For acoustic modes, when $n \to 0$, the growth rates are asymptotically small, i.e. for, $n \to 0$, $Im(\omega^a) \to 0$, where superscript a represents acoustic modes. For this limiting case, equation (2.23) simplifies to,

$$\cos\left(\frac{\omega L}{c}\right) = \frac{n}{2}e^{i\omega\tau}. \qquad (3.11)$$

The acoustic mode frequency ω^a can be written as, $\omega^a = Re(\omega^a) + iIm(\omega^a)$, where $Re(\omega^a)$ is the instability frequency and $Im(\omega^a)$ is the growth rate. For any value of n, the real part $Re(\omega^a)$ is assumed to have a small deviation ω_c^a to the value predicted in the limit of small n, that is ω_0^a (this is the classical acoustic mode frequency of a closed-open combustor). It is straightforward to calculate these instability frequencies of the acoustic mode, ω_0^a, because of the flame heat release effect. For the acoustic modes of a combustor without a flame, these frequencies are given as [Kinsler et al. (2000)]

$$\omega_0^a = (2m^a + 1)\frac{\pi c}{2L}. \qquad (3.12)$$

The real part $Re(\omega^a)$ can be written as, $Re(\omega^a) = \omega_0^a + \omega_c^a$, which enables us to present equation $\omega^a = Re(\omega^a) + iIm(\omega^a)$ as, $\omega^a = (\omega_0^a + \omega_c^a) + iIm(\omega^a)$. By substituting this expression for ω into equation (11), we get,

$$\cos\left\{\frac{\left((\omega_0^a + \omega_c^a) + iIm(\omega^a)\right)L}{c}\right\} = \frac{n}{2}e^{i\left((\omega_0^a + \omega_c^a) + iIm(\omega^a)\right)\tau},$$

Which can be further expanded into the following form,

$$\cos\left\{\frac{(\omega_0^a + \omega_c^a)L}{c}\right\}\cos\left\{\frac{iIm(\omega^a)L}{c}\right\} - \sin\left\{\frac{(\omega_0^a + \omega_c^a)L}{c}\right\}\sin\left\{\frac{iIm(\omega^a)L}{c}\right\}$$
$$= \frac{n}{2}e^{-Im(\omega^a)\tau}\left[\cos\left\{(\omega_0^a + \omega_c^a)\tau\right\} + i\sin\left\{(\omega_0^a + \omega_c^a)\tau\right\}\right] \qquad (3.13)$$

Assuming smallness of $Im(\omega^a)$, we can approximate the trigonometric terms in (13) as, $\cos\{iIm(\omega^a)L/c\} \approx 1$ and $\sin\{iIm(\omega^a)L/c\} \approx iIm(\omega^a)L/c$, and also $e^{-Im(\omega^a)\tau} \approx 1$. This will simplify equation (13) further. The real part of equation (13) then becomes,

$$\cos\left(\frac{(\omega_0^a + \omega_c^a)L}{c}\right) = \frac{n}{2}\cos\left((\omega_0^a + \omega_c^a)\tau\right). \tag{3.14}$$

And the imaginary part of equation (13) assumes the following form,

$$-Im(\omega^a)\frac{L}{c}\sin\left(\frac{(\omega_0^a + \omega_c^a)L}{c}\right) = \frac{n}{2}\sin\left((\omega_0^a + \omega_c^a)\tau\right). \tag{3.15}$$

The real part (14) can be further simplified to,

$$\cos\left(\omega_0^a\frac{L}{c}\right) - \omega_c^a\frac{L}{c}\sin\left(\omega_0^a\frac{L}{c}\right) = \frac{n}{2}\left[\cos(\omega_0^a\tau) - \omega_c^a\tau\sin(\omega_0^a\tau)\right], \tag{3.16}$$

which leads us to the following expression for ω_c^a,

$$\omega_c^a = \frac{\cos(\omega_0^a\tau)}{\tau\sin(\omega_0^a\tau) - (-1)^{m^a}\dfrac{2}{n}\dfrac{L}{c}}. \tag{3.17}$$

The equation for the imaginary part (15) can be further rearranged as,

$$Im(\omega^a) = -(-1)^{m^a}\frac{nc}{2L}\left[\sin(\omega_0^a\tau) + \omega_c^a\tau\cos(\omega_0^a\tau)\right]. \tag{3.18}$$

Substituting ω_c^a, given by (17), into (18), yields the final expression for the growth rate for $n \to 0$ and a central flame location (i.e. $x_q = L/2$),

$$Im(\omega^a) = -\frac{nc}{2L}\left[\frac{\tau - (-1)^{m^a}\dfrac{2L}{nc}\sin(\omega_0^a\tau)}{\tau\sin(\omega_0^a\tau) - (-1)^{m^a}\dfrac{2L}{nc}}\right]. \tag{3.19}$$

125

Hence, the growth rate for the unstable acoustic modes, subjected to the type (i) instability (classical acoustic mode instability), can be predicted by equation (19). This formula is valid for a special case of $x_q = L/2$ and no cross-section and temperature jump. However, a similar exercise can be performed for any generalized value of flame location, cross-section, and temperature jump. The formula can be given as,

$$Im(\omega^a) = N/D,\qquad(3.19\ a)$$

Where, N and D are given as,

$$N = -2n\left[\begin{array}{c} \left\{(\alpha+1)\beta_1\sin(\omega_0^a\beta_1)+(\alpha-1)\beta_2\sin(\omega_0^a\beta_2)\right\} \\ \sin(\omega_0^a\beta_3)\sin(\omega_0^a\beta_4)\sin(\omega_0^a\tau)+2n\tau\sin^2(\omega_0^a\beta_3)\sin^2(\omega_0^a\beta_4) \\ +\left\{(\alpha+1)\cos(\omega_0^a\beta_1)+(\alpha-1)\cos(\omega_0^a\beta_2)\right\} \\ \left\{\left(\beta_3\cos(\omega_0^a\beta_3)\sin(\omega_0^a\beta_4)+\beta_4\sin(\omega_0^a\beta_3)\cos(\omega_0^a\beta_4)\right)\sin(\omega_0^a\tau)\right. \\ \left. +\tau\sin(\omega_0^a\beta_3)\sin(\omega_0^a\beta_4)\cos(\omega_0^a\tau)\right. \end{array}\right]$$

$$D = \left[\begin{array}{c} -\left\{(\alpha+1)^2\beta_1^2\sin^2(\omega_0^a\beta_1)+(\alpha-1)^2\beta_2^2\sin^2(\omega_0^a\beta_2)\right\} \\ -2(\alpha^2-1)\beta_1\beta_2\sin(\omega_0^a\beta_1)\sin(\omega_0^a\beta_2) \\ -4n^2\left\{\beta_3^2\cos^2(\omega_0^a\beta_3)\sin^2(\omega_0^a\beta_4)+\beta_4^2\sin^2(\omega_0^a\beta_3)\cos^2(\omega_0^a\beta_4)\right\} \\ -8n^2\beta_3\beta_4\sin(\omega_0^a\beta_3)\cos(\omega_0^a\beta_3)\sin(\omega_0^a\beta_4)\cos(\omega_0^a\beta_4) \\ -2n\tau\left\{(\alpha+1)\beta_1\sin(\omega_0^a\beta_1)+(\alpha-1)\beta_2\sin(\omega_0^a\beta_2)\right\} \\ \sin(\omega_0^a\beta_3)\sin(\omega_0^a\beta_4)\sin(\omega_0^a\tau) \\ +4n\left\{\begin{array}{l}(\alpha+1)\beta_1\beta_3\sin(\omega_0^a\beta_1)\cos(\omega_0^a\beta_3)\sin(\omega_0^a\beta_4) \\ +(\alpha+1)\beta_1\beta_4\sin(\omega_0^a\beta_1)\sin(\omega_0^a\beta_3)\cos(\omega_0^a\beta_4) \\ +(\alpha-1)\beta_2\beta_3\sin(\omega_0^a\beta_2)\cos(\omega_0^a\beta_3)\sin(\omega_0^a\beta_4) \\ +(\alpha-1)\beta_2\beta_4\sin(\omega_0^a\beta_2)\sin(\omega_0^a\beta_3)\cos(\omega_0^a\beta_4)\end{array}\right\}\cos(\omega_0^a\tau) \end{array}\right]$$

Here, α, β_1 and β_2 are constants specified by equation (2.28), whereas β_3 and β_4

are as follows: $\beta_3 = \dfrac{x_q}{c_1}$ and $\beta_4 = \dfrac{\left(x_q - L\right)}{c_2}$.

In figure 15, the growth rate (19) is plotted against time lag for the first 3 acoustic

modes (that is, m^a =0, 1, 2). At first glance the pattern seems to be complicated: at τ

=6.6 ms all acoustic modes grow simultaneously, whereas, at τ =2.2 ms and τ =11

ms, all acoustic modes decay. A detailed discussion can be found in e.g. Poinsot T.

and Veynante D (2011), and Lieuwen T., and Yang V. (2005). A similar result like

figure 15 and the corresponding discussions can also be found from Bauerheim et al.

(2016), for azimuthal combustion instability modes in annular chambers. The intrinsic

modes are likely to be dominant when all acoustic modes decay. For example, figure

2.11 shows that both the second and third intrinsic modes (m^i =1 and m^i =2) become

unstable at τ = 11 ms, whereas the second intrinsic mode (m^i =1) becomes unstable

at τ = 2.2 ms, making intrinsic modes the key driver of combustion instability. This

has also been verified with the help of the contour plot of figure 2.21, which showed

that the first and second intrinsic mode become unstable in this parameter range,

whereas all the acoustic modes decay simultaneously, making the intrinsic mode a

sole driver of combustion instability.
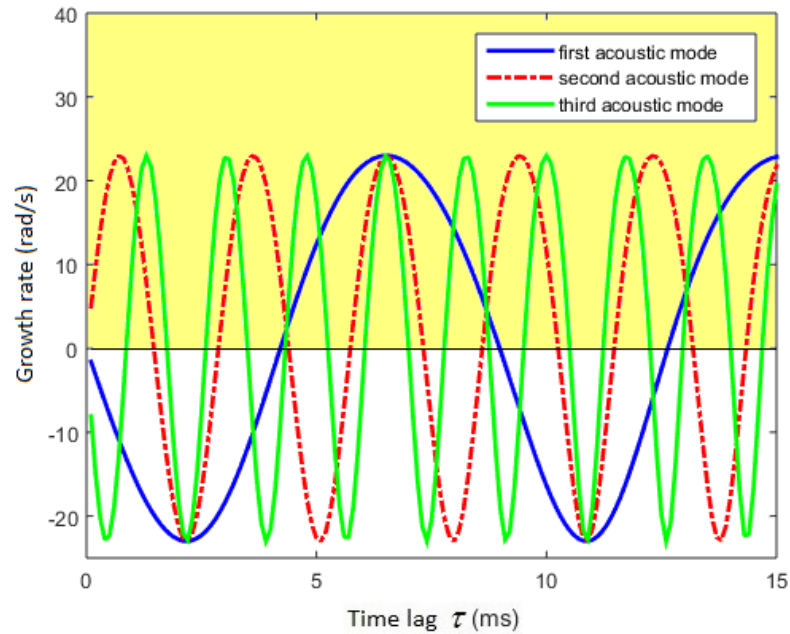
Figure 3.15: The growth rates for the first three acoustic modes, corresponding to m^a =0, 1, 2 (for $n = 0.1$, c =345 m/s, L =0.75 m in equation (19)). Equation (19) is applicable for the special case of $x_q = L/2$. The domain of instability is marked in yellow. In the close vicinity of 6.6 ms, all three acoustic modes grow simultaneously, whereas in the vicinity of 2.2 ms and 11 ms, all of these modes decay simultaneously.

3.5.2. Instability of the intrinsic modes – the instability of the second type

The dependence on the n-threshold and growth rate for instabilities of flame intrinsic modes for a closed-open combustor, has been discussed in detail in chapter 2. It has also been pointed out in the previous section that when acoustic modes decay, the intrinsic modes are the sole drivers of the combustor instability.

3.5.3. Instability of the acoustic modes coupled with intrinsic modes – the instability of the third type

This particular type is due to linear coupling between the acoustic and intrinsic modes. Due to the out of phase relation between acoustic pressure and flame heat release rate, acoustic modes decay in certain domains on the $n - \tau$ plane. In such a domain, the first type of instability cannot occur. The decaying acoustic modes can be

affected by one of the decaying flame intrinsic modes and as a result become unstable. It is important to understand the details of the coupling phenomenon. So, here, similar to § 4 of chapter 2, we evaluate the instability frequency, the threshold value of n and the growth rate for the coupled acoustic-intrinsic modes. Again, as in the previous section, our analytical approach is confined to the linear setting only.

3.5.3.1. Instability frequency

The deviation of the real part of instability frequency from its value at $n=0$, for the case when the acoustic mode is coupled with one of the intrinsic modes, can be found as follows.

Substitution of $\omega = \left(\omega_0^a + \omega_c^a\right) + iIm\left(\omega^a\right)$ into equation (2.20) leads to,

$$
\begin{aligned}
&\left(\alpha+1\right)\cos\left\{\left(\omega_0^a + \omega_c^a + iIm\left(\omega^a\right)\right)\beta_1\right\} + \left(\alpha-1\right)\cos\left\{\left(\omega_0^a + \omega_c^a + iIm\left(\omega^a\right)\right)\beta_2\right\} \\
&\quad + 2ne^{i\left(\omega_0^a + \omega_c^a + iIm\left(\omega^a\right)\right)\tau}\sin\left\{\left(\omega_0^a + \omega_c^a + iIm\left(\omega^a\right)\right)\frac{x_q}{c_1}\right\} \\
&\quad\quad \sin\left\{\left(\omega_0^a + \omega_c^a + iIm\left(\omega^a\right)\right)\frac{\left(x_q - L\right)}{c_2}\right\} = 0
\end{aligned}
$$

(3.20)

Here, α, β_1 and β_2 are constants specified by equation (2.28). By definition, the growth rate for acoustic modes $Im\left(\omega^a\right)$ is zero on the neutral curve on the $n-\tau$ plane, i.e. $Im\left(\omega^a\right)=0$ at $n=n_{th}^a$. Then on the neutral curve, the imaginary part of equation (20) takes the form,

$$
2in_{th}^a\sin\left(\left(\omega_0^a + \omega_c^a\right)\tau\right)\sin\left(k_1 x_q\right)\sin\left(k_2\left(x_q - L\right)\right) = 0.
$$

(3.21)

The obvious solution of this equation for the acoustic mode is $n_{th}^a = 0$. Acoustic modes might become unstable at $n_{th}^a = 0$, the instability of type (i). However, equation (21) also suggests a second set of solutions for the acoustic modes, due to vanishing of the second multiplier,

$$\sin\left(\left(\omega_0^a + \omega_c^a\right)\tau\right) = 0.$$ (3.22)

Equation (22) can be rearranged as,

$$\omega_c^a \tau = m\pi - \omega_0^a \tau \quad (m \text{ is an integer})$$

$$\text{or, } \omega_c^a \tau/\pi = m - \omega_0^a \tau/\pi.$$ (3.23a, b)

Equation (23) provides us with an explicit solution for the correction to the real part of frequency, for the case when acoustic mode is coupled with one of the intrinsic modes, as follows,

$$\omega_c^a = \frac{m\pi}{\tau} - \left(2m^a + 1\right)\frac{\pi c}{2L} \quad (m \text{ is an integer}).$$ (3.24)

Once ω_c^a is known from (24), the frequency of marginal instability follows from the expression, $Re\left(\omega^a\right) = \omega_0^a + \omega_c^a$.

3.5.3.2. The threshold value of n for coupled intrinsic-acoustic mode instability

Using equation (24), the real part of equation (20) can be rewritten for the neutral curve as follows,

$$(\alpha + 1)\cos\left\{\left(\omega_0^a + \omega_c^a\right)\beta_1\right\} + (\alpha - 1)\cos\left\{\left(\omega_0^a + \omega_c^a\right)\beta_2\right\} - \\ 2n_{th}^a \cos\left(\omega_c^a \tau\right)\sin\left(k_1 x_q\right)\sin\left\{k_2\left(x_q - L\right)\right\} = 0$$ (3.25)

The explicit solution for the acoustic mode instability threshold (n_{th}^a) can be derived from equation (25) on the neutral curve,

$$n_{th}^a = \frac{(\alpha+1)\cos\left\{\left(\omega_0^a + \omega_c^a\right)\beta_1\right\} + (\alpha-1)\cos\left\{\left(\omega_0^a + \omega_c^a\right)\beta_2\right\}}{2\cos\left(\omega_c^a \tau\right)\sin\left(k_1 x_q\right)\sin\left\{k_2\left(x_q - L\right)\right\}}.$$

(3.26)

where, α, β_1 and β_2 are given by equation (2.28). Equation (26) is similar to equation (2.33) for the case of intrinsic modes. The only differentiating term is ω_c^a instead of ω_c^i in equation (2.33). Thus, when a mode becomes unstable on the $n-\tau$ plane, it might not be possible to say confidently, without extra analysis, whether the mode is acoustic or intrinsic.

3.5.3.3. The growth rate prediction for the acoustic modes

Similar to § 4 of chapter 2, the growth rate for the acoustic modes can be found by making use of an expansion with respect to the deviation from the neutral curve on the $n-\tau$ plane. Because equations (2.33) and (26) are identical, the growth rate for the coupled acoustic mode will be governed by an equation identical to (2.47), with the intrinsic mode characteristics being replaced by acoustic mode characteristics.

The analytical expression of acoustic and intrinsic modes originates from the same dispersion relation (2.20). Thus, there can be cases when either acoustic or intrinsic modes can become unstable at the same threshold value of n, making it difficult to be sure in their identity at the point of instability. Unless we track down their trajectory manually in the $n-\tau$ parameter space, it is hard to comprehend which mode is becoming unstable.

3.6. Mathematical model of coupling: Evaluation of coupled mode frequencies

In this section we try to understand intrinsic-acoustic mode coupling and describe it by employing a simple mathematical model. We will try to solve the dispersion relation in the vicinity of the acoustic mode, when an intrinsic mode comes close to the chosen acoustic mode in the $n - \tau$ space. Thus, we identify the locus of the acoustic and the intrinsic mode that interacts with it in the $n - \tau$ space. We also discuss the stability behavior of these modes and understand under which scenarios either the acoustic mode alone or both acoustic and intrinsic modes become unstable.

3.6.1. Derivation of governing dispersion relation for coupling

It is reasonable to assume that with a small change of parameters, the acoustic modes do not deviate far from the neutral curve (in terms of decay rate). Hence, assuming the deviation of the frequency to be characterized by a small parameter $\Delta \omega$ and using our original dispersion relation (2.20), we can find the locus of the acoustic mode, as well as the nearby intrinsic modes. It can be further elucidated as to whether we have pure acoustic mode instability, pure intrinsic mode instability or coupled acoustic mode-intrinsic mode instability. When ω_0^a represents the frequency of the acoustic mode of the closed-open combustor in the absence of a flame, the perturbed frequency in the vicinity of the neutral curve can be written as $\omega^a = \omega_0^a + \Delta \omega$. In the present context, we assume the perturbation $\Delta \omega$ to be small compared to ω_0^a.

By substituting the ansatz $\omega^a = \omega_0^a + \Delta \omega$ into the general dispersion relation (2.20), we re-write it as follows,

$$(\alpha+1)\cos\left(\beta_1\left(\omega_0^a+\Delta\omega\right)\right)+(\alpha-1)\cos\left(\beta_2\left(\omega_0^a+\Delta\omega\right)\right)+$$

$$2n_0e^{i\omega^a\tau}\sin\left(\left(\omega_0^a+\Delta\omega\right)\frac{x_q}{c_1}\right)\sin\left(\left(\omega_0^a+\Delta\omega\right)\frac{\left(x_q-L\right)}{c_2}\right)=0 \qquad (3.27)$$

Assuming small values of $\Delta\omega$ and neglecting all the terms higher than order 2, the trigonometric terms in the expression (27) can be expanded as,

$$\cos\left(\beta_1\left(\Delta\omega\right)\right)=1-\beta_1^2\left(\Delta\omega\right)^2\Big/2,$$

$$\sin\left(\beta_1\left(\Delta\omega\right)\right)=\beta_1\left(\Delta\omega\right),$$

$$\cos\left(\left(\Delta\omega\right)\tau\right)=1-\left(\Delta\omega\right)^2\tau^2\Big/2,$$

$$\sin\left(\left(\Delta\omega\right)\tau\right)=\left(\Delta\omega\right)\tau. \qquad (3.28a,b,c,d)$$

Making use of these truncated expansions (28) in the dispersion relation (27) enables us to re-structure it as follows,

$$(\alpha+1)\left[\cos\left(\beta_1\omega_0^a\right)\left(1-\frac{\beta_1^2\left(\Delta\omega\right)^2}{2}\right)-\beta_1\Delta\omega\sin\left(\beta_1\omega_0^a\right)\right]+$$

$$(\alpha-1)\left[\cos\left(\beta_2\omega_0^a\right)\left(1-\frac{\beta_2^2\left(\Delta\omega\right)^2}{2}\right)-\beta_2\Delta\omega\sin\left(\beta_2\omega_0^a\right)\right]+$$

$$2n_0e^{i\omega_0^a\tau}\left\{\left(1-\frac{\left(\Delta\omega\right)^2\tau^2}{2}\right)+i\Delta\omega\tau\right\}$$

$$\left\{\left(1-\frac{\left(\Delta\omega\right)^2x_q^2}{2c_1^2}\right)\sin\left(\frac{\omega_0^a x_q}{c_1}\right)+\frac{\left(\Delta\omega\right)x_q}{c_1}\cos\left(\frac{\omega_0^a x_q}{c_1}\right)\right\}$$

$$\left\{\left(1-\frac{\left(\Delta\omega\right)^2\left(x_q-L\right)^2}{2c_2^2}\right)\sin\left(\frac{\omega_0^a\left(x_q-L\right)}{c_2}\right)+\frac{\left(\Delta\omega\right)\left(x_q-L\right)}{c_2}\cos\left(\frac{\omega_0^a\left(x_q-L\right)}{c_2}\right)\right\}=0$$

$$. \qquad (3.29)$$

Neglecting all the terms of $\Delta\omega$ higher than order 2, this equation can be written as a quadratic equation,

$$A\left(\Delta\omega\right)^2+B\left(\Delta\omega\right)+C=0. \qquad (3.30)$$

Then its solution can be written in the standard form as follows,

$$\Delta\omega_{1,2} = \frac{-B \pm \sqrt{(B^2 - 4AC)}}{2A}.$$
(3.31)

Where, the coefficients, A, B and C in (30) and (31) are,

$$A = -(\alpha+1)\frac{\beta_1^2}{2}\cos(\beta_1\omega_0^a) - (\alpha-1)\frac{\beta_2^2}{2}\cos(\beta_2\omega_0^a) +$$

$$2n_0 e^{i\omega_0^a\tau}\begin{bmatrix} \left\{\frac{(x_q-L)^2}{2c_2^2} - \frac{x_q^2}{2c_1^2} - \frac{\tau^2}{2}\right\}\sin\left(\frac{\omega_0^a x_q}{c_1}\right)\sin\left(\frac{\omega_0^a(x_q-L)}{c_2}\right) + \\ \frac{x_q(x_q-L)}{c_1 c_2}\cos\left(\frac{\omega_0^a x_q}{c_1}\right)\cos\left(\frac{\omega_0^a(x_q-L)}{c_2}\right) \\ +\frac{i\tau x_q}{c_1}\cos\left(\frac{\omega_0^a x_q}{c_1}\right)\sin\left(\frac{\omega_0^a(x_q-L)}{c_2}\right) \\ +\frac{i\tau(x_q-L)}{c_2}\sin\left(\frac{\omega_0^a x_q}{c_1}\right)\cos\left(\frac{\omega_0^a(x_q-L)}{c_2}\right) \end{bmatrix} = 0 \quad,$$

$$B = -(\alpha+1)\beta_1\sin(\beta_1\omega_0^a) - (\alpha-1)\beta_2\sin(\beta_2\omega_0^a) +$$

$$2n_0 e^{i\omega_0^a\tau}\begin{bmatrix} \frac{(x_q-L)}{c_2}\sin\left(\frac{\omega_0^a x_q}{c_1}\right)\cos\left(\frac{\omega_0^a(x_q-L)}{c_2}\right) + \\ \frac{x_q}{c_1}\cos\left(\frac{\omega_0^a x_q}{c_1}\right)\sin\left(\frac{\omega_0^a(x_q-L)}{c_2}\right) \\ +i\tau\sin\left(\frac{\omega_0^a x_q}{c_1}\right)\sin\left(\frac{\omega_0^a(x_q-L)}{c_2}\right) \end{bmatrix} = 0 \quad,$$

$$C = (\alpha+1)\cos(\beta_1\omega_0^a) + (\alpha-1)\cos(\beta_2\omega_0^a) +$$

$$2n_0 e^{i\omega_0^a\tau}\sin\left(\frac{\omega_0^a x_q}{c_1}\right)\sin\left(\frac{\omega_0^a(x_q-L)}{c_2}\right) \quad.$$
(3.32 a,b,c)

For the special case with the flame in the middle of the combustor, that is $x_q = L/2$, and cross-section and temperature jumps neglected, the coefficients A, B and C, as per (32), reduce to,

$$A = \left(-(-1)^{m^a} i\tau \frac{L}{c_0} + \frac{\tau^2}{2} \right) n e^{i\omega_0^a \tau}$$

$$B = -(-1)^{m^a} \left(2 + n e^{i\omega_0^a \tau} \right) \frac{L}{c_0} - i n e^{i\omega_0^a \tau} \tau . \qquad \text{(3.33 a,b,c)}$$

$$C = -n e^{i\omega_0^a \tau}$$

By using (30), the correction to the frequency is obtained. The two frequencies (of acoustic mode and nearby intrinsic mode) can be obtained using the relation: $\omega^a = \omega_0^a + \Delta\omega$. This approach thus helps us to find whether, in the $n - \tau$ space, any of the intrinsic modes are in the vicinity of the acoustic mode and whether they interact with it.

Further examples show that strong mode-coupling occurs for finite n close to the threshold value. For small n, the acoustic mode decays (if the Rayleigh index is negative) and does not feel the intrinsic mode. For subcritical and threshold values of n, it interacts with the intrinsic mode that comes closer in the $n - \tau$ space and becomes unstable at the same frequency as that of the intrinsic mode, whereas the intrinsic mode either becomes unstable or remains stable for large n. Once unstable or close to being unstable, the acoustic mode seems to lose its identity and behaves exactly like the intrinsic mode it interacts with. This aspect will be discussed in greater details in the next section. As mentioned in §5.3, as the coupled acoustic mode behaves exactly like an intrinsic mode when it is close to becoming unstable, from now on we will refer to such coupled modes as *coupled intrinsic modes*. However, to mark the "initial" identity of these modes, i.e. identity for small n, we

use additional identifiers: *coupled intrinsic mode ('born acoustic'* or in short ***BA*)** and *coupled intrinsic mode ('born intrinsic'* or in short ***BI*)**. This nomenclature convention will be followed in the rest of the work. It is also possible to analytically find the value of n (see Appendix V) for which the coupled modes have equal real frequencies (but different decay rate) on the complex frequency plane. Therefore, the point where their paths on the complex frequency plane start to cross each other can also be found. However, this crossing does not take place for all types of coupling. The picture will be made clearer in the next section, where we describe different types of acoustic mode-intrinsic mode coupling.

3.6.2. Four types of intrinsic-acoustic mode coupling: Loci of acoustic and intrinsic modes in $n - \tau$ space

The analytical solution derived in the previous section provides an explicit solution for the acoustic mode and the nearby intrinsic mode. These solutions can be plotted on the $n - \tau$ plane and we can perform a visual inspection as to whether the acoustic mode and intrinsic mode come close to one another and engage in the coupling.

These kinds of plots can be generated for any chosen acoustic mode with any given value of τ. For a specific τ, n will be increased in small steps from zero to some finite value and the corresponding acoustic and nearby intrinsic mode frequencies can be calculated using (30). Finally, these values can be plotted on a complex frequency plane thus, obtaining the loci of the acoustic and intrinsic modes on the complex frequency plane with n treated as a parameter.
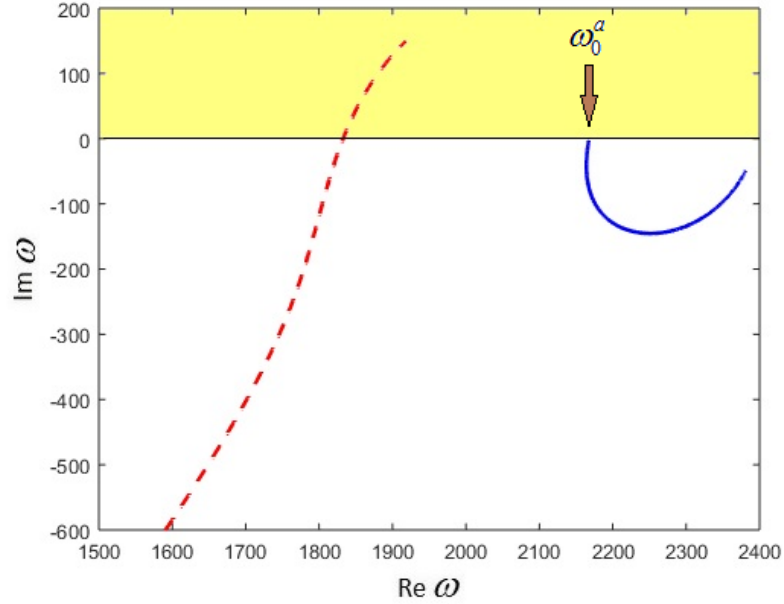
Figure 3.16: Loci of the coupled modes for $x_q = L/2$, $\tau = 5$ ms, $m^a = 1$, $m^i = 1$. n is varied from 0.0 to 1.0. Plots are generated with the help of quadratic equation (30). Coupled intrinsic modes (BA) and (BI) are represented by continuous blue and dashed red lines respectively. Yellow colour represents the domain of instability. The brown arrow indicates the frequency of acoustic mode (ω_0^a) of the closed-open combustor in the absence of a flame. This is the **first type of coupling**, where the coupled intrinsic mode (BI) becomes unstable at $\omega_c^i \tau = 0$, whereas the coupled intrinsic mode (BA) tends to become unstable at a higher frequency corresponding to $\omega_c^i \tau = \pi$. The mode numbers of the modes involved in coupling are same in this case. The effects of cross-section and temperature jump across the flame are not considered here.

Figure 16 shows an example of such a plot for the second acoustic mode ($m^a = 1$), when $\tau = 5$ ms and flame is at $x_q = L/2$. The domain of instability is marked in yellow. The arrow indicates the frequency of the acoustic mode (ω_0^a) of the closed-open combustor in the absence of a flame. The effects of cross-section and temperature jump across the flame are not considered for all subsequent plots. The figure illustrates coupling between the second acoustic and the second intrinsic mode ($m^i = 1$). Thus, in this particular case, the mode numbers for the acoustic and intrinsic modes involved in coupling are the same. Coupled intrinsic modes (BA) and (BI) are

represented by continuous blue and dashed red lines respectively. Figure 16 makes it obvious that as n increases from 0 to 1.0, the coupled intrinsic mode (BA) initially decays in the complex frequency plane and tends to become unstable at a frequency predicted by $\omega_c^i \tau = \pi$, whereas the coupled intrinsic mode (BI) becomes unstable at the same frequency predicted for it in the asymptotic limit of small n (i.e. at a frequency corresponding to $\omega_c^i \tau = 0$). Numerical validation of this and all subsequent plots will be given in the next section. Indeed, the coupled intrinsic mode (BI) becomes unstable at a much lower threshold of n than coupled intrinsic mode (BA), as seen by the neutral curve 2.12 in chapter 2. We name this form of coupling as the **first type of coupling,** where coupled intrinsic mode (BI) attains instability at a frequency corresponding to $\omega_c^i \tau = 0$ and the coupled intrinsic mode (BA) becomes unstable at a frequency corresponding to $\omega_c^i \tau = \pi$ (or $\omega_c^i \tau = -\pi$).

Another type of coupling is illustrated in figure 17, which is generated for the second acoustic mode ($m^a = 1$), when $\tau = 4.8$ ms and flame is at $x_q = L/2$. This figure also shows coupling between the second acoustic mode and the second intrinsic mode, similar to figure 16. As we increase n from 0 to 1.0, the coupled intrinsic mode (BA) becomes unstable at $\omega_c^i \tau = 0$, whereas the coupled intrinsic mode (BI) tends to become unstable at a higher frequency corresponding to $\omega_c^i \tau = \pi$. We name this scenario as the **second type of coupling**. The n-threshold for instability is higher for the coupled intrinsic mode (BI) than for the coupled intrinsic mode (BA). In §2.4, we mentioned that near the intersection of the segments of the neutral curve intrinsic and coupled-acoustic modes invariably change their identity. Figures 16 and 17 support this statement. It is obvious that a slight alteration of τ from 5 to 4.8 ms changed the type of intrinsic-acoustic mode coupling from the first to second.
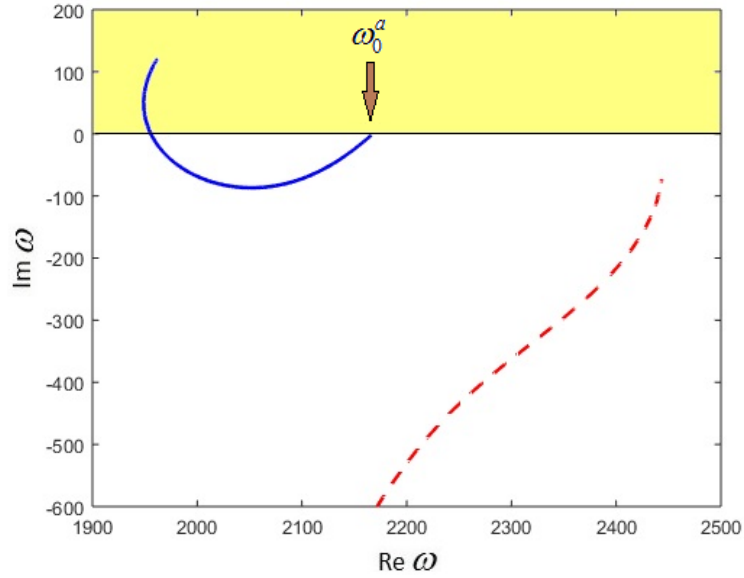
Figure 3.17: Loci of the coupled modes for $x_q = L/2$, τ =4.8 ms, m^a =1, m^i =1. n is varied from 0.0 to 1.0. Plots are based on quadratic equation (30). This is the **second type of coupling**, where the coupled intrinsic mode (BA) becomes unstable with $\omega_c^i \tau = 0$, whereas the coupled intrinsic mode (BI) tends to become unstable at a higher frequency corresponding to $\omega_c^i \tau = \pi$. The mode numbers of the modes involved in coupling are same in this case. Other parameters and notations are the same as in figure 16.
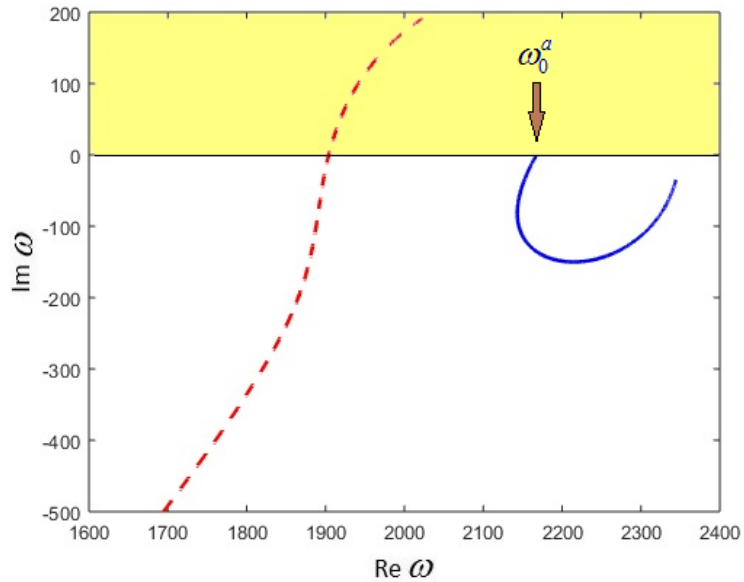
Figure 3.18: Loci of the coupled modes for x_q =0.3 m, τ =4.85 ms, m^a =1, m^i =1. n is varied from 0.0 to 2.5. Plots are generated with the help of quadratic equation (30). This is the **third type of coupling**, where the coupled intrinsic mode (BI) becomes unstable with $\omega_c^i \tau = 0$, whereas the coupled intrinsic mode (BA) tends to remain asymptotically stable at a frequency corresponding to $\sin(k_1 x_q) = 0$, as per equation (2.29). The mode numbers of the modes involved in coupling are the same in this case. Other parameters and notations are the same as in figure 16.

139

There are two more types of coupling possible, in addition to the first two types shown in figures 16 and 17. Figures 18 and 19 illustrate these two new types of coupling. Both figures are generated for the second acoustic mode (m^a =1) when the flame is at x_q =0.3 m. Figure 18 is for τ =4.85 ms, whereas figure 19 is for τ =4.75 ms. It can be seen from figure 18, that as n is varied from 0 to 2.5, the coupled intrinsic mode (BI) becomes unstable at $\omega_c^i \tau = 0$, whereas the coupled intrinsic mode (BA) tends to remain asymptotically stable at a frequency corresponding to $\sin(k_1 x_q) = 0$, as per equation (2.29). We interpret this as the **third type of coupling,** where despite mode coupling, we find only one unstable mode, whereas the other mode remains asymptotically stable at a frequency corresponding to $\sin(k_1 x_q) = 0$ or $\sin(k_2(x_q - L)) = 0$, as per equation (2.29). A closer observation of equation (2.29) shows that even though we considered the primary solution $\sin(\omega_c^i \tau) = 0$ to define our neutral curve, we have two more solutions corresponding to $\sin(k_1 x_q) = 0$ or $\sin(k_2(x_q - L)) = 0$. Both these solutions correspond to $n_{th} \to \infty$ as per (2.33), thus they do not manifest themselves on the neutral curve. When this form of coupling occurs on the neutral curve, we might be tempted to misinterpret them as pure intrinsic mode instability and assume that there is no coupling. But this is not the case. A simple test to distinguish between uncoupled domain (manifesting pure intrinsic instability) and third or fourth types of coupled domain will be suggested here. If the range of n_{th} values for instability in the domain is found to be very close to zero, we interpret it as a coupled domain. Because of the strongly decaying nature of intrinsic modes, they cannot be unstable at such small n_{th},

for any practical range of τ. If n_{th}, within the domain, is on the higher side i.e. (O(1)), then we interpret it as an uncoupled domain with pure intrinsic instability. Another form of coupling can be seen in figure 19, where an increase of n from 0 to 2.5 makes the coupled intrinsic mode (BA) unstable at $\omega_c^i \tau = 0$, whereas the coupled intrinsic mode (BI) tends to remain asymptotically stable at a frequency corresponding to $\sin(k_1 x_q) = 0$ as per equation (2.29). We interpret it as the **fourth type of coupling**. Another important aspect of figures 18 and 19 is that as we reduce τ from 4.85 ms to 4.75 ms, the type of coupling changes from the third to fourth.
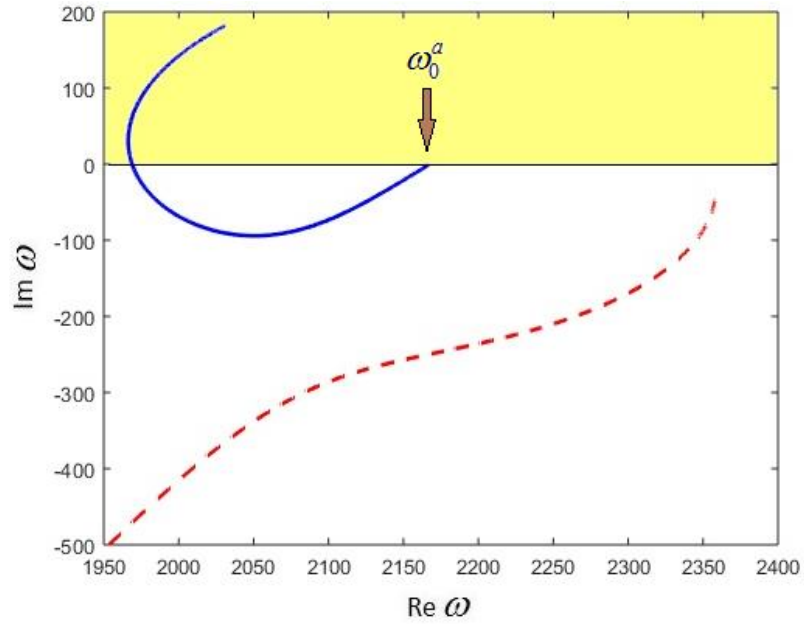
Figure 3.19: Loci of the coupled modes for x_q =0.3 m, τ =4.75 ms, m^a =1, m^i =1. n is varied from 0.0 to 2.5. Plots are generated with the help of quadratic equation (30). This is the **fourth type of coupling**, where the coupled intrinsic mode (BA) becomes unstable with $\omega_c^i \tau = 0$, whereas the coupled intrinsic mode (BI) tends to remain asymptotically stable at a frequency corresponding to $\sin(k_1 x_q) = 0$, as per equation (2.29). The mode numbers of the modes involved in coupling are the same in this case. Other parameters and notations are the same as in figure 16.

We have thus observed four main types of intrinsic-acoustic mode coupling:

i. In the **first type of coupling**, the coupled intrinsic mode (BI) becomes unstable at a frequency predicted by $\omega_c^i \tau = 0$, whereas the coupled intrinsic mode (BA) becomes unstable at a frequency predicted by either $\omega_c^i \tau = \pi$ or $\omega_c^i \tau = -\pi$. Figure 16 illustrates this type of coupling.

ii. In the **second type of coupling**, the coupled intrinsic mode (BA) becomes unstable at a frequency predicted by $\omega_c^i \tau = 0$, whereas the coupled intrinsic mode (BI) becomes unstable at a frequency predicted by either $\omega_c^i \tau = \pi$ or $\omega_c^i \tau = -\pi$. Figure 17 illustrates this type of coupling.

iii. In the **third type of coupling**, the coupled intrinsic mode (BI) becomes unstable with $\omega_c^i \tau = 0$, whereas the coupled intrinsic mode (BA) tends to remain asymptotically stable at a frequency corresponding to $\sin\left(k_1 x_q\right) = 0$ or $\sin\left(k_1 \left(x_q - L\right)\right) = 0$, as per equation (2.29). Figure 18 illustrates this type of coupling.

iv. In the **fourth type of coupling**, the coupled intrinsic mode (BA) becomes unstable with $\omega_c^i \tau = 0$, whereas the coupled intrinsic mode (BI) tends to remain asymptotically stable at a frequency corresponding to $\sin\left(k_1 x_q\right) = 0$ or $\sin\left(k_1 \left(x_q - L\right)\right) = 0$, as per equation (2.29). Figure 19 illustrates this type of coupling.

It is worth mentioning that all these types of coupling are independent of the individual mode numbers for the acoustic and intrinsic modes. The mode numbers for the acoustic and intrinsic modes can be the same or different for all these coupling types.

142

Thus, we have developed a compact and 'easy to deal with' quadratic equation model to generate the solutions for the acoustic and intrinsic modes involved in coupling. We can, also investigate, with the help of that equation, whether intrinsic and acoustic modes arrive at the close vicinity of each other in the complex frequency plane. The four types of coupling have been identified in this regard, based on the instability frequencies of the coupled modes. These four types of coupling are independent of the individual mode numbers of the acoustic and intrinsic modes. In the §s 10 and 11, it will be shown that by the slight tweaking of combustor parameters, it is possible to find the first and/or second type, as well as the third and/or fourth type of instability in the same neutral curve of an intrinsic mode. Once a mathematical model is developed, the numerical examination of its validity becomes the next logical step, with the topic being covered in § 6.1.

3.7. Numerical validation of the analytical solution predicted by the quadratic equation model

In this section, the analytical solution obtained, as per equation (30) in § 6, will be verified with the numerical result as per equation (2.20). Figures 20-26 represent the comparison of analytical and numerical results. The dashed red and continuous blue lines represent the analytical solutions for coupled intrinsic mode (BI) and (BA) respectively. The magenta circular and green diamond dots represent their numerical counterparts respectively, found by direct solution of equation (2.20). The instability domains are marked in yellow. The brown arrow represents the frequency of acoustic mode (ω_0^a) of the closed-open combustor in the absence of a flame. The effect of cross-section and temperature jumps will not be considered here, as also mentioned in § 6.

Figures 20-23 present a numerical validation of cases considered in figures 16-19 respectively. Figure 20, illustrating the first type of coupling, shows a good correspondence between analytical and numerical results for the coupled intrinsic mode (BA), whereas for the coupled intrinsic mode (BI), predictions do not seem to be that accurate. However, the analytical solution manages to accurately capture the instability frequency of the coupled intrinsic mode (BI) on the complex frequency plane. For numerical solutions, n is varied from (a) 0.0 to 1.0 and (b) 0.0 to 4.0. For analytical solutions, n is varied from 0.0 to 1.0 for both (a) and (b). For n exceeding 1.0 our analytical solution deviates drastically from the numerical solution, because the key assumption of the smallness of $\Delta\omega$ ceases to be valid. Since one of the coupled modes exhibits strong growth rate, while the other is decaying, the value of $\Delta\omega$ is no longer small. This trend is captured in figure 20 (b). Thus, the quadratic analytical model (30) predicts a slightly lower instability frequency for the coupled intrinsic mode (BA), as is evident from 20 (b). This is a general limitation of the quadratic analytical model (30): for too large n, the deteriorates. A similar observation can be made by considering figure 21, which illustrates the second type of coupling. The quadratic analytical model (30) seems to accurately track the trajectory of the numerical solution and instability frequency for the coupled intrinsic mode (BA). However, for the coupled intrinsic mode (BI) the same thing cannot be said. Figure 21 (b) shows that coupled intrinsic mode (BI) becomes unstable at too high n, indicating the possible advent of nonlinearity into the system, due to the strongly growing coupled intrinsic mode (BA). Eventually, this reduces the prediction accuracy of the analytical model (30) for the coupled intrinsic mode (BI).
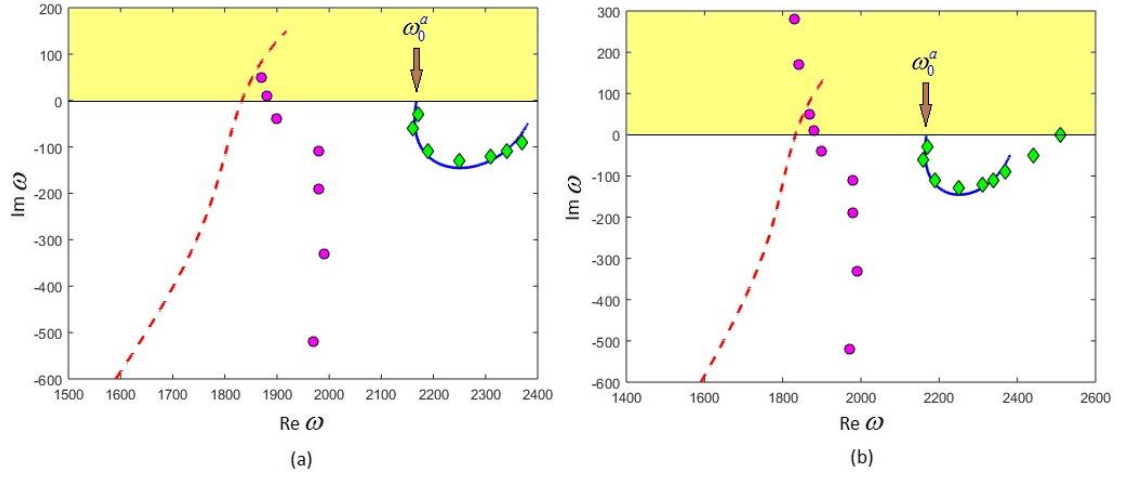
Figure 3.20: Numerical validation of analytical solution (30) for $x_q = L/2$, $\tau = 5$ ms, $m^a = 1$,

$m^i = 1$ (as shown in figure 16). Analytical solutions of coupled intrinsic modes (BA) and (BI) are represented by continuous blue and dashed red lines respectively. The green diamond and magenta circular dots represent their numerical counterparts, respectively by direct solution of equation (2.23). Yellow colour represents the domain of instability. The brown arrow represents the frequency of acoustic mode (ω_0^a) of the closed-open combustor in the absence of a flame. For numerical solutions, n is varied from (a) 0.0 to 1.0 and (b) 0.0 to 4.0. For analytical solutions, n is varied from 0.0 to 1.0 for both (a) and (b). For n higher than 1.0, the analytical solution deviates drastically from the numerical solution. This trend is captured in figure (b). This is the **first type of coupling**. As per numerical results of figure (b), the coupled intrinsic mode (BI) becomes unstable with $\omega_c^i \tau = 0$, whereas the coupled intrinsic mode (BA) becomes unstable at a higher frequency corresponding to $\omega_c^i \tau = \pi$.

145
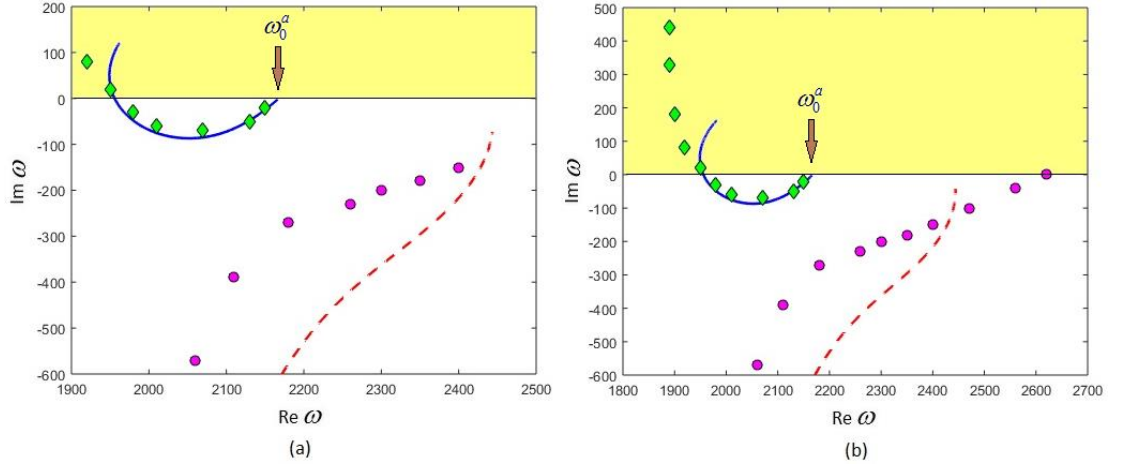
Figure 3.21: Numerical validation of analytical solution (30) for $x_q = L/2$, τ =4.8 ms, m^a =1, m^i =1 (as shown in figure 17). For numerical solutions, n is varied from (a) 0.0 to 1.0 and (b) 0.0 to 10.0. For analytical solutions, n is varied from 0.0 to 1.0 for both (a) and (b). This is the **second type of coupling**. As per numerical results of figure (b), the coupled intrinsic mode (BA) becomes unstable with $\omega_c^i \tau = 0$, whereas the coupled intrinsic mode (BI) becomes unstable at a higher frequency corresponding to $\omega_c^i \tau = \pi$. Other parameters and notations are the same as in figure 20.
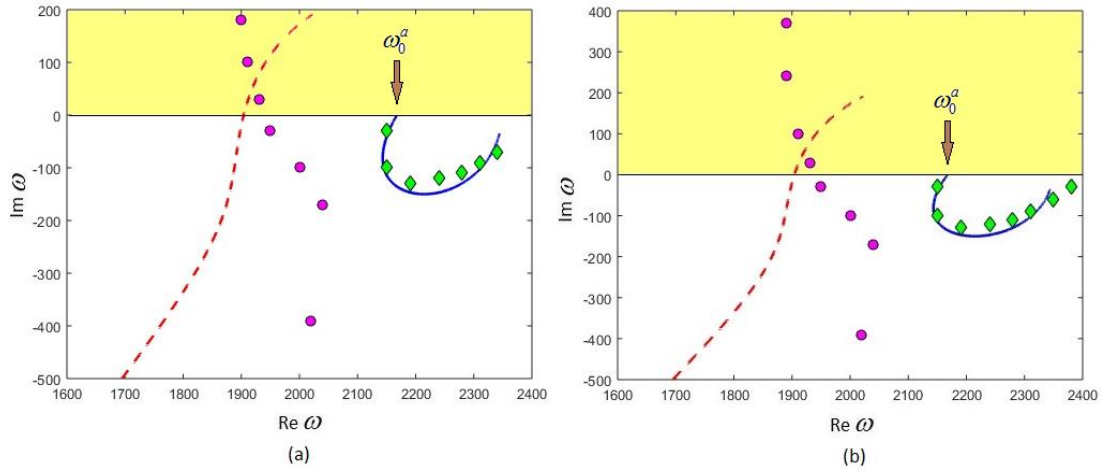
Figure 3.22: Numerical validation of analytical solution (30) for x_q =0.3 m, τ =4.85 ms, m^a =1, m^i =1 (as shown in figure 18). For numerical solutions, n is varied from (a) 0.0 to 2.5 and (b) 0.0 to 7.5. For analytical solutions, n is varied from 0.0 to 2.5 for both (a) and (b). For n higher than 2.5, the analytical solution deviates drastically from the numerical solution. This trend is captured in figures (a) and (b). This is the **third type of coupling**. As per the numerical results of figure (b), the coupled intrinsic mode (BI) becomes unstable with $\omega_c^i \tau = 0$, whereas the coupled intrinsic mode (BA) tends to remain asymptotically stable at a frequency corresponding to $\sin(k_1 x_q) = 0$, as per equation (2.29). Other parameters and notations are the same as in figure 20.

A numerical validation for the third and fourth types of coupling is given in figures 22 and 23. We consider the cases depicted in figures 18 and 19. Figure 22 shows that analytical model (30) offers good prediction accuracy for the instability frequency of the coupled intrinsic mode (BI), even though it fails to track the locus of the mode in the complex frequency plane with good accuracy. The locus of coupled intrinsic mode (BA) is captured accurately by the analytical model (30), where figure 22 (b) shows that this mode remains stable for $n = 7.5$, at a frequency corresponding to $\sin(k_1 x_q) = 0$ as per equation (2.29). Further increase of n (not shown here) does not allow this mode to cross the neutral line of instability. Indeed, this mode remains asymptotically stable for large n and for this case we obtain only one unstable solution (i.e. coupled intrinsic mode (BI)). Close observation of figure 23 shows that the analytical model (30) tracks the loci of both the coupled intrinsic modes (BA) and (BI) with a good accuracy. The instability frequency for the coupled intrinsic mode (BA) is predicted accurately. The other solution of the coupled intrinsic mode (BI) remains asymptotically stable for large n, as can be seen from 23 (b), hence we also only obtain one unstable solution for this case.
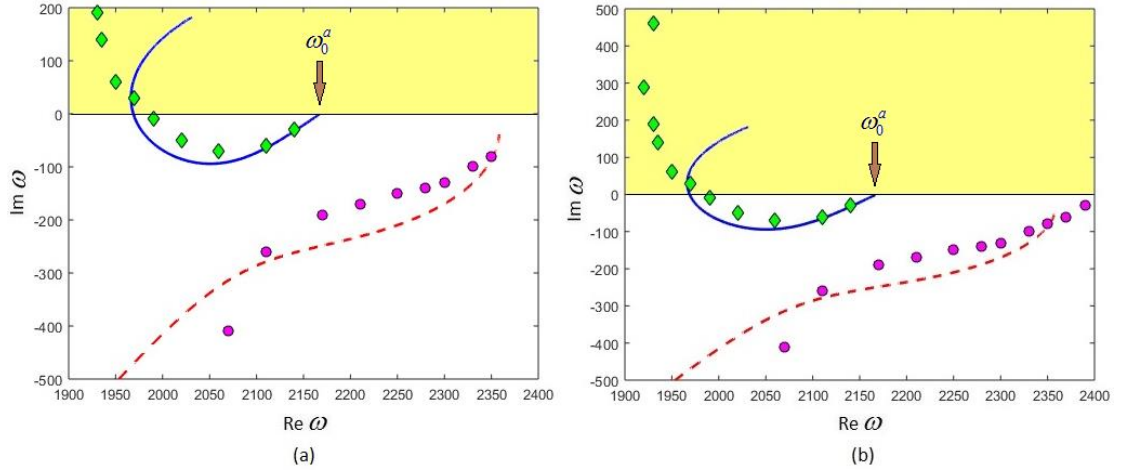
Figure 3.23: Numerical validation of analytical solution (30) for x_q =0.3 m, τ =4.75 ms, m^a =1, m^i =1 (as shown in figure 18). For numerical solutions, n is varied from (a) 0.0 to 2.5 and (b) 0.0 to 12.5. For analytical solutions, n is varied from 0.0 to 2.5 for both (a) and (b). This is the **fourth type of coupling**. As per the numerical results of figure (b), the coupled intrinsic mode (BA) becomes unstable with $\omega_c^i \tau = 0$, whereas the coupled intrinsic mode (BI) tends to remain asymptotically stable at a frequency corresponding to $\sin\left(k_1 x_q\right) = 0$, as per equation (2.29). Other parameters and notations are the same as in figure 20.

In general, because, for small n the intrinsic modes are far away from the boundary of stability, the small $\Delta\omega$ assumption in equation (30) is not valid for the intrinsic mode in the limit of small n. As n approaches the threshold of instability, the intrinsic mode approaches the neutral curve and thus, the accuracy of prediction of intrinsic mode frequency goes up.

Analytical model (30) can also be tested for accuracy for the coupling of acoustic modes with higher order intrinsic modes. Here we examine coupling with the third intrinsic mode (m^i =2). Figures 24-26 provide numerical validation for intrinsic - acoustic mode coupling, observed for the third intrinsic mode, near the point of intersection of the neutral curve segments $\omega_c^i \tau = 0$ and $\omega_c^i \tau = \pi$, of the main neutral loop on the extreme right of the neutral curve. The three figures are for time lag values chosen to be very close to the point of intersection of neutral segments

148

$\omega_c^i \tau = 0$ and $\omega_c^i \tau = \pi$ (that is τ =8.25 ms). These figures are for τ =7.9, 7.8 and 7.7 ms respectively. It is obvious that figure 24 illustrates the first type of coupling, whereas figures 25 and 26, which are for slightly lower values of τ, divulge the second type of coupling. Thus, this is an example where a slight alteration of τ near the point of intersection of neutral curve segments changes the type of coupling. This eventually leads to the change of identities of acoustic/intrinsic modes on the same neutral curve. This phenomenon has been mentioned in § 4.2 in chapter 2. A detailed discussion on this topic of the change of the type of coupling near the neutral curve segment intersection points will be provided in § 10.

The common aspect of these three figures is that the level of accuracy for the prediction of the locus of coupled intrinsic mode (BA) is very high. The same thing cannot be claimed for the coupled intrinsic mode (BI) though. The prediction accuracy is poor for the loci of the coupled intrinsic modes (BI) in all three cases when the coupled intrinsic mode (BI) stays away from the instability boundary. In figure 26, our analytical model, as per equation (30), entirely fails to catch the locus of the coupled intrinsic mode (BI). The reason for this has been already highlighted in this section. The coupled intrinsic mode (BA) in figure 24 and coupled intrinsic modes (BI) in figures 25 and 26, manifest instability at n =2.0, 2.5 and 3.0 respectively, as per the numerical results. The corresponding instability frequencies are not captured accurately by the analytical solution (30), due to the other growing mode resulting in large $\Delta\omega$. Barring this scenario, the prediction of the analytical model (30) is quite accurate near the neutral line for any n, as long as the assumption of small $\Delta\omega$ holds.
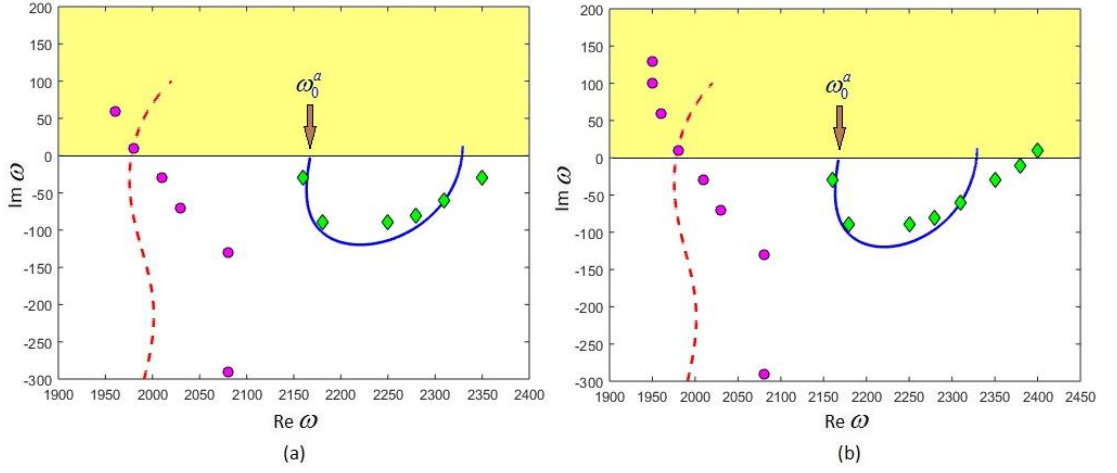
Figure 3.24: Numerical validation of analytical solution (30) for $x_q = L/2$, τ =7.9 ms, m^a =1, m^i =2. For numerical solutions, n is varied from (a) 0.0 to 1.0 and (b) 0.0 to 2.0. For analytical solutions, n is varied from 0.0 to 1.0 for both (a) and (b). For n higher than 1.0, the analytical solution deviates drastically from the numerical solution. This trend is captured in figures (a) and (b). This is the **first type of coupling**. As per the numerical results of figure (b), the coupled intrinsic mode (BI) becomes unstable with $\omega_c^i \tau = 0$, whereas the coupled intrinsic mode (BA) becomes unstable at a higher frequency corresponding to $\omega_c^i \tau = \pi$. Other parameters and notations are same as in figure 20.

Figure 3.25: Numerical validation of analytical solution (30) for $x_q = L/2$, τ =7.8 ms, m^a =1, m^i =2. For numerical solutions, n is varied from (a) 0.0 to 1.0 and (b) 0.0 to 2.5. For analytical solutions, n is varied from 0.0 to 1.0 for both (a) and (b). This is the **second type of coupling**. As per the numerical results of figure (b), the coupled intrinsic mode (BA) becomes unstable with $\omega_c^i \tau = 0$, whereas the coupled intrinsic mode (BI) becomes unstable at a higher frequency corresponding to $\omega_c^i \tau = \pi$. Other parameters and notations are the same as in figure 20.

150
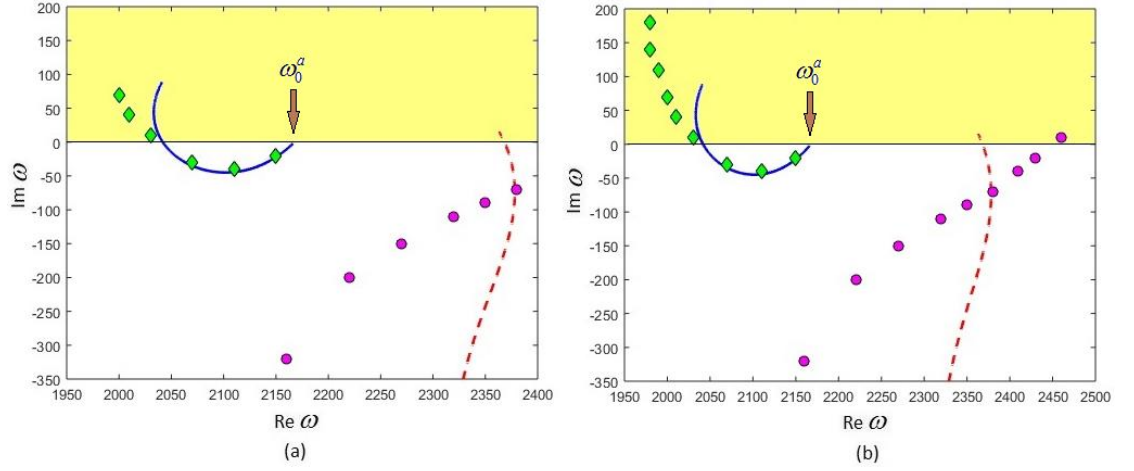
Figure 3.26: Numerical validation of analytical solution (30) for $x_q = L/2$, τ =7.7 ms, m^a =1, m^i =2. For numerical solutions, n is varied from (a) 0.0 to 1.0 and (b) 0.0 to 3.0. For analytical solutions, n is varied from 0.0 to 1.0 for both (a) and (b). This is the **second type of coupling**. As per the numerical results of figure (b), the coupled intrinsic mode (BA) becomes unstable with $\omega_c^i \tau = 0$, whereas the coupled intrinsic mode (BI) becomes unstable at a higher frequency corresponding to $\omega_c^i \tau = \pi$. Other parameters and notations are the same as in figure 20.

Hence, we can conclude that the prediction accuracy of our analytical model (30) is quite high when tracking down the locus of the coupled intrinsic mode (BA) on complex frequency plane. However, because the coupled intrinsic mode (BI) stays far away from the neutral curve for small values of n, the small $\Delta\omega$ assumption in equation (30) is not valid for the coupled intrinsic mode (BI) in the limit of small n. Hence, the locus of the coupled intrinsic mode (BI) on the complex frequency plane is not captured with a high fidelity on multiple instances. This calls for an improvement of the over-simplified analytical model that led to a quadratic equation. The inclusion of higher order terms in the equation should improve the accuracy of prediction and hence address this issue. This idea will be discussed in greater detail in the next section. For large n, if there is one strongly growing mode out of the two

coupled modes, this violates the assumption of linearity, which eventually prohibits us from accurately obtaining the instability frequency of the other mode for larger n.

3.8. Inclusion of higher order terms in the analytical model to increase the accuracy of modal frequency prediction

So far, we have used the quadratic equation (30) to deal with the acoustic-intrinsic mode coupling. As we have seen from the numerical validation section, even though the accuracy of the prediction of our analytical model is good enough for the coupled intrinsic modes (BA), it is not good enough for the coupled intrinsic modes (BI). In general, intrinsic modes that stay away from the acoustic modes and from the boundary of stability on the $n - \tau$ plane make it difficult for the quadratic equation (30) to track down its locus accurately on the $n - \tau$ plane. Hence, to increase the accuracy level of the analytical model, we are going to derive another equation to describe coupling by considering the higher order terms of $\Delta \omega$.

To start, we include higher order terms of sine and cosine expansion and neglect anything higher than order 4 for $\Delta \omega$. For simplification, we consider the flame to reside in the middle of the combustor (i.e. $x_q = L/2$) and ignore the cross-section and temperature jump across the flame. Thus, equivalent to equations (28), we can write,

$$\cos\left(\beta_1\left(\Delta\omega\right)\right)=1-\beta_1^2\left(\Delta\omega\right)^2\Big/2+\beta_1^4\left(\Delta\omega\right)^4\Big/24,$$

$$\sin\left(\beta_1\left(\Delta\omega\right)\right)=\beta_1\left(\Delta\omega\right)-\beta_1^3\left(\Delta\omega\right)^3\Big/6,$$

$$\cos\left(\left(\Delta\omega\right)\tau\right)=1-\left(\Delta\omega\right)^2\tau^2\Big/2+\left(\Delta\omega\right)^4\tau^4\Big/24,$$

$$\sin\left(\left(\Delta\omega\right)\tau\right)=\left(\Delta\omega\right)\tau-\left(\Delta\omega\right)^3\tau^3\Big/6. \tag{3.34}$$

Making use of the sine and cosine expansions, as per (34), we can arrive at a quartic equation to define the coupling of modes in a similar way to the quadratic equation (30),

$$A(\Delta\omega)^4 + B(\Delta\omega)^3 + C(\Delta\omega)^2 + D(\Delta\omega) + E = 0. \qquad (3.35)$$

The coefficients of this quartic equation are:

$$
\begin{aligned}
A &= ne^{i\omega_0^a\tau}\left[(-1)^{m^a} i\tau \frac{L}{6c_0}\left(\tau^2 + \frac{L^2}{c_0^2}\right) - \frac{\tau^4}{24}\right] \\[2mm]
B &= (-1)^{m^a}\left(2 + ne^{i\omega_0^a\tau}\right)\frac{L^3}{6c_0^3} + \frac{ne^{i\omega_0^a\tau}\tau^2}{2}\left[i\frac{\tau}{3} + (-1)^{m^a}\frac{L}{c_0}\right] \\[2mm]
C &= \left[-(-1)^{m^a} i\tau \frac{L}{c_0} + \frac{\tau^2}{2}\right]ne^{i\omega_0^a\tau} \\[2mm]
D &= -(-1)^{m^a}\left(2 + ne^{i\omega_0^a\tau}\right)\frac{L}{c_0} - ine^{i\omega_0^a\tau}\tau \\[2mm]
E &= -ne^{i\omega_0^a\tau}
\end{aligned}
\qquad (3.36)
$$

Thus, equation (35) can be solved to obtain four solutions: one for the acoustic mode and another for the intrinsic mode in close vicinity of the acoustic mode. Indeed, equation (35) gives rise to 4 solutions, but, as it will be shown in the next section, two of these solutions need not be considered.

Thus, to enhance the accuracy level of our analytical model, we have developed a quartic equation in $\Delta\omega$, in contrast to the quadratic equation in $\Delta\omega$ (30). The outcome of this higher order analytical model will be discussed in the next section, where this analytical model is compared to the numerical result.

3.9. Numerical validation of the analytical solution predicted by the quartic equation

In this section we will redo the plots of figures 20-21 and 24-26, but this time using the analytical solution prescribed by equation (35). We will also perform a comparative study of figures 20-21 and 24-26 to check whether the inclusion of higher order terms in the analytical model enhances the prediction accuracy (particularly for the coupled intrinsic modes (BI)). Figures 27-31 represents these kinds of plots. For generating numerical data, the same method as prescribed in figure 20-21 and 24-26 has been adopted. Moreover, the notations and parameters used in figures 27-31 are the same as in figures 20-21 and 24-26.

A close look at figures 27-31 will tell us that the figures manifest a good correspondence between the analytical and numerical solutions, both for the coupled intrinsic modes (BA) and for the coupled intrinsic modes (BI) (unlike the previous case). The analytical solution for the coupled intrinsic modes (BI) closely follows the locus as predicted by the numerical solution, even for the cases where coupled intrinsic modes (BI) stay far away from the neutral line. For example, in figures 27 and 28, the analytical solution as per (35) closely follows the numerical solution of coupled intrinsic mode (BI) and in figure 27 it follows the apparently twisted locus of coupled intrinsic mode (BI) (which was not captured with analytical solution (30)). Similar observations can be made for figures 29-31, where the analytical solution as per (35) is corroborated well by the numerical solution. Figures 29-31 correspond to the same three cases as prescribed in figures 24-26. Indeed, the inclusion of higher order terms in the analytical model has greatly enhanced the accuracy of prediction for the loci of coupled intrinsic modes (BI). It is also worth noting that the prediction accuracy for the loci of the coupled intrinsic modes (BA) remains good, just like the

previous case. However, it is not an important factor to know the loci of the coupled intrinsic modes (BI) too accurately, when it stays too far away from the line of stability. But, in some cases, if that knowledge becomes important, our current model as per (35) can capture that information with very high fidelity. Just like the analytical model (30), in the case for large n, if there is one strongly growing mode out of the two coupled modes, the linearity assumption is violated. This eventually prohibits us from accurately obtaining the instability frequency of the other mode in the limit of large n. This can be visualized in panel (b) in figures 27-31, where the analytical solutions have been provided only until the limit of linearity.

(a)   (b)
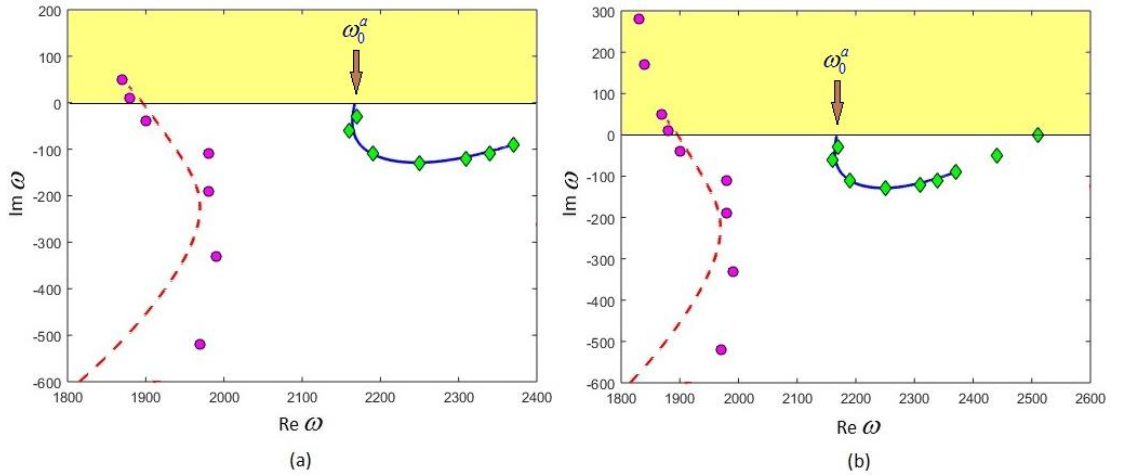
Figure 3.27: Numerical validation of analytical solution (35) for $x_q = L/2$, $\tau = 5$ ms, $m^a = 1$, $m^i = 1$ (as shown in figure 16). For numerical solutions, n is varied from (a) 0.0 to 1.0 and (b) 0.0 to 4.0. For analytical solutions, n is varied from 0.0 to 1.0 for both (a) and (b). For n higher than 1.0, the analytical solution does not capture the trend evident from numerical solution. This is the **first type of coupling**. As per the numerical results of figure (b), the coupled intrinsic mode (BI) becomes unstable with $\omega_c^i \tau = 0$, whereas the coupled intrinsic mode (BA) becomes unstable at a higher frequency corresponding to $\omega_c^i \tau = \pi$. Other parameters and notations are same as in figure 20.
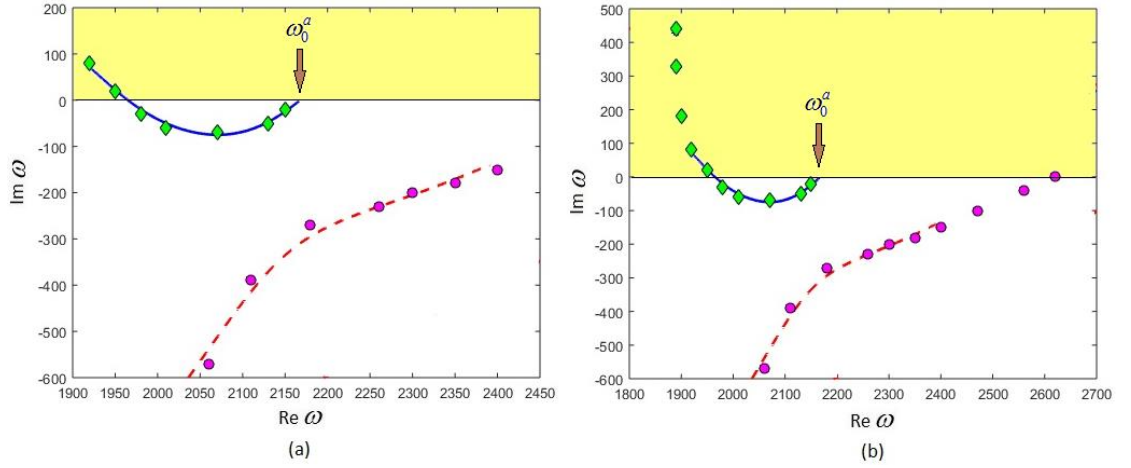
Figure 3.28: Numerical validation of analytical solution (35) for $x_q = L/2$, τ =4.8 ms, m^a =1, m^i =1 (as shown in figure 17). For numerical solutions, n is varied from (a) 0.0 to 1.0 and (b) 0.0 to 10.0. For analytical solutions, n is varied from 0.0 to 1.0 for both (a) and (b). This is the **second type of coupling**. As per the numerical results of figure (b), the coupled intrinsic mode (BA) becomes unstable with $\omega_c^i \tau = 0$, whereas the coupled intrinsic mode (BI) becomes unstable at a higher frequency corresponding to $\omega_c^i \tau = \pi$. Other parameters and notations are the same as in figure 20.
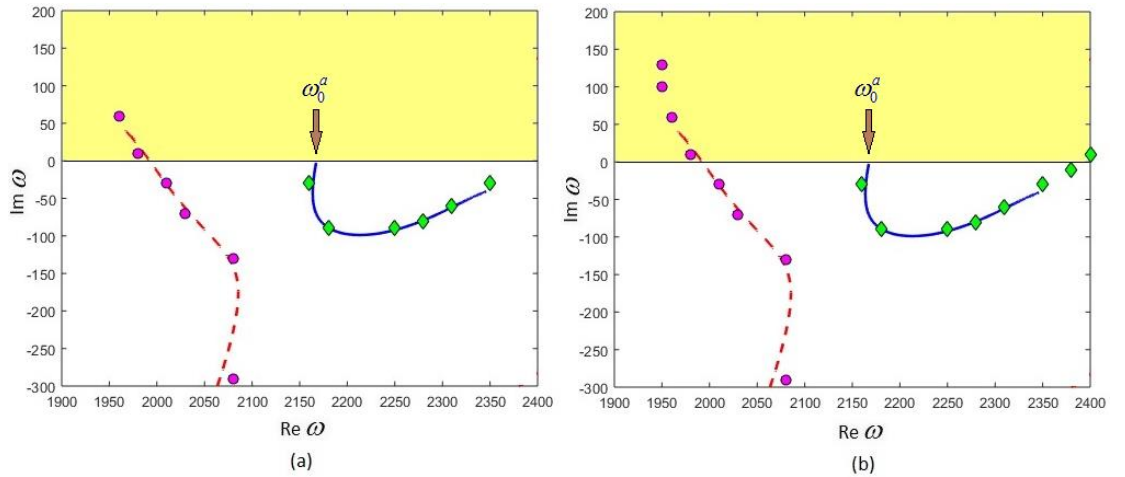
Figure 3.29: Numerical validation of analytical solution (35) for $x_q = L/2$, τ =7.9 ms, m^a =1, m^i =2. For numerical solutions, n is varied from (a) 0.0 to 1.0 and (b) 0.0 to 2.0. For analytical solutions, n is varied from 0.0 to 1.0 for both (a) and (b). This is the **first type of coupling**. As per the numerical results of figure (b), the coupled intrinsic mode (BI) becomes unstable with $\omega_c^i \tau = 0$, whereas the coupled intrinsic mode (BA) becomes unstable at a higher frequency corresponding to $\omega_c^i \tau = \pi$. Other parameters and notations are the same as in figure 20.

156
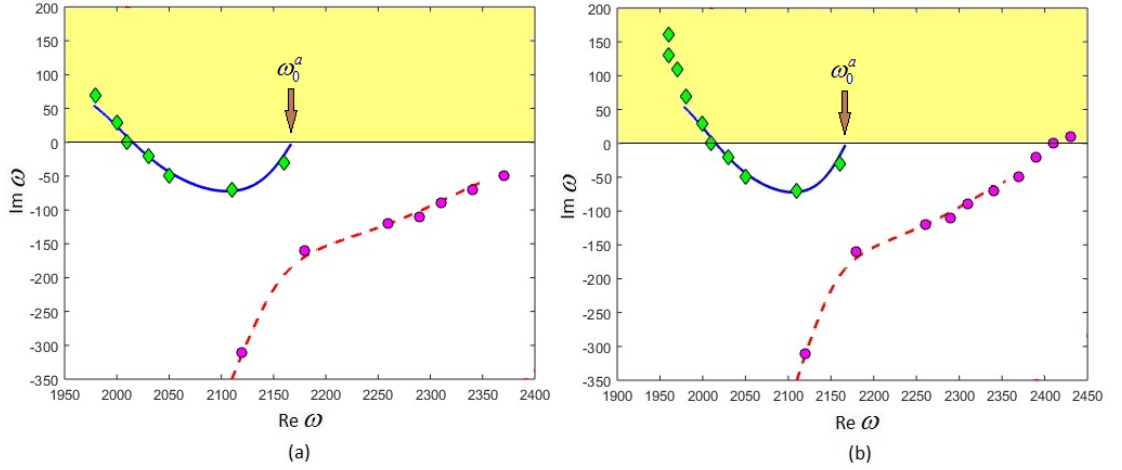
Figure 3.30: Numerical validation of analytical solution (35) for $x_q = L/2$, τ =7.8 ms, m^a =1, m^i =2. For numerical solutions, n is varied from (a) 0.0 to 1.0 and (b) 0.0 to 2.5. For analytical solutions, n is varied from 0.0 to 1.0 for both (a) and (b). This is the **second type of coupling**. As per the numerical results of figure (b), the coupled intrinsic mode (BA) becomes unstable with $\omega_c^i \tau = 0$, whereas the coupled intrinsic mode (BI) becomes unstable at a higher frequency corresponding to $\omega_c^i \tau = \pi$. Other parameters and notations are the same as in figure 20.
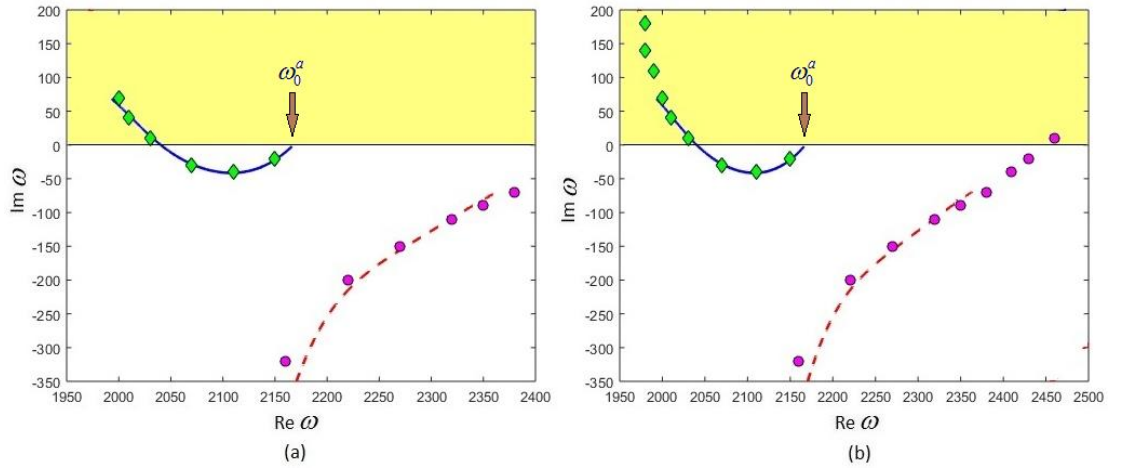
Figure 3.31: Numerical validation of analytical solution (35) for $x_q = L/2$, τ =7.7 ms, m^a =1, m^i =2. For numerical solutions, n is varied from (a) 0.0 to 1.0 and (b) 0.0 to 3.0. For analytical solutions, n is varied from 0.0 to 1.0 for both (a) and (b). This is the **second type of coupling**. As per the numerical results of figure (b), the coupled intrinsic mode (BA) becomes unstable with $\omega_c^i \tau = 0$, whereas the coupled intrinsic mode (BI) becomes unstable at a higher frequency corresponding to $\omega_c^i \tau = \pi$. Other parameters and notations are the same as in figure 20.

Thus, we have seen that the inclusion of higher order terms into our analytical model greatly improves the prediction accuracy of the loci of the coupled intrinsic modes (BI) in the complex frequency plane. The prediction accuracy is improved even when the coupled intrinsic mode (BI) stays well away from the line of stability. The quartic equation (35) also predicts the locus of coupled intrinsic mode (BA) quite efficiently, just like the quadratic equation (30). A comparative study of the performance of the quadratic equation (30) against the quartic equation (35) will be made in § 12.

3.10. The complete picture of the intrinsic-acoustic mode coupling near the intersection of neutral curve segments

It has been mentioned previously in § 4.2 of chapter 2 that the domain close to the neutral curve segment intersection points manifest strong coupling between intrinsic and acoustic modes. This statement has also been validated by figure 2.12 in chapter 2, where it was shown that near the intersection points of the neutral curve segments coupled acoustic and intrinsic modes invariably change their identity. This phenomenon will be discussed in this section with the help of a few examples. For all the figures in this section, we consider the flame to reside at $x_q = L/2$ and no cross-section and temperature jump across the flame. We make use of the quartic equation (35) to attain better accuracy.

3.10.1. Coupling near neutral segment intersections for the second intrinsic mode

This example will be cited for the points of intersection of neutral curve segments $\omega_c^i \tau = 0$ and $\omega_c^i \tau = \pi$, as well as $\omega_c^i \tau = 0$ and $\omega_c^i \tau = -\pi$ for the rightmost neutral loop of the second intrinsic mode. We will try to identify what type of coupling exists

158

at these points of intersection and how the intrinsic-acoustic mode coupling is affected if the τ is slightly altered from the points of intersection.

3.10.1.1. Coupling at the point of intersection of the extreme right neutral loop segments $\omega_c^i \tau = 0$ and $\omega_c^i \tau = \pi$

Primarily, we focus on the intrinsic-acoustic mode coupling at the points of intersection of the extreme right neutral loop segments $\omega_c^i \tau = 0$ and $\omega_c^i \tau = \pi$, that is $\tau = 5.425$ ms. This situation is captured in figure 32 (a). For all the subsequent figures, the coupled intrinsic modes (BA) and (BI) are represented by continuous blue and dashed red lines respectively. Yellow colour marks the domain of instability. The brown arrow indicates the frequency of acoustic mode (ω_0^a) of the closed-open combustor in the absence of a flame.

Figure 32 (a) shows that for this value of τ, as the value of n is increased, the second intrinsic mode arrives in the close vicinity of the second acoustic mode on the complex frequency plane. They engage in the first type of coupling, the coupled intrinsic mode (BI) becomes unstable following $\omega_c^i \tau = 0$ and the coupled intrinsic mode (BA) becomes unstable at a still higher frequency corresponding to $\omega_c^i \tau = \pi$. For this case, the threshold value of n is the same for both coupled modes, as can also be seen from figure 2.12.

In the subsequent two sections, we will deviate the τ value slightly from the point of intersection of neutral curve segments $\omega_c^i \tau = 0$ and $\omega_c^i \tau = \pi$ to either side, to find out what kind of impact it has on the intrinsic-acoustic mode coupling scenario.
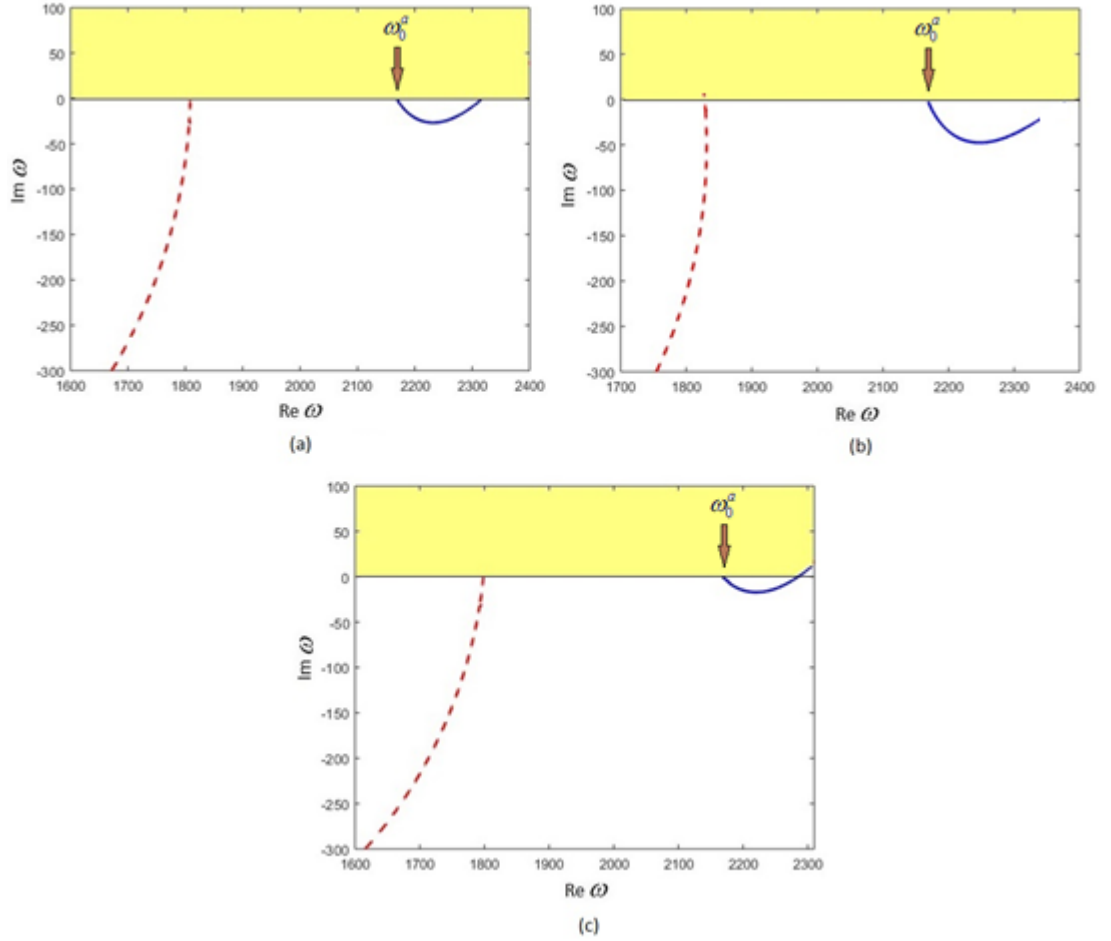
Figure 3.32: Loci of the coupled modes for $x_q = L/2$, $m^a = 1$, $m^i = 1$, when (a) $\tau = 5.425$ ms; (b) $\tau = 5.3$ ms and (c) $\tau = 5.5$ ms. The value of τ for (a) corresponds to the intersection point of the largest neutral loop segments $\omega_c^i \tau = 0$ and $\omega_c^i \tau = \pi$ on the extreme right of the second intrinsic mode neutral curve, whereas (b) corresponds to a point slightly left and (c) corresponds to points slightly right of this intersection point respectively. n is varied from 0.0 to 0.9. Plots are generated with the help of quartic equation (35). Coupled intrinsic modes (BA) and (BI) are represented by solid blue and dashed red lines respectively. The domain of instability is marked in yellow. The brown arrow represents the frequency of acoustic mode (ω_0^a) of the closed-open combustor in the absence of a flame. (a), (b) and (c) illustrate the **first type of coupling**, where the coupled intrinsic modes (BI) become unstable with $\omega_c^i \tau = 0$, whereas, the coupled intrinsic mode (BA) become unstable at a higher frequency corresponding to $\omega_c^i \tau = \pi$.

3.10.1.2. Coupling to the left of the point of intersection of extreme right neutral loop segments $\omega_c^i \tau = 0$ and $\omega_c^i \tau = \pi$

Primarily, we consider a set of points on the neutral curve to the left of the intersection point mentioned in § 10.1.1. Figure 32 (b) shows the intrinsic-acoustic mode coupling scenario for $\tau = 5.3$ ms.

It is obvious from figure 32 (b) that the second intrinsic and second acoustic mode couple with each other via the first type of coupling. The coupled intrinsic mode (BI) becomes unstable at a frequency corresponding to $\omega_c^i \tau = 0$ and the coupled intrinsic mode (BA) becomes unstable at a still higher frequency corresponding to $\omega_c^i \tau = \pi$. The threshold of instability for the coupled intrinsic mode (BA) is higher than that of the coupled intrinsic mode (BI). The scenario changes slightly, as shown in figure 17, for a lower value of τ ($\tau = 4.8$ ms), which changes the coupling type from the first to second. The coupled intrinsic mode (BA) becomes unstable, corresponding to $\omega_c^i \tau = 0$ at a much lower threshold of n, compared to the coupled intrinsic mode (BI) that becomes unstable at a frequency corresponding to $\omega_c^i \tau = \pi$. The corresponding n-threshold values are provided by figure 2.12 of Chapter 2.

Thus, as we move to the left of the intersection point mentioned in § 10.1.1, we find a transition from the first type to the second type of coupling. In general, the coupled intrinsic modes (BA) tend to become unstable at much lower n-threshold values compared to the coupled intrinsic mode (BI).

3.10.1.3. Coupling to the right of the point of intersection of extreme right neutral loop segments $\omega_c^i \tau = 0$ and $\omega_c^i \tau = \pi$

Now we can shift our attention to the right of the intersection point prescribed in § 10.1.1. Figure 32 (c) shows the coupling phenomenon in this domain for a time lag of $\tau = 5.5$ ms.

The figure makes it obvious that in this case we have the first type of coupling. The coupled intrinsic mode (BI) becomes unstable with $\omega_c^i \tau = 0$ and the coupled intrinsic mode (BA) becomes unstable at a higher frequency, predicted by $\omega_c^i \tau = \pi$. The threshold in n for the coupled intrinsic mode (BA) is lower than that of the coupled intrinsic mode (BI). This trend remains consistent if we keep on moving further to the right of the neutral curve until we reach the boundary of linear coupling. Most importantly, unlike § 10.1.2, the first type of coupling at no point transmutes into second type of coupling.

We can therefore say that on the right-hand side of the intersection point mentioned in § 10.1.1, we always have the first type of coupling, within the boundary of linear coupling. In this domain, the coupled intrinsic mode (BA) tends to become unstable at a much lower threshold value of n, compared to the coupled intrinsic mode (BI).

3.10.1.4. Coupling at the point of intersection of extreme right neutral loop segments $\omega_c^i \tau = 0$ and $\omega_c^i \tau = -\pi$

An analysis similar to that of §s 10.1.1-10.1.3 can also be conducted at the intersection point of the neutral curve segments $\omega_c^i \tau = 0$ and $\omega_c^i \tau = -\pi$ for the extreme right neutral loop of the second intrinsic mode. This intersection lies at $\tau = 10.2$ ms. Figure 33 illustrates the coupling scenario for this intersection point.

Figure 33 (a) shows that for this τ, the second intrinsic mode comes into the close vicinity of the first acoustic mode. In fact, it has been checked numerically that for the extreme right intersection point of the neutral curve, the intrinsic mode always couples with the first acoustic mode. Figure 33 (a) shows evidence of the first type of coupling, where the coupled intrinsic mode (BI) becomes unstable at a frequency corresponding to $\omega_c^i \tau = 0$, whereas the coupled intrinsic mode (BA) becomes unstable at a lower frequency given by $\omega_c^i \tau = -\pi$. These modes both become unstable at the same threshold value of n.

In the subsequent two sections, we will alter the τ values slightly on either side of the intersection point of the neutral curve segments $\omega_c^i \tau = 0$ and $\omega_c^i \tau = -\pi$ and find out how this changes the intrinsic-acoustic mode coupling scenario.
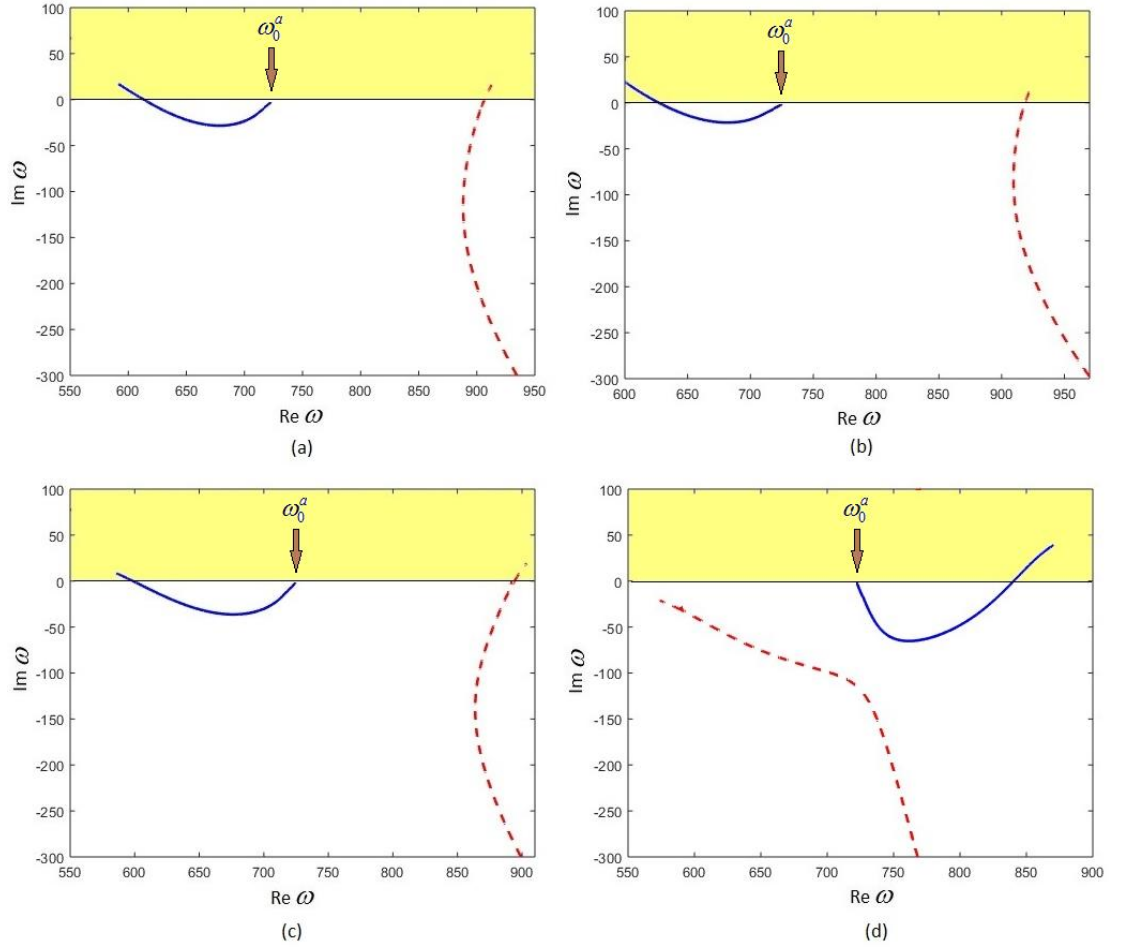
Figure 3.33: Loci of the coupled modes for $x_q = L/2$, $m^a = 0$, $m^i = 1$, when (a) $\tau = 10.2$ ms; (b) $\tau = 10.0$ ms; (c) $\tau = 10.4$ ms and (d) $\tau = 11.2$ ms. The τ value for (a) corresponds to the intersection point of the largest neutral loop segments $\omega_c^i \tau = 0$ and $\omega_c^i \tau = -\pi$ on the extreme right of the second intrinsic mode neutral curve, whereas (b) corresponds to a point slightly left and (c) and (d) correspond to points slightly right of this intersection point respectively. n is varied from 0.0 to 0.9. Plots are generated with the help of quartic equation (35). Coupled intrinsic mode (BA) and (BI) are represented by continuous blue and dashed red lines respectively. Yellow colour represents the domain of instability. The brown arrow represents the frequency of acoustic mode (ω_0^a) of the closed-open combustor in the absence of a flame. (a), (b) and (c) represent the **first type of coupling**, where the coupled intrinsic modes (BI) become unstable with $\omega_c^i \tau = 0$, whereas the coupled intrinsic mode (BA) become unstable at a lower frequency corresponding to $\omega_c^i \tau = -\pi$. (d) represents the **second type of coupling**, where the coupled intrinsic mode (BA) becomes unstable with $\omega_c^i \tau = 0$, whereas the coupled intrinsic mode (BI) tends to become unstable at a lower frequency corresponding to $\omega_c^i \tau = -\pi$. Thus, the type of intrinsic-acoustic mode coupling can change near the point of intersection of neutral curve segments.

3.10.1.5. Coupling to the left of the point of intersection of extreme right neutral loop segments $\omega_c^i \tau = 0$ and $\omega_c^i \tau = -\pi$

In this section we analyze the domain on the left-hand side of the intersection point described in § 10.1.4. Figure 33 (b) illustrates coupling in such a domain for $\tau = 10$ ms.

Figure 33 (b) shows the first type of coupling, where the coupled intrinsic mode (BI) becomes unstable at a frequency corresponding to $\omega_c^i \tau = 0$, whereas the coupled intrinsic mode (BA) becomes unstable at a lower frequency corresponding to $\omega_c^i \tau = -\pi$ and at a lower value of n-threshold compared to the coupled intrinsic mode (BI). This trend remains consistent in this domain and the coupling type does not get transformed from the first to the second.

Thus, in the domain to the left of the intersection point prescribed in § 10.1.4, there exists the first type of coupling and the coupled intrinsic mode (BA) becomes unstable at a lower value of n-threshold compared to the coupled intrinsic mode (BI).

3.10.1.6. Coupling to the right of the point of intersection of extreme right neutral loop segments $\omega_c^i \tau = 0$ and $\omega_c^i \tau = -\pi$

We now shift our attention to the right side of the domain of the point of intersection prescribed in § 10.1.4. The coupling phenomenon in this domain is elucidated with the help of figures 33 (c) and 33 (d), drawn for time lag values of 10.4 ms and 11.2 ms respectively.

Figure 33 (c), which is in the immediate vicinity of the intersection point mentioned in § 10.1.4, shows the first type of coupling, just like figures 33 (a, b). The coupled

165

intrinsic mode (BA) becomes unstable at a higher n-threshold than the coupled intrinsic mode (BI). The scenario changes completely when we move further to the right of the coupling domain, where as per figure 33 (d), at $\tau = 11.2$ ms, we observe the second type of coupling. The coupled intrinsic mode (BA) becomes unstable at a frequency corresponding to $\omega_c^i \tau = 0$ and the coupled intrinsic mode (BI) tends to become unstable at a still lower frequency corresponding to $\omega_c^i \tau = -\pi$. The coupled intrinsic mode (BA) becomes unstable at a much lower n-threshold value than the coupled intrinsic mode (BI). These observations are consistent with the numerical verification shown in figure 2.12 in chapter 2.

Thus, to the right of the intersection point described in § 10.1.4, the coupling domain possesses both first and second types of coupling. In the immediate vicinity of the intersection point, we find the first type of coupling, where the n-threshold for the coupled intrinsic mode (BI) is lower than the coupled intrinsic mode (BA). Further to the right we observe the second type of coupling, where the coupled intrinsic mode (BA) becomes unstable at much lower n-threshold than the coupled intrinsic mode (BI).

In this section, we have presented a comprehensive picture of the types of coupling near the points of intersection of the neutral loop segments. It has been found that for the neutral loop on the extreme right:

i. the coupling domains to the left of the first intersection point (between $\omega_c^i \tau = 0$ and $\omega_c^i \tau = \pi$) and on the right of the second intersection point (between $\omega_c^i \tau = 0$ and $\omega_c^i \tau = -\pi$) demonstrate both first and second types of coupling, and

ii. the coupling domains on the right of the first intersection point and on the left of the second intersection point only demonstrate the first type of coupling.

Hence, our mathematical model based upon the quartic equation has been proved to be able to provide a clear picture of the intricate behavior of the intrinsic-acoustic mode coupling domains near the intersections of the neutral curve segments. Something worth noting is that near the intersection points of neutral curve segments we not only we observe the first and second types of coupling but also the third and fourth types of coupling. For example, from figures 18 and 19 we have seen that for x_q =0.3 m, τ =4.85 ms the second intrinsic mode and the second acoustic modes couple in the type 3 route. For x_q =0.3 m, τ =4.75 ms the second intrinsic mode and the second acoustic modes couple in the type 4 route. Both these points lie on the left-hand side of the intersection of neutral lines $\omega_c^i \tau = 0$ and $\omega_c^i \tau = \pi$ of the extreme right neutral loop of second intrinsic mode when the flame is at x_q =0.3 m. On the left-hand side of the intersection of neutral lines $\omega_c^i \tau = 0$ and $\omega_c^i \tau = \pi$ for the extreme right neutral loop, when the flame is at x_q =0.3 m, there is also the presence of first and second types of coupling. This feature will be shown in the next section. Thus, in the coupling domains of neutral curves, we can have all four types of coupling present, for certain combustor parameters (like flame location, cross-section and temperature jump across flame).

3.11. Intrinsic-acoustic mode coupling on the $n-\tau$ plane

3.11.1. The domain of coupling on the $n-\tau$ plane

Examples of typical intrinsic mode stability maps on the $n-\tau$ plane were presented in figures 2.8 and 2.11. In this section, we identify the domains on the $n-\tau$ plane where intrinsic-acoustic mode coupling exists. In the domain where the coupling

exists, two solutions are dragged close to each other. Hence on the $n-\tau$ plane, we find two co-existing solutions instead of one.

In all cases, it is straightforward to identify the domain on the $n-\tau$ plane where two solutions co-exist, as illustrated below by figures 34 and 35. Both figures are drawn for the second intrinsic mode. Figure 34 and 35 correspond to two different flame locations $x_q = L/2$ and $x_q = 0.3$ m. We neglect the effect of cross-section and temperature jump across the flame. The hatched area indicates the domain with multiple instability islands, narrowing with the decrease of τ. In figure 34 (a) we show just the large neutral curve loop on the extreme right and in 34 (b) we show another loop to its immediate left. The blue, red and green lines correspond to the segments $\omega_c^i \tau = 0$, $\omega_c^i \tau = \pi$ and $\omega_c^i \tau = -\pi$ of the neutral curve respectively. Brown and lavender mark the stability domain of the intrinsic and coupled acoustic modes respectively. Yellow marks the instability domain due to the first and second types of coupling between intrinsic and coupled acoustic mode, whereas pink marks the instability domain due to the third and fourth type of coupling. The domains enclosed by the thick purple vertical lines represent the domain of coupling, where two solutions exist for a particular value of τ. These bounded regions can be seen, for example, near the first and second points of intersections of the neutral loop segments for the extreme right neutral loop. In all other domains outside this coupling domain, there is either no solution (that is linear stability for intrinsic mode) or only one solution (that is linear instability for intrinsic mode alone). Similar bounded domains of coupling can also be seen in figure 34 (b), where the bounded domains have also been marked for smaller loops. For this case, there are multiple thin coupling domains in short span of τ. This is an intricate coupling scenario, which is otherwise very hard to capture using numerical analysis.

Another important aspect is that near the intersection points of neutral curve segments, one mode (either intrinsic or acoustic) becomes unstable at smaller (or sometimes much smaller) values of n, whereas the other mode becomes unstable at higher (or sometimes much higher) values of n. In the linear analysis of most practical systems, the solutions lying on the $\omega_c^i \tau = \pi$ and $\omega_c^i \tau = -\pi$ lines, above the points of intersection with $\omega_c^i \tau = 0$, may not be feasible, because too high values of n in practical combustors will correspond to non-linear regimes, breaking the validity of our current linear analysis. However, any solution lying at or below the point of intersections will be of major interest and of practical significance. It has also been shown in § 10 that near the points of intersection of neutral segments, the intrinsic and coupled acoustic modes, invariably change their identity (also evident from numerical solutions of figure 2.12).
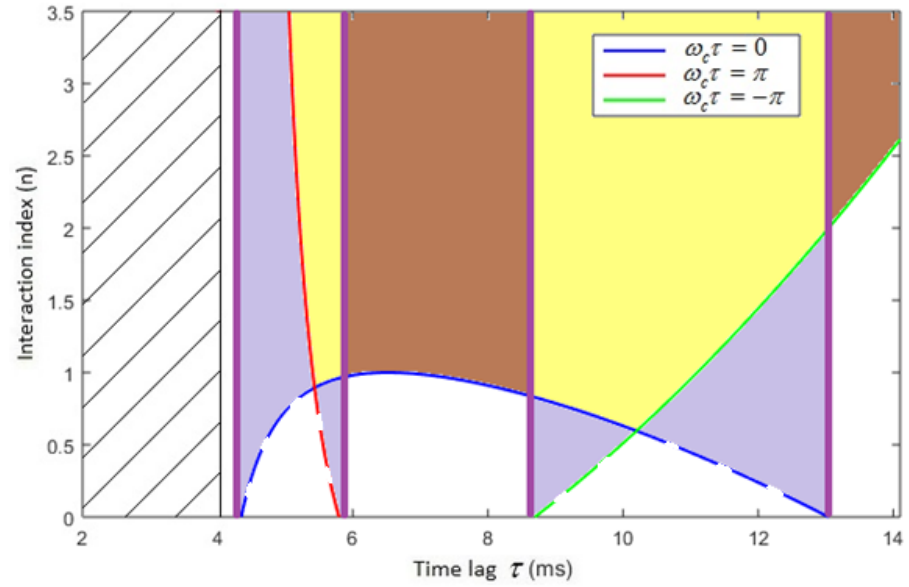
(a)
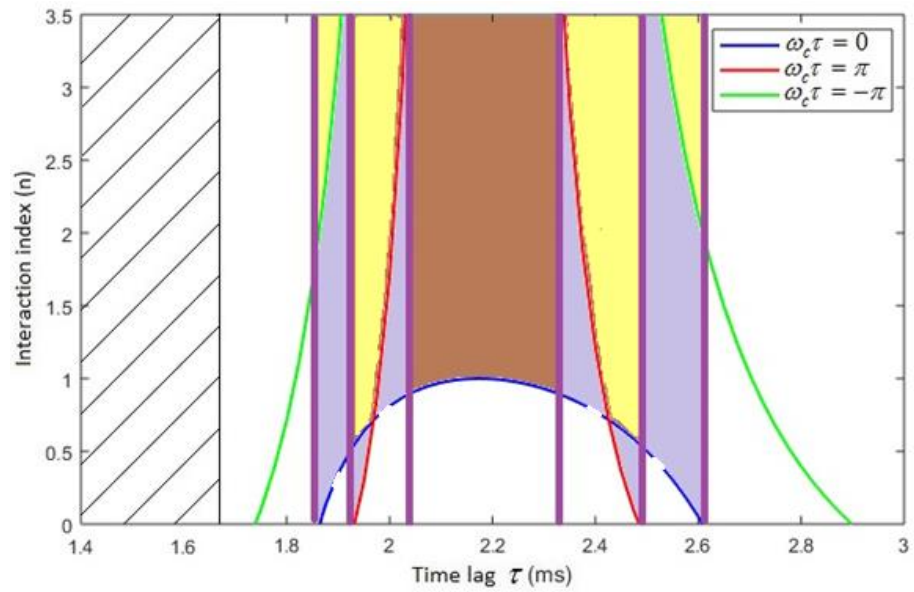
(b)

Figure 3.34: Neutral curve and stability domain on the $n - \tau$ plane for the second intrinsic mode ($m^i = 1$). Figures (a) and (b) differ only in scale. Figure (a) focuses on the extreme right neutral loop. Figure (b) focuses on the first neutral loop to the left of the extreme right neutral loop. Blue, red and green lines correspond to the segments $\omega_c^i \tau = 0$, $\omega_c^i \tau = \pi$ and $\omega_c^i \tau = -\pi$ of the neutral curve respectively. The instability domain for intrinsic mode and coupled acoustic modes are marked in brown and lavender respectively. The common domain of instability for intrinsic and coupled acoustic modes is marked in yellow. This is also the domain of the first and second types of coupling. The domain bound by thick purple vertical lines near the point of intersection of neutral curve segments represent the domain boundary of intrinsic-acoustic mode linear coupling. Figure (a) shows two distinct coupling domains near intersections of the neutral curve segments. Figure (b) presents multiple coupling domains in short intervals within the same neutral loop. Other parameters and notation are the same as in Fig.2.8.

170
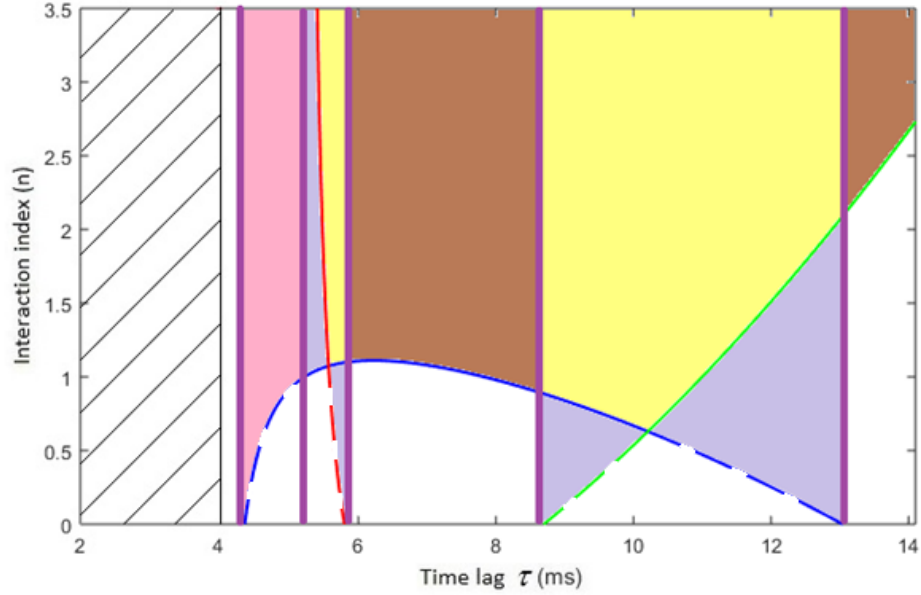
Figure 3.35: Neutral curve and stability domain on the $n - \tau$ plane for the second intrinsic mode ($m^i = 1$) for $x_q = 0.3$ m. This figure focuses on the extreme right neutral loop only.

Notations and other parameters are the same as in figure 34. Yellow colour represents the domain of the first and second types of coupling between intrinsic and acoustic modes. Pink colour represents the domain of the third and fourth types of coupling between intrinsic and acoustic modes. Near the right intersection point of neutral lines, there is a coupling domain where the first and second types of coupling exist. Near the left intersection point, the coupling type changes to the third and fourth types from the first and second types.

A similar observation can also be made regarding figure 35, where all four types of coupling are visible. It has been mentioned at the end of § 10, that near the intersection of neutral curve segments, the first and second types of coupling can transmute into third and fourth types of coupling, as is also evident from figure 35. Visual inspection of the third and fourth types of coupling domains in the neutral curve may prompt one to misinterpret it is an uncoupled domain, as we see only one unstable solution, whereas the other solution remains asymptotically stable for large n. However, there is a test criterion that we can apply to distinguish between an uncoupled domain (manifesting pure intrinsic instability) and the third or fourth types of coupling. If the range of n-threshold values for instability in the domain is very close to zero, then it must be a coupled domain. The strongly decaying nature of

intrinsic modes prohibits it to be unstable at such small n-threshold values for a practical range of τ. If the n-threshold within the domain is on the higher side (O(1)), then it is a domain of uncoupled pure intrinsic instability. Thus, a slight tweaking of combustor parameters could make all four types of coupling visible on the neutral curve.

Therefore, it is possible to identify the domain of coupling solely by making a visual inspection of the neutral curves of any intrinsic mode. Within the domain of coupling, there are always two solutions for a particular value of τ: one is coupled intrinsic (BI) and another one is coupled intrinsic (BA). All four types of coupling can be visible by a slight alteration in combustor parameters. Also, near the point of intersection, the type of coupling can change with a slight perturbation in τ.

3.11.2. Significance of isolated $\omega_c^i \tau = \pi$ and $\omega_c^i \tau = -\pi$ neutral curve segments in the stability map

It was mentioned in the discussion of figure 2.8 that there are infinitely many isolated almost-vertical lines due to $\omega_c^i \tau = \pi$ and $\omega_c^i \tau = -\pi$ neutral curve segments located between the neutral curve loops. It was also mentioned that these are predominantly the lines of coupling between intrinsic and acoustic modes. This subsection is dedicated to a detailed discussion of their role.
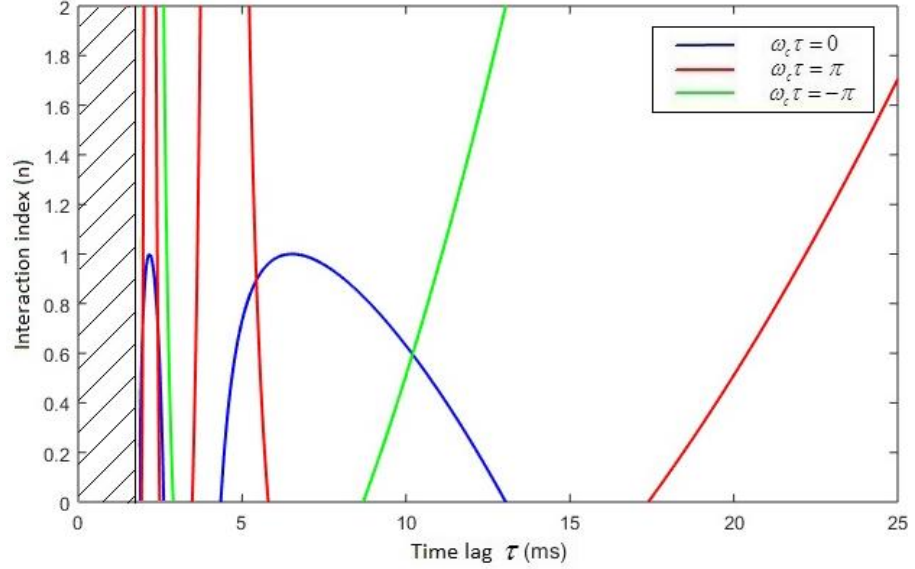
Figure 3.36: The neutral curve on the $n - \tau$ plane for the second intrinsic mode (m^i =1). Parameters and notations are the same as in Fig.2.8. The figure shows that there are isolated almost-vertical lines representing neutral curve segments $\omega_c^i \tau = \pi$ and $\omega_c^i \tau = -\pi$, lying on either side of the main neutral loop. These lines are the lines of coupling due to intrinsic-acoustic mode interaction.

We start with a discussion of the neutral curves for the second intrinsic mode, plotted in figure 36. It can be seen from figure 36 that on both sides of the main neutral curve loop there are isolated almost-vertical lines corresponding to $\omega_c^i \tau = \pi$ and $\omega_c^i \tau = -\pi$.

We know that for $\omega_c^i \tau = \pi$ and $\omega_c^i \tau = -\pi$ neutral curve segments to exist, a corresponding coupling segment $\omega_c^i \tau = 0$ must also exist. An acoustic mode cannot have a $\pm \pi/\tau$ frequency shift in the absence of any intrinsic modes nearby. Thus, it leads to the next question: what is the significance of these lines and do they matter in the stability diagram at all?

To answer this question, consider figures 37 and 38. In figure 37 there are 4 panels, each of them showing the neutral curves for one intrinsic mode. The four panels are of the same scale and represent, from top to the bottom, the first (m^i =0), second (m^i

=1), third (m^i =2) and fourth (m^i =3) intrinsic modes respectively. To maintain the simplicity of the diagram, only two neutral loops from the extreme right are depicted. In figure 38, all of these neutral curves for these modes overlap, generating a combined stability picture. From figure 37 we can see that on either side of the main neutral loop of the extreme right, there are isolated vertical/semi-vertical lines due to $\omega_c^i \tau = \pi$ and $\omega_c^i \tau = -\pi$. The most critical aspect is that the $\omega_c^i \tau = \pi$ line for any mode is equivalent to the $\omega_c^i \tau = -\pi$ line of the immediate higher order mode. For example, the isolated line, due to $\omega_c^i \tau = \pi$ on the extreme right of the first intrinsic mode, manifests once again in the stability diagram of the second intrinsic mode as a $\omega_c^i \tau = -\pi$ line for the main neutral loop on the extreme right. This gives us an idea that these two lines might indeed be one and should hence show for those modes where they find an intersection with the neutral line $\omega_c^i \tau = 0$ and not for other modes, where it exists as an isolated line. Besides, from the intrinsic-acoustic mode coupling perspective, isolated $\omega_c^i \tau = \pi$ and $\omega_c^i \tau = -\pi$ lines are absurd. This statement is also verified by figure 38. From figure 38 we see that all $\omega_c^i \tau = \pi$ and $\omega_c^i \tau = -\pi$ lines find intersections with the $\omega_c^i \tau = 0$ neutral line, making the intrinsic-acoustic mode coupling scenario possible. The only isolated line shown in figure 38 is the green line, which is part of the fifth intrinsic mode (not shown in this figure).
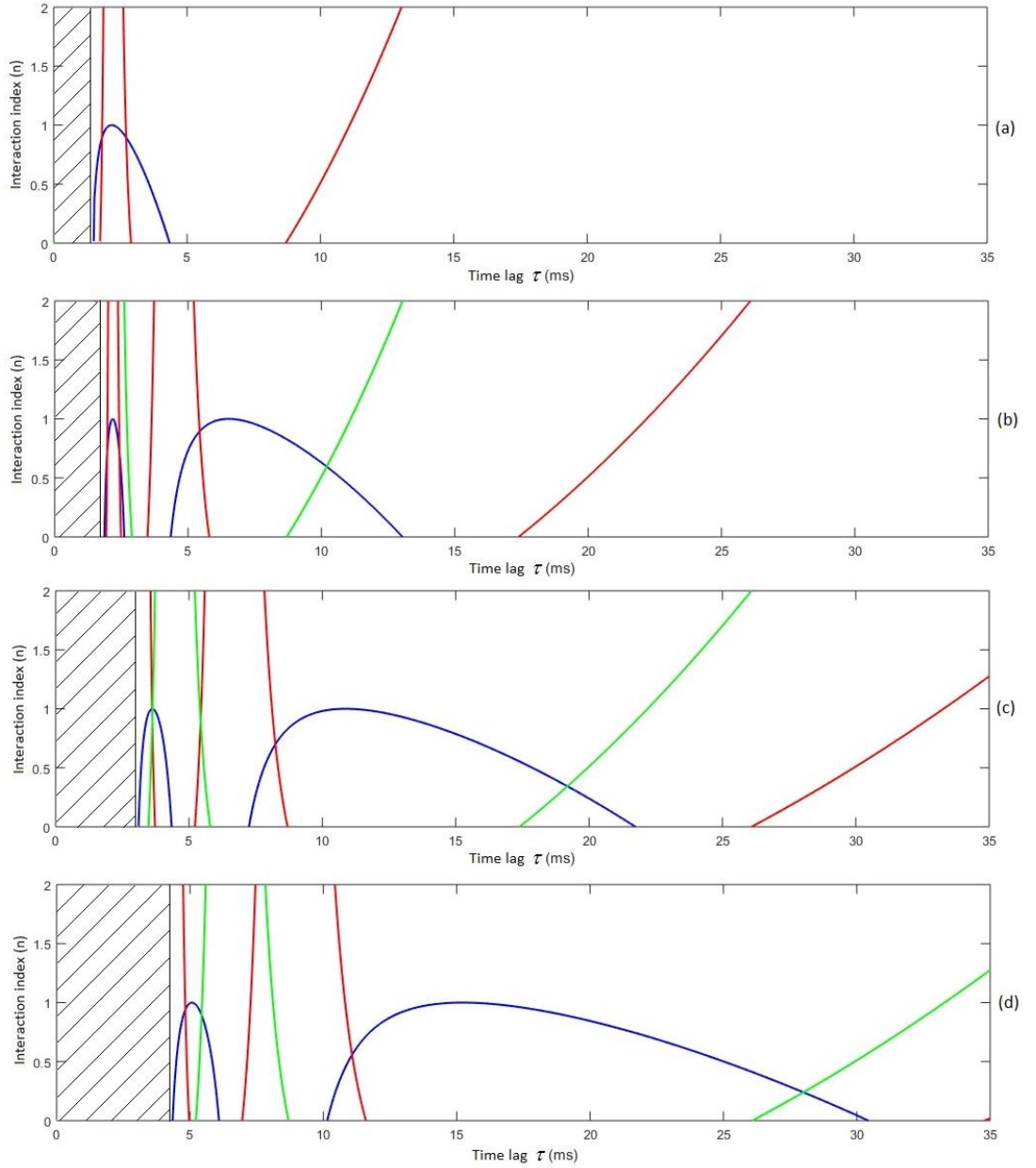
Figure 3.37: Neutral curve on the $n - \tau$ plane for the first (m^i =0), second (m^i =1), third (m^i =2) and fourth (m^i =3) intrinsic mode, shown separately in panels (a), (b), (c) and (d) but on the same τ scale. Other parameters and notation are the same as in Fig.2.8. The figure shows that there are isolated, almost-vertical, lines representing neutral curve segments $\omega^i_c \tau = \pi$ and $\omega^i_c \tau = -\pi$, lying on either side of the main neutral loop for each mode. These lines are the lines of coupling due to intrinsic-acoustic mode interaction and thus they should coexist with neutral curve segment $\omega^i_c \tau = 0$. This will lead to the existence of two solutions for the same τ. The neutral curve segment $\omega^i_c \tau = -\pi$ for a higher order mode is equivalent to the neutral curve segment $\omega^i_c \tau = \pi$ for the next lower order mode. This observation is consistent for all 4 figures above. This indicates that the isolated, almost-vertical, lines, due to $\omega^i_c \tau = \pi$ and $\omega^i_c \tau = -\pi$, are the same for the subsequent two modes.
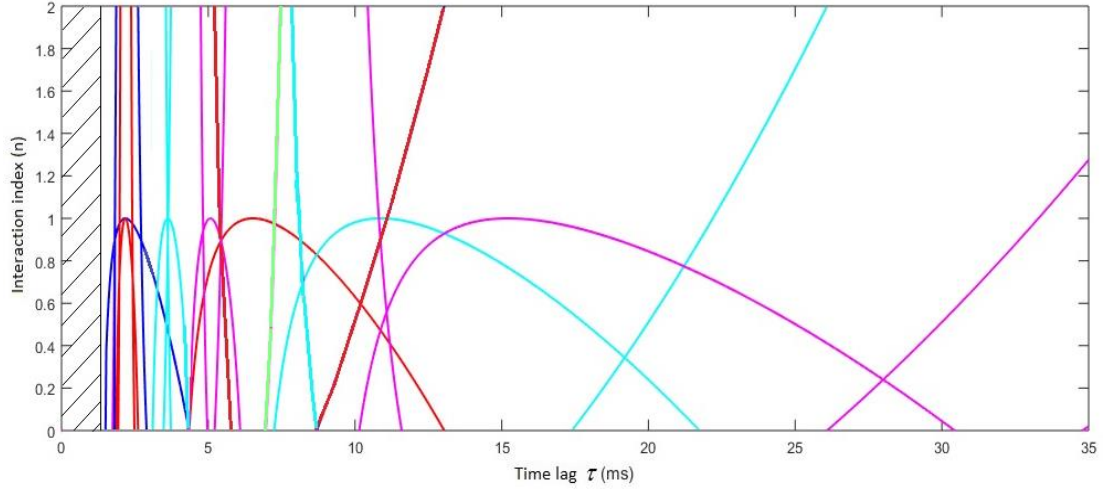
Figure 3.38: The neutral curve on the $n-\tau$ plane for the first (m^i =0), second (m^i =1), third (m^i =2) and fourth (m^i =3) intrinsic mode combined. Blue, red, cyan and magenta lines correspond to the neutral curves for the first, second, third and fourth intrinsic modes respectively. The hatched area indicates the domain with multiple instability islands that narrow as τ decreases. Other parameters and notation are the same as in Fig.2.8. The figure shows that there are no isolated, almost-vertical, neutral curve segments $\omega_c^i \tau = \pi$ and $\omega_c^i \tau = -\pi$ lying anywhere (except the green line, which represents neutral curve segment for fifth intrinsic mode (m^i =4)). This makes it self-evident that the neutral curve segment $\omega_c^i \tau = -\pi$ for the higher order mode is equivalent to the neutral curve segment $\omega_c^i \tau = \pi$ for the immediate next lower order mode, as claimed in figure 37. Thus, the isolated neutral curve segments lose identity when all modes overlap to generate an integrated stability diagram. This observation has been checked for consistency by considering more than 4 modes.

Thus, we have managed to answer the outstanding question of why we see isolated almost-vertical lines due to $\omega_c^i \tau = \pi$ and $\omega_c^i \tau = -\pi$ in the stability diagrams of intrinsic modes. We can conclude that any isolated line of this kind belongs to either an immediate higher or an immediate lower order intrinsic mode, where it finds an intersection with the corresponding $\omega_c^i \tau = 0$ neutral line, making the intrinsic-acoustic mode coupling feasible. When all modes overlap onto each other, these isolated lines appear as part of the neutral loops of immediate higher or lower order mode.

3.12. Comparison of quartic equation against the quadratic equation model

The study in § 10 has been based upon quartic equation (35). There is a specific reason behind giving preference to the quartic equation (35) over the quadratic equation model (30). Here this issue will be discussed in further detail. It has been mentioned before that despite having an apparent simplicity to deal with, the quadratic equation lacks accuracy in terms of tracking the trajectory of the intrinsic mode far away from the neutral curve. However, this is not the only problem. Near the intersection points of neutral curve segments, when we try to deal with the matter of intrinsic-acoustic mode coupling using the quadratic equation (30), we often find that the locus of the intrinsic mode is often wrongly tracked down, with the quadratic equation giving a false impression that the intrinsic modes are growing, when in fact these modes are decaying. Apart from this, there are also cases when the quadratic equation (30) fails to accurately predict the intrinsic mode frequency on the neutral curve. These aspects will be discussed in detail in the subsequent subsection, where we consider different time lag domains for the second and third intrinsic modes and show that the performance of the quadratic equation indeed deteriorates drastically.

In the first case, we consider three different time lag domains for the second intrinsic mode, to compare the performance of the quadratic equation (30) and the quartic equation (35). Figures 39 (a)- 39 (c) show three such figures for the second intrinsic mode. Figure 39 (a), (b) and (c) are for time lag values corresponding to the first intersection point (between $\omega_c^i \tau = 0$ and $\omega_c^i \tau = \pi$) of the neutral loop segments on the extreme right (τ =5.425 ms) and two points slightly left (τ =5.3 ms) and right (τ =5.5 ms) of the first intersection point respectively. In all three cases, the second

intrinsic mode comes near to the second acoustic mode. Thus, we capture the complete coupling region in the vicinity of the first intersection point of the extreme right neutral loop. The most important aspect of figure 39 (a) is that the locus of the coupled intrinsic mode (BI) on the $n - \tau$ plane is predicted to be in the unstable domain on the plane. This is wrong, as shown by the analytic prediction by quartic equation (35) (also validated numerically, but not shown here). Moreover, figure 39 (a) clearly shows that the quadratic equation, also fails to predict the instability frequency of the coupled intrinsic mode (BI) for this case. Similar observations can also be made for figures 39 (b) and 39 (c), where we see that figure 39 (b) predicts the instability frequency of the coupled intrinsic (BI) mode with poor accuracy, whereas figure 39 (c) predicts the growth of the coupled intrinsic mode (BI) instead of decay. Their counterparts, based on quartic equation (35), predict the instability frequencies with good accuracy, as well as predicting the decay of these modes.

A similar comparison can also be carried out for the third intrinsic mode. Figure 39 (d)corresponds to a time lag value slightly to the right of the first intersection point of the neutral loop segments, $\omega_c^i \tau = 0$ and $\omega_c^i \tau = \pi$, on the right, for the third intrinsic mode. This is $\tau = 8.4$ ms. The third intrinsic mode comes near to the second acoustic mode. It is obvious from this figure that the quadratic equation (30) fails to predict the instability frequency of the coupled intrinsic mode (BI) by a large margin. In contrast, the quartic equation (35) does a much better job. The actual value of the instability frequency of the coupled intrinsic mode (BI) can be computed from equation (2.32) in chapter 2. This prediction can be used as a tool to check the accuracy of the coupling models (30) and (35).
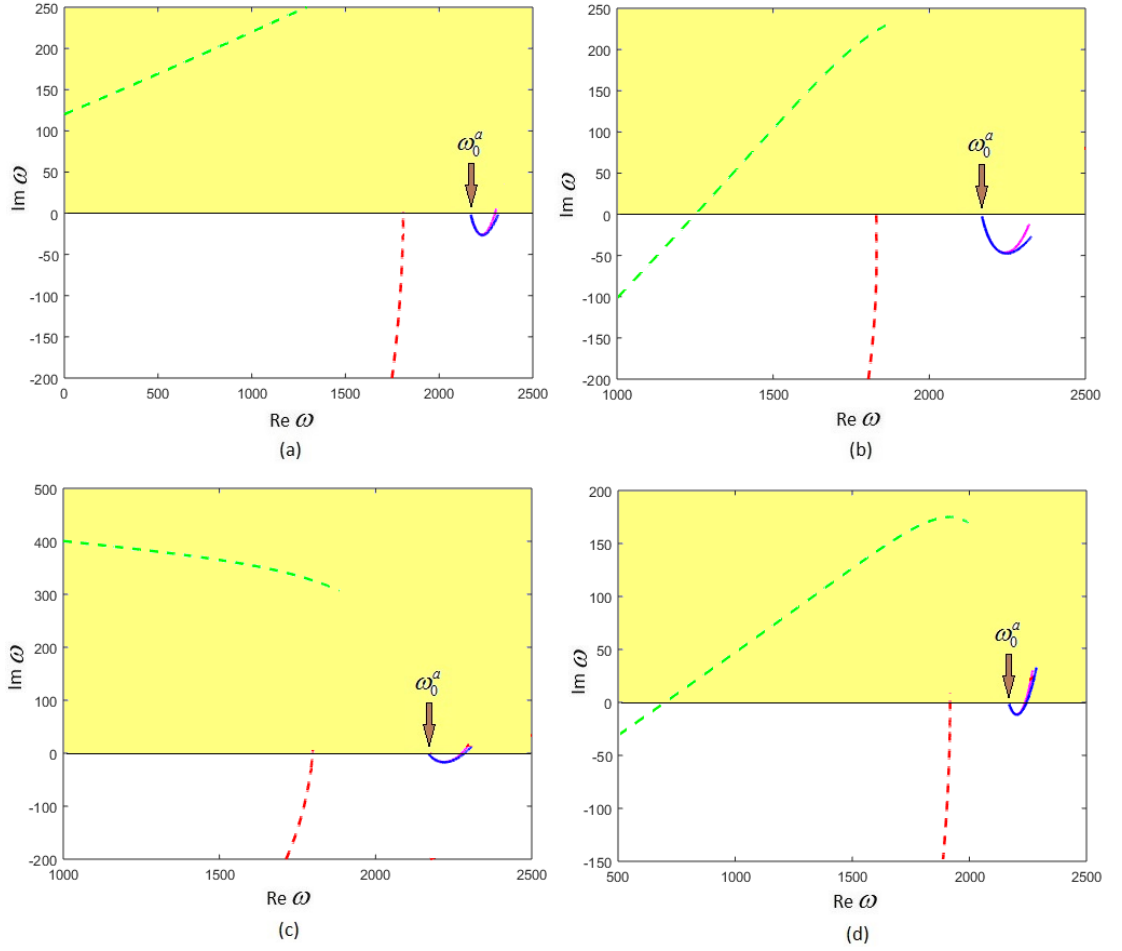
Figure 3.39: Loci of the coupled modes for (a) τ =5.425 ms, m^a =1, m^i =1; (b) τ =5.3 ms, m^a =1, m^i =1; (c) τ =5.5 ms, m^a =1, m^i =1 and (d) τ =8.4 ms, m^a =1, m^i =2. All these plots are for $x_q = L/2$. n is varied from 0.0 to 0.9. Plots are simultaneously generated with the help of quadratic equation (30) and quartic equation (35). Coupled intrinsic mode (BA) and coupled intrinsic mode (BI) are represented by continuous magenta and dashed green lines respectively, depicting the prediction by the quadratic equation (30). Coupled intrinsic mode (BA) and coupled intrinsic mode (BI) are represented by continuous blue and dashed red lines respectively, depicting the prediction by quartic equation (35). In most of the cases, blue and magenta lines almost overlap with each other. Yellow colour represents the domain of instability. The brown arrow represents the frequency of acoustic mode (ω_0^a) of the closed-open combustor in the absence of flame. These cases represent the **first type of coupling**, where the coupled intrinsic mode (BI) becomes or tends to become unstable with $\omega_c^i \tau = 0$, whereas the coupled intrinsic mode (BA) becomes or tends to become unstable at a higher frequency corresponding to $\omega_c^i \tau = \pi$. The loci of the coupled intrinsic modes (BA) are captured properly by equation (30), whereas the loci of the coupled intrinsic mode (BI) are not captured properly, showing the limitations of the quadratic equation (30). For all these cases, the quartic equation (35) offers a better quality of prediction (also validated numerically, but not shown here).

179

Thus, we have made a point that the accuracy of the quadratic equation (30) decreases drastically in the close vicinity of the intersection of the neutral curve segments. The quadratic equation either fails to predict the instability frequency of the coupled intrinsic mode (BI) with a good level of accuracy or predicts the growth of the coupled intrinsic mode (BI) instead of decay. In contrast, the quartic equation (35) does a much better job near the neutral curve intersection points and hence should be used as a preferred choice to predict intrinsic-acoustic mode coupling in this domain.

3.13. Conclusions

We have derived an analytical model of linear coupling of acoustic-intrinsic modes for a closed-open combustor. The phenomenon of the coupling of acoustic-intrinsic modes had not been considered in the literature and our model is the first mathematical model able to capture the main features of the coupling. To derive the model, we perturbed the original dispersion relation (2.20) in the vicinity of an acoustic mode and tried to find whether there is an intrinsic mode nearby in the $n - \tau$ space with which it can couple. In that process, we identified a new form of instability not reported so far in the literature, to the best our knowledge. This form of instability is neither pure acoustic nor pure intrinsic, rather a product of a coupling between the conventional acoustic and recently discovered intrinsic modes [Hoeimakers et al. (2014)]. As the simplest model, we came up with a quadratic equation that provided the basis of our analysis of mode coupling. The roots of the quadratic equation correspond to the frequency and decay/growth rate for the coupled modes. We have tracked the loci of these roots in the $n - \tau$ space and identified their qualitative behavior. We can summarize our advancement in the intrinsic-acoustic mode coupling scenario in the following way:

i. The intrinsic-acoustic mode coupling scenario is possible when acoustic pressure and flame heat release are out of phase with each other (that is, the Rayleigh index is negative), which forces the acoustic mode to decay for small values of n. This is a scenario when classical combustion instability is not possible. As the value of n is increased, the intrinsic mode decay rate reduces and comes near to the acoustic mode, which gives rise to the four different possibilities of intrinsic-acoustic mode coupling. In all these scenarios, the acoustic mode that is coupled to the intrinsic mode stops behaving like an acoustic mode and displays all the features of an intrinsic mode. Therefore, we refer to the intrinsic and coupled acoustic modes as coupled intrinsic modes and to distinguish them based on their origin, we named them 'born acoustic' (BA) and 'born intrinsic' (BI). The four types of coupling between intrinsic and acoustic modes are as follows:

1. In the **first type of coupling**, the coupled intrinsic mode (BI) becomes unstable at a frequency predicted by $\omega_c^i \tau = 0$, whereas the coupled intrinsic mode (BA) becomes unstable at a frequency predicted by either $\omega_c^i \tau = \pi$ or $\omega_c^i \tau = -\pi$.

2. In the **second type of coupling**, the coupled intrinsic mode (BA) becomes unstable at a frequency predicted by $\omega_c^i \tau = 0$, whereas the coupled intrinsic mode (BI) becomes unstable at a frequency predicted by either $\omega_c^i \tau = \pi$ or $\omega_c^i \tau = -\pi$.

3. In the **third type of coupling**, the coupled intrinsic mode (BI) becomes unstable with $\omega_c^i \tau = 0$, whereas the coupled intrinsic mode (BA) tends to remain asymptotically stable at a frequency corresponding to $\sin(k_1 x_q) = 0$ or $\sin(k_1(x_q - L)) = 0$ as per equation (2.29).

4. In the **fourth type of coupling**, the coupled intrinsic mode (BA) becomes unstable with $\omega_c^i \tau = 0$, whereas the coupled intrinsic mode (BI) tends to remain asymptotically stable at a frequency corresponding to $\sin(k_1 x_q) = 0$ or $\sin(k_1(x_q - L)) = 0$ as per equation (2.29).

ii. The regions of the neutral curve close to the intersection of the neutral curve segments $\omega_c^i \tau = 0$ and $\omega_c^i \tau = \pi$, as well as $\omega_c^i \tau = 0$ and $\omega_c^i \tau = -\pi$, show strong evidence of coupling. Near these intersections, we find two sets of solutions for the n-threshold for a given τ. In general, the larger values of n-threshold correspond to the coupled intrinsic mode (BI) and the smaller values correspond to the coupled intrinsic mode (BA). Thus, for a weak flame with low interaction index, even though the intrinsic mode does not become unstable on its own, it triggers the instability of one of the nearby acoustic modes. However, close to the intersection of neutral curve segments, coupled modes invariably change their identity. Close to the neutral curve intersection, the n-threshold for the coupled intrinsic mode (BA) is higher than the n-threshold of the coupled intrinsic mode (BI). As we move further away from the neutral curve segment intersection point, the n-threshold for the coupled intrinsic mode (BI) becomes higher than that of the coupled intrinsic mode (BA). Apart from the vicinity of the neutral curve segment intersection, the neutral loops on the left-hand side of the stability plots (corresponding to small τ values) demonstrate strong coupling.

iii. We have verified our result by numerics and the accuracy of our analytical result is found to be good. The accuracy of prediction is good, as we stay close to the neutral line of stability, where the actual acoustic mode-intrinsic mode coupling takes place. However, as we try to extend our linear analysis for regions far away from the

neutral line, the accuracy level of the analytical model drops. The quartic equation model (35) proved to perform much better than the quadratic equation (30) and should therefore be utilized where the accuracy of analytical prediction is of paramount importance.

In our present analysis, we have confined our attention to the linear coupling of acoustic and intrinsic modes. Due to the nonlinearity present in the heat release rate oscillation, we will also have non-linear coupling in a practical combustion system. Study of non-linear acoustic mode-intrinsic mode coupling lies beyond the scope of the present work.

Chapter 4

Flame intrinsic instability for combustors with open-open end conditions

4.1. Introduction: Decoupling of intrinsic mode instability frequency from combustor parameters on the neutral curve

In chapter 2 we described flame intrinsic instability via an analytical and numerical route for the case of a closed-open combustor. The analytical analysis was based on the result of equation (2.29), which shows that on the neutral curve, the intrinsic mode frequency is the same as the frequency in the asymptotic limit of small n. It also showed that on the neutral curve, intrinsic instability frequency is independent of the combustor parameters (like flame location, cross-section and temperature jump), even though the neutral curve itself depends on these parameters. This prompts the following questions:

i. Why is the intrinsic instability frequency independent of the combustor parameters on the neutral curve?

ii. Are there any other end conditions of the combustor for which this kind of decoupling of intrinsic instability frequency from the combustor parameters on the neutral curve takes place?

The first question has been answered briefly in § 4.1.2 of chapter 2. The detailed physical explanation of this phenomenon is still a matter of investigation. The second question can be answered with the help of generalized dispersion relation when $R_1(0)$ and $R_2(L)$ are retained in the original form in equations (2.3) and (2.4),

$$(1+\alpha)\left\{e^{i\omega\beta_1} - R_1(0)R_2(L)e^{-i\omega\beta_1}\right\} + (1-\alpha)\left\{R_2(L)e^{i\omega\beta_2} - R_1(0)e^{-i\omega\beta_2}\right\} + ne^{i\omega\tau}$$
$$\left\{e^{i\omega\beta_1} + R_2(L)e^{i\omega\beta_2} - R_1(0)e^{-i\omega\beta_2} - R_1(0)R_2(L)e^{-i\omega\beta_1}\right\} = 0$$

$$(4.1)$$

where α, β_1 and β_2 are given by equation (2.28). Clearly, when $R_1(0) = 1$ and $R_2(L) = -1$, equation (1) is simplified to equation (2.20). Making use of $\omega^i = \left(\omega_0^i + \omega_c^i\right) + i Im\left(\omega^i\right)$, like we did in § 4.1.1 of chapter 2, the exponential terms in the equation (1) can be expanded as,

$$e^{ik\beta_1} = e^{i\left(\omega_0^i + \omega_c^i + i Im\left(\omega^i\right)\right)\beta_1} = e^{-Im\left(\omega^i\right)\beta_1}\left\{\cos\left(\left(\omega_0^i + \omega_c^i\right)\beta_1\right) + i\sin\left(\left(\omega_0^i + \omega_c^i\right)\beta_1\right)\right\}.$$

$$(4.2)$$

Making a substitution as per equation (2) in equation (1), the resultant equation can be further simplified at the neutral curve. At the neutral curve, the growth rate is equal to 0, $Im\left(\omega^i\right) = 0$, when $n = n_{th}^i$, and thus, $\omega^i = \left(\omega_0^i + \omega_c^i\right)$. The real part of equation (1) at the neutral curve can be written as,

$$(1+\alpha)(1 - R_1(0)R_2(L))\cos\left(\omega^i\beta_1\right) + (1-\alpha)(R_2(L) - R_1(0))\cos\left(\omega^i\beta_2\right)$$
$$- n_{th}^i \left[\begin{array}{l} \cos\left(\omega_c^i\tau\right)\left\{(1 - R_1(0)R_2(L))\cos\left(\omega^i\beta_1\right) + (R_2(L) - R_1(0))\cos\left(\omega^i\beta_2\right)\right\} \\ -\sin\left(\omega_c^i\tau\right)\left\{(1 + R_1(0)R_2(L))\sin\left(\omega^i\beta_1\right) + (R_2(L) + R_1(0))\sin\left(\omega^i\beta_2\right)\right\} \end{array}\right] = 0$$

$$(4.3)$$

And, the imaginary part of equation (1) can be written as,

$$(1+\alpha)(1+R_1(0)R_2(L))\sin(\omega\beta_1)+(1-\alpha)(R_2(L)+R_1(0))\sin(\omega\beta_2)$$

$$-n_{th}^i\left[\begin{array}{l}\cos(\omega_c^i\tau)\{(1+R_1(0)R_2(L))\sin(\omega\beta_1)+(R_2(L)+R_1(0))\sin(\omega\beta_2)\}\\+\sin(\omega_c^i\tau)\{(1-R_1(0)R_2(L))\cos(\omega\beta_1)+(R_2(L)-R_1(0))\cos(\omega\beta_2)\}\end{array}\right]=0.$$

(4.4)

In general, solving equations (3) and (4) is not straightforward. The equations can be solved analytically under some assumptions on $R_1(0)$ and $R_2(L)$. One of the options was used in § 4.1 of chapter 2 for the case of a closed-open combustor. It is obvious that for an ideal closed-open combustor, $R_1(0)=1$ and $R_2(L)=-1$. In that case, the equations simply return to the form prescribed by equations (2.33) and (2.29). Equation (2.29) shows that on the neutral curve, the intrinsic instability frequency becomes independent of the combustor parameters. Interestingly however, these are not the only end conditions for which this kind of decoupling of instability frequency from combustor parameters takes place. A close observation of equations (3) and (4) suggests that this kind of decoupling can also occur for different end conditions. For example, when $R_1(0)=-1$ and $R_2(L)=-1$, that is when both ends of the combustor are open, equation (3) also manifests decoupling of the intrinsic instability frequency from the combustor parameters. An identical thing happens when both ends of the combustor are closed, that is $R_1(0)=1$ and $R_2(L)=1$. But clearly, this particular scenario is of little practical interest for the present design of combustors. Nonetheless, it should not be neglected as there might be possible applications of this case in other fields of interest. We will, however, refrain from the analytical study of this case for the time being. For decoupling, , in either equation (3) or (4), other terms, apart from one term containing $\sin(\omega_c^i\tau)$ or $\cos(\omega_c^i\tau)$, need to vanish. Thus, we only get certain combinations of $R_1(0)$ and $R_2(L)$ for which

multiple multipliers, containing $R_1(0)$ and $R_2(L)$ terms in equations (3) or (4), vanish. These combinations are: (i) $R_1(0)=1, R_2(L)=-1$, (ii) $R_1(0)=-1$, $R_2(L)=-1$ and (iii) $R_1(0)=1$, $R_2(L)=1$. Any other combination of reflection coefficients (including the ones with imaginary parts due to acoustic losses at the ends) prohibits decoupling on the neutral curve.

Hence, we have identified that the phenomenon of the decoupling of intrinsic instability frequency from the combustor parameters is not restricted to closed-open combustors alone. This phenomenon exists for another type of combustor design. For example, a combustor with open-open end condition. Thus, it is possible to find the key properties of the flame intrinsic mode (that is instability frequency, the n-threshold for instability, growth rate) for a combustor with open-open end conditions. This chapter is dedicated to that study.

The current chapter is organized as follows: In **§ 2** we develop the mathematical model to derive the acoustic dispersion relation for a combustor with open-open end conditions, assuming cross-section and temperature jump across the flame. We also show the existence of two solutions, similarly to § 3.1 of chapter 2, and the similarity of the intrinsic flame mode expression in the asymptotic limit of small n for any combustor. In **§ 3** we consider the decoupling of the intrinsic mode from the combustor parameters for the case of an open-open combustor. Then, we derive the n-threshold for the intrinsic mode to become unstable, which leads to neutral curves on $n-\tau$ plane. Further, we arrive at an expression of linear growth/decay rate for the intrinsic mode near the neutral curve. The numerical validation of the analytical results of § 3 is performed in **§ 4**, where we also examine the acoustic and intrinsic modes in the complex frequency plane. In **§ 5**, we study the effect of various

combustor parameters such as flame location, cross-section jump and temperature jump on the neutral curves and growth rates. Similar to chapter 3, we explain the intrinsic mode-acoustic mode coupling phenomenon for a combustor with open-open end conditions in **§ 6**. We also identify a special flame location within the combustor, where acoustic and intrinsic modes are naturally decoupled from each other. In **§ 7,** we highlight the salient similarities and differences between the flame intrinsic instability of a closed-open combustor and that of a combustor with open-open end conditions. Finally, we make some concluding comments in **§ 8**.

4.2. Mathematical model for a combustor with open-open end conditions: Derivation of the dispersion relation

In chapter 2, we focused on the analytic study of flame intrinsic instability for a closed-open combustor. In this chapter, we focus our attention on the study of intrinsic flame instability for a combustor with open-open end conditions. Again, as we came across in a short discussion in § 1 of chapter 2, the open end assumption for the acoustic end of a combustor is an idealization, which has its own limitations for practical gas turbine combustor assembly [Lamarque and Poisnot (2008)]. However, this simplified assumption is suitable to delve into the basic physics of the intrinsic flame modes inside the combustor. Hence, we confine our study to the 1-D analytical formulation of an open-open combustor, based upon the $n - \tau$ model and develop physical insight into the stability behavior of flame intrinsic instability in multi-dimensional parameter space, in a similar fashion to the closed-open combustor. In the interim stages, we identify and discuss the salient similarities and differences between the stability behavior of intrinsic flame modes for a closed-open and an open-open combustor.

Figure 1 provides a schematic sketch of an open-open combustor with a compact heat source at $x = x_q$, with x being the longitudinal coordinate with the origin at the left open end of the combustor. $A_1, A_2/B_1$ and B_2 are the pressure amplitudes for the forward/backward going waves in the upstream and the downstream region respectively. The mean temperature is assumed to jump from T_1 to T_2 across the flame. The cross-sectional area jumps across the flame from S_1 to S_2. The effect of mean flow is neglected in this analysis.
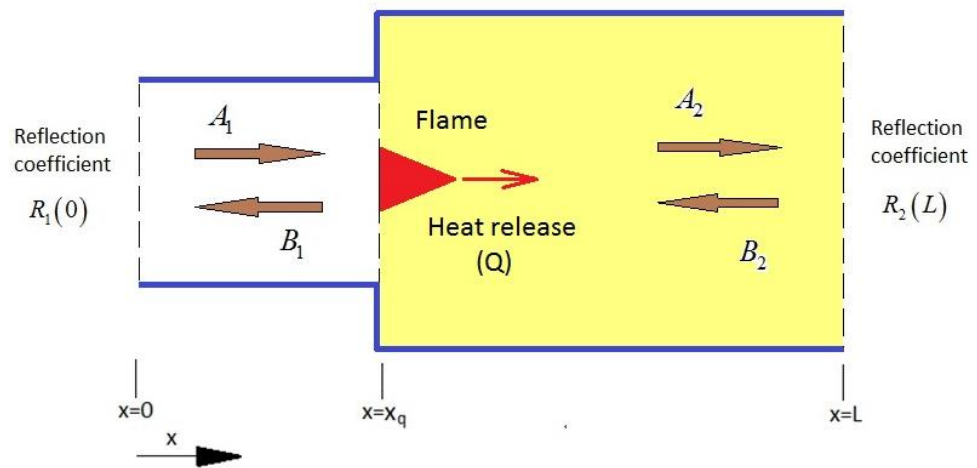
Figure 4.1: Schematic sketch of a combustor with open-open end conditions. The combustor has a cross-sectional area jump at the flame location $x = x_q$. Thick brown arrows symbolize the forward/ backward traveling waves upstream/downstream of the flame. A shaded yellow region marks the domain of higher temperature after the temperature jump across the flame.

The acoustic pressure and particle velocity at the upstream region and at the downstream region of the flame can be written with the help of equations (2.1) and (2.2). However, the boundary condition on the left will be different to the one in § 2 of chapter 2. For open-open combustor, the boundary conditions at two ends can be represented as follows:

$$\text{at } x = 0, \ A_1/B_1 = R_1(0) = -1, \text{ and}$$

189

$$\text{at } x = L, \ B_2 e^{-ikL} \big/ A_2 e^{ikL} = R_2(L) = -1. \tag{4.5, 4.6}$$

The pressure and mass balance at $x = x_q$ can be written in an identical way to equations (2.13) and (2.16) and the heat release rate at $x = x_q$ is given by $\tilde{Q}(t)$. Similar to § 2 of chapter 2, it is assumed that the heat source acts like a monopole with a volume outflow $(\gamma - 1)(\tilde{Q}/\rho c_1^2)$, where γ represents the ratio of specific heats of air (c_p / c_v). The linear heat release law can be assumed to be of the $n - \tau$ form specified in equation (2.17) [Truffin and Poinsot (2005)]. Here, n and τ are the interaction index and time lag respectively. In the frequency domain, this can be written as per the form provided in equation (2.18). The set of homogeneous equations for A_1, B_1, A_2 and B_2 is presented in the following matrix form similar to equation (2.19).

$$\begin{bmatrix} 1 & 1 & 0 & 0 \\ e^{ik_1 x_q} & e^{-ik_1 x_q} & -e^{ik_2 x_q} & -e^{-ik_2 x_q} \\ \left(1 + ne^{i\omega\tau}\right)e^{ik_1 x_q} & \left(-1 - ne^{i\omega\tau}\right)e^{-ik_1 x_q} & -\left(\frac{S_2}{S_1}\right)\left(\frac{\rho_1 c_1}{\rho_2 c_2}\right)e^{ik_2 x_q} & \left(\frac{S_2}{S_1}\right)\left(\frac{\rho_1 c_1}{\rho_2 c_2}\right)e^{-ik_2 x_q} \\ 0 & 0 & -e^{ik_2 L} & -e^{-ik_2 L} \end{bmatrix} \begin{Bmatrix} A_1 \\ B_1 \\ A_2 \\ B_2 \end{Bmatrix} = \begin{Bmatrix} 0 \\ 0 \\ 0 \\ 0 \end{Bmatrix}$$

$$\tag{4.7}$$

We hereafter arrive at a compact dispersion relation, which provides the basis of all analytical derivations in the subsequent sections. For a nontrivial solution of the eigen-value problem (7) to exist the determinant of the 4×4 matrix in (7) must be zero, which yields

$$\left[(S_2/S_1)(\rho_1/\rho_2)(c_1/c_2) + 1\right]\sin\left((k_2 - k_1)x_q - k_2 L\right) +$$
$$\left[(S_2/S_1)(\rho_1/\rho_2)(c_1/c_2) - 1\right]\sin\left(k_2 L - (k_1 + k_2)x_q\right) + 2ne^{i\omega\tau}\cos k_1 x_q \sin k_2(x_q - L) = 0.$$

$$\tag{4.8}$$

We denote the function on the left-hand side of transcendental equation (8) as detuning $g(\omega)$. Thus, dispersion relation (8) can be re-written compactly as,

$$g(\omega) = 0. \tag{4.9}$$

The dispersion relation can be simplified for special cases, when there is no cross-section and temperature jumps across the flame, that is $S_1 = S_2$ and $T_1 = T_2$, and thus $c_1 = c_2$, $\rho_1 = \rho_2$ and $k_1 = k_2 = k$. Eventually, the dispersion relation (8) reduces to

$$\sin kL - ne^{i\omega\tau} \cos kx_q \sin k(x_q - L) = 0. \tag{4.10}$$

The dispersion relation (10) can be further simplified, when the flame is located exactly in the center of the combustor, i.e. at $x_q = L/2$. This case will be examined in § 6.4.

A solution of the dispersion relation (8) and (10) generates the eigen-frequencies ω of the system. Equation (8) describes the most general case (an open-open combustor with a cross-section and temperature jump across the flame), while equation (10) is the reduced versions of (8) for special cases. The real part of ω is the frequency and the imaginary part is the growth/decay rate. The nature of this dispersion relation (8) and (10) makes them convenient for analytical study. There is no method to directly solve these transcendental equations for all combustor parameters. However, as explained in § 4.1 of chapter 2, these equations allow factorization on the neutral curve and we can extract useful information about modal frequency and growth rate near the neutral curve.

4.2.1. Acoustic and flame intrinsic modes in a combustor with open-open end condition

As we have shown in § 3 of chapter 2, in the asymptotic limit of small n there are always an infinite number of strongly decaying flame intrinsic modes in a closed-open combustor. These modes are independent of the acoustic modes and in the limit of small n, these modes do not feel the combustor boundaries and other parameters of the system. It is important to understand whether these features hold for the other types of combustor as well. We use the generalized dispersion relation (1) as the starting point for our subsequent analysis. It is important to remember that there is no general method enabling one to solve transcendental equations of this type. However, with the assumption that intrinsic flame modes have large decay rates in the asymptotic limit of small n (as observed in § 3 of chapter 2 for a closed-open combustor, manifested in the mode shapes for small n in § 3 of chapter 3 and also will be shown numerically in the subsequent sections of the current chapter), we will be able to obtain an analytical expression for the intrinsic mode frequency in the limit of small n for any combustor with the $n-\tau$ flame model.

We start the analytical study in this section with the generalized dispersion relation (1). Multiplying both sides of (1) by $e^{i\omega\beta_1}$, we arrive at,

$$(1+\alpha)\left\{e^{2i\omega\beta_1} - R_1(0)R_2(L)\right\} + (1-\alpha)\left\{R_2(L)e^{i\omega(\beta_1+\beta_2)} - R_1(0)e^{i\omega(\beta_1-\beta_2)}\right\} + ne^{i\omega\tau}$$
$$\left\{e^{2i\omega\beta_1} + R_2(L)e^{i\omega(\beta_1+\beta_2)} - R_1(0)e^{i\omega(\beta_1-\beta_2)} - R_1(0)R_2(L)\right\} = 0$$

$$\text{(4.11)}$$

By the same reasoning (as for a closed-open combustor in § 3.1 of chapter 2 and also supported by the mode shapes examined in § 3 of chapter 3), the solution for the intrinsic modes for the full dispersion relation (8) must have a large negative

imaginary part. Thus, for these new roots, all the exponents in (11) (that is, $2i\omega\beta_1$, $i\omega\left(\beta_1+\beta_2\right)$ and $i\omega\left(\beta_1-\beta_2\right)$) are highly negative as well. Hence, for small n,

$$e^{2i\omega\beta_1} \to 0, \; e^{i\omega(\beta_1+\beta_2)} \to 0, \; e^{i\omega(\beta_1-\beta_2)} \to 0.$$

Then dispersion relation (11) reduces to the following simplified form that exhibits decoupling of intrinsic modes in the limit of small n from the effect of combustor end conditions $R_1(0)$ and $R_2(L)$,

$$\left[\left(\alpha+1\right)+ne^{i\omega\tau}\right]R_1(0)R_2(L)=0. \tag{4.12}$$

Equation (12) is indeed consistent with our observations of mode shapes made in § 3 of chapter 3, where we found that in the limit of small n, intrinsic modes are so localized that they do not feel the acoustic boundaries. Equation (12) leads us to an explicit dispersion relation for intrinsic modes in the limit of small n, valid for any combustor,

$$\left(\alpha+1\right)+ne^{i\omega\tau}=0. \tag{4.13}$$

Equation (13) generates the explicit solution for intrinsic mode frequency in the asymptotic limit of small n as follows,

$$\omega=\left(2m^i+1\right)\left(\pi/\tau\right)-\left(i/\tau\right)\ln\left[\left(\alpha+1\right)/n\right]\approx\left(2m^i+1\right)\left(\pi/\tau\right)+\left(i/\tau\right)\ln\left(n\right). \tag{4.14}$$

Here, m^i is the mode number of the flame intrinsic modes. As expected, the expression for the modal frequency of any combustor in the limit of small n, as given by equation (14), is the same as equation (2.26) for a closed-open combustor and the result provided by Hoeijmakers et al. (2014) for an infinite tube with a flame inside. The salient features of (14) are that the modal frequencies for the intrinsic mode do not depend on any parameters of the combustor including the end conditions. Another salient feature is that the intrinsic modes have their own mode numbers, completely

independent of the mode numbers of the acoustic modes. In the limit of small n there is always an infinite number of intrinsic modes present in the system for any n and τ. In the limit of small n, these modes are equally spaced. The real part of the flame intrinsic mode frequency depends solely on the time lag and is given by the expression, $\left(2m^i + 1\right)\left(\pi/\tau\right)$. The decay rates are independent of the mode number (m^i), inversely proportional to τ and logarithmically dependent on n and the temperature and cross-section jump of the combustor. These modes are heavily damped in the asymptotic limit of small n Therefore, they do not feel end conditions of the combustor, also evident from equation (12). Hence, we can say that feature-wise, the intrinsic modes behave exactly in a similar manner for any combustor in the asymptotic limit of small n.

In summary, we have obtained an analytical expression for the frequencies of the intrinsic modes for any combustor in the asymptotic limit of small n. In this asymptotic limit, intrinsic modes are independent of the end conditions of the combustor. These modes are infinite in number, independent from the acoustic modes and strongly damped in the asymptotic limit of small n. They can become unstable only once the value of n exceeds a certain threshold. The stability features and growth rates for the intrinsic modes will be discussed in the subsequent sections for the open-open combustors.

4.3.   Intrinsic flame instability: Neutral curves and growth rates

In the previous section, we mentioned that in the limit of small n the flame intrinsic modes are strongly decaying. However, as we increase n, the decay rate decreases, reaching zero at some threshold value of n, making the intrinsic mode unstable. It is

possible to find the instability frequency, the threshold of n for instability and the growth rate for flame intrinsic modes. This section is dedicated to this. In § 3.1, we find the exact analytical expression for the intrinsic mode frequency at the neutral curve. Then, in § 3.2, we will find the exact threshold value of n for intrinsic mode instability and also find the neutral curve in the $n - \tau$ parameter space. Finally, in § 3.3, we evaluate the linear growth/decay rates near the neutral curve.

4.3.1. Decoupling on the neutral curve

On the complex frequency plane, the intrinsic mode locus can be tracked as we increase n and at certain threshold value of n, these modes become unstable. Let us now denote ω_c^i as the discrepancy between the eigen-frequency ω^i and ω_0^i, the small n prediction given by a real part of (2.26). Like in § 4.1 of chapter 2, here we do not *a priori* assume ω_c^i / ω_0^i to be small in our analysis. In a similar way to § 4.1 of chapter 2, we can use the following expression of ω^i in the dispersion relation (8),

$$\omega^i = \left(\omega_0^i + \omega_c^i\right) + iIm\left(\omega^i\right),$$

and thus, the complete dispersion relation (8) can be re-written as,

$$(\alpha+1)\sin\left\{\left(\omega_0^i + \omega_c^i + iIm\left(\omega^i\right)\right)\beta_1\right\} + (\alpha-1)\sin\left\{\left(\omega_0^i + \omega_c^i + iIm\left(\omega^i\right)\right)\beta_2\right\}$$
$$+2ne^{i\left(\omega_0^i + \omega_c^i + iIm\left(\omega^i\right)\right)\tau}\cos\left\{\left(\omega_0^i + \omega_c^i + iIm\left(\omega^i\right)\right)x_q/c_1\right\}$$
$$\sin\left\{\left(\omega_0^i + \omega_c^i + iIm\left(\omega^i\right)\right)\left(x_q - L\right)/c_2\right\} = 0 \tag{4.15}$$

where α, β_1 and β_2 are given by equation (2.28). We can use the identity, $e^{i\omega_0^i\tau} = -1$ and simplify equation (15) further. By definition, $Im\left(\omega^i\right)$ is equal to zero for the threshold value of n, i.e. $Im\left(\omega^i\right) = 0$ at $n = n_{th}^i$. This specifies the neutral

curve, as already mentioned in § 4.1 of chapter 2. Thus, on the neutral curve, the real part of (15) reduces to,

$$2in_{th}^i \sin\left(\omega_c^i \tau\right)\cos\left(k_1 x_q\right)\sin\left(k_2\left(x_q - L\right)\right) = 0. \tag{4.16}$$

It is easy to see that this equation is factorized. It is satisfied when just one multiplier containing ω_c^i vanishes, that is,

$$\sin\left(\omega_c^i \tau\right) = 0. \tag{4.17}$$

This gives us a simple explicit expression for ω_c^i,

$$\omega_c^i = m\pi/\tau, \tag{4.18}$$

where m is an integer (not to be confused with the intrinsic mode number m^i). Making use of ω_c^i, as per (18), the frequency for the neutral intrinsic mode can be calculated using $Re\left(\omega^i\right) = \omega_0^i + \omega_c^i$, which leads to (on the neutral curve $\omega^i = Re\left(\omega^i\right)$),

$$\omega^i = \left(2m^i + 1\right)\left(\pi/\tau\right) + \left(m\pi/\tau\right). \tag{4.19}$$

Again, based on extensive (but not comprehensive) numerical analysis of the full dispersion relation (8), we hypothesize that $\omega_c^i \tau \le 2\pi$, otherwise any ω_c^i deviation $2\pi/\tau$ would correspond to a change of modal identity. Therefore, we assume ω_c^i to follow a similar condition to one for a closed-open combustor, prohibiting such an exchange of identities,

$$-2\pi/\tau < \omega_c^i < 2\pi/\tau.$$

According to (18), on the $m = 0$ part of the neutral curve on the $n - \tau$ plane, $\omega_c^i = 0$. This suggests an identical frequency corresponding to the value predicted in the limit

of small n. As per the explanation in the previous paragraph, apart from the $m=0$ option, we have only two other possibilities, namely $m=\pm 1$, which means an intrinsic mode frequency shift by a factor π/τ on either side of ω_0^i.

4.3.2. The threshold of n for intrinsic instability: Exact solution for the neutral curve

The exact solution for the threshold of n (n_{th}^i) for the intrinsic mode to become unstable in the $n-\tau$ plane will be derived in this section. For each intrinsic mode, we generate neutral curves, which represent the boundaries of stability domains on the $n-\tau$ plane.

Making use of equation (18) for ω_c^i, the imaginary part of (15) on the neutral curve can be rewritten as,

$$(\alpha+1)\sin\left\{\left(\omega_0^i+\omega_c^i\right)\beta_1\right\}+(\alpha-1)\sin\left\{\left(\omega_0^i+\omega_c^i\right)\beta_2\right\}-$$
$$2n_{th}^i\cos\left(\omega_c^i\tau\right)\cos\left(k_1 x_q\right)\sin\left\{k_2\left(x_q-L\right)\right\}=0 \quad , \qquad (4.20)$$

which yields us the threshold n_{th}^i,

$$n_{th}^i = \frac{(\alpha+1)\sin\left\{\left(\omega_0^i+\omega_c^i\right)\beta_1\right\}+(\alpha-1)\sin\left\{\left(\omega_0^i+\omega_c^i\right)\beta_2\right\}}{2\cos\left(\omega_c^i\tau\right)\cos\left(k_1 x_q\right)\sin\left\{k_2\left(x_q-L\right)\right\}}, \qquad (4.21)$$

where α, β_1 and β_2 are provided by (2.28). Primarily, we examine the same special case of $x_q=L/2$ as for closed-open combustors. In this case, expression (21) can be significantly simplified. For the segment of the neutral curve corresponding to $\omega_c^i\tau=0$, we find

$$n_{th,(0)}^i = 2. \qquad (4.22)$$

197

For the segments of the neutral curve corresponding to $\omega_c^i \tau = \pi$ and $\omega_c^i \tau = -\pi$ the

expressions for n_{th}^i take the form

$$n_{th,(\pi)}^i = -2, \text{ and } n_{th,(-\pi)}^i = -2 . \qquad \text{(4.23 a,b)}$$

Thus, when the flame is located in the middle of the combustor with open-open end

conditions, the threshold of n is clearly independent of the flame location and attains

a constant value of 2 on the neutral line segment $\omega_c^i \tau = 0$. Of course, at this flame

location, the threshold of n is negative on the neutral line segments $\omega_c^i \tau = \pi$ and

$\omega_c^i \tau = -\pi$ as per equation (23). This aspect is completely different when compared

to the combustor with closed-open end conditions, where the threshold of n depends

on the flame location in the middle of the combustor as well, an observation that was

made in § 4.2 of chapter 2. Equation (21) stipulates that the threshold of n is 1 when

$x_q = 0$ on the neutral curve segment $\omega_c^i \tau = 0$ and -1 on the neutral curve segments

$\omega_c^i \tau = \pi$ and $\omega_c^i \tau = -\pi$. Thus, the threshold of n increases as the flame is moved

away from the flame location $x_q = 0$ to $x_q = L/2$. This is indeed a general trend and

it will be shown in the subsequent sections, as we move the flame location from

$x_q = 0$ to $x_q = L$, the maximum value of the n-threshold on the neutral loop on the

extreme right increases.

Figure 2 (a) shows a neutral curve for the second intrinsic mode of an open-open

combustor when the flame is situated at $x_q = L/3$. The blue, red and green are used

to plot the neutral curve segments corresponding to $\omega_c^i \tau = 0$, $\omega_c^i \tau = \pi$ and

$\omega_c^i \tau = -\pi$ respectively. The continuous lines indicate intrinsic modes and the dashed

lines are for the coupled acoustic modes. However, near the intersection points of neutral line segments, the modes invariably change their identity, which will be validated in the numerical section. Indeed, this aspect is similar to that of a combustor with closed-open end conditions discussed in § 4.2 of chapter 2. The yellow area represents the instability domain for the intrinsic mode. The hatched area indicates the domain with multiple instability islands, narrowing as τ decreases. It can be seen that there are some apparent similarities between the neutral curves for the second intrinsic mode for a combustor with open-open end conditions and closed-open end conditions. Each neutral loop is a combination of neutral segments $\omega_c^i \tau = 0$, $\omega_c^i \tau = \pi$ and $\omega_c^i \tau = -\pi$, except the loop on the extreme right, which is created by a combination of $\omega_c^i \tau = 0$ and $\omega_c^i \tau = \pi$ (the segment corresponding to $\omega_c^i \tau = -\pi$ does not feature in this loop). Moreover, in contrast to figure 2.8, the n-threshold saturates for higher time lags, making the intrinsic instability a possibility for any mode for large τ. This feature is distinctively different from a combustor with closed-open end conditions, where each mode becomes linearly stable when the time lag exceeds a certain value. The n-threshold value at the point of saturation can be seen to be higher than that of a combustor with closed-open end conditions, where the maximum n-threshold was found to be 1 when the flame is located at $x_q = L/2$. Indeed, in the case of open-open end conditions, the saturated values of n-threshold can be obtained from equation (21) under the assumption of large time lag. With the assumption that $\sin(\gamma) \approx \gamma$ and $\cos(\gamma) \approx 1$, for small γ, the saturated value of n-threshold comes out to be,

$$n_{th}^i = \frac{\left[(\alpha+1)\beta_1 + (\alpha-1)\beta_2\right]c_2}{2(x_q - L)}. \tag{4.24}$$

It can further be shown from (24) that the saturated value of n-threshold increases as x_q increases.
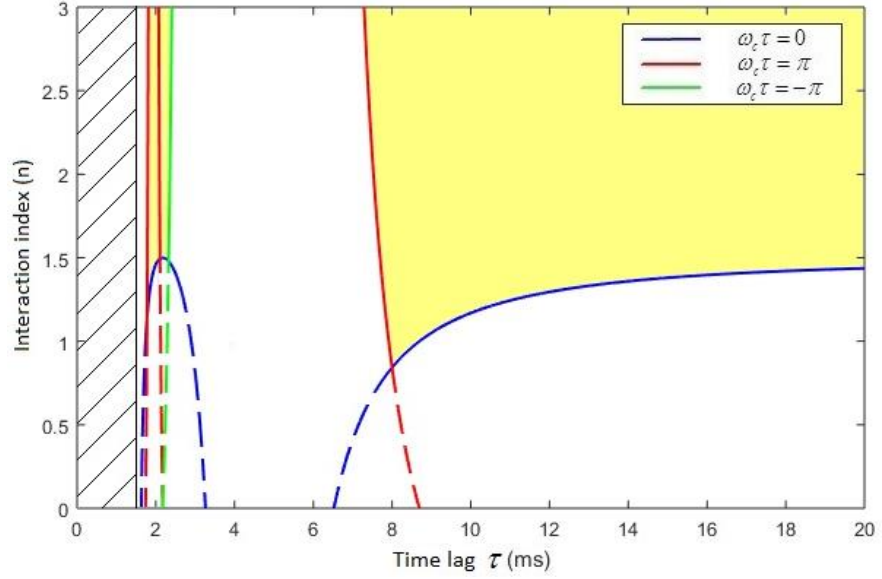
Figure 4.2(a): Neutral curve and stability domain on the $n-\tau$ plane for the second intrinsic mode ($m^i=1$) of an open-open combustor. The instability domain is marked in yellow. Blue, red and green lines correspond to the segments $\omega^i_c \tau = 0$, $\omega^i_c \tau = \pi$ and $\omega^i_c \tau = -\pi$ of the neutral curve respectively. The solid lines show segments of the neutral curve for the second intrinsic mode. The dashed lines show their continuations which are also exact solutions of (21); we interpret them as neutral curves for acoustic modes coupled to the intrinsic mode. The hatched area indicates the domain with multiple instability islands, narrowing as τ decreases. The specific values of the parameters used are the parameters of the test rig at IIT Madras (Vishnu et al. (2015), Vishnu (2013)): the length L is 0.75 m, the cross-section S is 0.0016 m², the temperature T is assumed as constant throughout the duct and equal to 297 K (We neglect temperature jump across flame for this figure). The flame is located at $x_q = L/3$

, $c_1 = c_2 = 345$ m/s.

Figure 2 (b) is an extension of figure 2 (a) showing that the neutral loops on the left of the neutral curve are indeed a repetitive structure. In figure 2 (a) we have shown only two neutral loops, whereas in figure 2 (b) we have shown 3 neutral loops. Similar to the combustor with closed-open end conditions, in the case of the combustor with open-open end conditions there are an infinite number of smaller neutral loops on the left of these three loops in figure 2 (b). This infinite number of closely spaced loops is

hidden by hatched lines. All the subsequent discussions will be mainly focused on the neutral loop existing on the extreme right.
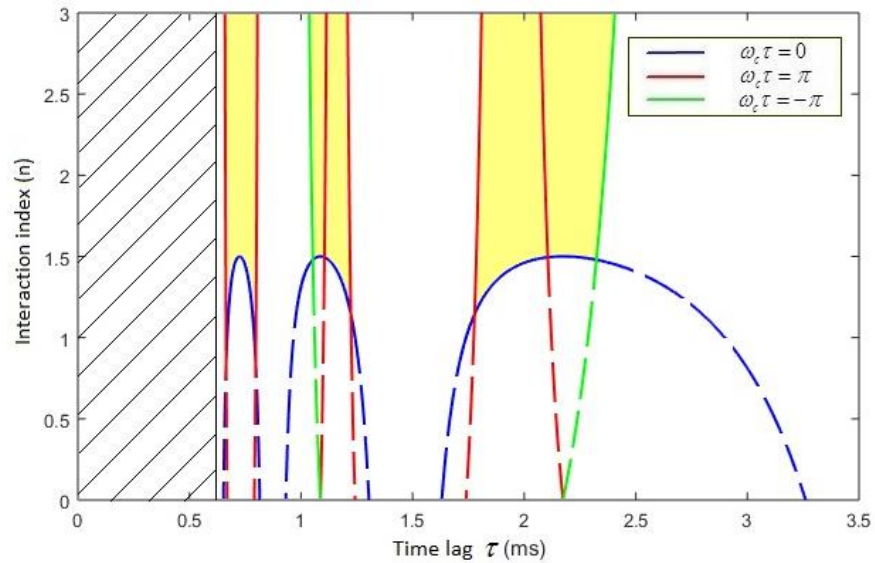
Figure 4.2(b): Neutral curve and stability domain on the $n - \tau$ plane for the second intrinsic mode (m^i =1) of an open-open combustor. The figure is the same as figure 2 (a) but on a different scale. The figure is extended to show more of the domains with multiple instability islands, narrowing as τ decreases.
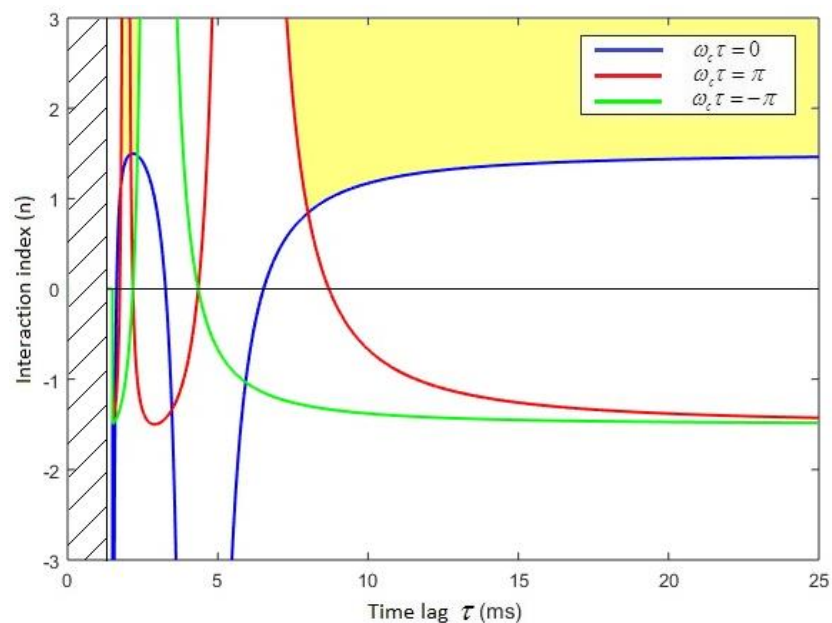
Figure 4.2(c): Neutral curve and stability domain on the $n - \tau$ plane for the second intrinsic mode (m^i =1) of an open-open combustor. The figure is the same as figure 2 (a) but on a different scale. This figure is intended to depict that the n-threshold attains negative values for certain time lags. However, as n-threshold cannot practically be a negative number, the negative portion of the neutral loop segments will be truncated in all the subsequent figures.

At this point, it is important to mention that like for the closed-open combustor, the analytical solution (21) can also generate a negative n-threshold for open-open combustors. This aspect is illustrated by figure 2 (c), which extends figure 2 (a) into the domain of negative n. Obviously, the negative n-threshold is non-physical, but an extended $n - \tau$ plane gives a better idea of how segments of the neutral curve are related. However, from now on we will concentrate only on the positive part of the $n - \tau$ plane.

Figures 3 (a) and (b) show the neutral curves for the second intrinsic mode of an open-open combustor for two different flame locations, $x_q = 0.1$ m and $x_q = 0.4$ m respectively. In comparison to figure 2, figures 3 (a) and 3 (b) differ in a couple of notable features. The first distinctive feature is the shape of the neutral curve corresponding to $\omega_c^i \tau = 0$. In figure 2 (a), the neutral curves corresponding to $\omega_c^i \tau = 0$ have finite values of n-threshold, whereas in figure 3 (a), the neutral loop on the left and for 3 (b), the neutral loop on the right are not confined and bounded everywhere. Theoretically, this indicates that there is an infinite value of n-threshold for certain time lags. Another important distinctive feature of figures 3 (a) and (b) is the domain of coupling of the intrinsic and acoustic mode. The domain of coupling is much narrower (bounded by two red lines due to $\omega_c^i \tau = \pi$) compared to figure 2, where there is only one neutral line due to $\omega_c^i \tau = \pi$ on the extreme right neutral loop and the domain of coupling is all the way from the left of the neutral segment $\omega_c^i \tau = \pi$ to the left end of the extreme right neutral loop. Indeed, the flame location $x_q = L/3$ is a special case when the domain of coupling is not narrow and there exists only one neutral curve segment $\omega_c^i \tau = \pi$ on the extreme right neutral loop. For all other flame

locations, two neutral curve segments $\omega_c^i \tau = \pi$ exist, making the domain of coupling much smaller. It is important to mention at this point that by the domain of coupling, we mean type 1 and 2 coupling as explained in chapter 3. Apart from these two types, one would suspect that would also have coupling types 3 and 4 in combustors, details of which will be discussed in § 6. Moreover, the maximum n-threshold in figure 3 (b) (for $x_q = 0.4$ m) is higher than in 2 (a) (for $x_q = L/3 = 0.25$ m), which is again higher than in figure 3 (a) (for $x_q = 0.1$ m). Hence the maximum n-threshold increases as x_q increases.

Figure 4 shows the neutral curve for the first intrinsic mode when $x_q = L/3$. Clearly, according to equation (21) $n_{th}^i \to \infty$ as $\omega_c^i \tau = -\pi$ for the first intrinsic mode. Hence, just like a closed-open combustor, for an open-open combustor the $\omega_c^i \tau = -\pi$ neutral curve segment does not constitute a boundary of the stability domain for the first intrinsic mode. As explained in the previous paragraph, for any flame location $x_q \neq L/3$, there exist two neutral curve segments due to $\omega_c^i \tau = \pi$ on the extreme right neutral curve, making the domain of intrinsic mode-acoustic mode coupling much narrower than that of the case when $x_q = L/3$. The complete coupling picture will be presented in § 6.
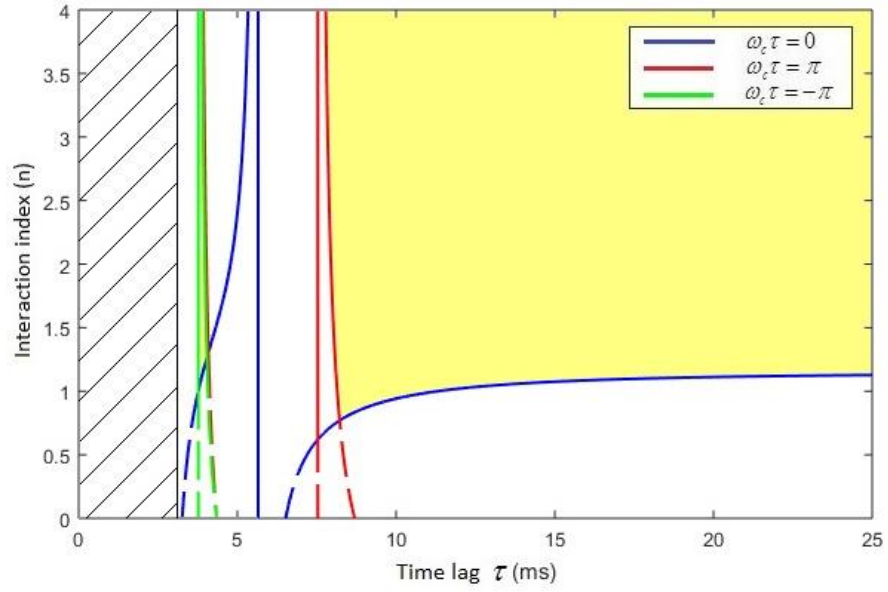
(a)
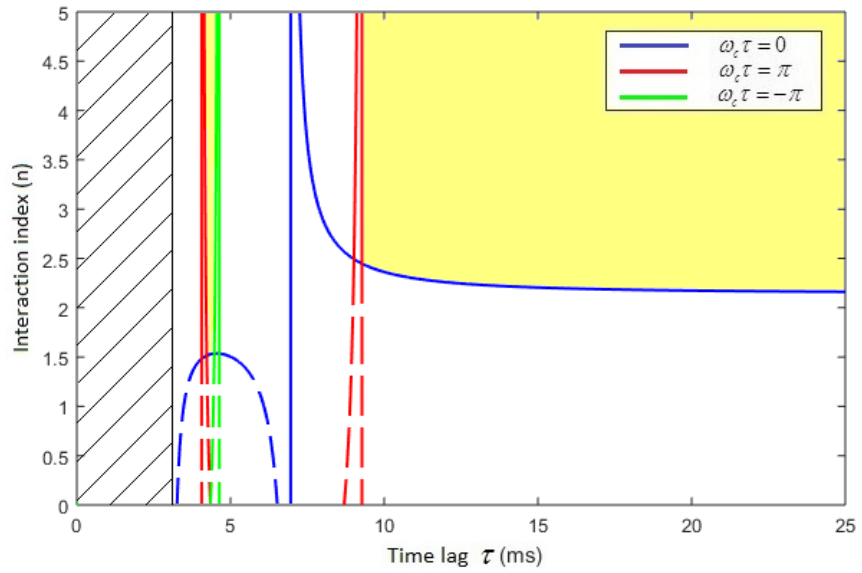
(b)

Figure 4.3: Neutral curve and stability domain on the $n-\tau$ plane for the second intrinsic mode (m^i =1) of an open-open combustor. The flame is located at (a) $x_q = 0.1$ m and (b) $x_q = 0.4$ m. The instability domain is marked in yellow. The hatched area indicates the domain with multiple instability islands, narrowing as τ decreases. Other parameters and notations are the same as in figure 2 (a).
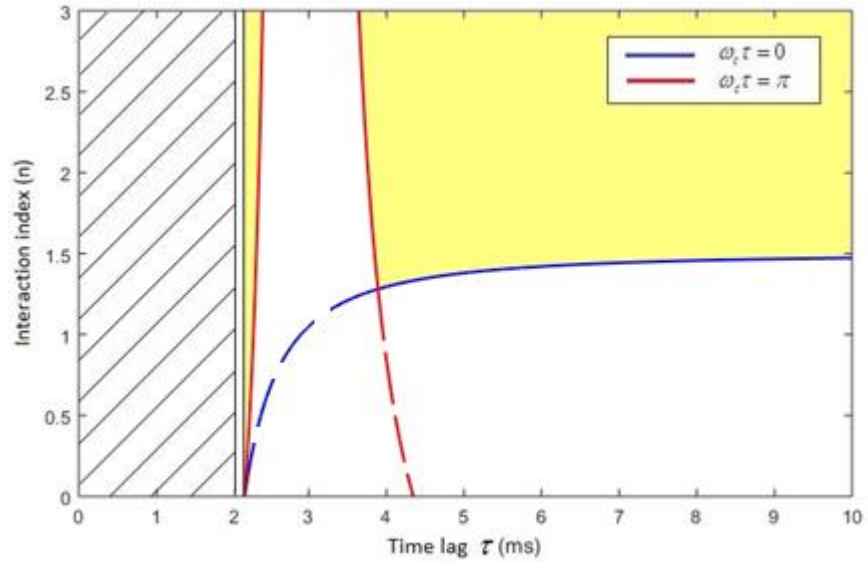
Figure 4.4: Neutral curve and stability domain on the $n - \tau$ plane for the first intrinsic mode (m^i =0) of an open-open combustor. Blue and red lines correspond to the segments $\omega_c^i \tau = 0$ and $\omega_c^i \tau = \pi$ of the neutral curve respectively. The instability domains for intrinsic modes are marked in yellow. The hatched area indicates the domain with multiple instability islands, narrowing as τ decreases. Other parameters are same as in figure 2 (a).
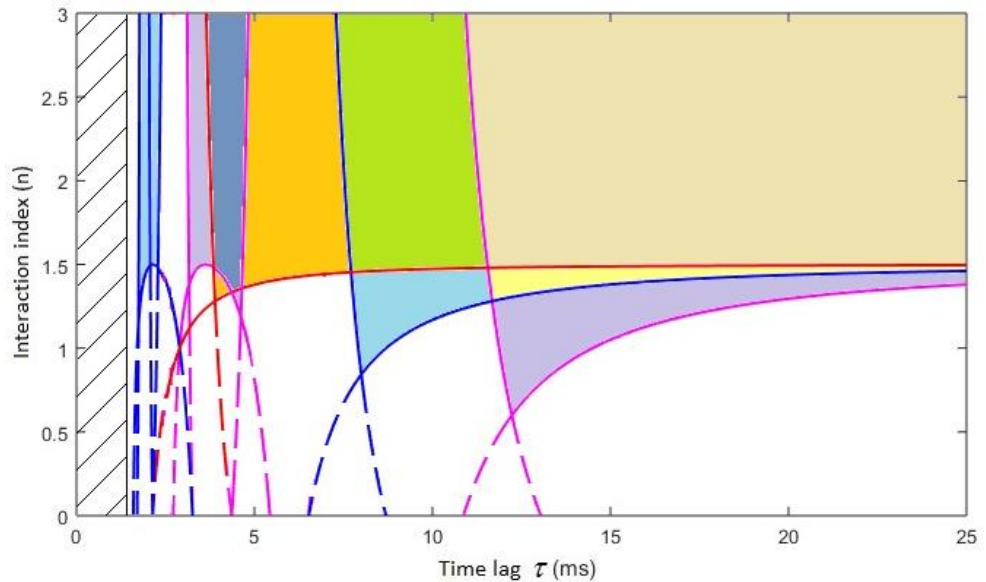
Figure 4.5: The neutral curves and stability domain on the $n - \tau$ plane for the first (m^i =0), second (m^i =1) and third (m^i =2) intrinsic modes of an open-open combustor. Red, blue and magenta colour represent the neutral curves for the first, second and third intrinsic modes respectively. The common domain of instability for the first and second modes is marked in lime, for the second and third intrinsic modes, it is marked as yellow and for first and third intrinsic modes is marked as blue-gray. The light-yellow colour represents the domain where all three modes are unstable. Gold, light turquoise, and lavender colour mark the non-overlapping domains of instability for the first, second and third intrinsic modes respectively. The notation and parameters are the same as in Fig.2.

205

Indeed, we can overlap the neutral curves for multiple intrinsic modes to get an idea about the overall instability domain similar to the case of the closed-open combustor. Figure 5 shows such a multi-mode instability map. We show the first (m^i =0), second (m^i =1) and third (m^i =2) intrinsic modes using red, blue and magenta lines respectively. The figure illustrates that (i) as the mode number m^i increases, the neutral curve main loop shifts to the right; (ii) the span of the islands of instability on the left increases; (iii) the segments corresponding to $\omega_c^i \tau = \pi$ and $\omega_c^i \tau = -\pi$ become less steep for higher modes. These tendencies are identical to those exhibited in figure 2.11 for a closed-open combustor. Another important aspect is the domain marked in light yellow in the asymptotic limit of large τ. This domain represents the common instability domain for the first three intrinsic modes. This feature is undoubtedly different from the case of a closed-open combustor, where there is no common domain of instability for all intrinsic modes (see figure 2.11 for example) and for very large τ, any intrinsic mode becomes linearly stable. For an open-open combustor, the intrinsic modes are potentially unstable even for the large time lag. The threshold of n also tends to decrease for higher order modes in the asymptotic limit of large τ and the corresponding n_{th}^i can be calculated using formula (24).

Moreover, figures 2-5 suggest, that the characteristic values of n_{th}^i are smaller than the threshold values of n for an infinite tube [Hoeijmakers et al. (2015)], an observation also made in § 4.2 of chapter 2 for a closed-open combustor. Hence, the intrinsic modes can become unstable at a much lower value of n than the theoretical prediction for an infinite tube.

Thus, we have arrived at an explicit analytical expression (21) for the neutral curves on the $n - \tau$ plane for an open-open combustor, similar to a closed-open combustor

discussed in § 4.2 of chapter 2. There are some apparent similarities between the neutral curves for intrinsic modes in a closed-open and open-open combustor. For an open-open combustor, the neutral curves for the flame intrinsic modes have two qualitatively different regions. The region on the left, i.e. for smaller values of τ, comprises loops of reducing τ widths, made of strongly coupled acoustic-intrinsic modes. Also, the region on the right exhibits a single large loop which stretches to infinity in τ. This is unlike the large neutral loop for a closed-open combustor, which ceases to exist above a certain time lag, making the mode linearly stable for large τ. For an open-open combustor, the neutral curve has three distinct segments corresponding to $\omega_c^i \tau = 0$, $\omega_c^i \tau = \pi$ and $\omega_c^i \tau = -\pi$ in the $n - \tau$ space, apart from the first intrinsic mode, where the neutral curve segments due to $\omega_c^i \tau = -\pi$ do not exist, as it predicts zero frequency and infinite n_{th}^i as per (21). The $\omega_c^i \tau = \pi$ and $\omega_c^i \tau = -\pi$ segments predict higher values of n_{th}^i compared to the $\omega_c^i \tau = 0$ segments. These segments become less steep as the mode number, m^i, increases. Unlike a closed-open combustor, for an open-open combustor we have a domain in the asymptotic limit of large τ on the $n - \tau$ plane, where the really large number of intrinsic modes are linearly unstable. The second intersection point that we see for a closed-open combustor of the neutral lines $\omega_c^i \tau = 0$ and $\omega_c^i \tau = -\pi$ does not exist for the large neutral curve loop of an open-open combustor. We can also analytically find the locations of the intersection points of the neutral curve segments $\pm \omega_c^i \tau = \pi$ and $\omega_c^i \tau = 0$ in a similar manner to that of § 4.2 of chapter 2 and Appendix I.

4.3.3.   Growth rate of intrinsic modes

The growth rate is the key element that we need to explain in combustion instability. Again, for the same reason as § 4.3 of chapter 2, we concentrate on the growth/decay rates near the neutral curve only.

We consider a point (n, τ) on the $n - \tau$ plane located very close to the neutral curve for a specific mode m^i. The deviation from the neutral curve is denoted by n_1^i, hence, $n - n_{th}^i = n_1^i << n_{th}^i$. Similar to § 4.3 of chapter 2, the eigen-frequency in the chosen point (n, τ) differs from its value on the neutral curve ω_0^i for the same τ. This deviation is denoted as ω_1^i. As per numerical observation, close to the neutral curve, the real frequency only marginally shifts. Therefore, we assume that the real part of ω_1^i is negligibly small compared to its imaginary part and of little interest near the neutral curve. The imaginary part of ω_1^i, on the other hand, represents the growth/decay rate. For any frequency perturbation ω_1^i, due to deviation n_1^i near the neutral curve, we can write the following condition,

$$\text{When, } n = n_{th}^i + n_1^i, \ \omega = \omega_0^i + \omega_1^i.$$

For simplicity, we only consider the first order term in n_1^i. Higher order corrections in n_1^i can be dealt with in an identical manner. We refrain from that exercise for the time being. Substituting these expressions for n and ω into the original dispersion relation (8) and neglecting higher order terms in ω_1^i in the sin and cos function expansions we obtain,

208

$$(\alpha+1)\left\{\sin\left(\omega_0^i\beta_1\right)+\omega_1^i\beta_1\cos\left(\omega_0^i\beta_1\right)\right\}+(\alpha-1)\left\{\sin\left(\omega_0^i\beta_2\right)+\omega_1^i\beta_2\cos\left(\omega_0^i\beta_2\right)\right\}$$

$$+2\left(n_{th}^i+n_1^i\right)\left(1+i\omega_1^i\tau\right)e^{i\omega_0^i\tau}\left\{\cos\left(\omega_0^i\,x_q/c_1\right)-\omega_1^i\left(x_q/c_1\right)\sin\left(\omega_0^i\,x_q/c_1\right)\right\}\quad.$$

$$\left\{\sin\left(\omega_0^i\left(x_q-L\right)/c_2\right)+\omega_1^i\left(\left(x_q-L\right)/c_2\right)\cos\left(\omega_0^i\left(x_q-L\right)/c_2\right)\right\}=0$$

$$(4.25)$$

Neglecting higher order terms in ω_1^i and subtracting the original dispersion relation (8) for $\omega=\omega_0^i$ from (25), we obtain a perturbed form of the dispersion relation (8), which directly yields an explicit analytical expression for the growth/decay rate ω_1^i,

$$\omega_1^i=\frac{2n_1^i e^{i\omega_0^i\tau}\cos\left(\omega_0^i\,x_q/c_1\right)\sin\left(\omega_0^i\left(x_q-L\right)/c_2\right)}{-\left[(\alpha+1)\beta_1\cos\left(\omega_0^i\beta_1\right)+(\alpha-1)\beta_2\cos\left(\omega_0^i\beta_2\right)+\Sigma\right]}.\qquad(4.26)$$

where, Σ is,

$$\Sigma=2n_{th}^i\,e^{i\omega_0^i\tau}\left\{\begin{array}{c}i\tau\cos\left(\omega_0^i\,x_q/c_1\right)\sin\left(\omega_0^i\left(x_q-L\right)/c_2\right)\\[2mm]-\left(x_q/c_1\right)\sin\left(\omega_0^i\,x_q/c_1\right)\sin\left(\omega_0^i\left(x_q-L\right)/c_2\right)\\[2mm]+\left(\left(x_q-L\right)/c_2\right)\cos\left(\omega_0^i\,x_q/c_1\right)\cos\left(\omega_0^i\left(x_q-L\right)/c_2\right)\end{array}\right\}.$$

while α, β_1 and β_2 are given by (2.28). Through a numerical examination of multiple examples, it has been observed that the real part of ω_1^i is indeed insignificant, as was assumed in the beginning of this derivation. Thus, $\omega_1^i\approx Im\left(\omega_1^i\right)$ and represents the growth/decay rate. The equation (26) shows a dependence on the combustor parameters, which is the same as for closed-open combustors.

Thus, we have found an explicit formula for the intrinsic mode growth/decay rates near the neutral curve on the $n-\tau$ plane. The growth rate formula has retained dependence on various combustor parameters. For simplicity, we only consider the first order term in n_1^i. Nonetheless, higher order corrections in n_1^i are straightforward

analytical extensions. The accuracy of the analytical results using first order terms in n_1^i will be demonstrated by comparison with the numerical solution in § 4.

4.4. Numerical validation

In this section, the analytical results of § 3 will be validated numerically. Here we examine the full dispersion relation (8) numerically. We consider the parameters of the test rig at IIT Madras (Vishnu et al. (2015), Vishnu (2013)): the length L is 0.75 m, the cross-section S is 0.0016 m², the temperature T is assumed constant throughout the duct and equal to 297 K (however in § 5, we incorporate the effect of temperature jump). The flame is located at $x_q = L/2$. The same parameters were used for plotting all the stability diagrams.

4.4.1. Place of acoustic and intrinsic modes on the complex frequency plane

In § 3.2 of chapter 2, we have demonstrated the usefulness of the contour plots of frequency detuning as a method to identify the loci of the acoustic and intrinsic modes on the complex frequency plane as we increase n. These kinds of plots are effective in finding, not only the relative positions of acoustic and intrinsic modes on the complex frequency plane for different n, but also the frequencies at which these modes become unstable. The contour plots are made using the absolute value of detuning function $g(\omega)$ prescribed in the full dispersion relation (8, 9). Figures 6-8 are such contour plots for an open-open combustor. Basic features of contour plots like these have already been explained in § 3.2 of chapter 2 for a closed-open combustor.

In figures 6-8, acoustic modes are marked with blue squares, while intrinsic modes are shown by orange triangles. The instability domain is marked in yellow. The

acoustic mode frequencies are $m_a \left(\pi c / L \right)$ (for m_a = 0, 1, 2…) and have almost zero growth in figure 6, because the n selected (n =0.025) is very close to zero. The iso-lines of the absolute value of the function $g \left(\omega \right)$ onto the complex ω plane in figures 6-8 provide the view of the whole plane. The innermost closed loops of the iso-lines are the solutions for modal frequency ω.

Figure 6 is split into two panels to represent the acoustic and intrinsic modes separately. The intrinsic modes are strongly decaying when n =0.025, thus making it reasonable to represent the acoustic and intrinsic modes in two separate panels. The time lag selected for this figure is 3 ms. The intrinsic modes in the lower panel are equally spaced in this limit of n, as predicted by equation (20). This feature is the same as that of a closed-open combustor. In contrast, the acoustic modes in the upper panel have equal spacing but a different distribution pattern than for a closed-open combustor. The fundamental frequency of an open-open combustor is twice as big than for a closed-open combustor. We also have both odd and even harmonics in an open-open combustor, whereas the closed-open combustor only supports the odd harmonics [Kinsler et al. (2000)]. All these features are well captured in contour plots 6-8 and figures 2.3-2.5 in § 3.2 of chapter 2. In figure 6, in the chosen frequency range, there are three intrinsic modes with strong decay rates, as shown in the bottom panel. In figure 7, when n is increased from 0.025 to 1.1, the first intrinsic and the second acoustic mode become unstable. The decay rates for all other intrinsic modes reduce significantly. All these features are consistent with what we observed for a closed-open combustor in § 3.2 of chapter 2.
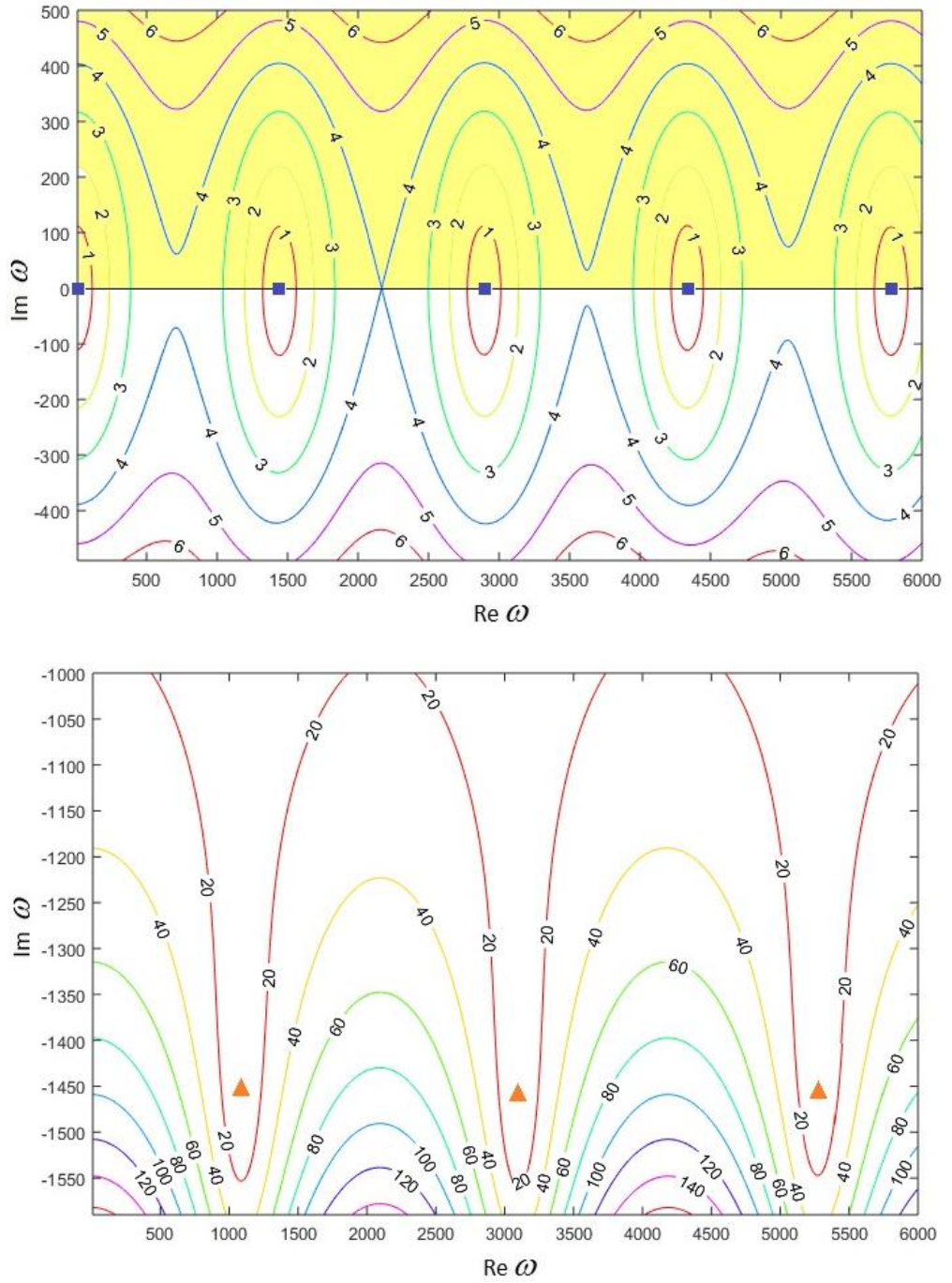
Figure 4.6: Contour plot of detuning $\left| g\left(\omega\right) \right|$ for $n = 0.025$ and $\tau = 3.0$ ms. Other parameters are the same as in Fig.2. Two sections are parts of the same contour plot. The domain of instability is marked in yellow. Blue squares and orange triangles represent the acoustic and intrinsic modes respectively.

In figure 8, when we increase the time lag further from 3 to 5 ms, the intrinsic mode frequency reduces, as is predicted by equation (14). The first acoustic and the third intrinsic modes have become unstable for this time lag. The extensive numerical

simulations show that all the intrinsic modes have the potential to become unstable beyond a certain threshold of n, as predicted by equation (21). In some cases, the acoustic mode can also become unstable at one of the nearby frequencies of the intrinsic mode in the complex frequency plane. For example, in figure 7, the second acoustic mode becomes unstable at the second intrinsic mode frequency. Clearly, this is an intrinsic-acoustic mode coupling scenario, a phenomenon that has been explained in chapter 3 for a closed-open combustor. We will shed some light on this intrinsic-acoustic mode coupling phenomenon in § 6, in the context of an open-open combustor.

Thus, like § 3.2 of chapter 2, we have shown a set of contour plots for an open-open combustor for different time lags and have shown that contour plots are effective for compact visual representation of stable/unstable modes on the complex frequency plane. Increasing n seems to reduce the decay rate of the intrinsic modes, whereas increasing τ reduces the frequencies of the intrinsic mode. All the intrinsic modes show a tendency to become unstable beyond a certain threshold value of n. In addition, for some τ, intrinsic modes can also couple to one of the acoustic modes in their close vicinity in the complex frequency plane.
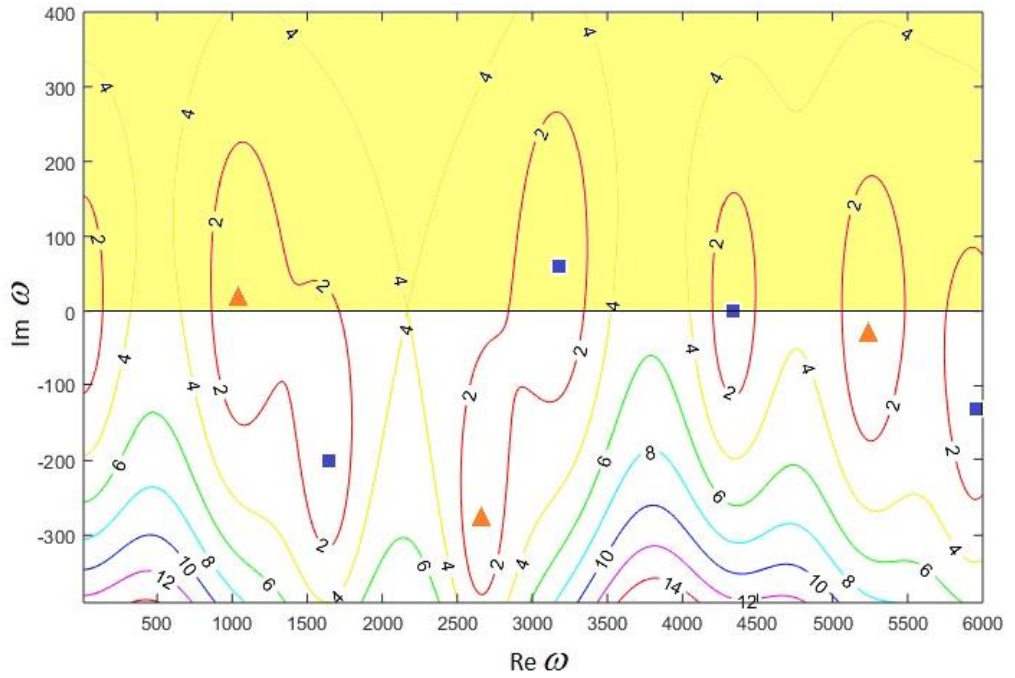
Figure 4.7: Contour plot of detuning $|g(\omega)|$ for $n = 1.1, \tau = 3.0$ ms. Notations and other parameters are the same as in Fig 6.
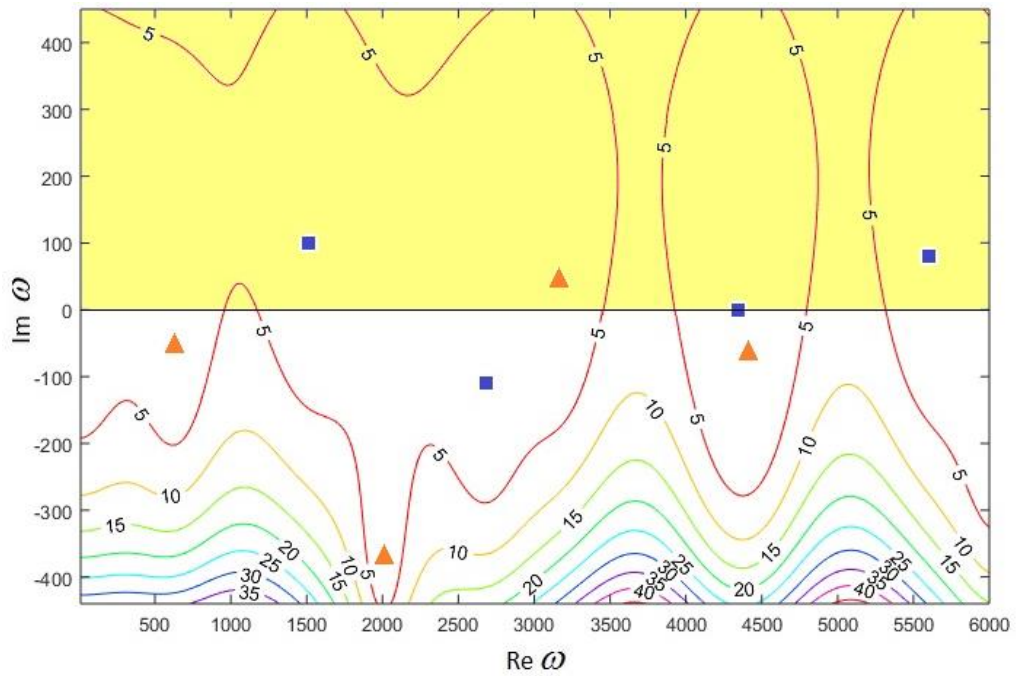
Figure 4.8: Contour plot of detuning $|g(\omega)|$ for $\tau = 5.0$ ms and $n = 1.1$. Notations and other parameters are the same as in Fig.6.

4.4.2.   Numerical validation of the neutral curves

The analytical results for the neutral curve shown in figure 2 will be corroborated numerically in this section. Figure 9 shows a sample comparison of the analytical prediction of n_{th}^i, given by equation (21), with that of the exact numerical solution for $m^i = 1$ at $x_q = L/3$. The analytical solutions for the intrinsic and coupled acoustic modes are represented by continuous and dashed blue lines respectively. Their numerical counterparts are represented by green circles and red squares respectively. Figure 9 shows good correspondence between the analytical and numerical results. The individual identity of acoustic and intrinsic mode can be traced numerically, by increasing the value of n in small increments, tracking their locus in the complex frequency plane. Alternately, we can use simple analytical models for coupling as described in chapter 3. Figure 9 proves that for both the narrow islands of instability on the left and the main instability domain on the right, the numerical results corroborate well with the analytical solution of (21). Extensive numerical simulations, for small τ, also prove that the combination of neutral curves $\omega_c^i \tau = 0$, $\omega_c^i \tau = \pi$ and $\omega_c^i \tau = -\pi$, is indeed a repetitive pattern for any mode. Near the point of intersection of neutral lines, coupled-acoustic and intrinsic modes invariably change their identity, some instances of which can be found from figure 9. A comprehensive model for intrinsic mode-acoustic mode coupling will be useful to explain this phenomenon. It is important to recall that this kind of switching of modal identity has been observed for a closed-open combustor as well (refer to figure 2.12).
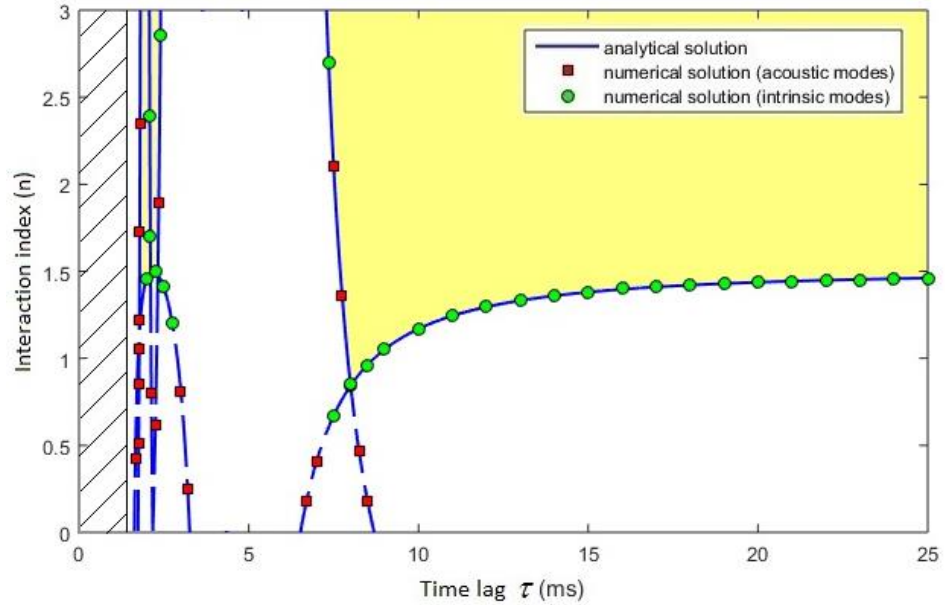
Figure 4.9: Neutral curve: comparison of analytical and numerical results for $m^i = 1$. Solid and dashed lines show the analytical solutions for intrinsic and acoustic modes respectively. Numerical solutions are shown by coloured symbols: by green circles and red squares. Notation and other parameters are the same as in Fig.2.

4.4.3. Numerical validation of the growth rate

The explicit expression for the intrinsic mode growth rate, as per equation (26), is based on a first order perturbation in n. It is important to validate this assumption numerically. Moreover, the range in which this growth rate formula is applicable, is also a matter that will be established numerically.

Figure 10 shows a comparison of the analytical prediction of the growth rates given by (26), with that of the numerical results for $m^i = 1$ and $\tau = 9$ ms. Near n_{th}^i (1.05 for this case), that is, near the neutral line of stability, analytical and numerical predictions match up quite nicely. However, as we move away from the neutral line, analytical predictions deviate from the numerical results. The prediction is quite good within a band of thirty percent shift of n near the neutral line. Beyond this range, modes are either stable or linear theory does not hold. It is also of interest to check

whether formula (26) works well at the point of intersection of neutral curve segments, that is, in the domain of intrinsic-acoustic mode coupling. Figure 11 presents the comparison of analytical and numerical results at $\tau = 8$ ms (that is, at the point of intersection of neutral curve segments $\omega_c^i \tau = 0$ and $\omega_c^i \tau = \pi$) for the first intrinsic mode. In this case, we also see that the numerical and analytical results are in good agreement with each other near the n_{th}^i (0.85 for this case). We can therefore conclude that the analytical prediction for the growth rate is in good agreement with the numerical solution in the vicinity of n_{th}^i: where it is of most interest. Our approximate solution (26) considers only the leading order term of expansion in n_1^i (the departure of n from n_{th}^i). The single order expansion provides a good level of accuracy near the neutral line for all the cases we have studied so far. If we look for higher orders of accuracy in some scenarios, we need to consider a higher order expansion in n_1^i in our perturbation equation. This, however, will not be carried out in the present work.

Hence, we can confirm that the compact analytical prediction of the linear growth rate (26) works very well for all τ, including in the vicinity of intersections of different segments of the neutral curve. The growth/decay rate depends on various combustor parameters. A parametric study of the growth rate and neutral curves will be performed in the next section.
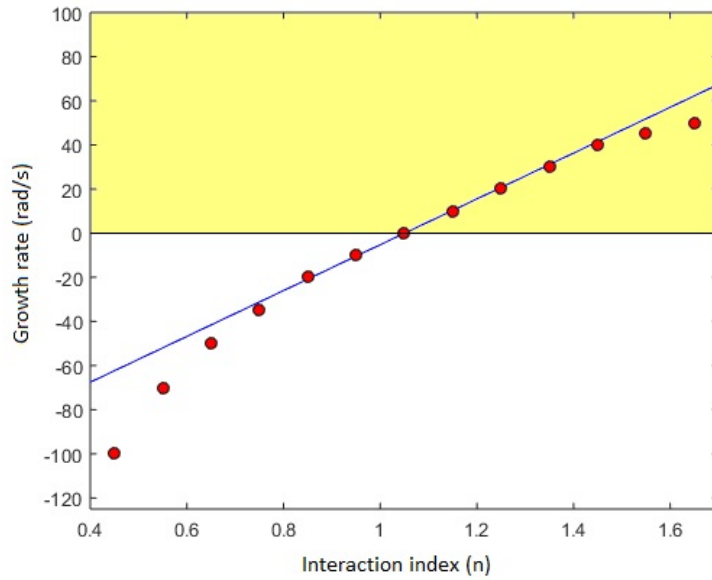
Figure 4.10: Growth rate for $m^i = 1$ at $\tau = 9$ ms: comparison of the analytical result (26) and numerical solution of the original dispersion relation (8). The blue line and red circles show the analytical and numerical solution respectively. The instability domain is marked in yellow. The parameters of the system are the same as in Fig.2.
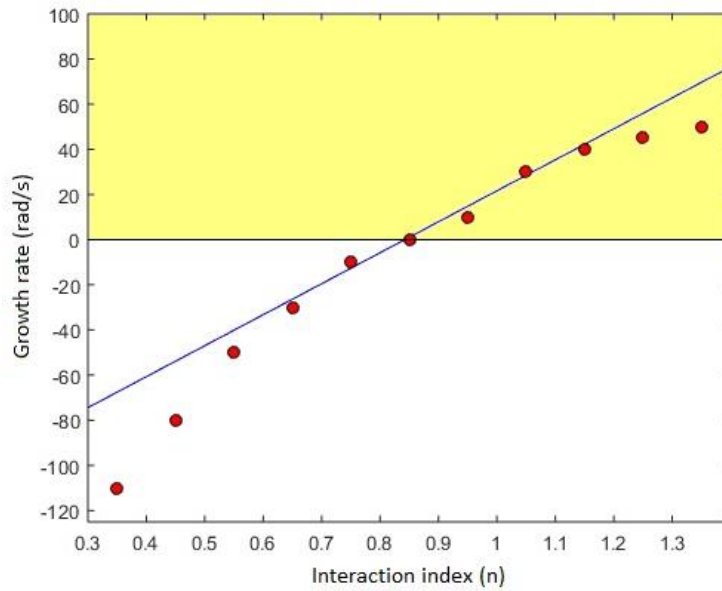
Figure 4.11: Growth rate for $m^i = 1$ at $\tau = 8$ ms (at the point of intersection of neutral curve segments $\omega_c^i \tau = 0$ and $\omega_c^i \tau = \pi$): comparison of the analytical result (26) and numerical solution of the original dispersion relation (8). The notations and other parameters of the system are the same as in Fig.10.

218

4.5.   Effect of parameters (flame location, cross-section jump, temperature jump) on stability behavior of intrinsic modes

As per equation (21), the threshold of n depends on various combustor parameters. The same thing can be said about the growth rate, as per equation (26). In this section, we try to identify how n_{th}^{i} and growth rate depend on the three main parameters of an open-open combustor model: (i) cross-section jump, (ii) temperature jump and (iii) flame location. It is also of significant interest to find out whether, for a certain parameter domain, the n-threshold can decrease or growth rate can increase, in other words, intrinsic mode instability is triggered.

Figure 12 (a) illustrates the effect of cross-section jump on the neutral curve main loop, plotted on the basis of (21). This figure shows two different cases for the cross-section jump: (i) $S_2/S_1 =1$ and (ii) $S_2/S_1 =2$. Lavender colour marks the instability domain for $S_2/S_1 =1$. The common domain of instability is marked in yellow. In all subsequent figures, the common instability domain is also marked in yellow. It can be seen from the figure that the inclusion of cross-section jump lifts the overall neutral curve and shifts it slightly to the right. This means that the n-threshold of intrinsic instability is lifted due to cross-section jump. Figure 12 (b) shows the change of n-threshold due to the inclusion of cross-section jump for three different time lag values of 8ms, 8,7 ms, and 10 ms. These three lines are represented by blue, green and red respectively. Clearly, the red, green and blue curves have an upward slope, zero slope, and downward slope respectively. This means that the n-threshold increases at $\tau =10$ ms, reduces at $\tau =8$ ms and remains constant at $\tau =8.7$ ms. These observations can also be made visually from figure 12 (a). Thus n-threshold can either be

increased, decreased or kept constant due to the inclusion of cross-section jump in the system.

(a)

(b)
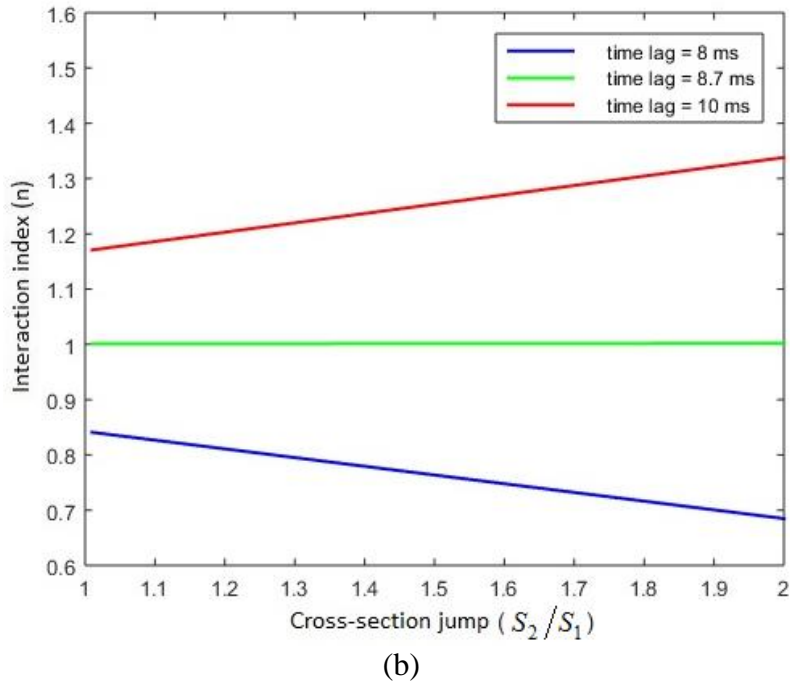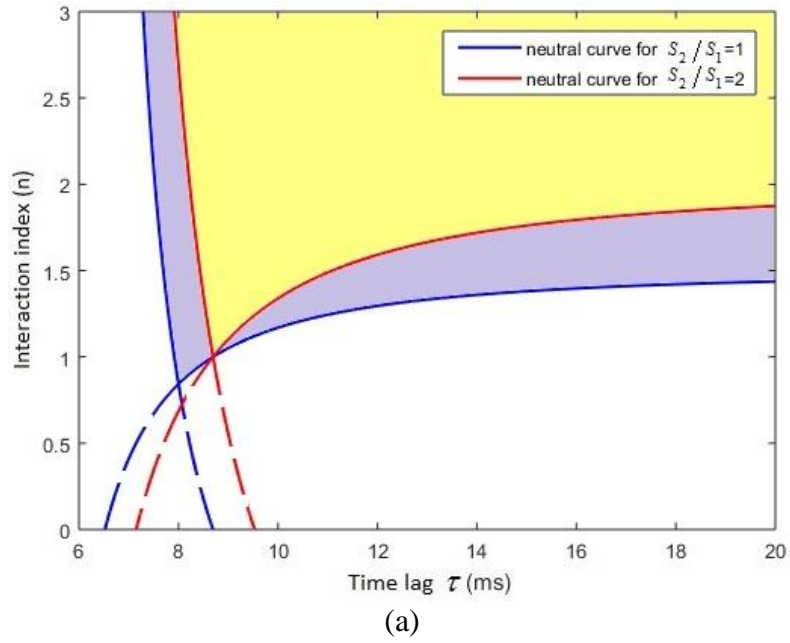
Figure 4.12 (a): Effect of cross-section jump on the stability domain for $m^i = 1$. The plot is based on (21) and shows no jump ($S_2/S_1 = 1$) and with ($S_2/S_1 = 2$) cross-section jump configurations. Lavender colour marks the instability domains for the case $S_2/S_1 = 1$. The common instability domain for these two cases is marked in yellow. (b): The threshold of n as a function of cross-section jump for $m^i = 1$. Blue, green and red lines correspond to n-threshold values for time lag= 8ms, 8.7 ms, and 10 ms respectively. For both figures, other parameters and notation are the same as in Fig.2.
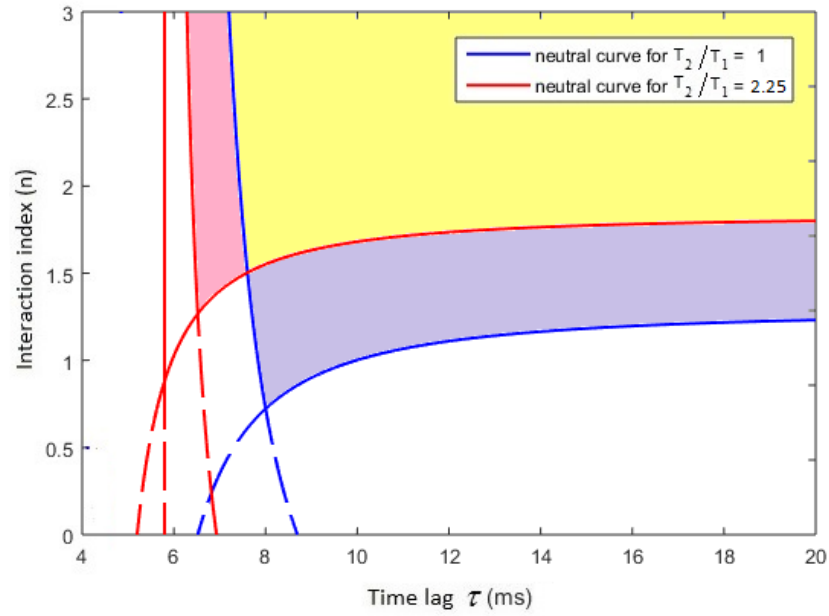
(a)
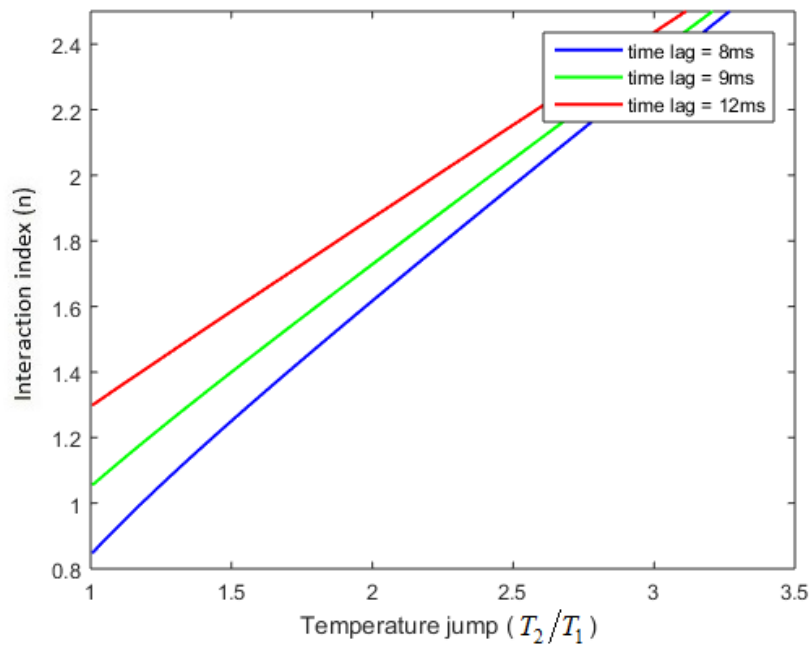
(b)

Figure 4.13(a): Effect of temperature jump on stability domain for $m^i = 1$. The plot is based on (21) and shows configurations with no jump, i.e. $T_2/T_1 = 1$ (or, $c_2/c_1 = 1$)) and with $T_2/T_1 = 2.25$ (or, $c_2/c_1 = 1.5$)) temperature jump. Lavender and pink mark the instability domains for the cases $c_2/c_1 = 1$ and $c_2/c_1 = 1.5$ respectively, with the common instability domain being marked in yellow. (b): The threshold of n as a function of temperature jump for $m^i = 1$. Blue, green and red lines correspond to n-threshold values for time lag= 8ms, 9 ms, and 12 ms respectively. For both figures, other parameters and notation are the same as in Fig.2.

The effect of temperature jump on n_{th}^i (τ) is slightly different. Figure 13 (a), plotted on the basis of (21), compares two different cases of temperature jump: (i) for T_2/T_1 =1 (or, c_2/c_1 =1) and (ii) T_2/T_1 =2.25 (or, c_2/c_1 =1.5). The lavender and pink colour represent the instability domains due to these two cases. The temperature jump lifts the neutral curve and stretches the span of the neutral loop to the left. Hence, the inclusion of temperature jump in the system increases the n_{th}^i for all time lags. This statement can further be verified with the help of figure 13(b), which represents the effect of temperature jump on n-threshold for three different time lags of 8, 9 and 12 ms. It can be clearly seen that for all three of these time lags, the n-threshold monotonically increases with respect to temperature jump. Thus. temperature jump increases the n-threshold for intrinsic instability in an open-open combustor.

Figure 14(a), plotted on the basis of (21), demonstrates the effect of flame location on n_{th}^i (τ). The figure is drawn for two different flame locations, x_q =0.25 m and 0.35 m. Lavender colour represents the instability domain for x_q =0.25 m. The neutral curve shifts slightly up as the flame is shifted from x_q =0.25 m to x_q =0.35 m. In other words, the n-threshold increases as the flame is moved from x_q =0.25 m to x_q =0.35 m. This is a generalized trend that can also be seen in figure 14(b). In figure 14(b), for three different time lags of 8 ms, 9 ms, and 12 ms, we find that as x_q increases, the n-threshold increases, indicating that the small x_q values in an open-open combustor correspond to the critical region from an intrinsic instability perspective. For a closed-open combustor, it was shown that in the absence of cross-section and temperature jump, the flame location yielding the minimal n_{th}^i is at the

middle of the combustor. This statement is not valid for an open-open combustor, where there are no minima of n_{th}^i in the middle of the combustor, because n_{th}^i has a constant value of 2, as per (22).
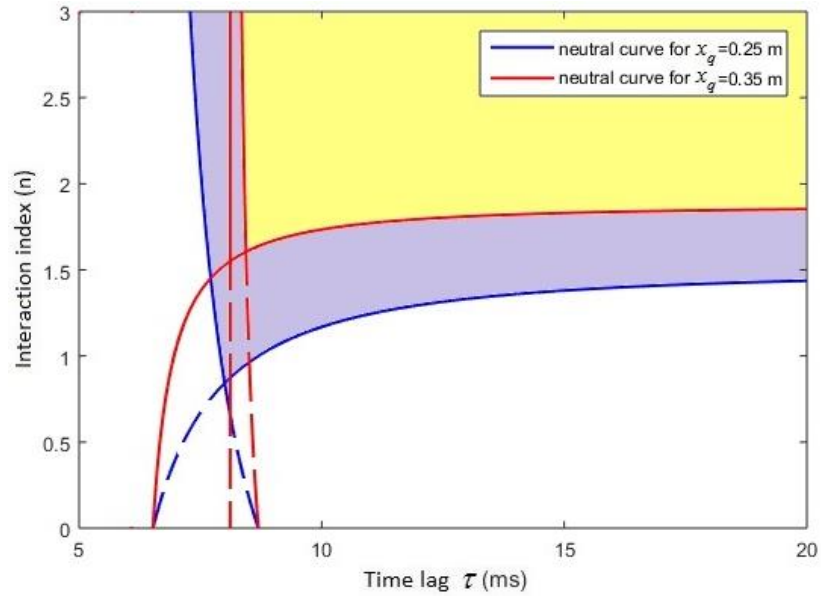
(a)
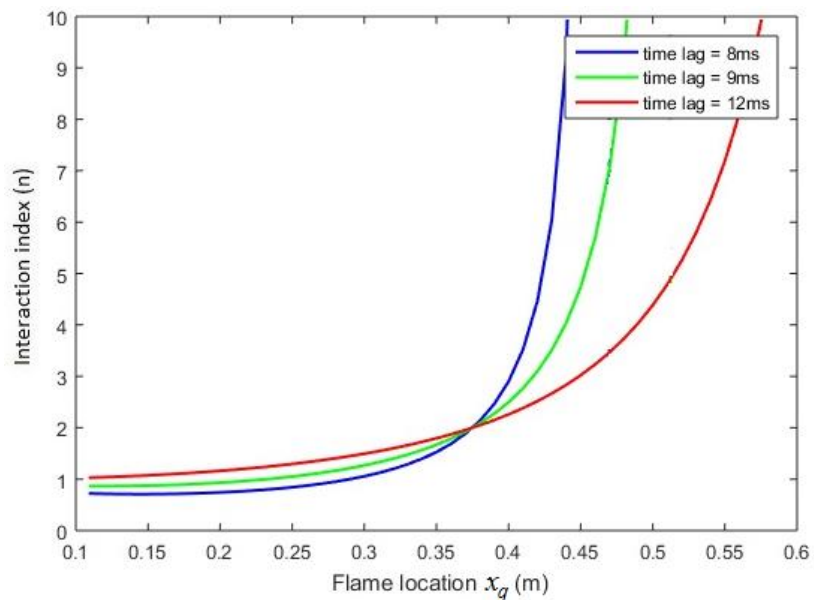
(b)

Figure 4.14(a): Effect of flame location on stability domain for $m^i = 1$. The plot is based on (21) and shows two flame locations: x_q =0.25m and 0.35m. Lavender marks the instability domains for x_q =0.25m. The common instability domain for these two cases is marked in yellow. (b): The threshold of n as a function of flame location for $m^i = 1$. Blue, green and red lines correspond to n-threshold values for time lag= 8ms, 9 ms, and 12 ms respectively. For both figures, other parameters and notation are the same as in Fig.2.

A similar parametric study can be performed for the growth rates of the intrinsic modes. Figure 15 (a), (b) and (c) show the effect on the growth rate of cross section jump, temperature jump, and flame location respectively. Growth rates are calculated using the explicit analytical solution (26). Figure 15 (a) shows two different cases for time lag, 8 ms and 12 ms, where cross-section jumps of $S_2/S_1 =1$ and $S_2/S_1 =2$ are introduced for each case. The growth rate decreases due to cross section jump for both time lags (8 ms and 12 ms). Figure 15 (b) shows the growth rate for time lag = 9 ms, where temperature jumps of $T_2/T_1 =1$ (or, $c_2/c_1 =1$) and $T_2/T_1 =2.25$ (or, $c_2/c_1 =1.5$) are introduced for each case. The introduction of temperature jump reduces the growth rate for a time lag of 9 ms. Figure 15 (c) shows the growth rate for time lag = 9 ms for two different flame locations of $x_q =0.25$ m and $x_q =0.35$ m. This figure makes it clear that the growth rate decreases as x_q is increased from 0.25 m to 0.35 m. It means that the intrinsic flame instabilities will be critical for small values of x_q, an observation which is the opposite for a closed-open combustor, where the most critical point for intrinsic instability situates at the middle of the combustor.

Thus, by selecting the right system parameters, such as cross section jump, temperature jump, and flame location, we will be able to increase/decrease the n^i_{th} and decrease/increase the growth rate, hence dampening/instigating the intrinsic mode instability. The flame location for small x_q is found to be most critical for intrinsic flame instability.

(a)

(b)

(c)
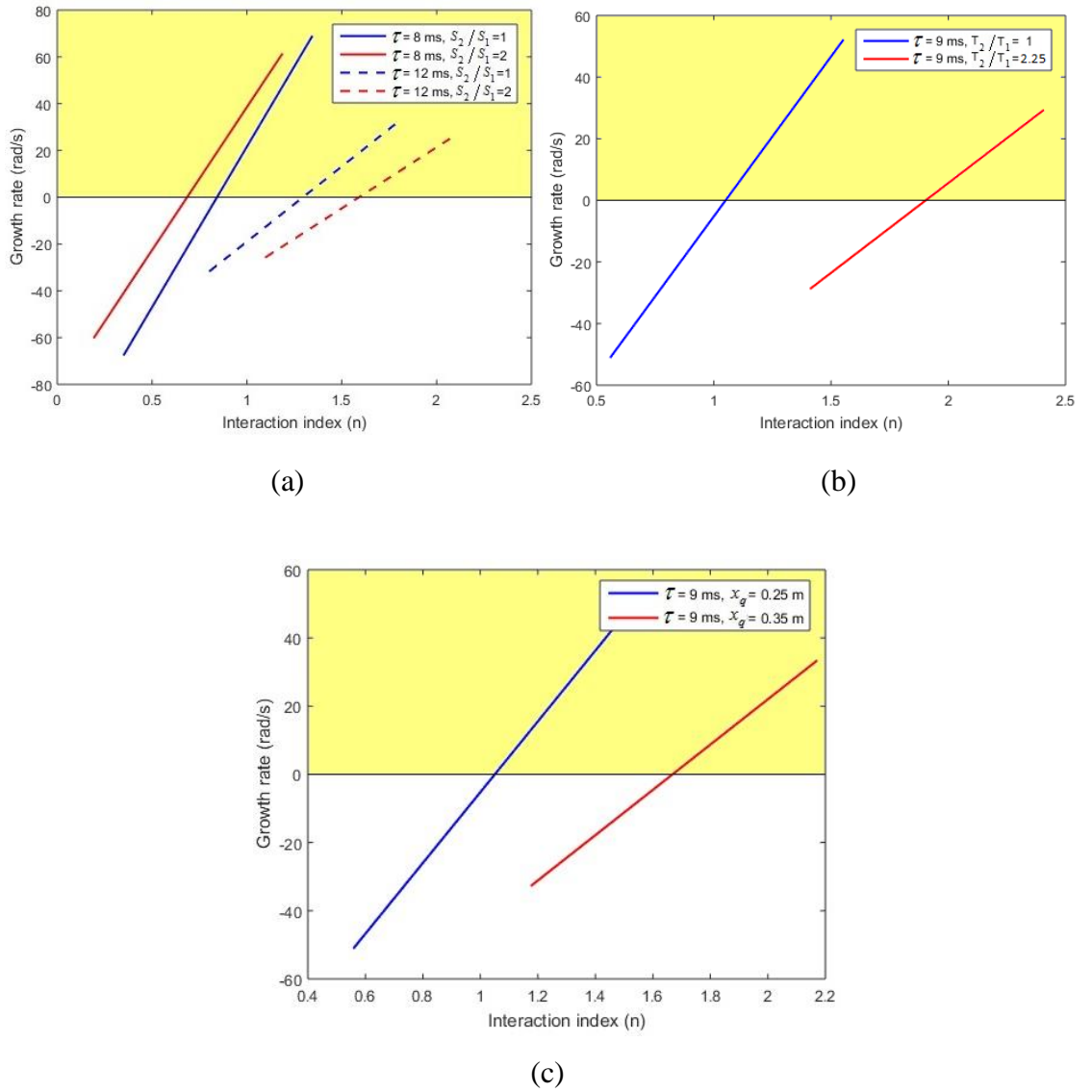
Figure 4.15: Effect of cross-section jump, temperature jump and flame location on growth rates for $m^i = 1$ (based on (26)). (a): Two different time lags (8 and 12 ms) are indicated by solid and dashed lines. Two values of cross section jump ($S_2/S_1 = 1$ and $S_2/S_1 = 2$) are marked in blue and red. (b): Two values of temperature jumps $T_2/T_1 = 1$ (or, $c_2/c_1 = 1$) and $T_2/T_1 = 2.25$ (or, $c_2/c_1 = 1.5$) are marked in blue and red for time lag=9 ms. (c): Two values of flame locations $x_q = 0.25$ m and $x_q = 0.35$ m at time lag = 9 ms are marked in blue and red. Other parameters and notation are the same as in Fig. 2. Yellow colour marks the domain of instability.

4.6. Coupling of intrinsic and acoustic modes for a combustor with open-open end conditions

It has been discussed in § 1 of chapter 3 that when the Rayleigh index is negative, the decaying acoustic mode might couple to one of the intrinsic modes in its close vicinity in the complex frequency plane. We have provided a comprehensive picture for the coupling in a closed-open combustor. It was shown that once coupled to the intrinsic mode, the acoustic mode completely loses its identity and starts to behave as an intrinsic mode. The coupled modes were thus referred to as coupled intrinsic modes. However, to distinguish between the acoustic and intrinsic mode in terms of their origin, we used the terminologies coupled intrinsic mode (born intrinsic or BI) and coupled intrinsic mode (born acoustic or BA). In this section we carry out a similar analysis for an open-open combustor. Primarily, we develop a simple mathematical model of linear coupling. Following this, we perform a numerical validation of our analytical model. Through this exercise, we mathematically identify the nature of the coupled modes when an acoustic mode is triggered by an intrinsic mode to instability. We use the same nomenclature as in chapter 3 to define the coupled modes.

4.6.1. Mathematical model of linear coupling

Like in § 6 of chapter 3, where we developed a mathematical model of coupling for a closed-open combustor, in this case it is also assumed that on the complex frequency plane, the acoustic modes do not depart far (in terms of decay/growth rate) from the neutral curve We therefore perturb the solution of acoustic modes by a small parameter $\Delta\omega$. This technique of perturbation enables us to find not only the locus of the acoustic mode, but also the locus of the nearby intrinsic mode. The perturbed

form of the frequency is as follows, where ω_0^a is the modal frequency of the open-open combustor without a flame,

$$\omega^a = \omega_0^a + \Delta\omega.$$

On substituting this ansatz, the generalized dispersion relation (8) can be written as,

$$(\alpha+1)\sin\left(\beta_1\left(\omega_0^a+\Delta\omega\right)\right)+(\alpha-1)\sin\left(\beta_2\left(\omega_0^a+\Delta\omega\right)\right)+$$
$$2n_0e^{i\omega_0^a\tau}\cos\left(\left(\omega_0^a+\Delta\omega\right)\frac{x_q}{c_1}\right)\sin\left(\left(\omega_0^a+\Delta\omega\right)\frac{\left(x_q-L\right)}{c_2}\right)=0 \qquad (4.27)$$

Assuming small values of $\Delta\omega$, and thus neglecting all the terms higher than order 2, the trigonometric terms in the above expression can be written as per equation (3.28). With these replacements, the dispersion relation (27) can be re-written in the following way,

$$(\alpha+1)\left[\sin\left(\beta_1\omega_0^a\right)\left(1-\frac{\beta_1^2\left(\Delta\omega\right)^2}{2}\right)+\beta_1\Delta\omega\cos\left(\beta_1\omega_0^a\right)\right]+$$
$$(\alpha-1)\left[\sin\left(\beta_2\omega_0^a\right)\left(1-\frac{\beta_2^2\left(\Delta\omega\right)^2}{2}\right)+\beta_2\Delta\omega\cos\left(\beta_2\omega_0^a\right)\right]+$$
$$2n_0e^{i\omega_0^a\tau}\left\{\left(1-\frac{\left(\Delta\omega\right)^2\tau^2}{2}\right)+i\Delta\omega\tau\right\}$$
$$\left\{\left(1-\frac{\left(\Delta\omega\right)^2 x_q^2}{2c_1^2}\right)\cos\left(\frac{\omega_0^a x_q}{c_1}\right)-\frac{\left(\Delta\omega\right)x_q}{c_1}\sin\left(\frac{\omega_0^a x_q}{c_1}\right)\right\}$$
$$\left\{\left(1-\frac{\left(\Delta\omega\right)^2\left(x_q-L\right)^2}{2c_2^2}\right)\sin\left(\frac{\omega_0^a\left(x_q-L\right)}{c_2}\right)+\frac{\left(\Delta\omega\right)\left(x_q-L\right)}{c_2}\cos\left(\frac{\omega_0^a\left(x_q-L\right)}{c_2}\right)\right\}=0$$
$$\text{. (4.28)}$$

Neglecting all the terms of $\Delta\omega$ higher than order 2, the equation (28) can be simplified to the following quadratic equation,

227

$$A(\Delta\omega)^2 + B(\Delta\omega) + C = 0. \tag{4.29}$$

The analytical solution for the quadratic equation (29) can be written as follows,

$$\Delta\omega_{1,2} = \frac{-B \pm \sqrt{(B^2 - 4AC)}}{2A}. \tag{4.30}$$

Where, the coefficients, A, B and C are,

$$A = -(\alpha+1)\frac{\beta_1^2}{2}\sin(\beta_1\omega_0^a) - (\alpha-1)\frac{\beta_2^2}{2}\sin(\beta_2\omega_0^a) +$$

$$2n_0 e^{i\omega_0^a\tau} \begin{bmatrix} \left\{-\dfrac{(x_q-L)^2}{2c_2^2} - \dfrac{x_q^2}{2c_1^2} - \dfrac{\tau^2}{2}\right\}\cos\left(\dfrac{\omega_0^a x_q}{c_1}\right)\sin\left(\dfrac{\omega_0^a(x_q-L)}{c_2}\right) - \\[2mm] \dfrac{x_q(x_q-L)}{c_1 c_2}\sin\left(\dfrac{\omega_0^a x_q}{c_1}\right)\cos\left(\dfrac{\omega_0^a(x_q-L)}{c_2}\right) \\[2mm] -\dfrac{i\tau x_q}{c_1}\sin\left(\dfrac{\omega_0^a x_q}{c_1}\right)\sin\left(\dfrac{\omega_0^a(x_q-L)}{c_2}\right) \\[2mm] +\dfrac{i\tau(x_q-L)}{c_2}\cos\left(\dfrac{\omega_0^a x_q}{c_1}\right)\cos\left(\dfrac{\omega_0^a(x_q-L)}{c_2}\right) \end{bmatrix} = 0$$

$$B = (\alpha+1)\beta_1\cos(\beta_1\omega_0^a) + (\alpha-1)\beta_2\cos(\beta_2\omega_0^a) +$$

$$2n_0 e^{i\omega_0^a\tau} \begin{bmatrix} \dfrac{(x_q-L)}{c_2}\cos\left(\dfrac{\omega_0^a x_q}{c_1}\right)\cos\left(\dfrac{\omega_0^a(x_q-L)}{c_2}\right) - \\[2mm] \dfrac{x_q}{c_1}\sin\left(\dfrac{\omega_0^a x_q}{c_1}\right)\sin\left(\dfrac{\omega_0^a(x_q-L)}{c_2}\right) \\[2mm] +i\tau\cos\left(\dfrac{\omega_0^a x_q}{c_1}\right)\sin\left(\dfrac{\omega_0^a(x_q-L)}{c_2}\right) \end{bmatrix} = 0$$

$$C = (\alpha+1)\sin(\beta_1\omega_0^a) + (\alpha-1)\sin(\beta_2\omega_0^a) +$$

$$2n_0 e^{i\omega_0^a\tau}\cos\left(\dfrac{\omega_0^a x_q}{c_1}\right)\sin\left(\dfrac{\omega_0^a(x_q-L)}{c_2}\right) \tag{4.31a,b,c}$$

Once the correction to the frequency is obtained, using formula (30), the two frequencies (of coupled modes) can be obtained using $\omega^a = \omega_0^a + \Delta\omega$. The solutions tell us, whether, in $n - \tau$ space, any of the intrinsic modes are in the vicinity of the acoustic mode and whether they interact with it. In the subsequent section, we perform some case studies in different parts of the neutral curve and identify different types of coupling. It is important to remember that the intrinsic-acoustic mode coupling does not exist on every part of the neutral curve. It is only near the point of intersection of neutral curve segments that we find intrinsic-acoustic mode coupling. In other sections of the neutral curve, there exists only one solution for the intrinsic mode.

4.6.2.   Four types of intrinsic mode-acoustic mode coupling: Loci of the coupled modes in the $n - \tau$ space

The analytical solution (30), derived in the previous section, provides an explicit solution for the acoustic mode and the nearby intrinsic mode. Like we did in § 6 of chapter 3 for a closed-open combustor, in the case of an open-open combustor we can also perform visual inspection on the loci of coupled modes on the complex frequency plane, as we change the parameter n. Therefore, we can find the identity of these modes when they cross the neutral line of stability. We focus on the domain near a particular acoustic mode on the complex frequency plane for a specific value of τ. We then find the loci of coupled modes in that domain as a function of parameter n. Figures 16-19 present plots of this kind.

Figures 16-19 are plots focused near the domain of the second acoustic mode (m^a =1). Figures 16-17 are made for the flame location x_q =L/3 and for two different values of τ: τ =7.5 ms and τ =7.4 ms respectively. Figures 18-19 are made for the

flame location x_q =0.35 m and for two different τ values: τ =7.1 ms and τ =7.0 ms respectively. Summarizing the observations made in figures 16-19 we can distinguish four different types of coupling, similar to § 6 of chapter 3. They are:

i. **The first type of coupling:** the coupled intrinsic mode (BI) becomes unstable at a frequency predicted by $\omega_c^i \tau = 0$, whereas the coupled intrinsic mode (BA) becomes unstable at a frequency predicted by either $\omega_c^i \tau = \pi$ or $\omega_c^i \tau = -\pi$. Figure 16 illustrates this type of coupling.

ii. **The second type of coupling**: the coupled intrinsic mode (BA) becomes unstable at a frequency predicted by $\omega_c^i \tau = 0$, whereas the coupled intrinsic mode (BI) becomes unstable at a frequency predicted by either $\omega_c^i \tau = \pi$ or $\omega_c^i \tau = -\pi$. Figure 17 illustrates this type of coupling.

iii. **The third type of coupling**: the coupled intrinsic mode (BI) becomes unstable at $\omega_c^i \tau = 0$, whereas the coupled intrinsic mode (BA) tends to remain asymptotically stable at a frequency corresponding to $\cos\left(k_1 x_q\right) = 0$ or $\sin\left(k_1\left(x_q - L\right)\right) = 0$, as per equation (16). Figure 18 illustrates this type of coupling.

iv. **The fourth type of coupling:** the coupled intrinsic mode (BA) becomes unstable at $\omega_c^i \tau = 0$, whereas the coupled intrinsic mode (BI) tends to remain asymptotically stable at a frequency corresponding to $\cos\left(k_1 x_q\right) = 0$ or $\sin\left(k_1\left(x_q - L\right)\right) = 0$, as per equation (16). Figure 19 illustrates this type of coupling.

In all these examples of coupling, the second acoustic mode couples with the second intrinsic mode. In figure 16 for τ =7.5 ms, the second intrinsic mode decay rate decreases with the increase of n, while the second acoustic mode initially decays

with an increase of n. At a threshold value of n, both these coupled modes become unstable. While the coupled intrinsic mode (BI) becomes unstable, corresponding to $\omega_c^i \tau = 0$, the coupled intrinsic mode (BA) becomes unstable at a higher frequency, corresponding to $\omega_c^i \tau = \pi$. This is the **first type** of intrinsic-acoustic mode coupling. On the neutral curve in figure 2, this coupling point exists slightly left of the intersection point of neutral lines $\omega_c^i \tau = 0$ and $\omega_c^i \tau = \pi$.
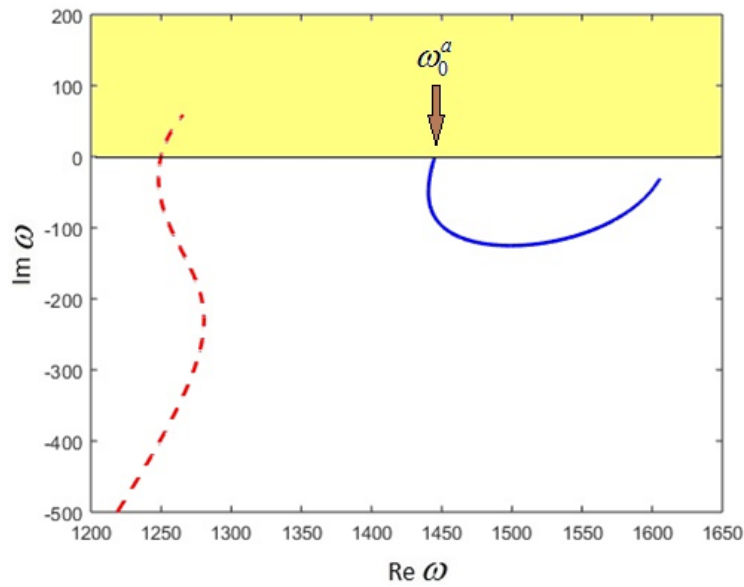
Figure 4.16: Loci of the coupled modes for $\tau = 7.5$ ms, $x_q = 0.25$ m, $m^a = 1$, $m^i = 1$. n is varied from 0.0 to 0.75. Plots are generated on the basis of quadratic equation (30). Coupled intrinsic mode (BA) and coupled intrinsic mode (BI) are represented by a dotted red line and continuous blue line respectively. The domain of instability is marked in yellow. The brown arrow indicates the frequency of acoustic mode (ω_0^a) of the open-open combustor in the absence of a flame. This is an example of the **first type of coupling**, where the coupled intrinsic mode (BI) becomes unstable at $\omega_c^i \tau = 0$, whereas the coupled intrinsic mode (BA) tends to become unstable at a higher frequency corresponding to $\omega_c^i \tau = \pi$. In this case, the mode numbers of the acoustic and intrinsic modes involved in coupling are the same. Other parameters are the same as in figure 2.

When τ is lowered slightly, to $\tau = 7.4$ ms, we get to see the **second type** of coupling, visible in figure 17. Here the coupled intrinsic mode (BA) becomes unstable, corresponding to $\omega_c^i \tau = 0$, whereas the coupled intrinsic mode (BI) becomes unstable

at a higher frequency, corresponding to $\omega_c^i \tau = \pi$. Thus, due to a slight alteration of τ, the coupled modes change their identity on the neutral line. This point has also been highlighted in figure 9, where we performed numerical validation of the neutral curves. Clearly, on the right-hand side of the coupled domain (the domain where both neutral lines $\omega_c^i \tau = 0$ and $\omega_c^i \tau = \pi$ exist) in figure 2, we find only one solution for the intrinsic mode. This is a coupling free domain. The neutral curves to the left of the main neutral loop in figure 2, are very thin in their spread and the neutral lines, $\omega_c^i \tau = 0$, $\omega_c^i \tau = \pi$ and $\omega_c^i \tau = -\pi$, are very close to each other. These small neutral loops manifest strong coupling between the intrinsic and acoustic modes. There are two more types of intrinsic mode-acoustic mode coupling possible, which will be discussed in the following section.
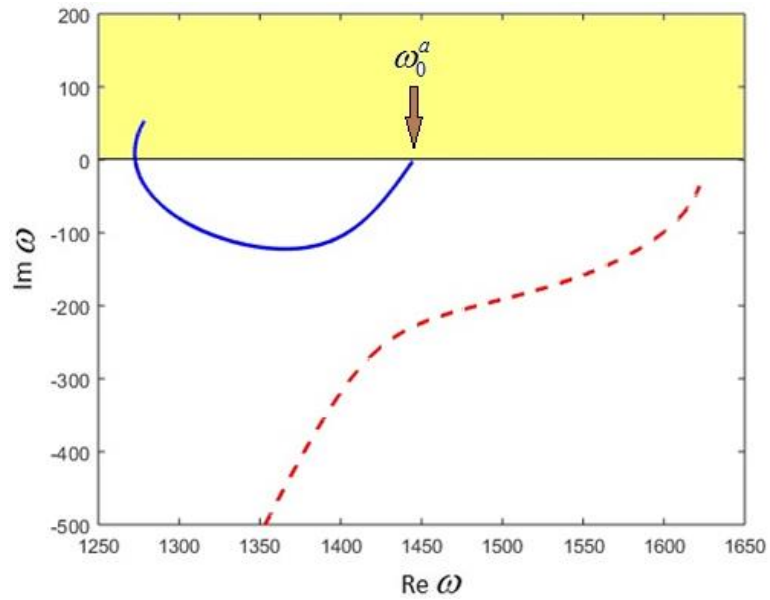
Figure 4.17: Loci of the coupled modes for $\tau = 7.4$ ms, $x_q = 0.25$ m, $m^a = 1$, $m^i = 1$. n is varied from 0.0 to 0.75. Plots are generated with the help of quadratic equation (30). This is an example of the **second type of coupling**, where the coupled intrinsic mode (BA) becomes unstable with $\omega_c^i \tau = 0$, whereas the coupled intrinsic mode (BI) tends to become unstable at a higher frequency corresponding to $\omega_c^i \tau = \pi$. In this case, the mode numbers of the acoustic and intrinsic modes involved in coupling are the same. Notations and other parameters are the same as in figure 16.

These two types of coupling have been explained in figures 18 and 19. In figure 18, the coupled intrinsic mode (BI) becomes unstable, corresponding to $\omega_c^i \tau = 0$. The coupled intrinsic mode (BA), that is in the close vicinity, initially decays and then tends to become unstable at a higher frequency corresponding to $\cos\left(k_1 x_q\right) = 0$. In fact, the coupled intrinsic mode (BA) remains asymptotically stable for large n. This statement can be validated from equation (21), where we find that when $\cos\left(k_1 x_q\right) = 0$, $n_{th}^i \to \infty$. Thus, in this **third type** of coupling, there is only one unstable solution and that is for the coupled intrinsic mode (BI). This type of coupling can also be seen in the neutral curve. For example, in figure 3 (a), for $x_q = 0.1$, we can see a domain like this on the left of the first neutral line $\omega_c^i \tau = \pi$ in the main neutral loop, where only one solution exists. The domain of the first two types of coupling exists on the right side of the first neutral line $\omega_c^i \tau = \pi$. Similarly, we can explain the **fourth type** of coupling using figure 19. In this type of coupling, the coupled intrinsic mode (BA) becomes unstable, corresponding to $\omega_c^i \tau = 0$, and the nearby coupled intrinsic mode (BI) remains asymptotically stable at a higher frequency corresponding to $\cos\left(k_1 x_q\right) = 0$. Hence, in this case, we again only find one unstable solution. All these four types of coupling exist not only in the main neutral loop on the extreme right, but also on the small neutral loops on the left of the neutral curve. Moreover, these four types of coupling are independent of the individual mode numbers for the acoustic and intrinsic modes. The mode numbers for the acoustic and intrinsic modes can be the same or different for these types of coupling.
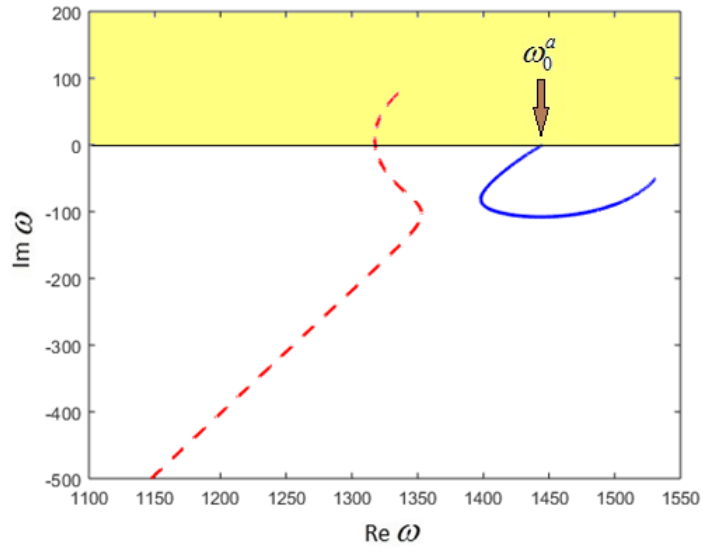
Figure 4.18: Loci of the coupled modes for τ =7.1 ms, x_q =0.35 m, m^a =1, m^i =1. n is varied from 0.0 to 0.75. Plots are generated with the help of quadratic equation (30). This is an example of the **third type of coupling**, where the coupled intrinsic mode (BI) becomes unstable at $\omega_c^i \tau = 0$, whereas the coupled intrinsic mode (BA) remains asymptotically stable at a frequency corresponding to $\cos\left(k_1 x_q\right) = 0$, as per equation (16). In this case, the mode numbers of the acoustic and intrinsic modes involved in coupling are the same. Notations and other parameters are the same as in figure 16.
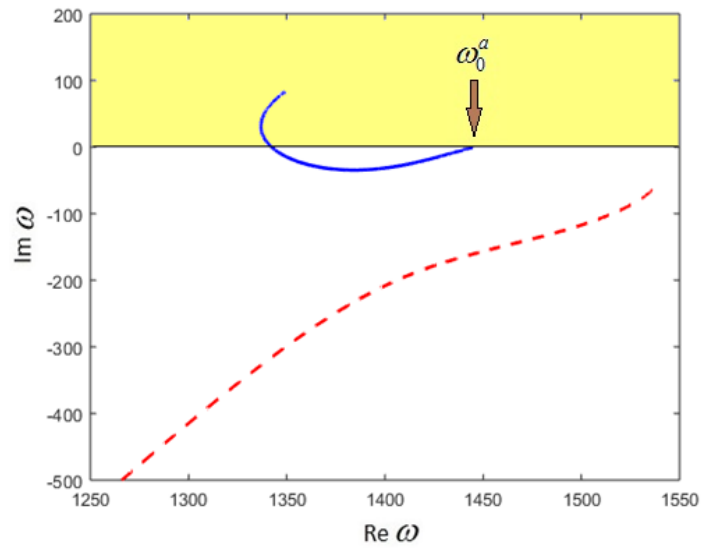
Figure 4.19: Loci of the coupled modes for τ =7 ms, x_q =0.35 m, m^a =1, m^i =1. n is varied from 0.0 to 0.75. Plots are generated with the help of quadratic equation (30). This is an example of the **fourth type of coupling**, where the coupled intrinsic mode (BA) becomes unstable at $\omega_c^i \tau = 0$, whereas the coupled intrinsic mode (BI) tends to remain asymptotically stable at a frequency corresponding to $\cos\left(k_1 x_q\right) = 0$, as per equation (16). In this case, the mode numbers of the acoustic and intrinsic modes involved in coupling are the same. Notations and other parameters are the same as in figure 16.

These four types of coupling can also be visualized on the neutral curves, as per figures 20 and 21. Figure 20 is produced for the second intrinsic mode, when the flame is located at x_q =0.35 m and figure 21 is applicable for the first intrinsic mode, when the flame is at x_q =L/3. In both these figures, domains of pure intrinsic and acoustic instabilities are marked by yellow and light yellow respectively. Lavender colour marks the domain where type 1 and 2 coupling exist between intrinsic and acoustic modes. Light turquoise colour represents the domain of type 3 and 4 coupling. In the domain of type 1 and 2 coupling, we find the existence of two solutions, one for coupled intrinsic mode (BI) and another for coupled intrinsic mode (BA). In the domain of type 3 and 4 coupling, we find only one solution, that is either for coupled intrinsic mode (BI) or coupled intrinsic mode (BA). The second mode in this scenario remains asymptotically stable at a frequency corresponding to either $\cos\left(k_1 x_q\right)=0$ or $\sin\left(k_1\left(x_q - L\right)\right)=0$, as per equation (16). In the neutral curve for the first intrinsic mode, in figure 21, we also find that a type 3 and 4 coupled domain is bound, on either side, by two type 1 and 2 coupled domains. This indicates that a slight alteration in τ can easily change the type of coupling that we see in combustion systems.

Thus our 'easy to deal with' quadratic equation (29) generates the solutions for the modes involved in coupling. An analytical model like this easily detects the relative position of the coupled modes on the complex frequency plane. We have identified, within a classical open-open combustor setup, that four different types of intrinsic mode-acoustic mode coupling can exist, all of which also exist in a closed-open combustor. The analytical model is supposed to be accurate near the neutral line of stability. However, this analytical model of a quadratic equation can be extended into

a quartic equation in a very straightforward manner, as explained in § 8 of chapter 3 for a closed-open combustor. For checking the fidelity of the analytical model, in the next section a numerical examination will also be performed for our current analytical model.
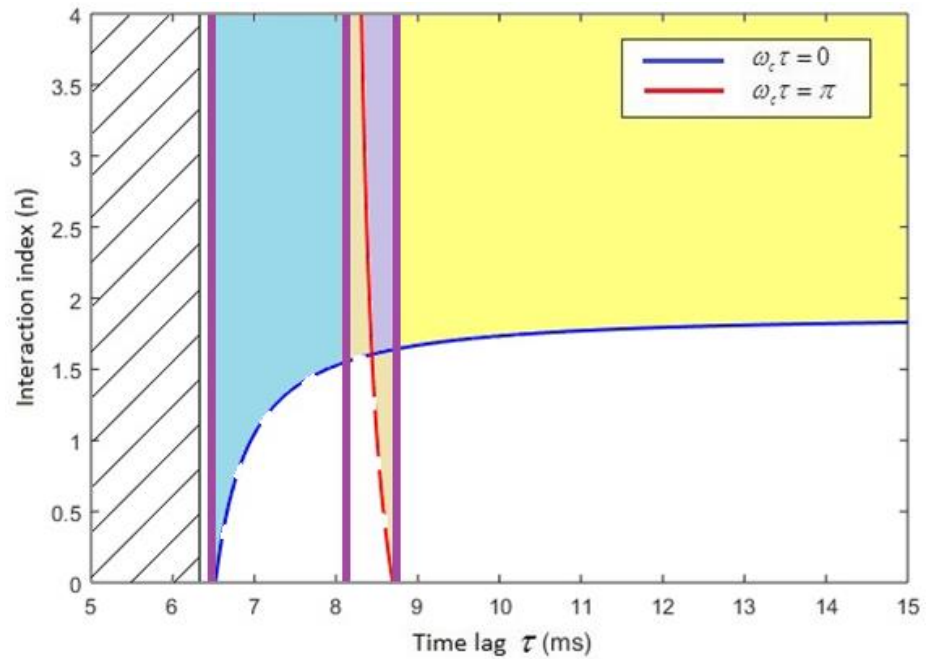
Figure 4.20: Neutral curve and stability domain on the $n - \tau$ plane for the second intrinsic mode (m^i =1, x_q =0.35 m). Blue and red lines correspond to the segments $\omega^i_c \tau = 0$ and $\omega^i_c \tau = \pi$ of the neutral curve respectively. The instability domains for intrinsic and coupled acoustic modes are marked in yellow and light yellow respectively. Lavender and light turquoise colours mark the domain of type 1,2 and type 3,4 coupling respectively. These domains are bound by thick purple vertical lines. The hatched area indicates the domain with multiple instability islands, narrowing as τ decreases. Other parameters are the same as in figure 2 (a).
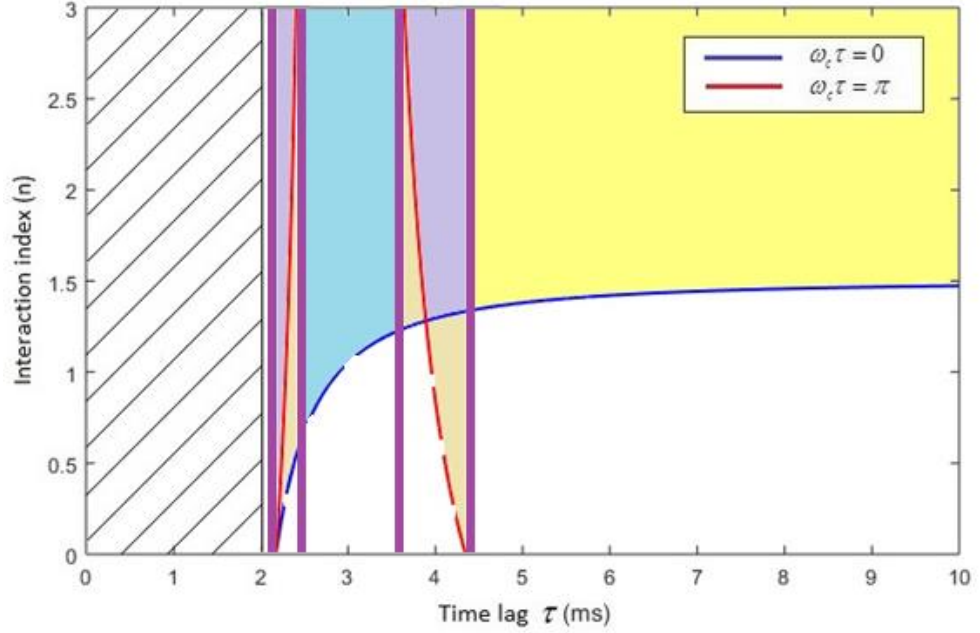
Figure 4.21: Neutral curve and stability domain on the $n - \tau$ plane for the first intrinsic mode (m^i =0), at x_q = L/3. Notations and other parameters are the same as for figure 20.

4.6.3. Numerical validation of analytical solution predicted by quadratic equation

In this section, the accuracy of the analytical solution (30) will be verified with the numerical result, as per equation (8). The quadratic equation (30) was derived by neglecting terms in $\Delta\omega$ with a higher than order 2. The applicability of this assumption needs to be checked for all four types of the coupling scenarios. The quadratic equation was found to perform well near the neutral curve for the coupled modes for a closed-open combustor in § 7 of chapter 3. We need to check whether this result is consistent for a combustor with an open-open end condition as well. Figures 22-25 are dedicated to that purpose. Figures 22-25 present numerical validation for the analytical results depicted in figures 16-19. The dotted red line and continuous blue line represent the analytical solutions for coupled intrinsic modes (BI) and coupled intrinsic mode (BA) respectively. The magenta circular and green

diamond dots represent their numerical counterparts respectively, by direct solution of equation (8).

Figure 22, which presents the first type of intrinsic-acoustic mode coupling, shows a good correspondence between analytical and numerical results for the coupled intrinsic mode (BA), whereas for the coupled intrinsic mode (BI), the analytical prediction does not seem to be that accurate. The same thing is true for figure 24, which shows the third type of coupling. In figure 23, which represents the second type of coupling, the prediction seems to be quite good for coupled intrinsic mode (BI) as well. A similarly good correspondence between the analytical and numerical results for coupled intrinsic mode (BI) can be found in figure 25, which depicts the fourth type of coupling. In general, for all these cases, the analytical prediction of the instability frequency is quite good for both the coupled modes (for type 1 and 2 coupling) and for coupled intrinsic mode (BI) or (BA) (for type 3 and 4 coupling, because there is only one instability frequency for these two types of coupling). Thus, making use of equation (30), we can accurately *a priori* estimate the unstable frequencies in the coupling scenario during the combustor design phase. The simplicity of the quadratic equation makes it a handy tool for unstable frequency prediction.

In all the figures, comparative study of the analytical and numerical study shows that the level of accuracy of the analytical solution provided by equation (30), for the prediction of the locus of coupled intrinsic mode (BA) in the complex frequency plane, is very high. The accuracy of prediction for coupled intrinsic mode (BI) is not as good when it is away from the neutral curve. The inclusion of higher order terms of $\Delta\omega$ in the mathematical model should improve the accuracy of prediction and hence address this issue. However, we do not pursue this line here and refrain from

developing a quartic equation for intrinsic mode-acoustic mode coupling, which is a straightforward exercise for generalized combustor parameters.
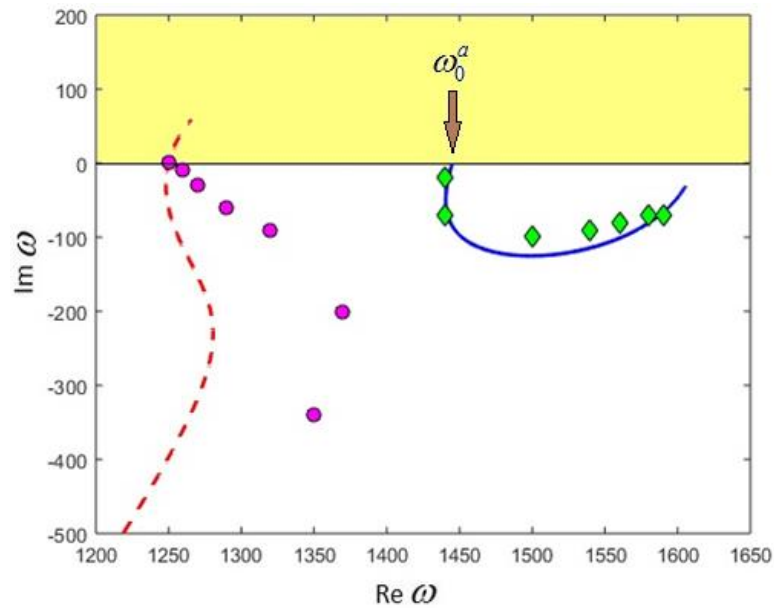
Figure 4.22: Numerical validation of analytical solution (30) for τ =7.5 ms, x_q =0.25 m, m^a =1, m^i =1. n is varied from 0.0 to 0.7. The dotted red and continuous blue lines represent the analytical solutions for coupled intrinsic mode (BI) and coupled intrinsic mode (BA) respectively. The magenta circular and green diamond dots represent their numerical counterparts respectively, by direct solution of equation (8). Yellow colour represents the domain of instability. The brown arrow indicates the frequency of acoustic mode (ω_0^a) of the open-open combustor in the absence of a flame. This is an example of the **first type of coupling**, where the coupled intrinsic mode (BI) becomes unstable at $\omega_c^i \tau = 0$, whereas the coupled intrinsic mode (BA) tends to become unstable at a higher frequency corresponding to $\omega_c^i \tau = \pi$. Other parameters are the same as in figure 2.
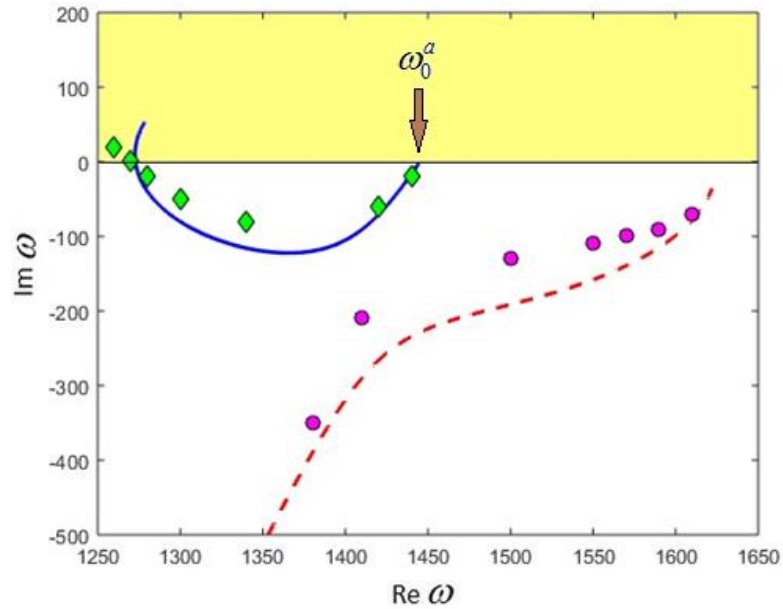
Figure 4.23: Numerical validation of analytical solution (30) for τ =7.4 ms, x_q =0.25 m, m^a =1, m^i =1. This is an example of the **second type of coupling**, where the coupled intrinsic mode (BA) becomes unstable with $\omega_c^i \tau = 0$, whereas the coupled intrinsic mode (BI) tends to become unstable at a higher frequency corresponding to $\omega_c^i \tau = \pi$. Notations and other parameters are the same as in figure 22.
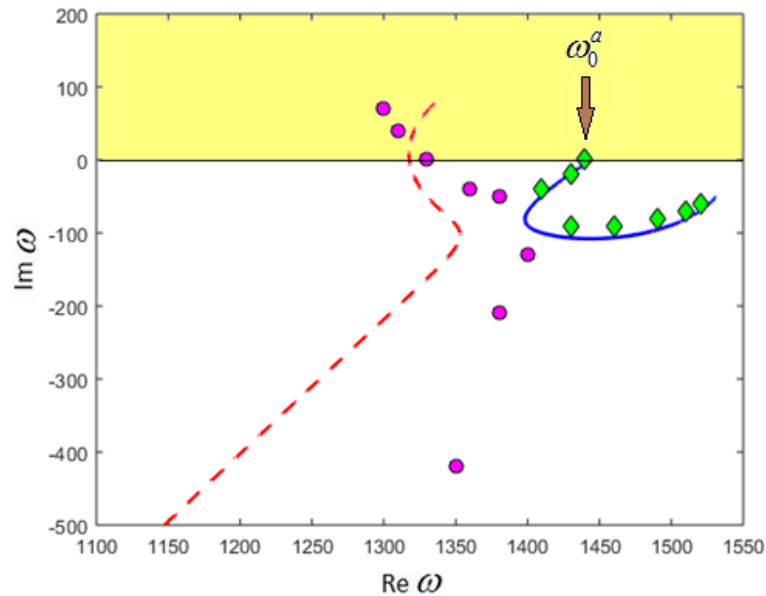
Figure 4.24: Numerical validation of analytical solution (30) for τ =7.1 ms, x_q =0.35 m, m^a =1, m^i =1. This is an example of the **third type of coupling**, where the coupled intrinsic mode (BI) becomes unstable with $\omega_c^i \tau = 0$, whereas the coupled intrinsic mode (BA) tends to remain asymptotically stable at a frequency corresponding to $\cos\left(k_1 x_q\right) = 0$, as per equation (16). Notations and other parameters are the same as in figure 22.
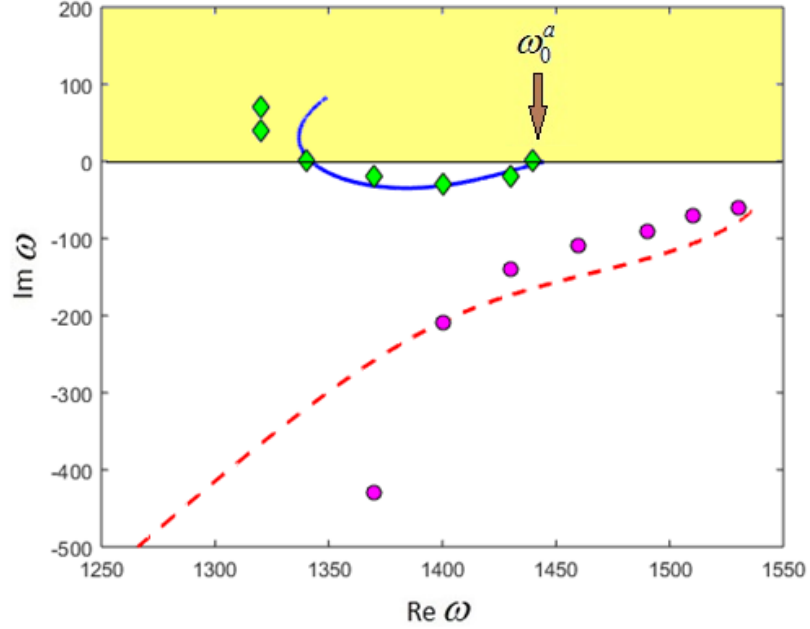
Figure 4.25: Numerical validation of analytical solution (30) for τ =7 ms, x_q =0.35 m, m^a =1, m^i =1. This is an example of the **fourth type of coupling**, where the coupled intrinsic mode (BA) becomes unstable with $\omega_c^i \tau = 0$, whereas the coupled intrinsic mode (BI) tends to remain asymptotically stable at a frequency corresponding to $\cos\left(k_1 x_q\right) = 0$, as per equation (16). Notations and other parameters are the same as in figure 22.

4.6.4. Uncoupling of acoustic and intrinsic modes when the flame is at the middle of the combustor

So far, we have examined linear coupling within the framework of a 1-D open-open combustor. In this section, we provide an example of a scenario of a tube with open-open boundary conditions and find a position within the tube where acoustic and intrinsic modes are naturally uncoupled.

When the flame sits in the middle of the combustor, that is $x_q = L/2$, the dispersion relation (8) simplifies to the following form, if we assume no temperature jump across the flame, that is, $\rho_1 = \rho_2$ and $c_1 = c_2 = c$,

$$\sin\left(\frac{\omega L}{c}\right)\left\{(\alpha + 1) + n_0 e^{i\omega\tau}\right\} = 0. \tag{4.32}$$

241

It is evident that equation (32) leads to two independent sets of solutions for any values of n_0 and τ. These are as follows:

i. Solution for the acoustic modes, i.e. $\sin\left(\dfrac{\omega L}{c}\right) = 0$, and

ii. Solution for the intrinsic modes, i.e. $(\alpha + 1) + n_0 e^{i\omega\tau} = 0$ (4.33 a, b)

Equation (33b) is identical to Hoeijmakers et al. (2014), for the case of a flame in an infinite tube (with anechoic boundary condition), and Mukherjee et al. (2016), for the case of a closed-open combustor when $n \to 0$. Moreover, equations (33 a,b) are self-evident that the acoustic and intrinsic modes get uncoupled and become independent of each other when the flame sits in the middle of the tube (that is $x_q = L/2$). This result is, however, based on the assumption that there is no temperature jump across the flame. With temperature jump, flame-acoustic coupling will, to a degree, occur.

Thus, we have identified that for the case of a tube with the open-open boundary condition, when we assume the flame to be in the middle of the tube and no temperature jump across the flame, the acoustic and intrinsic modes become uncoupled and do not interact with each other. However, coupling will occur when we incorporate temperature jump across the flame into our analysis.

4.7. Salient similarities and differences of flame intrinsic instability for combustors with closed-open and open-open end conditions

Upon performing an analysis of flame intrinsic instability for a closed-open combustor (in chapter 2) and for an open-open combustor (in this chapter), we are in

a position to identify the salient similarities and differences of intrinsic instabilities in these two types of combustor configurations. The current section will highlight these similarities and differences.

The neutral loops for both these two combustor types are combinations of neutral curve segments $\omega_c^i \tau = 0$, $\omega_c^i \tau = \pi$ and $\omega_c^i \tau = -\pi$. However, there is a fundamental difference for the neutral loop on the extreme right for these two cases. The neutral loop on the extreme right for a closed-open combustor consists of all three neutral curve segments $\omega_c^i \tau = 0$, $\omega_c^i \tau = \pi$ and $\omega_c^i \tau = -\pi$. Thus, it has two intersection points of these segments and also, for a sufficiently large time lag value, each intrinsic mode is stable. This scenario is slightly different for an open-open combustor, where the neutral loop on the extreme right consists of neutral curve segments $\omega_c^i \tau = 0$ and $\omega_c^i \tau = \pi$. The neutral curve segment $\omega_c^i \tau = -\pi$ is missing here. Hence, all the intersection points in this loop are due to neutral curve segments $\omega_c^i \tau = 0$ and $\omega_c^i \tau = \pi$. Therefore, the coupled frequency never exhibits a $-\pi/\tau$ shift. Also, in contrast to a closed-open combustor, for sufficiently large time lag values, any particular intrinsic mode is unstable in an open-open combustor. For these combustor setups, the intrinsic mode frequency is decoupled from all the combustor parameters on the neutral curve and is identical to the value found in the limit of small n.

The n-threshold dependence on the flame location is symmetric with respect to $x_q = L/2$ for a closed-open combustor, but not for an open-open combustor. For $S_2/S_1 = 1$ and $c_2/c_1 = 1$, $x_q = L/2$ is the location of n-threshold minima for a closed-open combustor, indicating $x_q = L/2$ in a closed-open combustor corresponds to the critical region from an intrinsic instability perspective. However, for an open-

open combustor, no such minima exist. For an open-open combustor, as x_q increases, the maximum n-threshold increases, indicating that the small values of x_q in an open-open combustor correspond to the critical region from an intrinsic instability perspective. Moreover, unlike closed-open combustors, in open-open combustors, for very large τ we have a huge number of simultaneously unstable intrinsic modes. In the closed-open combustor neutral curves, multiple intrinsic modes can indeed become unstable, but there exists no such τ domain where large numbers of intrinsic modes are unstable. The cross-section jump across the flame holds the potential to reduce n-threshold in an open-open combustor, unlike in a closed-open combustor. In contrast, the temperature jump was found to always enhance the n-threshold for an open-open combustor. In a closed-open combustor, temperature jump can lower the n-threshold for some τ.

The intrinsic-acoustic mode coupling scenario is identical for both closed-open and open-open combustors. In both types of combustors, we see the same four types of coupling between intrinsic and acoustic modes, depending on which mode becomes unstable (or remains asymptotically stable) at which frequency. The only difference is in the coupling behavior in the main neutral loop of instability. As mentioned in the beginning of this section, in a closed-open combustor we have intersection points between neutral curve segments: $\omega_c^i \tau = 0$ and $\omega_c^i \tau = \pi$, and $\omega_c^i \tau = 0$ and $\omega_c^i \tau = -\pi$, in the extreme right neutral loop. Thus, the coupled mode can have a frequency shift of $\pm \pi/\tau$. In an open-open combustor, intersection exists only between neutral curve segments $\omega_c^i \tau = 0$ and $\omega_c^i \tau = \pi$ in the extreme right neutral loop. Thus, the coupled mode exhibits a frequency shift of only π/τ.
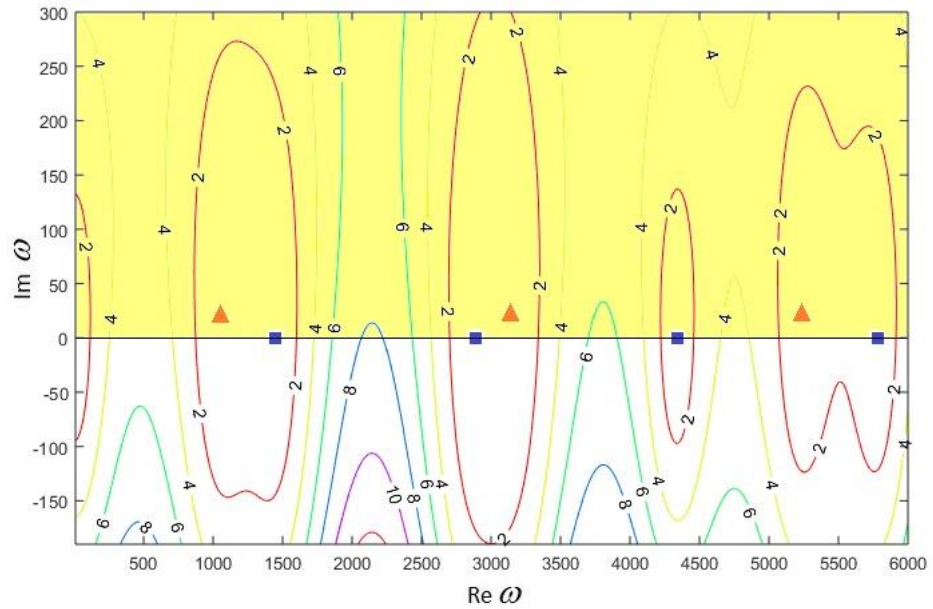
Figure 4.26: Contour plot of $|g(\omega)|$ for $\tau = 3.0$ ms and $n = 2.1$, $x_q = L/2$. Notation and other parameters are the same as in Fig.2. The domain of instability is marked in yellow. Blue squares and orange triangles represent the acoustic and intrinsic modes respectively.
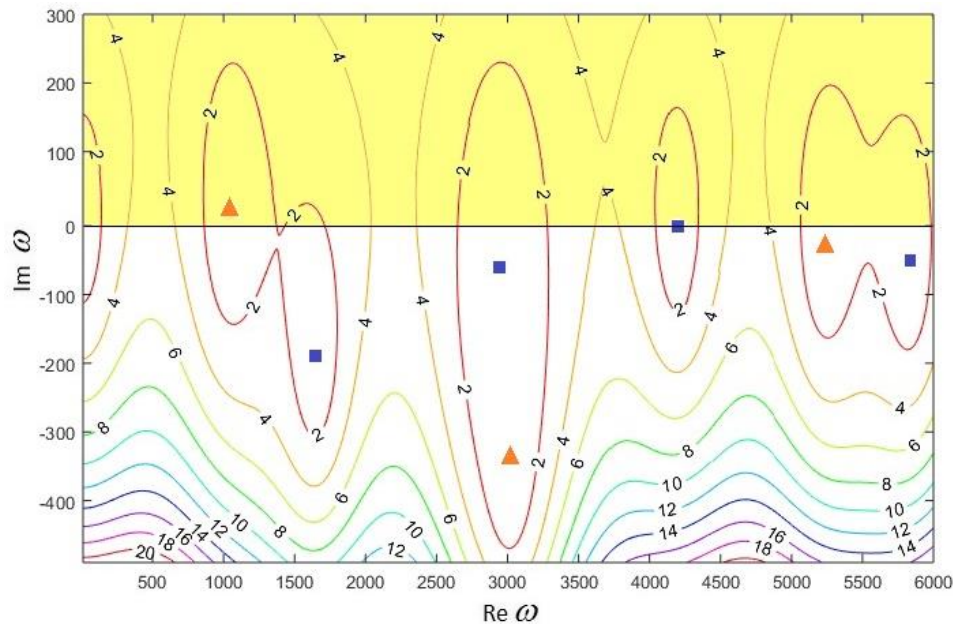
Figure 4.27: Contour plot of $|g(\omega)|$ for $\tau = 3.0$ ms and $n = 1.0$, $x_q = 0.20$ m. Notation and other parameters are the same as in Fig.2. The domain of instability is marked in yellow. Blue squares and orange triangles represent the acoustic and intrinsic modes respectively.

We noted in the concluding section of chapter 2, that under certain conditions in a closed-open combustor, the intrinsic mode can be unstable, while all the acoustic

modes decay simultaneously, thus driving the combustion instability. The same scenario can appear in an open-open combustor as well. Figures 26 and 27 illustrates two such cases using contour plots of $|g(\omega)|$. In figure 26, the flame is at the middle of the combustor, that is $x_q = L/2$. We see that for $n = 2.1$ the first three intrinsic modes are unstable, whereas the acoustic modes remain on the neutral curve of stability, just like they do when $n = 0$. Another example is shown in figure 27, where the flame resides at $x_q = 0.20$ m. We find that for $n = 1.0$, the first intrinsic mode is unstable, whereas all other modes (acoustic/intrinsic) are either stable or on the neutral curve. These two scenarios are examples of when an intrinsic mode, instead of an acoustic mode, drives the combustion instability.

Thus, indeed, there exist some similarities and dissimilarities in flame intrinsic instability within closed-open and open-open combustors. But in general, it cannot be said which combustor profile is more critical from an intrinsic flame instability perspective. Using the guidelines prescribed above, it must be checked on a case-by-case basis for all the flame and combustor parameters.

4.8. Conclusions

In the current chapter, we have analytically studied the features of flame intrinsic modes within a 1-D open-open combustor, making use of linear $n - \tau$ heat release. We also mathematically described the intrinsic-acoustic mode coupling scenario for the open-open combustor. Similar to § 6 of chapter 3, we derived a quadratic equation able to describe intrinsic-acoustic mode coupling. Our main observations made in this chapter can be summarized as follows:

i.   In the asymptotic limit of small n, the behavior of intrinsic modes for any 1-D combustor setup was found to be the same as that of a closed-open combustor. In this limit, there exists an infinite number of strongly decaying intrinsic modes. Their frequencies depend only on the time lag and mode number m^i of the intrinsic mode and are independent of other combustor and flame parameters. This mode number is independent of the mode number of the acoustic mode. In the limit of small n, the decay rate of the intrinsic modes does not depend on the mode number, is inversely proportional to τ and is logarithmically dependent on n. For small n, intrinsic modes do not feel the combustor boundaries and are independent of the flame location.

ii.   For any τ, each intrinsic mode becomes unstable above a certain threshold of n. The threshold depends on the combustor parameters and flame position, shown by equation (21). The neutral curve for each intrinsic mode consists of some combination of neutral curve segments $\omega_c^i \tau = 0$, $\omega_c^i \tau = \pi$ and $\omega_c^i \tau = -\pi$, where ω_c^i is the discrepancy between the real part of the frequency on the neutral curve and the real part of the frequency in the limit of small n. The neutral curve has two principal segments, one large loop on the extreme right (for larger time lag) and a series of smaller loops of reducing τ scale on the left (for smaller time lag). In contrast to a closed-open combustor, the large neutral loop on the extreme right only consists of neutral segments $\omega_c^i \tau = 0$ and $\omega_c^i \tau = \pi$ (except at the middle of the combustor, where n-threshold has a constant value of 2). The neutral curve segment $\omega_c^i \tau = -\pi$ does not feature there. The nature of the smaller neutral loops is exactly the same as that of a closed-open combustor. On the neutral curve, the intrinsic mode completely decouples from the combustor environment and the instability frequency is

independent of the flame location and the combustor parameters. Like in a closed-open combustor, in this case, the intrinsic modes (and the acoustic modes that get coupled to them) can become unstable at a much lower n-threshold than for a flame in an infinite tube (Hoeijmakers et al. (2014)). We have also developed an explicit analytical formula to predict the growth rates for each intrinsic mode. The neutral curves and the growth rate predictions have been successfully verified by numerics.

iii.   The intrinsic flame instabilities have been described analytically as a function of combustor parameters like the flame location, the cross-section and temperature jumps across the flame. Just as for a closed-open combustor, here as well, by manipulating the system parameters like cross section jump, temperature jump, and flame location, combustor designers can increase the n^i_{th} and decrease the growth rate, hence preventing/controling the intrinsic mode instability.

iv.   We have studied the scenario when intrinsic and acoustic modes come close to each other in the complex frequency plane. In the context of intrinsic-acoustic mode coupling, the four possible types have been identified:

1. In the **first type of coupling**, the coupled intrinsic mode (BI) becomes unstable at a frequency predicted by $\omega^i_c \tau = 0$, whereas the coupled intrinsic mode (BA) becomes unstable at a frequency predicted by either $\omega^i_c \tau = \pi$ or $\omega^i_c \tau = -\pi$.

2. In the **second type of coupling**, the coupled intrinsic mode (BA) becomes unstable at a frequency predicted by $\omega^i_c \tau = 0$, whereas the coupled intrinsic mode (BI) becomes unstable at a frequency predicted by either $\omega^i_c \tau = \pi$ or $\omega^i_c \tau = -\pi$.

3. In the **third type of coupling**, the coupled intrinsic mode (BI) becomes unstable at $\omega^i_c \tau = 0$, whereas the coupled intrinsic mode (BA) tends to remain asymptotically

stable at a frequency corresponding to $\cos\left(k_1 x_q\right) = 0$ or $\sin\left(k_1\left(x_q - L\right)\right) = 0$, as per equation (16).

4. In the **fourth type of coupling**, the coupled intrinsic mode (BA) becomes unstable at $\omega_c^i \tau = 0$, whereas the coupled intrinsic mode (BI) tends to remain asymptotically stable at a frequency corresponding to $\cos\left(k_1 x_q\right) = 0$ or $\sin\left(k_1\left(x_q - L\right)\right) = 0$, as per equation (16).

Clearly, in the first two types of coupling, we have two unstable frequencies in each case. In contrast, for the last two types of coupling, we have only one unstable frequency, while the other mode stays linearly stable for large n. All these types of coupling can also be seen in a closed-open combustor. The regions of the neutral curve close to the intersection of lines $\omega_c^i \tau = 0$ and $\omega_c^i \tau = \pi$, in the large neutral loop on the extreme right, show strong evidence of coupling. Moreover, the neutral loops on the left-hand side of the stability plots (corresponding to small τ values), manifest strong coupling, because the neutral curve segments $\omega_c^i \tau = 0$, $\omega_c^i \tau = \pi$ and $\omega_c^i \tau = -\pi$ stay very close to each other. Near the neutral curve intersection points, coupled modes invariably change their identity, thus changing the type of coupling. We have verified our result with numerics and the accuracy level of prediction by our analytical result is found to be good. The prediction is quite accurate as we stay close to the neutral line of stability, where the actual intrinsic-acoustic mode coupling takes place. However, as we try to capture the locus of the coupled intrinsic mode (BI) far away from the neutral curve, the accuracy level of the analytical model drops.

The present work was focused on the analytic study of linear intrinsic flame modes using the simplest $n - \tau$ model of a flame in an open-open combustor. The $n - \tau$ model itself could be improved in many respects. A particular improvement could

take into account the randomly distributed delay (e.g. Schuermans et al. (2004), Alemela et al. (2010)). A study of nonlinear dynamics of intrinsic modes and their nonlinear interactions with acoustic modes in an open-open combustor should be taken care of thoroughly. We can introduce mean flow in our analysis to identify how this affects the stability behavior of the intrinsic modes. The interaction between intrinsic modes of very low frequency and hydrodynamic modes should also be a topic of interest.

Chapter 5

Flame intrinsic instability in combustors with imperfect end conditions

5.1.   Introduction

In chapters 2 and 4, intrinsic modes in closed-open and open-open systems were examined under the assumption of perfect end conditions of the combustors. This is a mere approximation of a practical system. In reality, it is not necessarily a good approximation to say that the reflection coefficients are equal to ± 1, as it was assumed in chapters 2 and 4. Reflection coefficients are complex, meaning the reflection coefficient has a dissipative and a reactive part associated with it. The energy losses at the ends of the combustor account for the dissipative component in the reflection coefficient. A perfectly rigid or closed end will reflect the incident waves totally, without acoustic losses [Munjal (1987)], meaning the assumption made in chapter 2 and 3 for the closed end reflection coefficient being +1 is a valid one. However, this assumption is not so accurate for the open end. Acoustic radiations from the end of a duct will be impeded by the atmosphere, a phenomenon represented by a parameter called the radiation impedance, which is a complex number for any open duct [Munjal (1987)]. For cylindrical ducts and normal acoustic modes, the

exact solution for the radiation impedance has been provided by Levine and Schwinger (1948). The exact expression for reflection coefficient of the open end of a circular duct with radius r_0 is given as [Munjal (1987)],

$$R = \left(1 - 0.5k^2 r_0^2\right) \exp\left(\pi - 1.2 \tan^{-1}\left(k r_0\right)\right),$$

where, k is the wave number. Clearly, the reflection coefficient for an open end is nearly unity and the phase angle is slightly less than π, meaning that the coefficient is not exactly -1 as we assumed in chapters 2-4. This assumption is valid only when the non-dimensional number $k r_0$ (also known as the Helmholtz number) is small. This is, indeed, a low-frequency assumption. The reflection coefficient is a frequency dependent parameter in most of the cases. This feature of the reflection coefficient of open ends is illustrated by figure 1 (i) [Rammal and Lavrentjev (2008)]. Figures (a) and (b) correspond to 100 ^{0}C, whereas figures (c) and (d) correspond to 400 ^{0}C for the temperature of the flow. The figure also offers an experimental validation of the theoretical model by Munt (1977, 1990) for calculating reflection coefficients of open ends. Figure 1 (i) shows that at zero frequency, the amplitude is exactly 1 and the phase is exactly π, as is also visible from the equation above. With the increase of frequency, the amplitude and phase of the reflection coefficient reduce, as can be seen from figure 1 (i).

The reflection coefficient also changes for ducts with mean flow inside and can exceed unity (e.g., Munjal (1987)). The reason for this was explained as the strengthening of the forward-going acoustic wave pressure in the duct by a factor $\left(1 + M\right)$ and weakening of the backward-traveling acoustic wave pressure in the duct by a factor $\left(1 - M\right)$, where M represents the mean flow Mach number. Apart from that, the reflection coefficient is dependent on flow temperatures within the duct. It

was reported by Rammal and Lavrentjev (2008) that the amplitude of the reflection coefficient reduces with an increase of temperature, as can be seen from figure 1 (i) (c), and does not become greater than 1 at Helmholtz numbers up to 0.8 when mean flow is neglected. Hence, we can see that reflection coefficients are frequency dependent quantities and they have a dependence on flow velocities and flow temperatures within the duct.
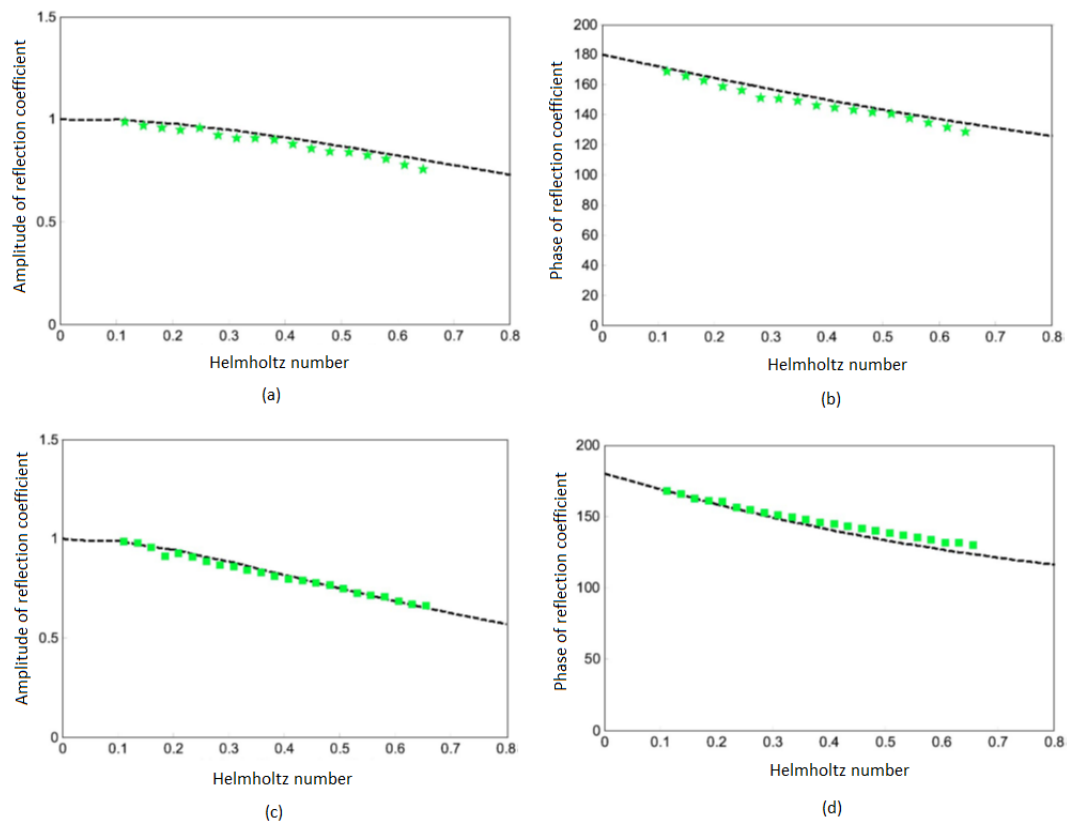
Figure 5.1 (i): (a, c) Amplitude and (b, d) phase of reflection coefficients of an open end vs non-dimensional Helmholtz number (kr_0, where k is the wave number and r_0 is the radius of the circular duct) [Rammal and Lavrentjev (2008)]. Figures (a) and (b) correspond to 100 ^{0}C, whereas figures (c) and (d) correspond to 400 ^{0}C for the temperature of the flow. Green circular dots are the experimentally measured values, whereas the thin dotted line is the theoretical prediction by Munt's model [Munt (1977, 1990)].

Information on the reflection coefficient of a dump combustor with a flame can be found from the work of Poinsot et al. (1986). Figure 1 (ii) represents some sample results of reflection coefficients measured between 400 Hz and 1000 Hz (this

frequency is below the first cut-off frequency of the transverse mode; thus, the plane wave assumption is valid). In a cold flow condition without a flame, as can be found from the panel (a), the reflection coefficient attains two minima at 500 Hz and 800 Hz respectively. When actual combustion is taken care of, the reflection coefficient in the low-frequency range (between 400 Hz and 600 Hz) increases and the minima is shifted to a higher frequency at around 800 Hz. Thus, the flame zone is found to respond actively to the incident pressure waves and the flame response amplitude even exceeds the incident pressure amplitude (as visible from the panel (b)). It was also reported as an observation from the experiment (supplemented by acoustic energy balance calculations) that measurement of the reflection coefficient, under stable conditions, offers a diagnostic mechanism for the prediction of combustion instability.
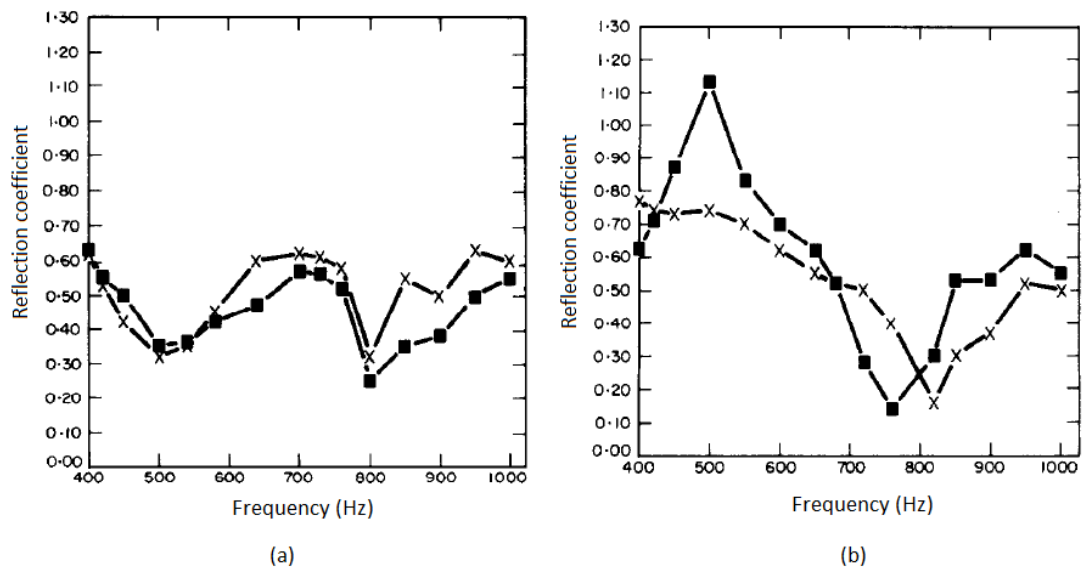
Figure 5.1 (ii): Reflection coefficient of a dump combustor (a) without and (b) with combustion [Poinsot et al. (1986)]. In panel (a) two different air flow rates of 80 g/s and 90 g/s are represented by the cross and square dots respectively. In panel (b) two different air flow rates of 78.5 g/s and 76.6 g/s are represented by the cross and square dots respectively.

Therefore, the assumption that the reflection coefficient at the open end is -1 and at the closed end is +1 is a strong idealization. Besides, in practical gas turbine combustor assembly there is a compressor upstream and a turbine downstream of the combustion chamber, which significantly affects the reflection coefficients at the ends [Silva et al. (2014), Lamarque and Poinsot (2008)]. In this chapter we address this matter and consider the effect of non-ideal or perturbed [Nayfeh (1993)] closed and open boundary conditions of the combustion chamber on the intrinsic mode instability.

The aim of this chapter is twofold: (i) to check whether a small perturbation of the end conditions can drastically alter the analytical results of chapter 2 and 4; (ii) to derive a modified overall picture of intrinsic mode behavior, corrected by considering the non-perfect end boundary conditions. Thus, we first perform the robustness check of our analytical solutions. It is necessary to check whether the solution clears the robustness test for all flame locations and other combustor parameters (like cross section and temperature jump). Upon establishing the robustness, the idealized end conditions can be corrected by explicitly accounting for imperfectness of the boundary conditions where possible.

The chapter is organized as follows: in **§ 2**, we check the robustness of the analytical description of flame intrinsic instability for a closed-open system, derived in chapter 2. In **§ 3**, we examine the robustness of the open-open combustors studied in chapter 4. Finally, in **§ 4**, we make concluding remarks.

5.2. Flame intrinsic instability for closed-open combustors with imperfect end conditions

The dispersion relations (2.20) to (2.23) are a result of the ideal case of perfectly closed-open boundary conditions of the combustor. In reality, imperfections in the boundary conditions have an effect on equations (2.3) and (2.4). We will verify whether the perturbation [Nayfeh (1993)] of our analytical results, due to the imperfections in the boundary condition, is scaled linearly with the imperfections or not.

5.2.1. Robustness of the instability frequencies and neutral curves

When $R_1(0)$ and $R_2(L)$ are retained in the original form in equations (2.3) and (2.4), we derive the generalized dispersion relation as shown in equation (4.1). The real and imaginary parts of equation (4.1) are written as (4.3) and (4.4) on the neutral curve. Now, we consider a case when the end condition of the combustor is not perfectly closed-open and in that case, we can write the reflection coefficients for the ends as,

$$R_1(0) = 1 - \varepsilon_1 r_1, \text{ and } R_2(L) = -1 + \varepsilon_2 r_2, \qquad (5.1, 2)$$

Where, ε_1 and ε_2 are two small parameters characterizing smallness of the deviation from ideal closed-open end condition, r_1 and r_2 are order one complex quantity, specified by the experimental data. r_1 and r_2 can further be written as $r_1 = Re(r_1) + iIm(r_1)$ and $r_2 = Re(r_2) + iIm(r_2)$. Replacing $R_1(0)$ and $R_2(L)$, as per equation (1) and (2), and neglecting the higher order terms, equations (4.3) and (4.4) reduce to the following forms on the neutral curve,

$$(1+\alpha)\Big[2\cos\big(\omega^i\beta_1\big)-\big(\varepsilon_1 Im(r_1)+\varepsilon_2 Im(r_2)\big)\sin\big(\omega^i\beta_1\big)\Big]+$$

$$(1-\alpha)\Big[-2\cos\big(\omega^i\beta_2\big)-\big(\varepsilon_2 Im(r_2)-\varepsilon_1 Im(r_1)\big)\sin\big(\omega^i\beta_2\big)\Big]$$

$$-n^i_{th}\begin{bmatrix}\cos\big(\omega^i_c\tau\big)\begin{cases}2\cos\big(\omega^i\beta_1\big)-\big(\varepsilon_1 Im(r_1)+\varepsilon_2 Im(r_2)\big)\sin\big(\omega^i\beta_1\big)\\[4pt]-2\cos\big(\omega^i\beta_2\big)-\big(\varepsilon_2 Im(r_2)-\varepsilon_1 Im(r_1)\big)\sin\big(\omega^i\beta_2\big)\end{cases}\\[20pt]+\sin\big(\omega^i_c\tau\big)\begin{cases}\big(\varepsilon_1 Im(r_1)+\varepsilon_2 Im(r_2)\big)\cos\big(\omega^i\beta_1\big)\\[4pt]-\big(\varepsilon_1 Re(r_1)+\varepsilon_2 Re(r_2)\big)\sin\big(\omega^i\beta_1\big)\\[4pt]-\big(\varepsilon_1 Im(r_1)+\varepsilon_2 Im(r_2)\big)\cos\big(\omega^i\beta_2\big)\\[4pt]-\big(\varepsilon_2 Re(r_2)-\varepsilon_1 Re(r_1)\big)\sin\big(\omega^i\beta_2\big)\end{cases}\end{bmatrix}=0 \qquad (5.3)$$

$$(1+\alpha)\begin{bmatrix}\big(\varepsilon_1 Im(r_1)+\varepsilon_2 Im(r_2)\big)\cos\big(\omega^i\beta_1\big)-\\[4pt]\big(\varepsilon_1 Re(r_1)+\varepsilon_2 Re(r_2)\big)\sin\big(\omega^i\beta_1\big)\end{bmatrix}$$

$$-(1-\alpha)\begin{bmatrix}\big(\varepsilon_1 Im(r_1)+\varepsilon_2 Im(r_2)\big)\cos\big(\omega^i\beta_2\big)+\\[4pt]\big(\varepsilon_2 Re(r_2)-\varepsilon_1 Re(r_1)\big)\sin\big(\omega^i\beta_2\big)\end{bmatrix}$$

$$-n^i_{th}\begin{bmatrix}\cos\big(\omega^i_c\tau\big)\begin{cases}\big(\varepsilon_1 Im(r_1)+\varepsilon_2 Im(r_2)\big)\cos\big(\omega^i\beta_1\big)-\\[4pt]\big(\varepsilon_1 Re(r_1)+\varepsilon_2 Re(r_2)\big)\sin\big(\omega^i\beta_1\big)\\[4pt]-\big(\varepsilon_1 Im(r_1)+\varepsilon_2 Im(r_2)\big)\cos\big(\omega^i\beta_2\big)-\\[4pt]\big(\varepsilon_2 Re(r_2)-\varepsilon_1 Re(r_1)\big)\sin\big(\omega^i\beta_2\big)\end{cases}\\[24pt]-\sin\big(\omega^i_c\tau\big)\begin{cases}2\cos\big(\omega^i\beta_1\big)-\big(\varepsilon_1 Im(r_1)+\varepsilon_2 Im(r_2)\big)\sin\big(\omega^i\beta_1\big)\\[4pt]-2\cos\big(\omega^i\beta_2\big)-\big(\varepsilon_2 Im(r_2)-\varepsilon_1 Im(r_1)\big)\sin\big(\omega^i\beta_2\big)\end{cases}\end{bmatrix}=0 \qquad (5.4)$$

Both equations (3) and (4) provide explicit expressions for n^i_{th}. Equating n^i_{th} from equations (3) and (4) leads to the following governing equation for ω^i_c,

$$\begin{bmatrix}2\big(\cos\big(\omega^i\beta_1\big)-\cos\big(\omega^i\beta_2\big)\big)\big\{(1+\alpha)\cos\big(\omega^i\beta_1\big)-(1-\alpha)\cos\big(\omega^i\beta_2\big)\big\}\\[4pt]+\varepsilon_1 Im(r_1)\big\{-(1+\alpha)\sin\big(2\omega^i\beta_1\big)-(1-\alpha)\sin\big(2\omega^i\beta_2\big)+2\sin\big(\omega^i\big(\beta_1+\beta_2\big)\big)\big\}\\[4pt]+\varepsilon_2 Im(r_2)\big\{-(1+\alpha)\sin\big(2\omega^i\beta_1\big)+(1-\alpha)\sin\big(2\omega^i\beta_2\big)+2\sin\big(\omega^i\big(\beta_1-\beta_2\big)\big)\big\}\end{bmatrix}\sin\big(\omega^i_c\tau\big)$$

$$=-2\alpha\Big[\varepsilon_1 Re(r_1)\sin\big(\omega^i\big(\beta_1-\beta_2\big)\big)+\varepsilon_2 Re(r_2)\sin\big(\omega^i\big(\beta_1+\beta_2\big)\big)\Big]\cos\big(\omega^i_c\tau\big)$$

$$. \quad (5.5)$$

The ω_c^i in equation (5) is assumed to have two constituent parts. The first part is $\omega_{c,0}^i$, which is the deviation of the instability frequency on neutral curve from the frequency in the limit of small n, for the case of perfect closed-open boundary conditions (as given by (2.31)). The second part is $\tilde{\omega}^i$, due to the imperfections present in the boundary conditions (that is $\varepsilon_1 r_1$ and $\varepsilon_2 r_2$). Therefore ω_c^i can be given as,

$$\omega_c^i = \omega_{c,0}^i + \tilde{\omega}^i. \tag{5.6}$$

Using (6), $\omega^i = \omega_0^i + \omega_c^i$ can also be restructured as $\omega^i = \omega_{0,t}^i + \tilde{\omega}^i$, where $\omega_{0,t}^i$ can be explained as the instability frequencies on the neutral curves for a combustor with perfectly closed-open end conditions,

$$\omega_{0,t}^i = \omega_0^i + \omega_{c,0}^i. \tag{5.7}$$

With the help of equations (6) – (7), the trigonometric expressions in equation (5) can be expanded in the following way, assuming smallness of $\tilde{\omega}^i$,

$$\sin\left(\omega_c^i \tau\right) = \sin\left\{\left(\omega_{c,0}^i + \tilde{\omega}^i\right)\tau\right\} = \sin\left(\omega_{c,0}^i \tau\right) + \tilde{\omega}^i \tau \cos\left(\omega_{c,0}^i \tau\right),$$

$$\cos\left(\omega_c^i \tau\right) = \cos\left\{\left(\omega_{c,0}^i + \tilde{\omega}^i\right)\tau\right\} = \cos\left(\omega_{c,0}^i \tau\right) - \tilde{\omega}^i \tau \sin\left(\omega_{c,0}^i \tau\right), \qquad \text{(5.8 a, b)}$$

$$\cos\left(\omega^i \beta_1\right) = \cos\left\{\left(\omega_{0,t}^i + \tilde{\omega}^i\right)\beta_1\right\} = \cos\left(\omega_{0,t}^i \beta_1\right) - \tilde{\omega}^i \beta_1 \sin\left(\omega_{0,t}^i \beta_1\right),$$

$$\cos\left(\omega^i \beta_2\right) = \cos\left\{\left(\omega_{0,t}^i + \tilde{\omega}^i\right)\beta_2\right\} = \cos\left(\omega_{0,t}^i \beta_2\right) - \tilde{\omega}^i \beta_2 \sin\left(\omega_{0,t}^i \beta_2\right),$$

$$\sin\left\{\omega^i\left(\beta_1 + \beta_2\right)\right\} = \sin\left\{\left(\omega_{0,t}^i + \tilde{\omega}^i\right)\left(\beta_1 + \beta_2\right)\right\}$$
$$= \sin\left\{\omega_{0,t}^i\left(\beta_1 + \beta_2\right)\right\} + \tilde{\omega}^i\left(\beta_1 + \beta_2\right)\cos\left\{\omega_{0,t}^i\left(\beta_1 + \beta_2\right)\right\},$$

$$\sin\left\{\omega^i\left(\beta_1 - \beta_2\right)\right\} = \sin\left\{\left(\omega_{0,t}^i + \tilde{\omega}^i\right)\left(\beta_1 - \beta_2\right)\right\}$$
$$= \sin\left\{\omega_{0,t}^i\left(\beta_1 - \beta_2\right)\right\} + \tilde{\omega}^i\left(\beta_1 - \beta_2\right)\cos\left\{\omega_{0,t}^i\left(\beta_1 - \beta_2\right)\right\}.$$

$$\text{(5.9 a, b, c, d)}$$

Where, $(\beta_1 - \beta_2)$ and $(\beta_1 + \beta_2)$ are deduced as the following, in terms of combustor parameters from equation (2.18),

$$\beta_1 - \beta_2 = 2(x_q - L)/c_2 \quad \text{and} \quad \beta_1 + \beta_2 = -2x_q/c_1 . \tag{5.10}$$

After further simplification of equation (5), by making use of (8) and (9), we arrive at the following compact expression for $\tilde{\omega}^i$,

$$\tilde{\omega}^i = \frac{-\alpha\left[\varepsilon_1 Re(r_1)\sin\left\{\omega_{0,t}^i(\beta_1 - \beta_2)\right\} + \varepsilon_2 Re(r_2)\sin\left\{\omega_{0,t}^i(\beta_1 + \beta_2)\right\}\right]}{\tau\left[(1+\alpha)\cos\left(\omega_{0,t}^i\beta_1\right) - (1-\alpha)\cos\left(\omega_{0,t}^i\beta_2\right)\right]\left\{\cos\left(\omega_{0,t}^i\beta_1\right) - \cos\left(\omega_{0,t}^i\beta_2\right)\right\}} . \tag{5.11}$$

Making use of $(\beta_1 - \beta_2)$ and $(\beta_1 + \beta_2)$, as given by (10), and α, β_1 and β_2, as given by (2.28), equation (11) can be rewritten in the following form, depicting the effect of all combustor parameters like flame location, cross-section jump, and temperature jump,

$$\tilde{\omega}^i = \frac{\left(\dfrac{S_2}{S_1}\dfrac{\rho_1}{\rho_2}\dfrac{c_1}{c_2}\right)\left[-\varepsilon_1 Re(r_1)\sin\left(\dfrac{2\omega_{0,t}^i(x_q - L)}{c_2}\right) + \varepsilon_2 Re(r_2)\sin\left(\dfrac{2\omega_{0,t}^i x_q}{c_1}\right)\right]}{\tau\left[\begin{array}{l}\left[\left(1+\dfrac{S_2}{S_1}\dfrac{\rho_1}{\rho_2}\dfrac{c_1}{c_2}\right)\cos\left\{\omega_{0,t}^i\left(\dfrac{x_q}{c_2} - \dfrac{x_q}{c_1} - \dfrac{L}{c_2}\right)\right\} - \right. \\ \left.\left(1-\dfrac{S_2}{S_1}\dfrac{\rho_1}{\rho_2}\dfrac{c_1}{c_2}\right)\cos\left\{\omega_{0,t}^i\left(\dfrac{L}{c_2} - \dfrac{x_q}{c_1} - \dfrac{x_q}{c_2}\right)\right\}\right] \\ \left[\cos\left\{\omega_{0,t}^i\left(\dfrac{x_q}{c_2} - \dfrac{x_q}{c_1} - \dfrac{L}{c_2}\right)\right\} - \cos\left\{\omega_{0,t}^i\left(\dfrac{L}{c_2} - \dfrac{x_q}{c_1} - \dfrac{x_q}{c_2}\right)\right\}\right]\end{array}\right]} . \tag{5.12}$$

It is clear from (12) that the perturbation at the corresponding ends of the combustor perturbs $\omega_{c,0}^i$ linearly in ε_1 and ε_2. This conclusion holds when cross-section jump is also taken into consideration. However, the effect of temperature jump introduces intricate effects of c_1 and c_2 into trigonometric expressions of (12), making it

difficult to analyze the equation further. For simplicity, we assume $S_1 = S_2$ and $T_1 = T_2$, and thus $c_1 = c_2 = c$, $\rho_1 = \rho_2$;

$$\tilde{\omega}^i = \frac{-\varepsilon_1 Re(r_1)\sin\left(\dfrac{2\omega_{0,t}^i\left(x_q - L\right)}{c}\right) + \varepsilon_2 Re(r_2)\sin\left(\dfrac{2\omega_{0,t}^i x_q}{c}\right)}{2\tau\cos\left(\dfrac{\omega_{0,t}^i L}{c}\right)\left\{\cos\left(\dfrac{\omega_{0,t}^i L}{c}\right) - \cos\left(\dfrac{\omega_{0,t}^i\left(2x_q - L\right)}{c}\right)\right\}}.$$ (5.13)

Once $\tilde{\omega}^i$ is obtained, using (13), ω_c^i can be found in the following way, as $\omega_{c,0}^i = m\pi/\tau$,

$$\omega_c^i = \frac{m\pi}{\tau} + \tilde{\omega}^i .$$ (5.14)

Where, $m = -1, 0, +1$, as explained in § 4.1 of chapter 2. The instability frequency for a combustor with non-ideal closed-open end conditions can be evaluated as a straightforward deduction from equation (14) and making use of $\omega^i = \omega_0^i + \omega_c^i$. Further, making use of (14), the threshold of n for non-ideal end conditions can be obtained from equation (3),

$$n_{th}^i = \frac{2\left[(1+\alpha)\cos\left(\omega^i\beta_1\right) - (1-\alpha)\cos\left(\omega^i\beta_2\right)\right] + \varepsilon_1 G_1 + \varepsilon_2 G_2}{2\cos\left(\omega_c^i\tau\right)\left\{\cos\left(\omega^i\beta_1\right) - \cos\left(\omega^i\beta_2\right)\right\}}.$$ (5.15)

where G_1 and G_2 are given by the following expressions,

$$G_1 = -(1+\alpha)Im(r_1)\sin\left(\omega^i\beta_1\right) + (1-\alpha)Im(r_1)\sin\left(\omega^i\beta_2\right)$$
$$+ n_{th,0}^i\left\{\begin{array}{l} Im(r_1)\left(\sin\left(\omega^i\beta_1\right) - \sin\left(\omega^i\beta_2\right)\right)\cos\left(\omega_c^i\tau\right) \\ + Im(r_1)\left(-\cos\left(\omega^i\beta_1\right) + \cos\left(\omega^i\beta_2\right)\right)\sin\left(\omega_c^i\tau\right) \\ + Re(r_1)\left(\sin\left(\omega^i\beta_1\right) - \sin\left(\omega^i\beta_2\right)\right)\sin\left(\omega_c^i\tau\right) \end{array}\right\} , \text{ and}$$

$$G_2 = -(1+\alpha) Im(r_2) \sin(\omega^i \beta_1) - (1-\alpha) Im(r_2) \sin(\omega^i \beta_2)$$

$$+ n_{th,0}^i \left\{ \begin{array}{l} Im(r_2)\big(\sin(\omega^i \beta_1) + \sin(\omega^i \beta_2)\big)\cos(\omega_c^i \tau) \\ + Im(r_2)\big(-\cos(\omega^i \beta_1) + \cos(\omega^i \beta_2)\big)\sin(\omega_c^i \tau) \\ + Re(r_2)\big(\sin(\omega^i \beta_1) + \sin(\omega^i \beta_2)\big)\sin(\omega_c^i \tau) \end{array} \right\}.$$

Here, $n_{th,0}^i$ is the threshold of n for ideal closed-open end conditions. In the limiting case, $\varepsilon_1 = \varepsilon_2 = 0$, from (14) and (15) we retrieve expressions (2.31) and (2.33) for a combustor with perfectly closed-open boundary condition. According to (15), the effect of ε_1 and ε_2 on n_{th}^i is linear in ε_1 and ε_2, hence, the effect is indeed small for small ε_1 and ε_2. The same observation can be made from equations (11)-(13), which depicts that, to leading order, the correction due to imperfection of the end conditions depends linearly on ε_1 and ε_2, any O(ε_1) or O(ε_2) imperfection in the end conditions perturbs the solution only linearly and hence only slightly. Therefore, we can conclude that our analytical solutions for the closed-open combustor are robust in general. However, there are some exceptions in this. As per equation (13), there are two cases when the solutions fail to retain their robustness. Those cases are as follows:

i. When $\cos(\omega_{0,t}^i L/c) = \cos(\omega_{0,t}^i (2x_q - L)/c)$, i.e. the flame lies close to one of the ends of the combustor. As per equation (15), the corresponding n_{th}^i goes to infinity, for this case.

ii. When on the neutral curve, we attain a condition of $\cos(\omega_{0,t}^i L/c) = 0$.

Regarding the first case, we note that when n_{th}^i goes to infinity, the notion of robustness will be irrelevant for that case, as the system is expected to behave as

261

linearly stable for all n. For the two aforementioned cases, when the analytical solutions derived in chapter 2 lose their robustness, they need to be studied separately in greater detail. In the present context, we refrain from this task.

A detailed explanation of the effect of the perturbation on acoustic end conditions of the combustor on neutral curves of intrinsic modes can be provided with the help of figures 2-7. In these figures, the blue line represents the neutral curve for the second intrinsic mode with ideal closed-open end conditions. The elliptical dots represent the area of the neutral curve when the robustness of analytical solution (15) does not hold. Panel (a), (b) and (c) in each figure represent three different cases when the linear perturbation is assumed on the acoustic end condition of the closed end, the open end and both the ends respectively. Thus, for panel (a), $\varepsilon_2 = 0$, for panel (b) $\varepsilon_1 = 0$ and for panel (c), both ε_1 and ε_2 are non-zero.

Figure 5.2: Neutral curves on the $n-\tau$ plane for the second intrinsic mode (m^i =1) of a closed-open combustor based on equation (15). Continuous blue lines represent the neutral curves for ε_1 =0.0 and ε_2 =0.0. Dashed-dotted green lines represent the neutral curves for (a) ε_1 =0.1, r_1 =1.0, ε_2 =0.0; (b) ε_1 =0.0, ε_2 =0.1, r_2 =1.0; and (c) ε_1 =0.1, r_1 =1.0, ε_2 =0.1, r_2 =1.0 respectively. Elliptical dots represent the areas on the neutral curves where the analytical solution (15) ceases to be robust. The parameters are the same as in figure 2.8.

In figures 2-4, linear real perturbation (ε_1 and/or ε_2) of 0.1, 0.3 and 0.5 respectively is assumed. The dashed-dotted green line depicts the perturbed solution. A common feature of all these figures is that the neutral segment corresponding to $\omega_c^i \tau = 0$ is very robust, particularly in between the intersection points of the neutral segments. In most of the cases, they tend to overlap with the neutral segments $\omega_c^i \tau = 0$, corresponding to the closed-open combustor with ideal end conditions and hence are hardly distinguishable. A massive perturbation of 50% does not change this feature, as evident from figure 4. However, the same is not true for the neutral segments $\omega_c^i \tau = \pm\pi$ attributed to the coupling of intrinsic-acoustic modes. The neutral segment $\omega_c^i \tau = -\pi$ is found to lose its robustness at 30% perturbation, as can be seen from figure 3. A possible reason is that equation (15) is a derivative of single mode perturbation analysis of intrinsic modes. However, in the coupled domain, we have two solutions and hence both solutions need to be perturbed simultaneously to arrive at the exact solution. Hence, the neutral segments $\omega_c^i \tau = \pm\pi$ are much less robust in contrast to the neutral segment $\omega_c^i \tau = 0$. In all these figures, panels (a) and (b) demonstrate more robustness compared to panel (c), as in panel (c), both end conditions are perturbed simultaneously.
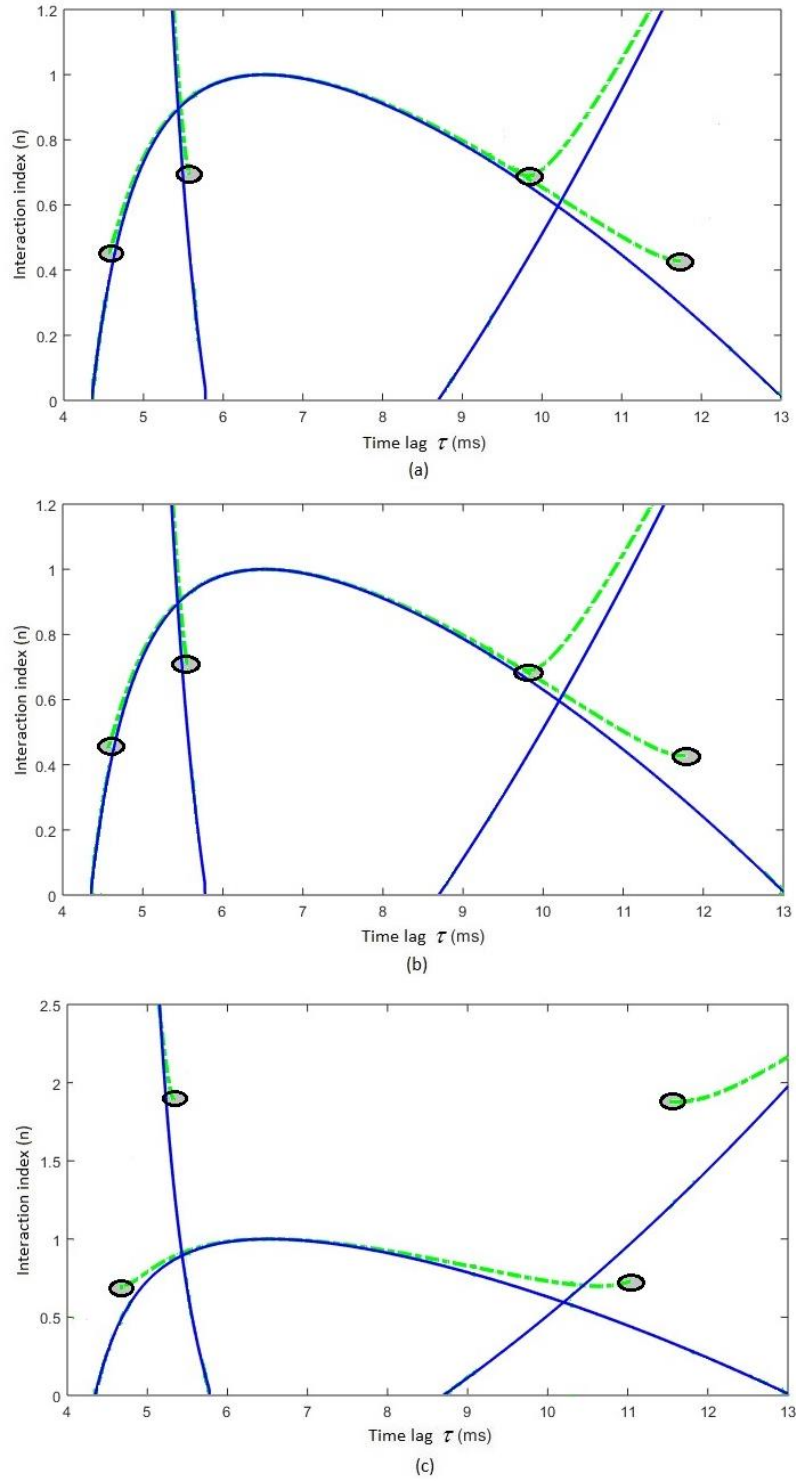
Figure 5.3: Neutral curves on the $n - \tau$ plane for the second intrinsic mode ($m^i = 1$) of a closed-open combustor, based on equation (15). Dashed-dotted green lines represent the neutral curves for (a) $\varepsilon_1 = 0.3$, $r_1 = 1.0$, $\varepsilon_2 = 0.0$; (b) $\varepsilon_1 = 0.0$, $\varepsilon_2 = 0.3$, $r_2 = 1.0$; and (c) $\varepsilon_1 = 0.3$, $r_1 = 1.0$, $\varepsilon_2 = 0.3$, $r_2 = 1.0$ respectively. Notations and other parameters are the same as in figure 2.
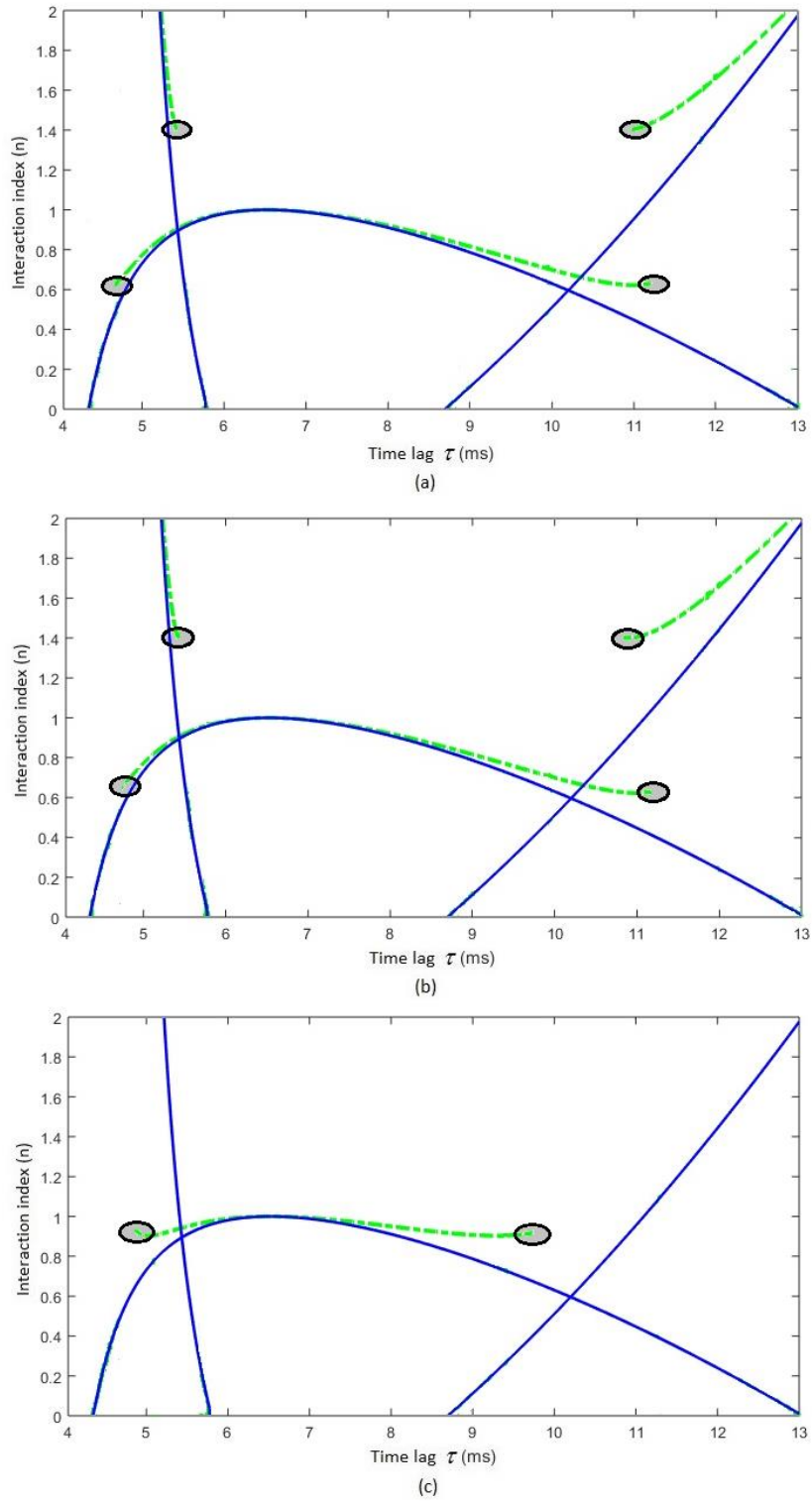
Figure 5.4: Neutral curves on the $n - \tau$ plane for the second intrinsic mode ($m^i = 1$) of a closed-open combustor, based on equation (15). Dashed-dotted green lines represent the neutral curves for (a) $\varepsilon_1 = 0.5$, $r_1 = 1.0$, $\varepsilon_2 = 0.0$; (b) $\varepsilon_1 = 0.0$, $\varepsilon_2 = 0.5$, $r_2 = 1.0$; and (c) $\varepsilon_1 = 0.5$, $r_1 = 1.0$, $\varepsilon_2 = 0.5$, $r_2 = 1.0$ respectively. Notations and other parameters are the same as in figure 2.

In figures 5-6, linear imaginary perturbation (ε_1 and/or ε_2) of $\pm i*0.1$ and $\pm i*0.3$ respectively is assumed. The dashed-dotted green lines correspond to the neutral curves due to $+i*0.1$ and $+i*0.3$ perturbations, whereas the dashed-dotted red lines correspond to the neutral curves due to $-i*0.1$ and $-i*0.3$ perturbations respectively. The neutral segments due to $+i*0.1$, and $+i*0.3$ perturbations tend to move to the left, whereas the neutral segments due to $-i*0.1$ and $-i*0.3$ perturbations tend to move to the right, compared to the neutral curve for ideal end conditions. As a general observation, it can be claimed that the imaginary perturbation has a more significant impact on all neutral segments than the real perturbation of end conditions. Nevertheless, the shifts in the neutral segments $\omega_c^i \tau = \pm \pi$ are more prominent. In figure 7, linear complex perturbation (ε_1 and/or ε_2) of $(1\pm i)*0.1$ and $(1\pm i)*0.3$ is assumed. This case is indeed a combination of figures 2 and 5, where we see a shift of the neutral curves either to the left or right, due to the imaginary part of the perturbation and loss of robustness in the $\omega_c^i \tau = \pm \pi$, due to real part of the perturbation. However, the neutral segment $\omega_c^i \tau = 0$ is found to retain robustness in between the point of intersections of the neutral segments $\omega_c^i \tau = 0$ and $\omega_c^i \tau = \pm \pi$.
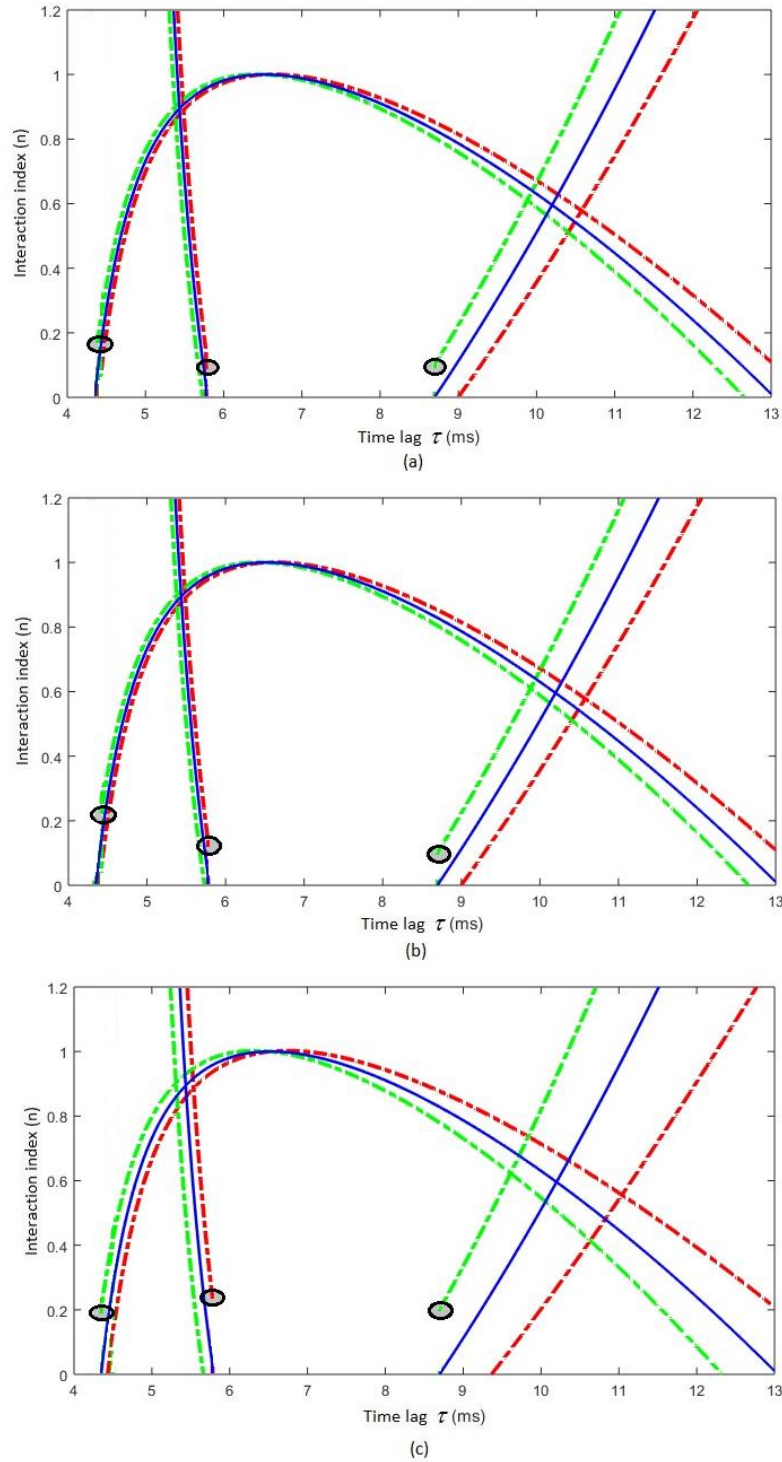
Figure 5.5: Neutral curves on the $n - \tau$ plane for the second intrinsic mode (m^i =1) of a closed-open combustor, based on equation (15). Dashed-dotted green lines represent the neutral curves for (a) ε_1 =0.1, $r_1 = i*1.0$, ε_2 =0.0; (b) ε_1 =0.0, ε_2 =0.1, $r_2 = i*1.0$; and (c) ε_1 =0.1, $r_1 = i*1.0$, ε_2 =0.1, $r_2 = i*1.0$ respectively. Dashed-dotted red lines represent the neutral curves for (a) ε_1 =0.1, $r_1 = -i*1.0$, ε_2 =0.0; (b) ε_1 =0.0, ε_2 =0.1, $r_2 = -i*1.0$; and (c) ε_1 =0.1, $r_1 = -i*1.0$, ε_2 =0.1, $r_2 = -i*1.0$ respectively. Notations and other parameters are the same as in figure 2.

Figure 5.6: Neutral curves on the $n - \tau$ plane for the second intrinsic mode (m^i =1) of a closed-open combustor, based on equation (15). Dashed-dotted green lines represent the neutral curves for (a) ε_1 =0.3, $r_1 = i * 1.0$, ε_2 =0.0; (b) ε_1 =0.0, ε_2 =0.3, $r_2 = i * 1.0$; and (c) ε_1 =0.3, $r_1 = i * 1.0$, ε_2 =0.3, $r_2 = i * 1.0$ respectively. Dashed-dotted red lines represent the neutral curves for (a) ε_1 =0.3, $r_1 = -i * 1.0$, ε_2 =0.0; (b) ε_1 =0.0, ε_2 =0.3, $r_2 = -i * 1.0$; and (c) ε_1 =0.3, $r_1 = -i * 1.0$, ε_2 =0.3, $r_2 = -i * 1.0$ respectively. Notations and other parameters are the same as in figure 2.

Figure 5.7: Neutral curves on the $n - \tau$ plane for the second intrinsic mode ($m^i = 1$) of a closed-open combustor, based on equation (15). Dashed-dotted green lines represent the neutral curves for (a) $\varepsilon_1 = 0.1$, $r_1 = 1.0 + i * 1.0$, $\varepsilon_2 = 0.0$; (b) $\varepsilon_1 = 0.0$, $\varepsilon_2 = 0.1$, $r_2 = 1.0 + i * 1.0$; and (c) $\varepsilon_1 = 0.1$, $r_1 = 1.0 + i * 1.0$, $\varepsilon_2 = 0.1$, $r_2 = 1.0 + i * 1.0$ respectively. Dashed-dotted red lines represent the neutral curves for (a) $\varepsilon_1 = 0.1$, $r_1 = 1.0 - i * 1.0$, $\varepsilon_2 = 0.0$; (b) $\varepsilon_1 = 0.0$, $\varepsilon_2 = 0.1$, $r_2 = 1.0 - i * 1.0$; and (c) $\varepsilon_1 = 0.1$, $r_1 = 1.0 - i * 1.0$, $\varepsilon_2 = 0.1$, $r_2 = 1.0 - i * 1.0$ respectively. Notations and other parameters are the same as in figure 2.

270

Hence, the assumption of complex perturbation on the acoustic ends of a closed-open combustor proves that the neutral segment $\omega_c^i \tau = 0$ is very robust in between the point of intersection of neutral segments, whereas the neutral segments $\omega_c^i \tau = \pm\pi$, due to coupling, tends to lose robustness for small linear perturbations. This case needs to be treated carefully as part of future studies.

5.2.2.   Robustness of the growth rate

The instability frequencies and the neutral curves for intrinsic modes are found to be quite robust, except for a few situations as highlighted in the previous section. The robustness of the growth rate can be checked in this context as well.

For generalized boundary conditions $R_1(0)$ and $R_2(L)$, the growth rate expression can be obtained by perturbing the generalized dispersion relation (4.1) using the condition: as $n = n_{th}^i + n_1^i$, $\omega = \omega_0^i + \omega_1^i$. The dispersion relation (4.1) can be subtracted from the resultant equation, giving rise to a perturbed version of the generalized dispersion relation (4.1). The explicit expression for growth rate, in terms of generalized boundary conditions, can be given as,

$$
\omega_1^i = \frac{n_1^i e^{i\omega^i \tau}\left[\begin{array}{l}\left(1-R_1(0)R_2(L)\right)\cos\left(\omega^i\beta_1\right)+\left(R_2(L)-R_1(0)\right)\cos\left(\omega^i\beta_2\right)\\ +i\left\{\left(1+R_1(0)R_2(L)\right)\sin\left(\omega^i\beta_1\right)+\left(R_2(L)+R_1(0)\right)\sin\left(\omega^i\beta_2\right)\right\}\end{array}\right]}{\left[\begin{array}{l}\left(1+\alpha\right)\beta_1\left\{\left(1-R_1(0)R_2(L)\right)\sin\left(\omega^i\beta_1\right)-i\left(1+R_1(0)R_2(L)\right)\cos\left(\omega^i\beta_1\right)\right\}\\ +\left(1-\alpha\right)\beta_2\left\{\left(R_2(L)-R_1(0)\right)\sin\left(\omega^i\beta_2\right)-i\left(R_2(L)+R_1(0)\right)\cos\left(\omega^i\beta_2\right)\right\}\\ -n_{th,0}^i e^{i\omega^i\tau}\left\{\begin{array}{l}\left(1-R_1(0)R_2(L)\right)\left(i\tau\cos\left(\omega^i\beta_1\right)-\beta_1\sin\left(\omega^i\beta_1\right)\right)\\ +\left(R_2(L)-R_1(0)\right)\left(i\tau\cos\left(\omega^i\beta_2\right)-\beta_2\sin\left(\omega^i\beta_2\right)\right)\\ +i\left(1+R_1(0)R_2(L)\right)\left(i\tau\sin\left(\omega^i\beta_1\right)+\beta_1\cos\left(\omega^i\beta_1\right)\right)\\ +i\left(R_2(L)+R_1(0)\right)\left(i\tau\sin\left(\omega^i\beta_2\right)+\beta_2\cos\left(\omega^i\beta_2\right)\right)\end{array}\right\}\end{array}\right]}.
$$

(5.16)

For obtaining the specific expression for the growth rate of intrinsic modes in a closed-open combustor with non-ideal end conditions (1, 2), we substitute the expressions for $R_1(0)$ and $R_2(L)$, as per (1, 2) in (16), and arrive at the following expression,

$$\omega_1^i = \frac{2n_1^i e^{i\omega^i \tau}\left(\cos\left(\omega^i \beta_1\right) - \cos\left(\omega^i \beta_2\right)\right) + \varepsilon_1 H_1 + \varepsilon_2 H_2}{2\left[\begin{array}{c}\left(1+\alpha\right)\beta_1 \sin\left(\omega^i \beta_1\right) - \left(1-\alpha\right)\beta_2 \sin\left(\omega^i \beta_2\right) \\ -n_{th,0}^i e^{i\omega^i \tau}\left\{\begin{array}{c} i\tau\left(\cos\left(\omega^i \beta_1\right) - \cos\left(\omega^i \beta_2\right)\right) \\ + \left(-\beta_1 \sin\left(\omega^i \beta_1\right) + \beta_2 \sin\left(\omega^i \beta_2\right)\right)\end{array}\right\}\end{array}\right]}. \tag{5.17}$$

H_1 and H_2 are given as follows, where $\omega_{1,0}^i$ represents the growth rate for a combustor with ideal closed-open end conditions,

$$H_1 = i\left(Re\left(r_1\right) + iIm\left(r_1\right)\right)\left[\begin{array}{c} n_1^i e^{i\omega^i \tau}\left(\sin\left(\omega^i \beta_1\right) - \sin\left(\omega^i \beta_2\right)\right) \\ + \omega_{1,0}^i\left\{\begin{array}{c}\left[\left(1+\alpha\right)\beta_1 \cos\left(\omega^i \beta_1\right) - \left(1-\alpha\right)\beta_2 \cos\left(\omega^i \beta_2\right)\right] \\ + n_{th}^i e^{i\omega^i \tau}\left\{\begin{array}{c} i\tau\left(\sin\left(\omega^i \beta_1\right) - \sin\left(\omega^i \beta_2\right)\right) + \\ \beta_1 \cos\left(\omega^i \beta_1\right) - \beta_2 \cos\left(\omega^i \beta_2\right)\end{array}\right\}\end{array}\right\}\end{array}\right],$$

$$H_2 = i\left(Re\left(r_2\right) + iIm\left(r_2\right)\right)\left[\begin{array}{c} n_1^i e^{i\omega^i \tau}\left(\sin\left(\omega^i \beta_1\right) + \sin\left(\omega^i \beta_2\right)\right) \\ + \omega_{1,0}^i\left\{\begin{array}{c}\left[\left(1+\alpha\right)\beta_1 \cos\left(\omega^i \beta_1\right) + \left(1-\alpha\right)\beta_2 \cos\left(\omega^i \beta_2\right)\right] \\ + n_{th}^i e^{i\omega^i \tau}\left\{\begin{array}{c} i\tau\left(\sin\left(\omega^i \beta_1\right) + \sin\left(\omega^i \beta_2\right)\right) + \\ \beta_1 \cos\left(\omega^i \beta_1\right) + \beta_2 \cos\left(\omega^i \beta_2\right)\end{array}\right\}\end{array}\right\}\end{array}\right].$$

Clearly, equation (17) tells us that any linear perturbation ε_1 and ε_2 will only perturb the growth rate expressions linearly. However, the only restriction to this statement appears due to the lack of robustness of n_{th}^i under certain conditions, as can be seen from the denominator of expression (17). The robustness of the growth rate expression (17) can further be proved using figure 8 for $m^i = 1$ at $\tau = 6$ ms. The

272

continuous blue line shows the growth rate for a combustor with ideal end conditions and the dashed-dotted green line represents the growth rate for complex perturbations of acoustic boundaries given by, (a) $\varepsilon_1=0.2$, $r_1=1.0+i*1.0$, $\varepsilon_2=0.2$, $r_2=1.0+i*1.0$ and (b) $\varepsilon_1=0.4$, $r_1=1.0+i*1.0$, $\varepsilon_2=0.4$, $r_2=1.0+i*1.0$. The two lines almost overlap each other for 8 (a) and shift slightly for 8 (b) (which represents a massive 40% perturbation of the boundary conditions), verifying that the solution (17) of the growth rate is indeed robust for this case. However, this is not true for all the cases. Figure 2 will show us, that for $\tau = 6$ ms, we have an uncoupled solution for the intrinsic mode corresponding to $\omega_c^i \tau = 0$ and this neutral segment is also found to be very robust, as explained in § 2.1. Thus, the robustness of the neutral curve ensures the robustness of the growth rate in this case. However, when the neutral curves are not robust, particularly near and within the domain of intrinsic-acoustic mode coupling, equation (17) loses robustness. As mentioned before, this specific case of the robustness of the analytical solution of coupling needs to be treated with further care in future.

In this section, we have checked the robustness our analytical solutions of the intrinsic flame instability for a closed-open combustor, developed in chapter 2. We found that the solutions are generally quite robust when considering all flame and combustor parameters, except for two cases. The first case is when the flame is located near one of the ends of the combustor and the second is when, on the neutral curve, we attain a condition of $\cos\left(\omega_{0,t}^i L/c\right)=0$. Further, the neutral curve for the uncoupled solution of the intrinsic mode is very robust, whereas the robustness study of intrinsic-acoustic mode coupling scenario calls for further attention in future.
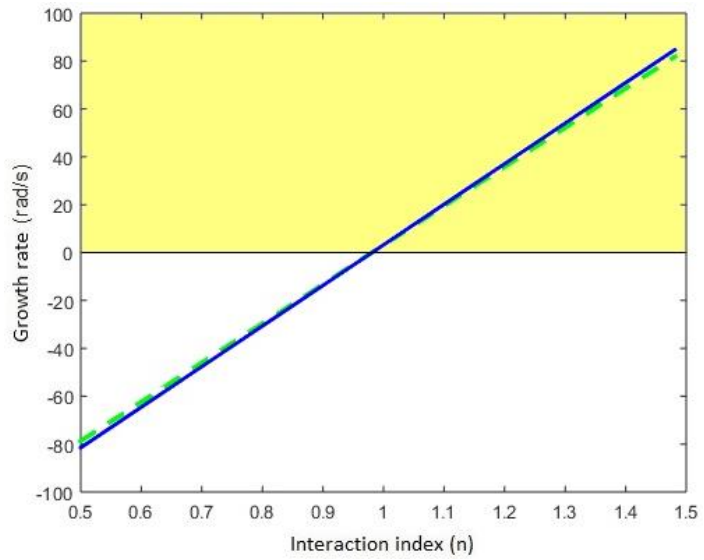
(a)
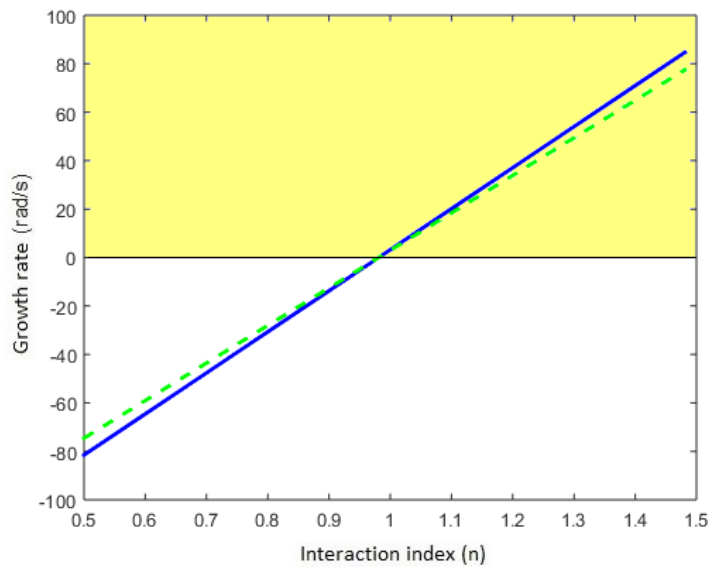
(b)

Figure 5.8: Growth rate for m^i =1 at τ = 6 ms for a closed-open combustor, based on equation (17). The continuous blue line represents the growth rate for ε_1 =0.0 and ε_2 =0.0. The dashed-dotted green line represents the growth rate for (a) ε_1 =0.2, r_1 =1.0+i *1.0, ε_2 =0.2, r_2 =1.0+i *1.0 and (b) ε_1 =0.4, r_1 =1.0+i *1.0, ε_2 =0.4, r_2 =1.0+i *1.0. The instability domain is marked in yellow. The parameters of the system are the same as in figure 2.

5.3. Flame intrinsic instability for open-open combustors with imperfect end conditions

An identical exercise to § 2 can also be conducted for a combustor with open-open end conditions. In chapter 4, we performed an analysis of a combustor with ideal open-open end conditions. In this section, we perturb the end conditions of the combustor slightly and evaluate the perturbed instability frequency and n-threshold for this new scenario. We also compare the results of § 2 with the current section and identify the salient similarities and differences.

5.3.1. Robustness of the instability frequencies and the neutral curves

When the end conditions of the combustor are not perfectly open, we can write the reflection coefficients as,

$$R_1(0) = -1 + \varepsilon_1 r_1, \text{ and } R_2(L) = -1 + \varepsilon_2 r_2, \qquad (5.18, 19)$$

Where, ε_1 and ε_2 are two small parameters, representing a deviation from the ideal end condition. Replacing $R_1(0)$ and $R_2(L)$, as per equation (18) and (19), the equations (4.3) and (4.4) reduce to the following forms on the neutral curve,

$$
(1+\alpha)\left[\begin{array}{l}\left(\varepsilon_1 Re(r_1)+\varepsilon_2 Re(r_2)\right)\cos\left(\omega^i\beta_1\right)\\+\left(\varepsilon_1 Im(r_1)+\varepsilon_2 Im(r_2)\right)\sin\left(\omega^i\beta_1\right)\end{array}\right]
$$

$$
+(1-\alpha)\left[\begin{array}{l}\left(\varepsilon_2 Re(r_2)-\varepsilon_1 Re(r_1)\right)\cos\left(\omega^i\beta_2\right)\\-\left(\varepsilon_1 Im(r_1)+\varepsilon_2 Im(r_2)\right)\sin\left(\omega^i\beta_2\right)\end{array}\right]
$$

$$
-n_{th}^i\left[\begin{array}{l}\cos\left(\omega_c^i\tau\right)\left\{\begin{array}{l}\left(\varepsilon_1 Re(r_1)+\varepsilon_2 Re(r_2)\right)\cos\left(\omega^i\beta_1\right)\\+\left(\varepsilon_1 Im(r_1)+\varepsilon_2 Im(r_2)\right)\sin\left(\omega^i\beta_1\right)\\+\left(\varepsilon_2 Re(r_2)-\varepsilon_1 Re(r_1)\right)\cos\left(\omega^i\beta_2\right)\\-\left(\varepsilon_1 Im(r_1)+\varepsilon_2 Im(r_2)\right)\sin\left(\omega^i\beta_2\right)\end{array}\right\}\\+\sin\left(\omega_c^i\tau\right)\left\{\begin{array}{l}-2\sin\left(\omega^i\beta_1\right)-\left(\varepsilon_1 Im(r_1)+\varepsilon_2 Im(r_2)\right)\cos\left(\omega^i\beta_1\right)\\+2\sin\left(\omega^i\beta_2\right)-\left(\varepsilon_2 Im(r_2)-\varepsilon_1 Im(r_1)\right)\cos\left(\omega^i\beta_2\right)\end{array}\right\}\end{array}\right]=0 \quad , \quad (5.20)
$$

$$
(1+\alpha)\left[-2\sin\left(\omega^i\beta_1\right)-\left(\varepsilon_1 Im(r_1)+\varepsilon_2 Im(r_2)\right)\cos\left(\omega^i\beta_1\right)\right]
$$

$$
-(1-\alpha)\left[-2\sin\left(\omega^i\beta_2\right)+\left(\varepsilon_2 Im(r_2)-\varepsilon_1 Im(r_1)\right)\cos\left(\omega^i\beta_2\right)\right]
$$

$$
-n_{th}^i\left[\begin{array}{l}\cos\left(\omega_c^i\tau\right)\left\{\begin{array}{l}-2\sin\left(\omega^i\beta_1\right)-\left(\varepsilon_1 Im(r_1)+\varepsilon_2 Im(r_2)\right)\cos\left(\omega^i\beta_1\right)\\+2\sin\left(\omega^i\beta_2\right)-\left(\varepsilon_2 Im(r_2)-\varepsilon_1 Im(r_1)\right)\cos\left(\omega^i\beta_2\right)\end{array}\right\}\\-\sin\left(\omega_c^i\tau\right)\left\{\begin{array}{l}\left(\varepsilon_1 Re(r_1)+\varepsilon_2 Re(r_2)\right)\cos\left(\omega^i\beta_1\right)\\+\left(\varepsilon_1 Im(r_1)+\varepsilon_2 Im(r_2)\right)\sin\left(\omega^i\beta_1\right)\\+\left(\varepsilon_2 Re(r_2)-\varepsilon_1 Re(r_1)\right)\cos\left(\omega^i\beta_2\right)\\-\left(\varepsilon_1 Im(r_1)+\varepsilon_2 Im(r_2)\right)\sin\left(\omega^i\beta_2\right)\end{array}\right\}\end{array}\right]=0 \quad . \quad (5.21)
$$

Both equation (20) and (21) provide explicit expressions for n_{th}^i. Equating n_{th}^i, from equations (20) and (21), leads to the following governing equation for ω_c^i, equivalent to (5),

$$
\left[\begin{array}{l}2\left(\sin\left(\omega^i\beta_1\right)-\sin\left(\omega^i\beta_2\right)\right)\left\{(1+\alpha)\sin\left(\omega^i\beta_1\right)-(1-\alpha)\sin\left(\omega^i\beta_2\right)\right\}\\+\varepsilon_1 Im(r_1)\left\{(1+\alpha)\sin\left(2\omega^i\beta_1\right)+(1-\alpha)\sin\left(2\omega^i\beta_2\right)-2\sin\left(\omega^i(\beta_1+\beta_2)\right)\right\}\\+\varepsilon_2 Im(r_2)\left\{(1+\alpha)\sin\left(2\omega^i\beta_1\right)+(1-\alpha)\sin\left(2\omega^i\beta_2\right)+2\sin\left(\omega^i(\beta_1-\beta_2)\right)\right\}\end{array}\right]\sin\left(\omega_c^i\tau\right)
$$

$$
=2\alpha\left[\varepsilon_1 Re(r_1)\sin\left(\omega^i(\beta_2-\beta_1)\right)+\varepsilon_2 Re(r_2)\sin\left(\omega^i(\beta_1+\beta_2)\right)\right]\cos\left(\omega_c^i\tau\right)
$$

$$
(5.22)
$$

The ω_c^i in equation (22) is assumed to have two parts, as mentioned in equation (6). Making use of equations (6) – (9), and accounting for small $\tilde{\omega}^i$,

$$\sin\left(\omega^i \beta_1\right) = \sin\left\{\left(\omega_{0,t}^i + \tilde{\omega}^i\right)\beta_1\right\} = \sin\left(\omega_{0,t}^i \beta_1\right) + \tilde{\omega}^i \beta_1 \cos\left(\omega_{0,t}^i \beta_1\right),$$

$$\sin\left(\omega^i \beta_2\right) = \sin\left\{\left(\omega_{0,t}^i + \tilde{\omega}^i\right)\beta_2\right\} = \sin\left(\omega_{0,t}^i \beta_2\right) + \tilde{\omega}^i \beta_2 \cos\left(\omega_{0,t}^i \beta_2\right),$$

in equation (22), we can arrive at an identical equation for $\tilde{\omega}^i$, similar to (11), for an open-open combustor,

$$\tilde{\omega}^i = \frac{\alpha\left[\varepsilon_1 Re\left(r_1\right)\sin\left\{\omega_{0,t}^i\left(\beta_2 - \beta_1\right)\right\} + \varepsilon_2 Re\left(r_2\right)\sin\left\{\omega_{0,t}^i\left(\beta_1 + \beta_2\right)\right\}\right]}{\tau\left[\left(1+\alpha\right)\sin\left(\omega_{0,t}^i \beta_1\right) - \left(1-\alpha\right)\sin\left(\omega_{0,t}^i \beta_2\right)\right]\left\{\sin\left(\omega_{0,t}^i \beta_1\right) - \sin\left(\omega_{0,t}^i \beta_2\right)\right\}}. \quad (5.23)$$

Making use of $\left(\beta_1 - \beta_2\right)$ and $\left(\beta_1 + \beta_2\right)$, as given by (10), and α, β_1 and β_2, as given by (2.28), equation (23) can be rewritten in the following form, depicting the effect of all combustor parameters like flame location, cross-section jump, and temperature jump,

$$\tilde{\omega}^i = \frac{\left(\dfrac{S_2}{S_1}\dfrac{\rho_1}{\rho_2}\dfrac{c_1}{c_2}\right)\left[-\varepsilon_1 Re\left(r_1\right)\sin\left(\dfrac{2\omega_{0,t}^i\left(x_q - L\right)}{c_2}\right) - \varepsilon_2 Re\left(r_2\right)\sin\left(\dfrac{2\omega_{0,t}^i x_q}{c_1}\right)\right]}{\tau\left[\begin{array}{l}\left[\left(1+\dfrac{S_2}{S_1}\dfrac{\rho_1}{\rho_2}\dfrac{c_1}{c_2}\right)\sin\left\{\omega_{0,t}^i\left(\dfrac{x_q}{c_2} - \dfrac{x_q}{c_1} - \dfrac{L}{c_2}\right)\right\} - \\ \left(1-\dfrac{S_2}{S_1}\dfrac{\rho_1}{\rho_2}\dfrac{c_1}{c_2}\right)\sin\left\{\omega_{0,t}^i\left(\dfrac{L}{c_2} - \dfrac{x_q}{c_1} - \dfrac{x_q}{c_2}\right)\right\}\right] \\ \left[\sin\left\{\omega_{0,t}^i\left(\dfrac{x_q}{c_2} - \dfrac{x_q}{c_1} - \dfrac{L}{c_2}\right)\right\} - \sin\left\{\omega_{0,t}^i\left(\dfrac{L}{c_2} - \dfrac{x_q}{c_1} - \dfrac{x_q}{c_2}\right)\right\}\right]\end{array}\right]}. \quad (5.24)$$

Again, it is clear from (24) that linear perturbations ε_1 and ε_2, at the ends of the combustor, perturb $\omega_{c,0}^i$ linearly. The inclusion of cross-section jump into the equation does not change this scenario. However, the effect of temperature jump across the flame introduces intricate effects of c_1 and c_2 into the trigonometric

277

expressions of (24), making it difficult to analyze this equation further. As a matter of

simplification, (24) can be visualized in a compact form if we assume $S_1 = S_2$ and

$T_1 = T_2$, and thus $c_1 = c_2 = c$, $\rho_1 = \rho_2$;

$$\tilde{\omega}^i = \frac{-\varepsilon_1 Re(r_1)\sin\left(\dfrac{2\omega_{0,t}^i\left(x_q - L\right)}{c}\right) - \varepsilon_2 Re(r_2)\sin\left(\dfrac{2\omega_{0,t}^i x_q}{c}\right)}{2\tau\sin\left(\dfrac{\omega_{0,t}^i L}{c}\right)\left\{\sin\left(\dfrac{\omega_{0,t}^i L}{c}\right) - \sin\left(\dfrac{\omega_{0,t}^i\left(2x_q - L\right)}{c}\right)\right\}}. \tag{5.25}$$

The corresponding n_{th}^i can be obtained from equation (21) as follows,

$$n_{th}^i = \frac{2\left[(1+\alpha)\sin\left(\omega^i\beta_1\right) - (1-\alpha)\sin\left(\omega^i\beta_2\right)\right] + \varepsilon_1 G_1 + \varepsilon_2 G_2}{2\cos\left(\omega_c^i\tau\right)\left\{\sin\left(\omega^i\beta_1\right) - \sin\left(\omega^i\beta_2\right)\right\}}. \tag{5.26}$$

Where G_1 and G_2 are given by the following expressions, where, $n_{th,0}^i$ is the

threshold of n for ideal open-open end conditions,

$$G_1 = (1+\alpha)Im(r_1)\cos\left(\omega^i\beta_1\right) - (1-\alpha)Im(r_1)\cos\left(\omega^i\beta_2\right)$$
$$-n_{th,0}^i\left\{\begin{array}{l} Im(r_1)\left(\cos\left(\omega^i\beta_1\right) - \cos\left(\omega^i\beta_2\right)\right)\cos\left(\omega_c^i\tau\right) \\ +Im(r_1)\left(\sin\left(\omega^i\beta_1\right) - \sin\left(\omega^i\beta_2\right)\right)\sin\left(\omega_c^i\tau\right) \\ +Re(r_1)\left(\cos\left(\omega^i\beta_1\right) - \cos\left(\omega^i\beta_2\right)\right)\sin\left(\omega_c^i\tau\right) \end{array}\right\} \text{, and}$$

$$G_2 = (1+\alpha)Im(r_2)\cos\left(\omega^i\beta_1\right) + (1-\alpha)Im(r_2)\cos\left(\omega^i\beta_2\right)$$
$$-n_{th,0}^i\left\{\begin{array}{l} Im(r_2)\left(\cos\left(\omega^i\beta_1\right) + \cos\left(\omega^i\beta_2\right)\right)\cos\left(\omega_c^i\tau\right) \\ +Im(r_2)\left(\sin\left(\omega^i\beta_1\right) - \sin\left(\omega^i\beta_2\right)\right)\sin\left(\omega_c^i\tau\right) \\ +Re(r_2)\left(\cos\left(\omega^i\beta_1\right) + \cos\left(\omega^i\beta_2\right)\right)\sin\left(\omega_c^i\tau\right) \end{array}\right\}.$$

Equation (23-25) suggests that the fluctuation of instability frequency ($\tilde{\omega}^i$), due to

imperfections in the boundary conditions, depends linearly on the fluctuation

parameters ε_1 and ε_2. Thus, the 1-D analytical solutions prescribed in chapter 4 for

combustors with open-open end conditions are generally quite robust. However, just as for a closed-open combustor, in the case of an open-open combustor, there also exist a couple of situations where the analytical solutions lose their robustness. These are as follows:

i. When $\sin\left(\omega_{0,t}^i L/c\right) = \sin\left(\omega_{0,t}^i \left(2x_q - L\right)/c\right)$, i.e. the flame lies close to $x_q = L$. As per equation (26), the corresponding n_{th}^i goes to infinity for this case. The analytical solutions retain their robustness when the flame is situated close to $x_q = 0$, as can be seen from (25) and (26). Clearly, this aspect is different from the first case mentioned in § 2.1.

ii. When on the neutral curve, we attain a condition of $\sin\left(\omega_{0,t}^i L/c\right) = 0$.

Similar to the previous section, we can say that when n_{th}^i goes to infinity, the aspect of robustness will be irrelevant, as the system is expected to behave as linearly stable for large n. Thus, the first case can be treated as not so important for practical combustors. For these two cases, when the solutions lose their robustness, they should be studied separately in greater detail.

A detailed explanation of the effect of the perturbation on the acoustic end conditions of the open-open combustor on the neutral curves of the intrinsic modes can be provided with the help of figures 9-11. In these figures, the blue line represents the neutral curve for the second intrinsic mode with ideal open-open end conditions. The elliptical dots represent the area of the neutral curve when the robustness of the analytical solution (26) does not hold anymore. Panel (a), (b) and (c) in each figure represent three different cases when the linear perturbation is assumed for the acoustic end condition of the open end on the left of the flame, open end of the right

of the flame and both the ends respectively. Thus, for panel (a), $\varepsilon_2 = 0$, for panel (b) $\varepsilon_1 = 0$ and for panel (c) both ε_1 and ε_2 are non-zero.

In figure 9, linear real perturbation (ε_1 and/or ε_2) of 0.1 is assumed. The dashed-dotted green line depicts the perturbed solution. Similar to the closed-open combustor, in this case, the neutral segment corresponding to $\omega_c^i \tau = 0$ is very robust. They tend to overlap with the neutral segments $\omega_c^i \tau = 0$ for an open-open combustor with ideal end conditions and hence, are hardly distinguishable. Selection of higher values of perturbations (ε_1 and ε_2) has further proved (not shown here) that the neutral segments $\omega_c^i \tau = \pm \pi$, attributed to the coupling of intrinsic-acoustic modes, tend to lose their robustness. A possible reason for this phenomenon is provided in § 2.1 for a closed-open combustor. In all these figures, panels (a) and (b) demonstrate more robustness compared to panel (c), as in panel (c), both end conditions are perturbed simultaneously.
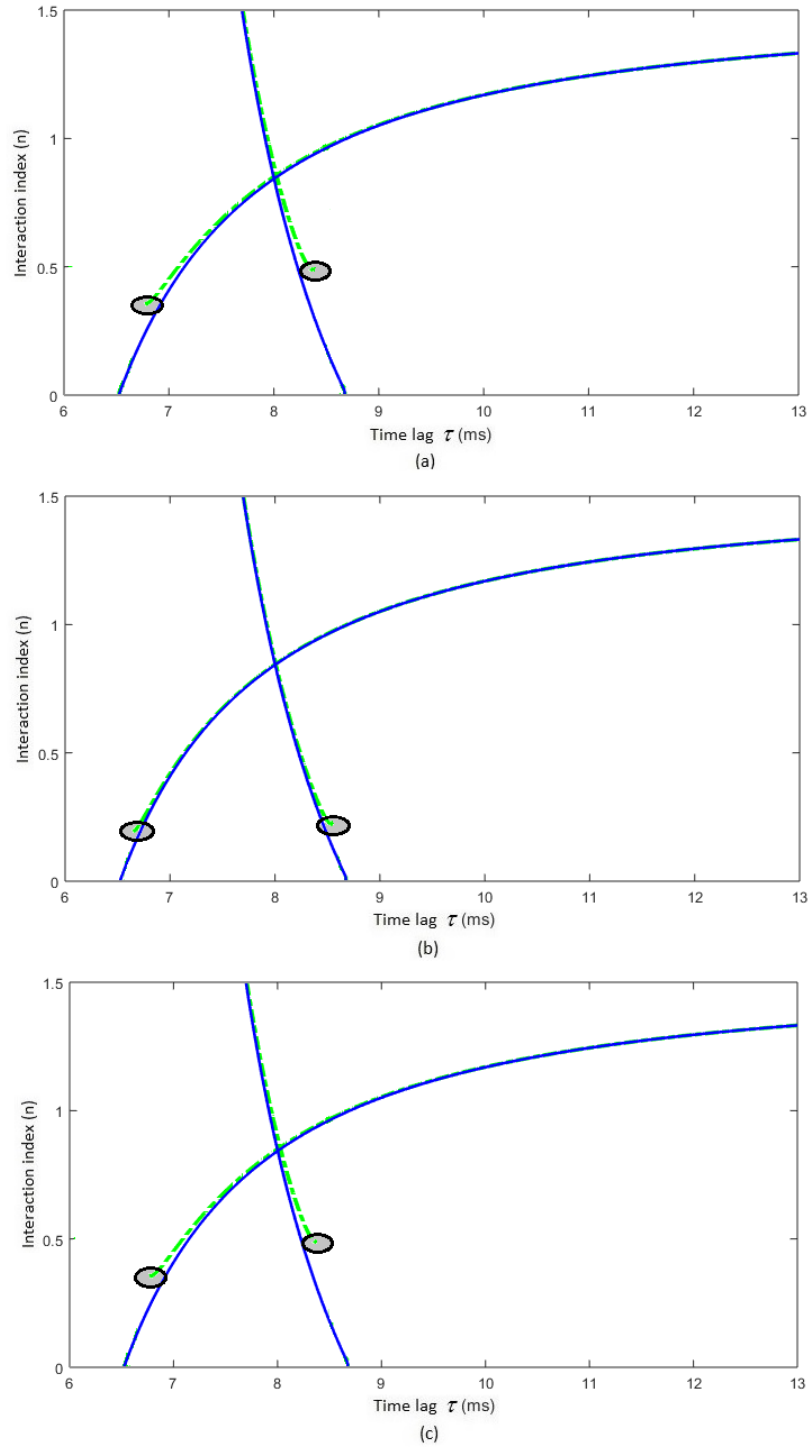
Figure 5.9: Neutral curves on the $n - \tau$ plane for the second intrinsic mode ($m^i = 1$) of an open-open combustor, based on equation (26). Continuous blue lines represent the neutral curves for $\varepsilon_1 = 0.0$ and $\varepsilon_2 = 0.0$. Dashed-dotted green lines represent the neutral curves for (a) $\varepsilon_1 = 0.1$, $r_1 = 1.0$, $\varepsilon_2 = 0.0$; (b) $\varepsilon_1 = 0.0$, $\varepsilon_2 = 0.1$, $r_2 = 1.0$; and (c) $\varepsilon_1 = 0.1$, $r_1 = 1.0$, $\varepsilon_2 = 0.1$, $r_2 = 1.0$ respectively. Elliptical dots represent the areas on the neutral curves where analytical solutions (26) cease to be robust. The parameters are the same as in figure 4.2.
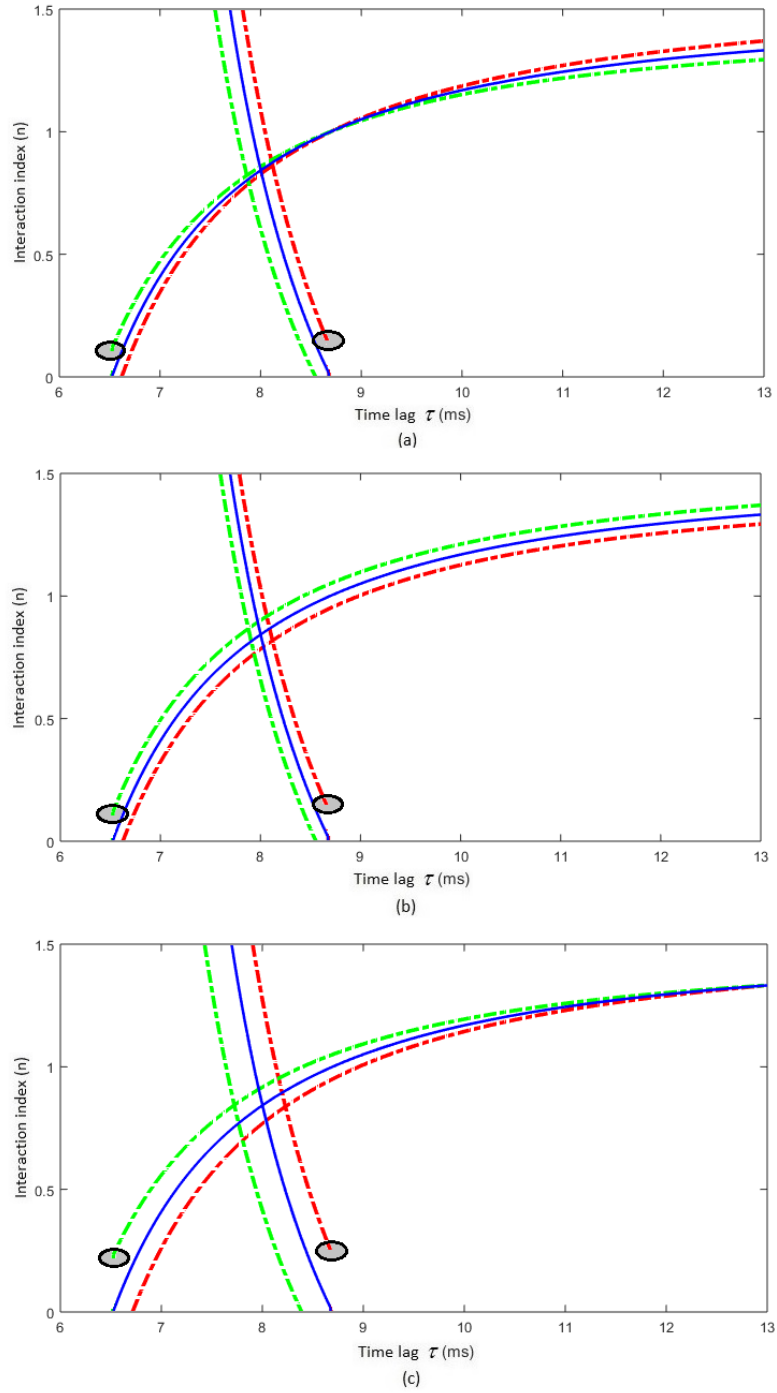
Figure 5.10: Neutral curves on the $n - \tau$ plane for the second intrinsic mode (m^i =1) of an open-open combustor, based on equation (26). Dashed-dotted green lines represent the neutral curves for (a) ε_1 =0.1, $r_1 = i * 1.0$, ε_2 =0.0; (b) ε_1 =0.0, ε_2 =0.1, $r_2 = i * 1.0$; and (c) ε_1 =0.1, $r_1 = i * 1.0$, ε_2 =0.1, $r_2 = i * 1.0$ respectively. Dashed-dotted red lines represent the neutral curves for (a) ε_1 =0.1, $r_1 = -i * 1.0$, ε_2 =0.0; (b) ε_1 =0.0, ε_2 =0.1, $r_2 = -i * 1.0$; and (c) ε_1 =0.1, $r_1 = -i * 1.0$, ε_2 =0.1, $r_2 = -i * 1.0$ respectively. Notations and other parameters are the same as in figure 9.

Figure 5.11: Neutral curves on the $n - \tau$ plane for the second intrinsic mode ($m^i = 1$) of an open-open combustor, based on equation (26). Dashed-dotted green lines represent the neutral curves for (a) $\varepsilon_1 = 0.1$, $r_1 = 1.0 + i*1.0$, $\varepsilon_2 = 0.0$; (b) $\varepsilon_1 = 0.0$, $\varepsilon_2 = 0.1$, $r_2 = 1.0 + i*1.0$; and (c) $\varepsilon_1 = 0.1$, $r_1 = 1.0 + i*1.0$, $\varepsilon_2 = 0.1$, $r_2 = 1.0 + i*1.0$ respectively. Dashed-dotted red lines represent the neutral curves for (a) $\varepsilon_1 = 0.1$, $r_1 = 1.0 - i*1.0$, $\varepsilon_2 = 0.0$; (b) $\varepsilon_1 = 0.0$, $\varepsilon_2 = 0.1$, $r_2 = 1.0 - i*1.0$; and (c) $\varepsilon_1 = 0.1$, $r_1 = 1.0 - i*1.0$, $\varepsilon_2 = 0.1$, $r_2 = 1.0 - i*1.0$ respectively. Notations and other parameters are the same as in figure 9.

In figure 10, linear imaginary perturbation (ε_1 and/or ε_2) of $\pm i *0.1$ is assumed. The dashed-dotted green lines correspond to the neutral curves due to $+i *0.1$ perturbation, whereas the dashed-dotted red lines correspond to the neutral curves due to $-i *0.1$ perturbation. The neutral segments due to $+i *0.1$ perturbation tend to move to the left, whereas the neutral segments due to $-i *0.1$ perturbation tend to move to the right, relative to the neutral curve for ideal end conditions. This observation is consistent with a closed-open combustor. Also, the imaginary perturbation has a more significant impact on all neutral segments than the real perturbation of end conditions. In figure 11, linear complex perturbation (ε_1 and/or ε_2) of $\left(1 \pm i\right)*0.1$ is assumed. This case is a combination of figures 9 and 10, where we see a shift of the neutral curves either to the left or right, due to the imaginary part of the perturbation and the loss of robustness in the neutral segment $\omega_c^i \tau = \pm \pi$, due to the real part of the perturbation. However, the neutral segment $\omega_c^i \tau = 0$ is found to retain its robustness.

Hence, the assumption of complex perturbation on the acoustic ends of an open-open combustor proves that the neutral segment $\omega_c^i \tau = 0$ is very robust, whereas the neutral segments $\omega_c^i \tau = \pm \pi$, due to coupling, tend to lose robustness for small linear perturbations.

5.3.2.   Robustness of the growth rate

The instability frequencies and the neutral curves for intrinsic modes are found to be quite robust, except for a few situations which are highlighted in the previous section. Similar to § 2.2, the robustness of the growth rate can be checked as well.

For obtaining the specific expression for the growth rate of intrinsic modes in an open-open combustor with non-ideal end conditions (18, 19), we plug the expressions of $R_1(0)$ and $R_2(L)$, as per (18, 19), into (16) and arrive at the following expression,

$$\omega_1^i = \frac{2 n_1^i e^{i\omega^i \tau}\left(\sin\left(\omega^i \beta_1\right) - \sin\left(\omega^i \beta_2\right)\right) + \varepsilon_1 H_1 + \varepsilon_2 H_2}{\begin{bmatrix} -(1+\alpha)\beta_1 \cos\left(\omega^i \beta_1\right) + (1-\alpha)\beta_2 \cos\left(\omega^i \beta_2\right) \\ 2\begin{bmatrix} -n_{th,0}^i e^{i\omega^i \tau}\begin{Bmatrix} i\tau\left(\sin\left(\omega^i \beta_1\right) - \sin\left(\omega^i \beta_2\right)\right) \\ +\left(\beta_1 \cos\left(\omega^i \beta_1\right) - \beta_2 \cos\left(\omega^i \beta_2\right)\right)\end{Bmatrix}\end{bmatrix}\end{bmatrix}}.$$ (5.27)

H_1 and H_2 are given as follows, where $\omega_{1,0}^i$ represents the growth rate for a combustor with ideal open-open end conditions,

$$H_1 = i\left(Re\left(r_1\right) + iIm\left(r_1\right)\right)\begin{bmatrix} -n_1^i e^{i\omega^i \tau}\left(\cos\left(\omega^i \beta_1\right) - \cos\left(\omega^i \beta_2\right)\right) \\ +\omega_{1,0}^i \begin{Bmatrix} \left[(1+\alpha)\beta_1 \sin\left(\omega^i \beta_1\right) - (1-\alpha)\beta_2 \sin\left(\omega^i \beta_2\right)\right] \\ -n_{th}^i e^{i\omega^i \tau}\begin{Bmatrix} i\tau\left(\cos\left(\omega^i \beta_1\right) - \cos\left(\omega^i \beta_2\right)\right) - \\ \beta_1 \sin\left(\omega^i \beta_1\right) + \beta_2 \sin\left(\omega^i \beta_2\right)\end{Bmatrix} \end{Bmatrix} \end{bmatrix},$$

$$H_2 = i\left(Re\left(r_2\right) + iIm\left(r_2\right)\right)\begin{bmatrix} -n_1^i e^{i\omega^i \tau}\left(\cos\left(\omega^i \beta_1\right) + \cos\left(\omega^i \beta_2\right)\right) \\ +\omega_{1,0}^i \begin{Bmatrix} \left[(1+\alpha)\beta_1 \sin\left(\omega^i \beta_1\right) + (1-\alpha)\beta_2 \sin\left(\omega^i \beta_2\right)\right] \\ -n_{th}^i e^{i\omega^i \tau}\begin{Bmatrix} i\tau\left(\cos\left(\omega^i \beta_1\right) + \cos\left(\omega^i \beta_2\right)\right) - \\ \beta_1 \sin\left(\omega^i \beta_1\right) - \beta_2 \sin\left(\omega^i \beta_2\right)\end{Bmatrix} \end{Bmatrix} \end{bmatrix}.$$

Clearly, equation (27) tells us that any linear perturbation ε_1 and ε_2 will only perturb the growth rate expressions linearly. However, the only restriction to this statement appears due to the lack of robustness of n_{th}^i under certain conditions, as can be seen from the denominator of expression (27). The robustness of growth rate expression (27) can further be proved using figure 12 for $m^i = 1$ at $\tau = 9$ ms. The continuous blue

line shows the growth rate for a combustor with ideal end conditions and the dashed-dotted green line represents the growth rate for complex perturbations of acoustic boundaries given by, (a) $\varepsilon_1=0.2$, $r_1=1.0+i*1.0$, $\varepsilon_2=0.2$, $r_2=1.0+i*1.0$ and (b) $\varepsilon_1=0.4$, $r_1=1.0+i*1.0$, $\varepsilon_2=0.4$, $r_2=1.0+i*1.0$. The two lines almost overlap each other in figure 12 (a) and are shifted slightly in 12 (b) (which depicts 40% perturbation of the boundary conditions), verifying that in this case, the solution (27) of the growth rate is indeed robust. However, this is not true for all the cases. Figure 9 tells us that for $\tau = 9$ ms, we have uncoupled solution for the intrinsic mode corresponding to $\omega_c^i \tau = 0$ and this neutral segment is also found to be very robust, as explained in § 3.1. Thus, in this case, the robustness of the neutral curve ensures the robustness of the growth rate. However, when the neutral curves are not robust, particularly near and within the domain of intrinsic-acoustic mode coupling, equation (27) will lose robustness.

In this section, we have checked the robustness of our analytical solutions for intrinsic flame instability for an open-open combustor, which were developed in chapter 4. We found that the solutions are generally quite robust for all but two cases, when considering all the flame and combustor parameters. The first case is when the flame is located near $x_q = L$ and the second case is when, on the neutral curve, we attain a condition of $\sin\left(\omega_{0,t}^i L/c\right) = 0$. Furthermore, the neutral curve for the uncoupled solution of the intrinsic mode is very robust, whereas the robustness study of the intrinsic-acoustic mode coupling scenario calls for further attention in future.
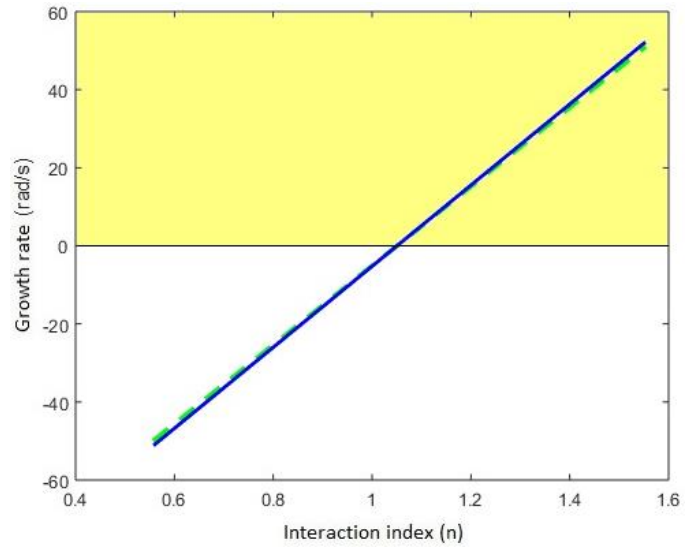
(a)
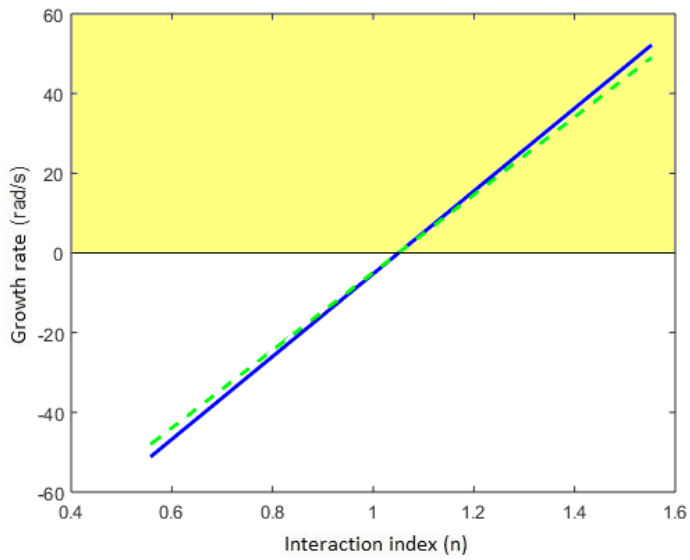
(b)

Figure 5.12: Growth rate for m^i =1 at τ = 9 ms for an open-open combustor, based on equation (27). The continuous blue line represents the growth rate for ε_1 =0.0 and ε_2 =0.0. The dashed-dotted green line represents the growth rate for (a) ε_1 =0.2, r_1 =1.0+i*1.0, ε_2 =0.2, r_2 =1.0+i*1.0 and (b) ε_1 =0.4, r_1 =1.0+i*1.0, ε_2 =0.4, r_2 =1.0+i*1.0. The instability domain is marked in yellow. The parameters of the system are the same as in figure 9.

5.4.   Conclusions

In this chapter, we have analyzed the effect of imperfect end conditions on the analytical results of instability frequency, n-threshold and the growth rate of flame

intrinsic modes, obtained for a closed-open and an open-open combustor in chapters 2 and 4 respectively. The analytical results described in chapter 2 and 4 have been found to be generally quite robust, except the following two cases:

i. When the flame lies close to one of the ends of the combustor for a closed-open combustor and when the flame lies near the end corresponding to $x_q = L$ for an open-open combustor. However, when the flame resides near the end corresponding to $x_q = 0$ for an open-open combustor, the analytical solutions retain their robustness.

ii. When on the neutral curve, we attain a condition of $\cos\left(\omega_{0,t}^{i} L/c\right) = 0$ for a closed-open combustor and $\sin\left(\omega_{0,t}^{i} L/c\right) = 0$ for an open-open combustor, where $\omega_{0,t}^{i}$ is the instability frequency on the neutral curves for a combustor with perfect end conditions.

For the first case, we can say that when n_{th}^{i} goes to infinity, the notion of robustness must be revisited, as the system is expected to behave as linearly stable for large n. The domain of coupling is found to be not so robust, as slight perturbations of the end conditions significantly perturb the neutral segments $\omega_{c}^{i}\tau = \pm\pi$. The reason for this is that the robustness analysis of the current chapter is based on the perturbation of the analytical solution for a single intrinsic mode. Whereas, in the coupled intrinsic-acoustic domain, we need to simultaneously perturb two solutions to obtain more accurate results. However, this lies in the scope of future work. Remarkably, the neutral segment corresponding to $\omega_{c}^{i}\tau = 0$ and the corresponding growth rate are found to be very robust between the points of intersections of the neutral curve segments. In fact, in this chapter, it has been shown that a significant 50% perturbation of the real part of the reflection coefficients of either end of the

combustor does not alter the neutral curve segment corresponding to $\omega_c^i \tau = 0$ significantly. The robustness of the analytical solution is not expected to hold for perturbations of such a magnitude. The exact position of the neutral curve must be obtained numerically for the actual boundary condition in each case. However, for a surprisingly wide range of perturbation magnitudes, a good perturbed approximation for the neutral curve can be obtained. Nonetheless, except for the situations mentioned above, the analytical solutions are found to be fairly robust for all flame locations and combustor parameters like cross-section jump. It requires a dedicated effort to derive analytical corrections to the "ideal" solutions for the cases when the solutions are not robust. The effect of temperature jump on the robustness of the analytical solution is found to be an intricate matter to analyze. This aspect also needs to be dealt with in further studies. Equations (12, 24) derived here provide a good starting point.

Chapter 6

Conclusions and outlook

6.1. Conclusions

Within the framework of the simplest 1-D model of a combustor with $n - \tau$ heat release, a new overall picture of linear flame intrinsic modes has been analytically derived. The main results and conclusions of the work can be summarized as follows:

(i)   The outstanding question of the emergence of intrinsic flame modes within the framework of the $n - \tau$ model of the combustor has been clarified. It has been shown that for any nonzero n and τ there is always an infinite number of intrinsic modes present for any combustor, whatever the end boundary conditions. These modes are strongly damped for small n and, to leading order in n, the real parts of the frequencies have been found: $\mathrm{Re}(\omega^i) = (2m^i + 1)(\pi/\tau)$, where m^i is the mode number. These frequencies are determined solely by τ and thus, do not depend on any characteristics of the combustor and the flame position. This is in contrast with the acoustic modes, whose frequencies are primarily determined by the combustor length, L (for example, $\omega^a = (2m^a + 1)(\pi c/2L)$ (for m^a=0, 1, 2…) for a closed-open combustor).   For small n, the strongly decaying nature of these modes make it practically impossible to detect them in combustion systems. This feature also makes

these modes insensitive to the flame location and the specific properties of the combustor end boundary conditions.

(ii)   It has been shown, that with an increase of n, the intrinsic modes for any τ have a tendency to become unstable at some threshold value of n. The threshold depends on the characteristics of the combustor and the flame position. The key finding is the factorization of intrinsic modes in the exact transcendental dispersion relation for closed-open and open-open combustors, which means that, on the neutral curves, the intrinsic modes do not depend on the combustor parameters. We have called this new phenomenon "decoupling of intrinsic modes". The fact that the frequencies of marginally unstable intrinsic modes are determined solely by τ, suggests that there are natural oscillations in the subsystem fuel injector-flame, determined by the ratio of the distance from the fuel injector to the flame front and the flow velocity. The exact solutions of the dispersion relation on the neutral curve allow us to exactly find the neutral curve. On the $n - \tau$ plane, the neutral curve for each intrinsic mode consists of a combination of neutral curve segments $\omega_c^i \tau = 0$, $\omega_c^i \tau = \pi$ and $\omega_c^i \tau = -\pi$, where ω_c^i is the discrepancy between the real part of the frequency on the neutral curve and the real part of the frequency in the limit of small n. The overall geometry of the instability domain bounded by the neutral curve has been revealed and proved to be quite complicated. It is bounded from below by an infinite sequence of loops, decreasing in their width in τ with a decrease of τ. Because of the loop width tending to zero, it would be close to impossible to capture such instability domains numerically. For the growth/decay rates of the intrinsic modes, the explicit dependence on all parameters of the combustor (the length, the cross-section and temperature jumps, the flame location) have been derived and verified by numerics. On this basis, by manipulating the system parameters such as

291

cross section jump, temperature jump, and flame location, one can decrease/increase the threshold n_{th}^i and increase/decrease the growth rate, hence instigating/preventing the intrinsic mode instability. It has been demonstrated that the intrinsic modes can be dominant for some values of τ, for example, for τ when all acoustic modes decay.

(iii)   A new type of combustion instability has been discovered and described analytically. The instability is caused by intrinsic-acoustic mode coupling. Four principal types of coupling between intrinsic and acoustic modes have been identified. The intrinsic-acoustic mode coupling instability scenario occurs when acoustic pressure and flame heat release are out of phase with each other (that is, the Rayleigh index is negative), which forces the acoustic mode to decay for small values of n and makes it impossible for classical combustion instability to occur. The coupled acoustic mode attains all the features of an intrinsic mode. It has been suggested to refer to such modes as "coupled intrinsic" and to distinguish their provenance, i.e. their identity for small n we introduce an identifier (born acoustic or born intrinsic). In general, the larger values of n-thresholds correspond to the coupled intrinsic mode (born intrinsic) and the smaller values correspond to the coupled intrinsic mode (born acoustic). Thus, for a weak flame with low interaction index, even though the intrinsic mode does not become unstable on its own, it might trigger the instability of one of the acoustic modes of close frequency. However, close to the intersection of the neutral curve segments, coupled modes invariably change their identity. A quadratic equation model that qualitatively captured the mode coupling and a quartic equation model that captured the phenomenon quantitatively with a good accuracy have been developed to describe coupling for a closed-open and open-open combustor. The analytical results have been validated by numerics.

(iv)   The effect of imperfect end conditions on the analytical predictions of instability frequency, neutral curves and growth rates of flame intrinsic modes for a closed-open and an open-open combustor has been examined analytically and numerically. The analytical results have been found to generally be quite robust, except the following two cases: (a) when the flame lies close to one of the ends of the combustor for a closed-open combustor and (b) when the flame lies near the end corresponding to $x_q = L$ for an open-open combustor. However, when the flame resides near the end corresponding to $x_q = 0$ of an open-open combustor, the analytical solutions retain their robustness. The neutral curve segment corresponding to $\omega_c^i \tau = 0$ and the corresponding growth rates are found to be particularly robust.

6.2. Scope of future work

The analytical work presented in the thesis focuses on the analytical description of intrinsic flame modes within a closed-open and open-open combustor. We have been able to develop a comprehensive description of combustion instability, that is, the instability frequencies, the neutral curve on the $n - \tau$ plane and the growth rate. The adopted analytical approach was based on the widely used $n - \tau$ model [Crocco and Cheng (1956)] for the flame description. We have proved that the presence of acoustic boundaries of a combustor can instigate the combustion instability. The intrinsic modes do couple with the combustor acoustic modes and thus, eventually give rise to extra unstable modes, i.e. in addition to those that would have been expected in the established theory based on a positive Rayleigh index. The coupled acoustic modes behave exactly like intrinsic modes, suggesting, that in fact, we have more potentially unstable intrinsic modes in a combustor, compared to the number of intrinsic modes found in the limit of small n. Thus, an overall picture of all types of

linear instabilities (the classical acoustic modes, the intrinsic modes studied here and coupled acoustic-intrinsic modes) for the simplest model of a combustor has been developed. Apart from providing answers to outstanding questions, the work also raised new questions. Here we discuss some possible extensions of the current work. The main finding of the work – the factorization of the intrinsic modes in closed-open and open-open combustors could be exploited in many models capturing more realistically certain aspects of the practical combustors.

The $n - \tau$ model, which provided the basis for the present study, can be improved by taking into account the randomly distributed delay. This has been successfully done for acoustic modes (e.g. Schuermans (2003), Sattelmayer (2000), Polifke et al. (2001)), but not yet for the intrinsic ones. The $n - \tau$ model assumes a fixed time lag between the velocity perturbation and heat release rate perturbation of a flame, which is rarely the case in real combustors. In a real combustion system, the time lag between velocity perturbation and flame heat release rate perturbation is not fixed. It is much better to treat it as a distributed quantity. This distribution is due to three main factors (Schuermans et al (2004)):

i. distributed fuel injection (in the case of multi-point fuel injection system);

ii. distribution in the flame geometry (the flame does not lie on a single axial plane which forms the basis of the $n - \tau$ flame models);

iii. flow turbulence.

Thus, a standard $n - \tau$ model with a single fixed τ assumes that the combustor has a single injector, the flame lies on a single axial plane and the flow is laminar. There were attempts to develop more realistic models by considering the distributed character of the time lag within the framework of a slightly modified $n - \tau$ model. In

this vein, a Gaussian distribution of time lags in the form $e^{-i\omega\tau_\phi - \frac{1}{2}\omega^2\sigma_\phi^2}$ was used by Schuermans (2003) to describe the three aforementioned effects, where τ_ϕ is the mean time lag and σ_ϕ is the standard deviation of time lags. As per a Gaussian distribution, for high frequencies and a large standard deviation, the equivalence ratio fluctuations at the flame front decay to zero. In other words, the distribution acts like a low pass filter. An earlier work of Sattelmayer (2000) shows that the distribution of the time lag also controls the combustion instability, apart from the mean time lag. Distribution of the time lag was shown to weaken the feedback loop between combustor acoustics, fuel concentration, and flame heat release fluctuations, thus resulting in combustion stabilization. Staggered fuel injectors or various kinds of injectors in combustors are used as a technique to control combustion instability [e.g., Straub and Richards (1998), Berenbrink and Hoffmann (2000)]. Most of the previous work was concerned with identifying the effect of the time lag distribution on the acoustic modes. It was found that the standard deviation, σ, acts as an acoustic damper and hence inhibits acoustic mode instability. In a recent study, Bomberg et al. (2015) made use of a distributed time lag flame model to find the flame intrinsic modes in a laminar flame holder stabilized and turbulent swirl stabilized combustors. Hence, an extension of the $n - \tau$ model into a distributed time lag model is highly desirable and, crucially, it is possible within the framework of the same analytical approach. The analytical description of the combustors with non-ideal end boundary conditions can be further improved if the perturbation approach is applied both to isolated intrinsic modes and the coupled acoustic-intrinsic ones. The coupled domain calls for further detailed study based on linear perturbations of the two modes.

Once the clarity within the framework of linear models is achieved, a study of nonlinear dynamics of intrinsic modes and their nonlinear interactions with acoustic

modes will be a natural next step, opening a vast new field. We can also introduce mean flow into our analysis to examine how it affects the stability behavior of the intrinsic modes. The interaction between intrinsic modes of very low frequency and hydrodynamic modes is also of great fundamental and practical interest. It has been shown that the neutral curve of the first intrinsic mode lacks the segment $\omega_c^i \tau = -\pi$ for an ideal closed-open combustor. However, they might exist for non-ideal boundary condition and also have really low-frequency instability. This issue must be explored. Instability of this type and the corresponding coupling with hydrodynamic instability is a promising direction of future work. A detailed study should also be made in the low time lag domain, where small scale neutral loops exist in close proximity to each other. As the operating parameter domains of combustors generally correspond to small time lags, a detailed study in this domain could lead to important insights. Comprehensive experimental validation of the analytical models presented in this thesis is certainly needed, which is likely to generate new theoretical questions.

APPENDIX I

AI.1. Intersection of the neutral curve segments $\omega_c^i \tau = 0$ and $\omega_c^i \tau = \pm\pi$

In § 4.2 of chapter 2, it was shown that the intrinsic mode neutral curve on the $n - \tau$ plane is made of the segments corresponding to $\pm\omega_c^i \tau = \pi$ and $\omega_c^i \tau = 0$. Here we will analytically find the locations of the intersection points of these segments. At the point of intersection of the neutral curve segments corresponding to $\omega_c^i \tau = \pi$ and $\omega_c^i \tau = 0$, the threshold values of n belonging to different segments are equal by definition, that is,

$$n^i_{th,(0)} = n^i_{th,(\pi)} . \tag{AI.1}$$

Assuming, for simplicity, that there are no cross-section and temperature jumps, the flame is located at $x_q = L/2$ and making use of (2.34), equation (1) reduces to,

$$\frac{2\cos\left((2m^i + 1)\dfrac{\pi L}{\tau c}\right)}{\cos\left((2m^i + 1)\dfrac{\pi L}{\tau c}\right) - 1} = \frac{2\cos\left((2m^i + 2)\dfrac{\pi L}{\tau c}\right)}{1 - \cos\left((2m^i + 2)\dfrac{\pi L}{\tau c}\right)} . \tag{AI.2}$$

The further simplified equation reads;

$$\cos\left((2m^i + 1)X\right) + \cos\left((2m^i + 2)X\right) - 2\cos\left((2m^i + 1)X\right)\cos\left((2m^i + 2)X\right) = 0,$$

$$\text{where } X = \frac{\pi L}{\tau c} . \tag{AI.3}$$

For particular m^i, equation (3) reduces to a polynomial equation. For example, for $m^i = 1$ the equation leads to the following polynomial equation,

297

$$g(X) = 64\cos^7 X - 112\cos^5 X - 8\cos^4 X + 52\cos^3 X + 8\cos^2 X - 3\cos X - 1 = 0.$$

Of course, (4) can always be solved numerically. Figure 1 shows a plot of $g(X)$ against τ. Its main feature is the presence of multiple solutions. The multiple solutions are due to the presence of multiple instability loops and hence multiple intersection points of $\omega_c^i \tau = \pi$ and $\omega_c^i \tau = 0$. Selection of the right solution is based on observation. The first and second points of intersection of $\omega_c^i \tau = \pi$ and $\omega_c^i \tau = 0$, as shown in figure 2.8 (a), correspond to the first and second largest values of τ (excluding from consideration $\tau = \infty$), as suggested by figure 1. These values here are $\tau = 14.75$ and 5.425 ms respectively (see figure 1). The first largest value corresponds to the first intersection that takes place below the neutral curve, as shown in figure 2.10. Higher intersection points of $\omega_c^i \tau = \pi$ and $\omega_c^i \tau = 0$ can be found as the third largest, fourth largest values of τ and so on, from figure 1.
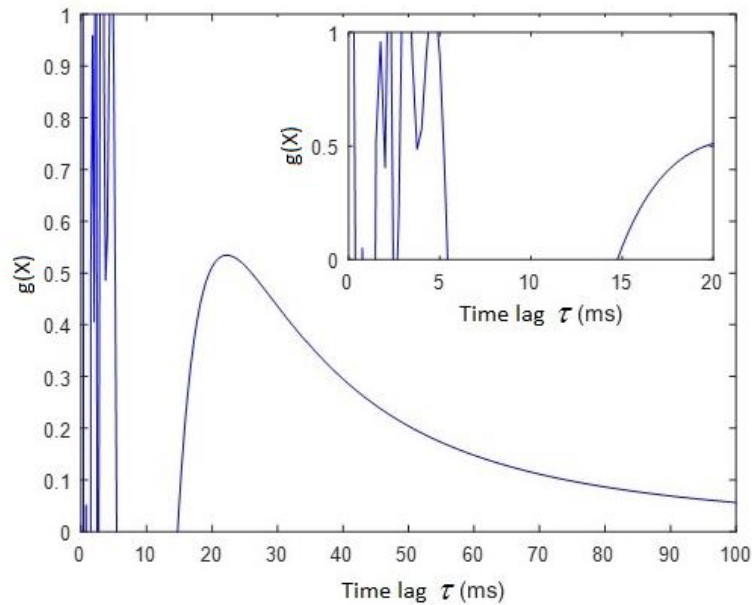
Figure AI.1: $g(X)$ vs time lag for $m^i = 1$. Inbox shows blow-up for small τ. Other parameters are the same as in Fig.2.8

Thus, it is possible to track the point of intersection of $\omega_c^i \tau = \pi$ and $\omega_c^i \tau = 0$ on the neutral curve using analytical formula (3) for $x_q = L/2$. This approach is not restricted to a particular value of x_q and can be applied to any x_q. The numerical solution of (3) predicts multiple solutions. Hence, for any intrinsic mode, multiple intersection points of neutral curve $\omega_c^i \tau = \pi$ and $\omega_c^i \tau = 0$ exist and could be found in a similar manner. The intersection points corresponding to $\omega_c^i \tau = 0$ and $\omega_c^i \tau = -\pi$ can be found in the same way. We stress that this approach provides exact results for the location of the intersection points. However, the price for finding the exact position of the intersection points is the need to solve the polynomial equation of high degree, which requires resorting to numerics. A handier alternative approach is to find a simple approximate formula for the intersections avoiding to resort to numerics, as mentioned in the § 4.2.3 of chapter 2 when dealing with asymptotic analysis.

APPENDIX II

AII.1. Local maxima of n_{th}^i for neutral curves

In § 4.2 of chapter 2 (also in Appendix I, § AI.1) we have found the value of n_{th}^i at the intersection of two segments of the neutral curve. However, it might also be interesting to have an idea of the maximal/minimal values of n_{th}^i corresponding to each segment. We can, at this point, attempt to find the values of τ for which n_{th}^i attains its local extremum. According to (2.34), n_{th}^i can be positive only when $\cos \lambda$ is negative, where $\lambda = \left(2m^i + 1\right)\pi L/(\tau c)$. Thus, to ensure positivity of n_{th}^i, we require,

$$\cos\left[\left(2m^i + 1\right)\pi L/(\tau c)\right] < 0. \tag{AII.1}$$

This produces an upper and lower bound on the values of τ for which a solution with positive n_{th}^i exists, where m is a positive integer and can have only odd values to satisfy (1).

$$\left(2L/c\right)\left(2m^i + 1\right)/\left(2m+1\right) < \tau < \left(2L/c\right)\left(2m^i + 1\right)/\left(2m-1\right). \tag{AII.2}$$

Differentiating both sides of equation (2.34) for $\omega_c^i \tau = 0$, we get the following equation: where $\lambda = \zeta/\tau$ and ζ is a constant, defined as $\zeta = \left(2m^i + 1\right)\pi L/c$,

$$dn_{th}^i / d\tau = \left\{-2\sin \lambda / \left(1 - \cos \lambda\right)^2\right\}\left(\zeta/\tau^2\right). \tag{AII.3}$$

The necessary condition for the extrema of n_{th}^i, $dn_{th}^i/d\tau = 0$, requires $\sin\lambda = 0$. This generates an explicit solution for λ: $\lambda = m\pi$, where m, according to (2), is a positive odd integer. For these values of m, $\cos\lambda = -1$. Thus, the value of τ corresponding to an extremum is,

$$\tau = \left(2m^i + 1\right)\left(L/c\right)\left(1/m\right). \qquad \text{(AII.4)}$$

Differentiating both sides of equation (3) with respect to τ, we get

$$d^2n_{th}^i/d\tau^2 = 2\left(\zeta^2/\tau^4\right)\cos\lambda/\left(1-\cos\lambda\right)^2. \qquad \text{(AII.5)}$$

Clearly, $d^2n_{th}^i/d\tau^2 < 0$ for $\cos\lambda = -1$. Thus, the values of τ specified by (4) correspond to maxima. According to (2.34) the maximum value of n_{th}^i is 1.

Hence, we have derived an analytical criterion for the positivity of n_{th}^i values and explained the specific feature of the neutral curve that shows multiple confined loops of instability. We have also derived a maximum value for n_{th}^i and the corresponding value of τ. The maximal value of n_{th}^i, for the segment of the neutral curve corresponding to $\omega_c^i \tau = 0$, comes out as 1. Similarly, for the neutral curve segments corresponding to $\omega_c^i \tau = \pi$ and $\omega_c^i \tau = -\pi$, it can be shown that the minimum value for this case is -1 and hence these segments of the neutral curve do not have any maxima.

APPENDIX III

AIII.1 Asymptotics for large τ

As figure 2.11 suggests, the largest loop of the neutral curve shifts towards larger values of τ, with an increase of the mode number. In this section, we will find asymptotics of n_{th}^i for the large time lag τ, that is $\tau >> \pi L/c$. The large τ assumption provides a way to explicitly find the intersection points for the neutral curve segments $\omega_c^i \tau = 0$ and $\omega_c^i \tau = \pm\pi$ belonging to the largest loop, as shown in figure 2.8 (a). At the intersection, n_{th}^i simultaneously satisfies equations for the neutral curve segments $\omega_c^i \tau = 0$ and $\omega_c^i \tau = \pm\pi$, given by (2.34). We begin our analysis with the left intersection: $\omega_c^i \tau = 0$ and $\omega_c^i \tau = \pi$. On equating n_{th}^i for $\omega_c^i \tau = 0$ and $\omega_c^i \tau = \pi$, from (2.34), we get

$$2\cos(\lambda)/\{\cos(\lambda)-1\} = 2\cos(\lambda+\delta)/\{1-\cos(\lambda+\delta)\}, \qquad \text{(AIII.1)}$$

where, λ, δ and normalized time lag τ_n are:

$$\lambda = (2m^i + 1)/\tau_n, \ \delta = 1/\tau_n \text{ and } \tau_n = \tau c/\pi L. \qquad \text{(AIII.2)}$$

We are now focusing on large τ asymptotics, i.e. δ, in (2), will be treated as a small parameter. Using this smallness of δ, equation (1) can be expanded in δ. On retaining just zero and linear terms we get,

$$2\cos\lambda - \delta\sin\lambda - 2\cos^2\lambda + 2\delta\sin\lambda\cos\lambda = 0, \qquad \text{(AIII.3)}$$

302

which immediately yields an explicit expression for δ,

$$\delta = \left(2\cos\lambda - 2\cos^2\lambda\right)/\left\{\sin\lambda\left(1 - 2\cos\lambda\right)\right\}. \qquad \text{(AIII.4)}$$

We can consider λ as a sum of a zero order term, λ_0, and a correction $\tilde{\lambda}$, $\lambda = \lambda_0 + \tilde{\lambda}$. To leading order in δ, $\delta = 0$ and equation (4) becomes,

$$2\cos\lambda_0 - 2\cos^2\lambda_0 = 0. \qquad \text{(AIII.5)}$$

Equation (5) yields two solutions for λ_0: $\cos\lambda_0 = 0,1$. The $\cos\lambda_0 = 1$ root corresponds to $\tau_n \to \infty$. Hence, we choose the second solution $\cos\lambda_0 = 0$, which leads to the explicit solution for λ_0: $\lambda_0 = \left(2m_{(+\pi,0)} + 1\right)\pi/2$, where $m_{(+\pi,0)} = 0,1,2,\dots$ The integer $m_{(+\pi,0)}$ is the intersection point number of the neutral curve segments $\omega_c^i \tau = 0$ and $\omega_c^i \tau = \pi$, with $m_{(+\pi,0)} = 0$ being the rightmost intersection point, while m^i is the mode number. Since not all intersections occur at positive n, $m_{(+\pi,0)}$ cannot take all integer values. This limitation on $m_{(+\pi,0)}$ will be discussed below. Inserting the two-term expansion for λ, in the form $\lambda = \lambda_0 + \tilde{\lambda}$, into (4), we get,

$$\delta = \left\{2\cos\left(\lambda_0 + \tilde{\lambda}\right) - 2\cos^2\left(\lambda_0 + \tilde{\lambda}\right)\right\}/\left\{\sin\left(\lambda_0 + \tilde{\lambda}\right)\left(1 - 2\cos\left(\lambda_0 + \tilde{\lambda}\right)\right)\right\}. \text{(AIII.6)}$$

Due to the presumed smallness of $\tilde{\lambda}$, we assume $\cos\tilde{\lambda} \approx 1$ and $\sin\tilde{\lambda} \approx \tilde{\lambda}$. Also, using $\sin\lambda_0 = (-1)^{m_{(+\pi,0)}}$, for $\cos\lambda_0 = 0$, we apply the following trigonometric identities in equation (6): $\cos\left(\lambda_0 + \tilde{\lambda}\right) \approx -(-1)^{m_{(+\pi,0)}}\tilde{\lambda}$ and $\sin\left(\lambda_0 + \tilde{\lambda}\right) \approx (-1)^{m_{(+\pi,0)}}$. On neglecting the higher order terms in $\tilde{\lambda}$, we obtain a

simplified expression for δ, from (6), of $\delta = -2\tilde{\lambda}$. Using this form,

$\lambda_0 = \left(2m_{(+\pi,0)} + 1\right)\pi\big/2$ and equation (2), we rewrite $\lambda = \lambda_0 + \tilde{\lambda}$ as follows,

$$\left(2m^i + 1\right)\big/\tau_n = \left(2m_{(+\pi,0)} + 1\right)\pi\big/2 - 1\big/\left(2\tau_n\right). \tag{AIII.7}$$

After further simplification, we arrive at an explicit expression for the normalized

time lag, τ_n, written as $\tau_{n(+\pi,0)}$, to stress the fact that it corresponds to the

intersection point of $\omega_c^i \tau = 0$ and $\omega_c^i \tau = \pi$, valid for large τ,

$$\tau_{n(+\pi,0)} = \left(4m^i + 3\right)\Big/\left\{\left(2m_{(+\pi,0)} + 1\right)\pi\right\}. \tag{AIII.8}$$

Using (2.34), n^i_{th} at the intersection can be found as,

$$n^i_{th(+\pi,0)} = \frac{2\cos\left\{\left(2m_{(+\pi,0)} + 1\right)\left(\dfrac{\pi}{2}\right)\left(1 - \dfrac{1}{4m^i}\right)\right\}}{\left[\cos\left\{\left(2m_{(+\pi,0)} + 1\right)\left(\dfrac{\pi}{2}\right)\left(1 - \dfrac{1}{4m^i}\right)\right\} - 1\right]}. \tag{AIII.9}$$

To ensure positive $n^i_{th(+\pi,0)}$, we require $\cos\left\{\left(2m_{(+\pi,0)} + 1\right)\left(\pi/2\right)\left(1 - 1/4m^i\right)\right\} < 0$,

thus $m_{(+\pi,0)}$ will be restricted to odd integers, i.e. $m_{(+\pi,0)} = 2j + 1$. The even

intersection points should be discarded from consideration. On substituting

$m_{(+\pi,0)} = 2j + 1$ into (9), we obtain the simplified form,

$$n^i_{th(+\pi,0)} = 2\sin\left(3\pi\big/8m^i\right)\Big/\left[\sin\left(3\pi\big/8m^i\right) + 1\right]. \tag{AIII.10}$$

This shows how $n^i_{th(+\pi,0)}$ tends to zero as m^i increases. Further, for $m^i \gg 1$,

$\sin\left(3\pi\big/8m^i\right) \approx 3\pi\big/8m^i$. Thus, for large m^i, (10) reduces to,

$$n^i_{th(+\pi,0)} \approx 6\pi/\left(3\pi + 8m^i\right) = 2\pi/\left(\pi + 8m^i/3\right). \qquad \text{(AIII.11)}$$

Similar consideration of the intersections of the neutral curve segments $\omega^i_c \tau = 0$ and $\omega^i_c \tau = -\pi$ yields,

$$\tau_{n(-\pi,0)} = \left(4m^i + 1\right)/\left\{\left(2m_{(-\pi,0)} + 1\right)\pi\right\}. \qquad \text{(AIII.12)}$$

Here $m_{(-\pi,0)}$ is an integer indicating the intersection point number of the neutral curve segments intersections $\omega^i_c \tau = 0$ and $\omega^i_c \tau = -\pi$, with $m_{(-\pi,0)}=0$ being the rightmost intersection point, while m^i is the mode number. However, in contrast to the previous case, to ensure the positive value of $n^i_{th(-\pi,0)}$, we require

$\cos\left\{\left(2m_{(-\pi,0)} + 1\right)(\pi/2)\left(1 + 1/4m^i\right)\right\} < 0$. Hence, the value of $m_{(-\pi,0)}$ will be restricted to even integers, i.e. $m_{(-\pi,0)} = 2j$, whereas the odd intersection points should be discarded from consideration for this case. Equivalent to (10), we can arrive at an identical expression for n^i_{th} in this case as well,

$$n^i_{th(-\pi,0)} = 2\sin\left(\pi/8m^i\right)/\left[\sin\left(\pi/8m^i\right) + 1\right]. \qquad \text{(AIII.13)}$$

This expression quantifies how $n^i_{th(-\pi,0)}$ tends to zero as m^i increases. A comparison of (10) and (13) shows that $n^i_{th(-\pi,0)} < n^i_{th(+\pi,0)}$. Thus, for this case, the intersection points of neutral curve segments correspond to lower values of n^i_{th} compared to the previous case. For large mode numbers, we arrive at an expression for $n^i_{th(-\pi,0)}$ which is identical to (11),

305

$$n^i_{th(-\pi,0)} \approx 2\pi \Big/ \big(\pi + 8m^i\big).$$ (AIII.14)

Figure 1 shows how the values of τ and n^i_{th} at the intersection (given by (8), (10), (12) and (13) respectively) depend on the mode number. The plots are for two particular intersection numbers: $m_{(+\pi,0)}=1$ and $m_{(-\pi,0)}=0$. As mentioned previously, intersection number $m_{(+\pi,0)}=0$ corresponds to negative n^i_{th}. Hence, we made plots for the intersection, $m_{(+\pi,0)}=1$. In figure 1(a), the region above $\tau = \pi L/c$ is marked in light gray to indicate the extremely optimistic interpretation of the domain of validity for the large τ assumption (recall, the true condition of validity is $\tau \gg \pi L/c$). The values of τ at the intersection of the neutral curve segments increase as the mode number increases, while n^i_{th} at the intersection decreases with $\big(2\pi \big/ \big(\pi + 8m^i/3\big)\big)$ or $\big(2\pi \big/ \big(\pi + 8m^i\big)\big)$ for high mode numbers.

The figure can be also viewed from a different perspective. For any given τ, a straight horizontal line in figure 1(a) would give the numbers of the modes whose large loops overlap for such a combustor. The intersection of this horizontal line with the solid straight line gives, in the generic case, a non-integer m^i. That is, this intersection falls in between the extreme right intersections of neutral curve segments for two subsequent modes. In § 4.4 of chapter 2, it is shown that only these two modes are important from the perspective of the prediction of maximal growth rate. All modes with numbers below these two modes are stable (for large n) for this τ, while all modes higher than these two, have a smaller growth rate. For example, τ =25 ms intersection of $\omega^i_c \tau = 0$ and $\omega^i_c \tau = -\pi$ falls between the third and fourth

intrinsic modes, whereas the intersection of $\omega_c^i \tau = 0$ and $\omega_c^i \tau = \pi$ falls between the

eighth and ninth intrinsic modes, as shown by the black dashed line projections on the

horizontal axis of figure 1(a) and/or relation (8, 12). Hence, it is these two modes

which are of crucial importance from the growth rate prediction perspective. Figure

1(b) also shows that the value of n_{th}^i at the $\omega_c^i \tau = 0$ $\omega_c^i \tau = -\pi$ intersection is always

lower than n_{th}^i at the $\omega_c^i \tau = 0$ $\omega_c^i \tau = \pi$ intersection, in accordance with (10) and (13).

Previously, considering figure 2.8, we noticed that for the second mode, n_{th}^i is

minimal at the intersection of the $\omega_c^i \tau = 0$ and $\omega_c^i \tau = -\pi$ segments of the neutral

curve for the extreme right loop in the curve. This proved to be the case for all modes.

Here, in figure 1, we also plot the exact numerical solutions for segments of the

neutral curve and manually track down the points of their intersections. The

agreement between the "exact" numerical results, shown in figure 1 by circles and the

analytical predictions is remarkable, given that the large τ asymptotics is not

formally applicable in the left corner of these figures.

Thus, to avoid dealing with large $m_{(+\pi,0)}$, large $m_{(-\pi,0)}$ and large τ regimes head on,

we found a simple analytical description of the points of intersection of the segments

of neutral curves $\omega_c^i \tau = 0$ and $\omega_c^i \tau = \pi$, as well as $\omega_c^i \tau = 0$ and $\omega_c^i \tau = -\pi$, assuming

large τ. At the intersection of neutral curve segments, n_{th}^i decreases with the

increase of mode number. n_{th}^i, at the intersection of $\omega_c^i \tau = 0$ and $\omega_c^i \tau = \pi$, is always

larger than n_{th}^i at the intersection of $\omega_c^i \tau = 0$ and $\omega_c^i \tau = -\pi$. The extreme right

intersection point of $\omega_c^i \tau = 0$ and $\omega_c^i \tau = -\pi$ (that is, the intersection of the large loop

with $m_{(-\pi,0)}=0$, as given by (12)) corresponds to the lowest value of n^i_{th} for any fixed

mode number.

(a)

(b)

Figure AIII.1: **(a)** Values of τ at the intersections of the neutral curve segments $\omega^i_c \tau = 0$ and $\omega^i_c \tau = \pm\pi$ vs mode number of the intrinsic mode. Solid red and dashed blue lines show the large τ asymptotic solution (12, 8) for the intersections $\omega^i_c \tau = 0$, $\omega^i_c \tau = -\pi$ (when $m_{(-\pi,0)}$ =0) and $\omega^i_c \tau = 0$, $\omega^i_c \tau = \pi$ (when $m_{(+\pi,0)}=1$) segment, respectively. Circles (red and blue) show their numerical counterparts found by plotting (2.34) and manually tracking down the points of intersection of the corresponding neutral curve segments. The light gray colour represents the region where the large τ assumption might be applicable. **(b)** n^i_{th} at the intersections of neutral curve segments $\omega^i_c \tau = 0$ and $\omega^i_c \tau = \pm\pi$ vs mode number of the intrinsic mode. Solid red and dashed blue lines show the analytical solution (13, 10) for $\omega^i_c \tau = 0$, $\omega^i_c \tau = -\pi$ (for $m_{(-\pi,0)}=0$) and $\omega^i_c \tau = 0$, $\omega^i_c \tau = \pi$ (for $m_{(+\pi,0)}=1$) intersections respectively. Circles (red and blue) show their numerical counterparts in panel (a). The instability domain is marked in yellow. The first intrinsic mode is not shown.

APPENDIX IV

AIV.1. Effect of flame location on n_{th}^{i}

In this section, the effect of flame location on the threshold value of n is analyzed. An attempt will be made to identify the flame location within the resonator, for which n_{th}^{i} attains its maximum or minimum. For simplicity, in this section, we assume no cross-section jump or temperature jump. For $S_2/S_1 = 1$, $\rho_2/\rho_1 = 1$ and $c_2/c_1 = 1$, the value of n_{th}^{i}, given by (2.33), takes the form,

$$n_{th}^{i} = \frac{\cos\left\{\left(\omega_0^i + \omega_c^i\right)\dfrac{L}{c}\right\}}{\cos\left(\omega_c^i \tau\right)\sin\left(\dfrac{\left(\omega_0^i + \omega_c^i\right)x_q}{c}\right)\sin\left\{\dfrac{\left(\omega_0^i + \omega_c^i\right)\left(x_q - L\right)}{c}\right\}} .$$ (AIV.1)

Note that the right-hand side of equation (1) is a symmetric function with respect to $x_q = L/2$, as $n_{th}^{i}\big|_{x_q=L/2+x} = n_{th}^{i}\big|_{x_q=L/2-x}$, for any x satisfying $0 < x < L/2$. Taking the logarithm of both sides of equation (1) leads to,

$$\log\left(n_{th}^{i}\right) = \log\left[\cos\left\{\left(\omega_0^i + \omega_c^i\right)\dfrac{L}{c}\right\}\right] - \log\left[\cos\left(\omega_c^i \tau\right)\right]$$

$$- \log\left[\sin\left(\dfrac{\left(\omega_0^i + \omega_c^i\right)x_q}{c}\right)\right] - \log\left[\sin\left\{\dfrac{\left(\omega_0^i + \omega_c^i\right)\left(x_q - L\right)}{c}\right\}\right] ,$$ (AIV.2)

And, on differentiating both sides of equation (2) with respect to x_q, we obtain,

$$\frac{dn_{th}^i}{dx_q} = \frac{-\dfrac{\left(\omega_0^i + \omega_c^i\right)}{c} \sin\left\{\dfrac{\left(\omega_0^i + \omega_c^i\right)\left(2x_q - L\right)}{c}\right\} n_{th}^i}{\sin\left(\dfrac{\left(\omega_0^i + \omega_c^i\right)x_q}{c}\right)\sin\left\{\dfrac{\left(\omega_0^i + \omega_c^i\right)\left(x_q - L\right)}{c}\right\}}. \qquad \text{(AIV.3)}$$

At the extrema (maximum or minimum) of n_{th}^i with respect to x_q, the necessary condition is $dn_{th}^i/dx_q = 0$, which can be reduced to

$$\sin\left\{\frac{\left(\omega_0^i + \omega_c^i\right)\left(2x_q - L\right)}{c}\right\} = 0. \qquad \text{(AIV.4)}$$

It is easy to see from it that the extremum flame location for n_{th}^i is $x_q = L/2$. This is true for any τ and any intrinsic mode. To find whether n_{th}^i has a maximum or minimum at $x_q = L/2$, we analyze the second derivative with respect to x_q,

$$\frac{d^2 n_{th}^i}{dx_q^2} = \frac{2\left(\omega_0^i + \omega_c^i\right)^2 n_{th}^i}{c^2 \cos\left(\omega_c^i \tau\right)\sin^2\left\{\left(\omega_0^i + \omega_c^i\right)\dfrac{L}{2c}\right\}}. \qquad \text{(AIV.5)}$$

Hence, at $x_q = L/2$, for any τ and any intrinsic mode for the segment $\omega_c^i \tau = 0$, $d^2 n_{th}^i/dx_q^2 > 0$, while for $\omega_c^i \tau = \pi$ and $\omega_c^i \tau = -\pi$, $d^2 n_{th}^i/dx_q^2 < 0$. Thus, n_{th}^i has a local minimum at $x_q = L/2$ on the $\omega_c^i \tau = 0$ segment and a maximum for $\omega_c^i \tau = \pi$ and $\omega_c^i \tau = -\pi$ for any τ.

Therefore, n_{th}^i indeed attains an extremum when the flame sits at the middle of the resonator. However, whether this extremum is a maximum or minimum depends on the segment of the neutral curve we focus on. For example, as mentioned previously,

at $x_q = L/2$, when $\omega_c^i \tau = 0$, n_{th}^i reaches a minimum and when $\omega_c^i \tau = \pi$ and $\omega_c^i \tau = -\pi$, n_{th}^i reaches a maximum.
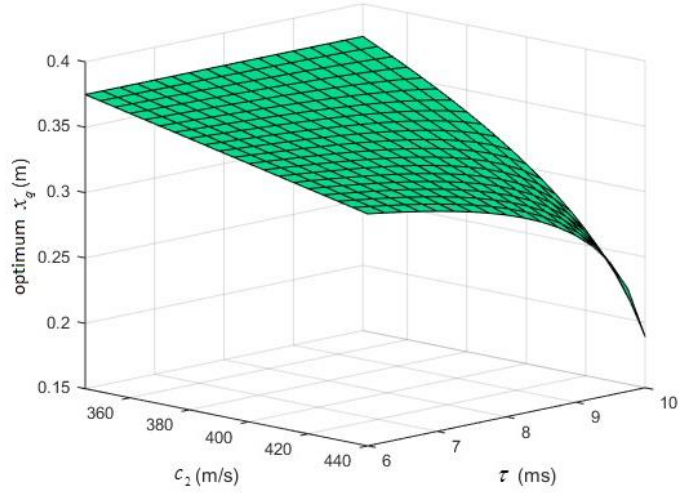
(a)
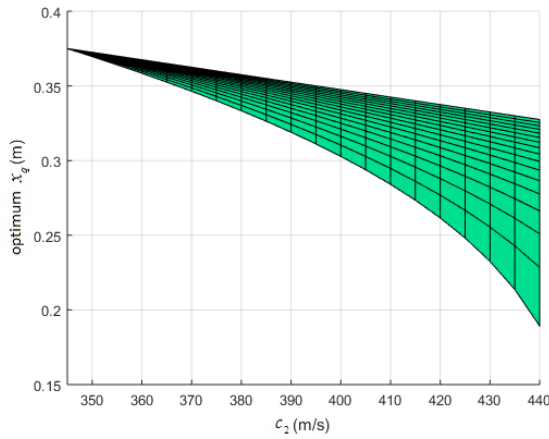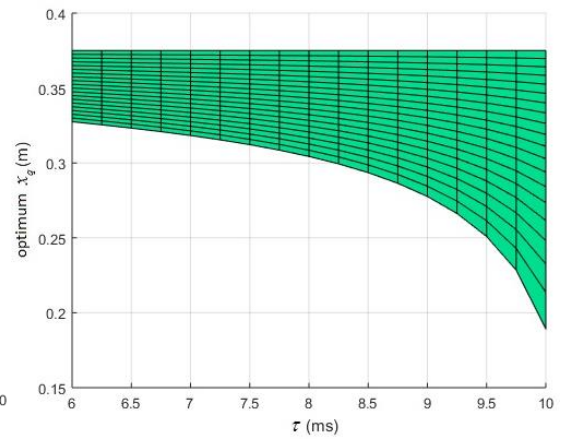
(b)   (c)

Figure AIV.1: Extremal flame location (x_q) given by (8), as function of τ and c_2, for the second intrinsic mode and $c_1 = 345$ m/s. The parameters are the same as in figure 2.8.

It is also possible to analytically find the extremal flame location considering the effect of cross-section and temperature jump. The threshold value (2.33) can be restructured as,

$$n_{th}^{i} = \left(\alpha \cot \left(\left(\omega_{0}^{i} + \omega_{c}^{i} \right) \frac{x_{q}}{c_{1}} \right) \cot \left(\left(\omega_{0}^{i} + \omega_{c}^{i} \right) \frac{\left(x_{q} - L \right)}{c_{2}} \right) + 1 \right) \Bigg/ \cos \left(\omega_{c}^{i} \tau \right). \quad \text{(AIV.6)}$$

Differentiating n_{th}^{i} with respect to x_{q} yields,

$$\frac{dn_{th}^{i}}{dx_{q}} = -\frac{\alpha \left(\omega_{0}^{i} + \omega_{c}^{i} \right)}{\cos \left(\omega_{c}^{i} \tau \right)} \left[\begin{array}{l} \dfrac{1}{c_{1}} \cos ec^{2} \left(\dfrac{\left(\omega_{0}^{i} + \omega_{c}^{i} \right) x_{q}}{c_{1}} \right) \cot \left(\dfrac{\left(\omega_{0}^{i} + \omega_{c}^{i} \right) \left(x_{q} - L \right)}{c_{2}} \right) + \\[3mm] \dfrac{1}{c_{2}} \cos ec^{2} \left(\dfrac{\left(\omega_{0}^{i} + \omega_{c}^{i} \right) \left(x_{q} - L \right)}{c_{2}} \right) \cot \left(\dfrac{\left(\omega_{0}^{i} + \omega_{c}^{i} \right) x_{q}}{c_{1}} \right) \end{array} \right].$$

$$\text{(AIV.7)}$$

The condition of its vanishing can further be written as,

$$F\left(x_{q} \right) = \frac{1}{c_{1}} \sin \left(\frac{2 \left(\omega_{0}^{i} + \omega_{c}^{i} \right) \left(x_{q} - L \right)}{c_{2}} \right) + \frac{1}{c_{2}} \sin \left(\frac{2 \left(\omega_{0}^{i} + \omega_{c}^{i} \right) x_{q}}{c_{1}} \right) = 0. \quad \text{(AIV.8)}$$

When $c_{1} = c_{2}$, (8) reduces to (4). Equation (8) must be solved numerically to find the optimum flame location. Interestingly, equation (8) is independent of the cross-section jump. Thus, the optimum flame location depends only on the temperature jump across the flame. Figure 1 shows a plot of the optimum flame location (x_{q}) as a solution of (8), depending on τ and c_{2}, for the second intrinsic mode. Figure 1 shows that if we increase c_{2}, the optimum value of the flame location (x_{q}) reduces, that is, it shifts slightly towards the closed end of the resonator. A similar observation can be made when we treat τ as a parameter. It is important to mention that beyond certain c_{2}, for any τ, we will not find any solution of (8). To understand why this happens, consider (8) for large c_{2}, then it reduces to

$$\sin \left(\frac{2 \left(\omega_{0}^{i} + \omega_{c}^{i} \right) x_{q}}{c_{1}} \right) = 0. \quad \text{(AIV.9)}$$

Clearly, this equation does not provide any solutions other than $x_q = 0$.

Hence, it is possible to find the optimum flame location for which n_{th}^i attains a maxima or minima, taking into account both the cross-section and temperature jump. Surprisingly, the optimum flame location proved to be independent of the cross-section jump. As the temperature jump increases, the extremum flame location tends to shift towards the closed end of the resonator.

AIV.2 Effect of temperature jump on n_{th}^i

The effect of the temperature jump across flame can be identified on n_{th}^i by considering equation (6) as a starting point. In this case, we will find extrema of n_{th}^i with respect to c_2 instead of T_2 and also make use of the relation between mean density jump and speed of sound jump across flame, as $\rho_2/\rho_1 = (c_2/c_1)^2$. Differentiating n_{th}^i with respect to c_2, as per equation (6) (assuming c_1 and other parameters constant), provides us with the following expression,

$$
\frac{dn_{th}^i}{dc_2} = \left(\frac{S_2}{S_1 c_1}\right) \frac{\cot\left(\frac{\left(\omega_0^i + \omega_c^i\right)x_q}{c_1}\right)}{\cos\left(\omega_c^i \tau\right)} \left[\cos ec^2\left(\frac{\left(\omega_0^i + \omega_c^i\right)\left(x_q - L\right)}{c_2}\right) + \cot\left(\frac{\left(\omega_0^i + \omega_c^i\right)\left(x_q - L\right)}{c_2}\right) \right]. \quad \text{(AIV.10)}
$$

Clearly, at extrema of n_{th}^i, $dn_{th}^i/dc_2 = 0$, meaning we have the following governing equation to define the extremum value of c_2,

313

$$\sin\left(\frac{2\left(\omega_0^i + \omega_c^i\right)\left(x_q - L\right)}{c_2}\right) = -\left(\frac{2\left(\omega_0^i + \omega_c^i\right)\left(x_q - L\right)}{c_2}\right). \tag{AIV.11}$$

The only solution that equation (11) offers us is as follows,

$$\frac{2\left(\omega_0^i + \omega_c^i\right)\left(x_q - L\right)}{c_2} = 0, \tag{AIV.12}$$

suggesting that the extremum $c_2 \to \infty$. Thus, n_{th}^i does not have any extrema with respect to c_2/c_1 or, in general, temperature jump across the flame.

AIV.3 Effect of cross-section jump on n_{th}^i

Effect of cross-section jump across the flame can also be evaluated like in § 2, by considering equation (6) as a starting point. Differentiating n_{th}^i with respect to S_2, as per equation (6) (assuming S_1 and other parameters constant), provides us with the following expression,

$$\frac{dn_{th}^i}{dS_2} = \frac{\left(\frac{\rho_1 c_1}{S_1 \rho_2 c_2}\right)\left[\cos\left\{\left(\omega_0^i + \omega_c^i\right)\beta_1\right\} + \cos\left\{\left(\omega_0^i + \omega_c^i\right)\beta_2\right\}\right]}{2\cos\left(\omega_c^i \tau\right)\sin\left(\frac{\left(\omega_0^i + \omega_c^i\right)x_q}{c_1}\right)\sin\left\{\frac{\left(\omega_0^i + \omega_c^i\right)\left(x_q - L\right)}{c_2}\right\}}. \tag{AIV.13}$$

At extrema of n_{th}^i, $dn_{th}^i/dS_2 = 0$, meaning we have the following governing equation to define the extremum value of S_2,

$$\cos\left\{\left(\omega_0^i + \omega_c^i\right)\beta_1\right\} + \cos\left\{\left(\omega_0^i + \omega_c^i\right)\beta_2\right\} = 0. \tag{AIV.14}$$

Quite surprisingly, any S_2 related term does not feature in equation (14). Hence, similar to the effect of temperature jump across the flame, we do not obtain any extrema of n^i_{th} with respect to cross-section jump across the flame.

In summary, a detailed parametric study in this section proves that n^i_{th} has extrema with respect to flame location. However, there are no such extrema of n^i_{th} with respect to temperature jump and cross-section jump across flame for a closed-open combustor.

APPENDIX V

AV.1. Value of n for which coupled intrinsic-acoustic modes attain the same frequency

It has been mentioned, in § 2 of Chapter 3, that a gradual increase of n from 0 brings the coupled modes closer in the complex frequency plane and, for a certain n, their frequencies are equal and start crossing each other. In this section, we make an attempt to analytically evaluate an expression of n, for which coupled modes have the same frequencies but different decay rates.

We start with equation (3.29) and consider a special case of $S_1 = S_2$ and $T_1 = T_2$, thus $c_1 = c_2 = c$, $\rho_1 = \rho_2$ and make use of A, B and C as per equation (3.33). When the frequencies of the coupled modes are equal and thus, $Re(\Delta\omega_1) = Re(\Delta\omega_2)$, this will automatically imply that $\left[(B^2 - 4AC) / 4A^2 \right]$ is a negative real number and does not possess any imaginary component. Hence, the necessary condition for the equal frequency of the coupled modes, $Re(\Delta\omega_1) = Re(\Delta\omega_2)$ can also be interpreted as, $Im\left[(B^2 - 4AC) / 4A^2 \right] = 0$. In that case, $Re(\Delta\omega_1) = Re(-B/2A)$ and the $\left[(B^2 - 4AC) / 4A^2 \right]$ only contributes in the decay rate, which is different for the coupled modes. The further implication of the aforementioned condition, $Im\left[(B^2 - 4AC) / 4A^2 \right] = 0$ is that,

$$Re\left(B^2 - 4AC\right)Im\left(A^2\right) - Im\left(B^2 - 4AC\right)Re\left(A^2\right) = 0. \quad \text{(AV.1)}$$

Further, $Re\left(B^2 - 4AC\right)$, $Im\left(B^2 - 4AC\right)$, $Re\left(A^2\right)$ and $Im\left(A^2\right)$ can be expanded into the following expressions, by making use of A, B and C as per equation (3.33),

$$Re\left(B^2 - 4AC\right) = 4\left(\frac{L^2}{c_0^2}\right) + 4n\left\{\left(\frac{L^2}{c_0^2}\right)\cos\left(\omega_0^a\tau\right) - (-1)^{m^a}\,\tau\frac{L}{c_0}\sin\left(\omega_0^a\tau\right)\right\}$$
$$+ n^2\left\{\left(\frac{L^2}{c_0^2} + \tau^2\right)\cos\left(2\omega_0^a\tau\right) + 2(-1)^{m^a}\,\tau\frac{L}{c_0}\sin\left(2\omega_0^a\tau\right)\right\},$$

$$Im\left(B^2 - 4AC\right) = 4n\left\{\left(\frac{L^2}{c_0^2}\right)\sin\left(\omega_0^a\tau\right) + (-1)^{m^a}\,\tau\frac{L}{c_0}\cos\left(\omega_0^a\tau\right)\right\}$$
$$+ n^2\left\{\left(\frac{L^2}{c_0^2} + \tau^2\right)\sin\left(2\omega_0^a\tau\right) - 2(-1)^{m^a}\,\tau\frac{L}{c_0}\cos\left(2\omega_0^a\tau\right)\right\},$$

$$Re\left(A^2\right) = \left(\frac{\tau^2}{4} - \frac{L^2}{c_0^2}\right)\cos\left(2\omega_0^a\tau\right) + (-1)^{m^a}\,\tau\frac{L}{c_0}\sin\left(2\omega_0^a\tau\right),$$

$$Im\left(A^2\right) = \left(\frac{\tau^2}{4} - \frac{L^2}{c_0^2}\right)\sin\left(2\omega_0^a\tau\right) - (-1)^{m^a}\,\tau\frac{L}{c_0}\cos\left(2\omega_0^a\tau\right). \quad \text{(AV.2 a,b,c,d)}$$

Plugging the expressions $Re\left(B^2 - 4AC\right)$, $Im\left(B^2 - 4AC\right)$, $Re\left(A^2\right)$ and $Im\left(A^2\right)$, as per (2), into (1) leads to a simplified quadratic equation in n,

$$A_1 n^2 + B_1 n + C_1 = 0, \quad \text{(AV.3)}$$

Where, A_1, B_1 and C_1 are represented by the following simplified expressions,

$$A_1 = -(-1)^{m^a}\,\tau\frac{L}{c_0}\left(\frac{\tau^2}{2} + \frac{3L^2}{c_0^2}\right),$$

$$B_1 = -\frac{L^2}{c_0^2}\left(3\tau^2 + \frac{4L^2}{c_0^2}\right)\sin\left(\omega_0^a\tau\right) - (-1)^{m^a}\,\tau^3\frac{L}{c_0}\cos\left(\omega_0^a\tau\right),$$

$$C_1 = \frac{L^2}{c_0^2} \left[\left(\tau^2 - \frac{4L^2}{c_0^2} \right) \sin\left(2\omega_0^a \tau \right) - \left(-1 \right)^{m^a} 4\tau \frac{L}{c_0} \cos\left(2\omega_0^a \tau \right) \right]. \qquad \text{(AV.4)}$$

Indeed, equation (3) generates two solutions of n for any case. In the case of the coupling of modes, one of them is positive and is of importance, the other solution is negative and thus does not carry any physical significance. For example, if we consider the test case explained in § 2 of chapter 3, we find two solutions of (3), n =0.4435, -1.65. n =0.4435 is in fact a true physical solution verified by numerical analysis. The other solution is non-physical and thus should be discarded.

We have derived a compact analytical expression to identify the n for which coupled modes have an equal frequency. At this n, both coupled modes have the same frequency but different decay rates. This analytical expression has been checked against numerics and is found to work with reasonable accuracy. However, we need to clarify that because of intrinsic limitations of the quadratic equation (3.30), mainly away from the neutral line, equation (3) cannot be trusted all the time. This equation needs to be improved further based on quartic equation (3.35). This lies in the scope of future work.

References

1.   Abarbanel H. D. I., Brown R., Sidorowich J. J., Tsimring L. S., 'The analysis of observed chaotic data in physical systems', *Reviews of Modern Physics*, Vol 65, No 4, October, (1993).

2.   Alemela P.R., Fanaca D., Hirsch C., Sattelmayer T., Schuermans B., 'Determination and scaling of thermo-acoustic characteristics of premixed flames', *International Journal of Spray and Combustion Dynamics*, Vol 2, No 2, 169-198, (2010).

3.   Altunlu A. C., Hoogt P. J. M., Boer A., 'Sensitivity of combustion driven structural dynamics and damage to thermo-acoustic instability: Combustion-acoustics-vibration', *Journal of Engineering for Gas Turbines and Power*, 136(5), GTP-13-1009, (2014).

4.   Ananthakrishnan N., Sudershan S., Sudhakar K., Verma A., 'Large amplitude limit cycles in resonantly coupled oscillators', *Journal of Sound and Vibration*, 231(5), 1377-1382, (2000).

5.   Balasubramanian K., Sujith R. I., 'Non-normality and nonlinearity in combustion-acoustic interaction in diffusion flames', *Journal of Fluid Mechanics*, Vol 594, 29-57, (2008).

6.   Bauerheim M., Nicoud F., Poinsot T., 'Theoretical analysis of the mass balance equation through a flame at zero and non-zero Mach numbers', *Combustion and Flame*, Vol. 162 (1), 60-67, (2015).

7.   Bauerheim M., Nicoud F., Poinsot T., 'Progress in analytical methods to predict and control azimuthal combustion instability modes in annular chambers', *Physics of Fluids*, Vol. 28 (2), (2016).

8.   Bellows B. D., Bobba M. K., Seitzman J. M., Lieuwen T., 'Nonlinear flame transfer function characteristics in a swirl stabilised combustor', *ASME Turbo Expo*, GT2006-91119, May 8-11, (2006).

9.   Berenbrink, P., Hoffmann, S., 'Suppression of dynamic combustion instabilities by passive and active means', *International Gas Turbine and Aeroengine Congress & Exposition*, ASME 2000-GT-0079, Munich, (2000).

10.   Blackshear P. L., 'Driving standing waves by heat addition', *National Advisory committee for Aeronautics*, Technical note: 2772, Washington, August, (1952).

11.   Bloxsidge C. J., Dowling A. P., Langhorne P. J., 'Reheat buzz: an acoustically coupled combustion instability. Part 2. theory', *Journal of Fluid Mechanics*, Vol 193, 445-473, (1988).

12.   Bomberg S., Emmert T., Polifke W., 'Thermal vs acoustic response of velocity sensitive premixed flames', *Proceedings of the Combustion Institute*, 35(3), 3185–3192, (2015).

13.   Boudy F., Durox D., Schuller T., Candel S., 'Nonlinear mode triggering in a multiple flame combustor', *Proceedings of the Combustion Institute*, 33, 1121-1128, (2011).

14.   Boyer L., Quinard J., 'On the dynamics of anchored flames', *Combustion and Flame*, 82, 51-65, (1990).

15.   Buechner H., Hirsch C., Leuckel W., 'Experimental investigations on the dynamics of pulsated premixed axial jet flames', *Combustion Science and Technology*, 94, 219-228, (1993).

16.   Campa G., Camporeale S.M., 'Influence of flame and burner transfer matrix on thermo-acoustic combustion instability modes and frequencies', *Proceedings of the ASME Turbo Expo*, Glasgow, GT2010-23104, (2010).

17.   Campa G., Camporeale S.M., 'Influence of nonlinear flame models on bifurcation process and limit cycles in gas turbine combustors', n³l - *International Summer School and Workshop on Non-Normal and Nonlinear Effects in Aero and Thermo-acoustics*, Munich, 18-21 June, (2013).

18.   Candel S. M., 'Combustion instabilities coupled by pressure waves and their active control', *Twenty-fourth International Symposium on Combustion, The Combustion Institute*, 1277-1296, (1992).

19.   Cao L., 'Practical method for determining the minimum embedding dimension of a scalar time series', *Physica D*, 110, 43-50, (1997).

20.   Courtine E., Selle L., Nicoud F., Polifke W., Silva C., Bauerheim M., Poinsot T., 'Causality and intrinsic thermo-acoustic instability modes', *Centre for Turbulent Research, Proceedings of the summer program*, (2014).

21.   Courtine E., Selle L., Poinsot T., 'DNS of intrinsic thermo-acoustic modes in laminar premixed flames', *Combustion and Flame*, 162, 4331-4341, (2015).

22.   Craik A. D. D., 'Wave interactions and fluid flows', *Cambridge University Press*, (1985).

23.   Crocco L., Cheng S.I., 'Theory of combustion instability in liquid propellant rocket motors', *Butterworths Scientific Publications*, (1956).

24.   Cuquel A., Durox D., Schuller T., 'Theoretical and experimental determination of the flame transfer function of confined premixed conical flames', *Seventh Mediterranean Combustion Symposium*, Sardinia, 11-15th September, (2011).

25.   Cuquel A., Durox D., Schuller T., 'Impact of flame base dynamics on the non-linear frequency response of conical flames', *Combustion, Flow and Spray Dynamics for Aerospace Propulsion*, 341, 171-180, (2013a).

26.   Cuquel A., Silva C., Nicoud F., Durox D., Schuller T., 'Prediction of the non-linear dynamics of a multiple flame combustor by coupling the describing function methodology with a Helmholtz solver', *ASME Turbo Expo*, San Antonio, June 3-7, (2013b).

27.   Culick, F. E. C., Lin, W. H., Jahnke, C. C., Sterling, J. D., *'Modelling for active control of combustion and thermally driven oscillations', Proceedings of the American Control Conference*, 2939-2948, (1991).

28.   Dec J. E., Keller J. O., Hongo I., 'Time resolved velocities and turbulence in the oscillating flow of a pulse combustor tail pipe', *Combustion and Flame*, 83, 271-292, (1991).

29.   Dowling A. P., 'The calculation of thermo-acoustic oscillations', *Journal of Sound and Vibration*, 180(4), 557-581, (1995).

30.   Dowling A. P., 'Nonlinear self-excited oscillations of a ducted flame', *Journal of Fluid Mechanics*, Vol 346, 271-290, (1997).

31.   Dowling A. P., 'A kinematic model of a ducted flame', *Journal of Fluid Mechanics*, Vol 394, 51-72, (1999).

32.   Dowling A. P., Stow S.R., 'Acoustic analysis of gas turbine combustors', *Journal of Propulsion and Power*, Vol 19, Issue 5, 751-764, Sep-Oct (2003).

33.   Dowling A. P., Mahmoudi Y., 'Combustion noise', *Proceedings of the Combustion Institute*, 35, 65-100, (2015).

34.   Ducruix, S., Durox, D., Candel S., 'Theoretical and experimental determinations of the transfer function of a laminar premixed flame', *Proceedings of the Combustion Institute*, Vol 28, 765–773, (2000).

35.   Durox D., Ducruix, S., Candel S., 'Experiments on collapsing cylindrical flames', *Combustion and Flame*, 125, 982-1000, (2001).

36.   Durox D., Schuller T., Candel S., 'Combustion dynamics of inverted conical flames', *Proceedings of the Combustion Institute*, 30, 1717-1724, (2005).

37.   Durox D., Schuller T., Noiray N., Candel S., 'Experimental analysis of nonlinear flame transfer functions for different flame geometries', *Proceedings of the Combustion Institute*, 32, 1391-1398, (2009a).

38.   Durox D., Schuller T., Noiray N., Birbaud A. L., Candel S., 'Rayleigh criterion and acoustic energy balance in unconfined self-sustained oscillating flames', *Combustion and Flame*, 156, 106-119, (2009b).

39.   Emmert T., Bomberg S., Polifke W., 'Intrinsic thermo-acoustic instability of premixed flames', *Combustion and Flame*, 162, 75-85, (2015).

40.   Emmert T., Bomberg S., Jaensch S., Polifke W., 'Acoustic and intrinsic thermo-acoustic modes of a premixed combustor', *Thirty-sixth International Symposium on Combustion*, Seoul, (2016).

41.   Fleifil M., Annaswamy A. M., Ghoneim Z. A., Ghoniem A. F., 'Response of a laminar premixed flame to flame oscillations: A kinematic model and thermo-acoustic instability results', *Combustion and Flame*, 106, 487-510, (1996).

42.   Freitag E., 'On the measurement and modeling of flame transfer functions at elevated pressure', *Ph.D. thesis, Technical University of Munich*, (2009).

43. Hathout J. P., Fleifil M., Annaswamy A. M., Ghoniem A. F., 'Heat release actuation for control of mixture inhomogeneity driven combustion instability', *Proceedings of the Combustion Institute*, 28, 721-730, (2000).

44. Higgins B., *Journal of Natural Philosophy and Chemical Arts*, 1: 129, (1777).

45. Hoeijmakers M., Kornilov V., Arteaga I. L., Goey P., Nijmeijer H., 'Intrinsic instability of flame-acoustic coupling', *Combustion and Flame*, 161, 2860-2867, (2014).

46. Hoeijmakers M., 'Flame-acoustic coupling in combustion instabilities', *Ph.D. thesis, Technical University of Eindhoven*, (2014).

47. Hoeijmakers M., Kornilov V., Arteaga I. L., Goey P., Nijmeijer H., 'Flame dominated thermo-acoustic instabilities in a system with high acoustic losses', *Combustion and Flame*, 169, 209-215, (2016).

48. Hubbard S., Dowling A. P., 'Acoustic resonances of an industrial gas turbine combustion system', *Journal of Engineering for Gas Turbines and Power-Transactions of the ASME*, Vol 123, Issue 4, 766-773, Oct (2001).

49. Juniper M. P., 'Triggering in thermo-acoustics', *International Journal of Spray and Combustion Dynamics*, Vol 4, No 3, 217-238, (2011).

50. Kabiraj L., 'Intermittency and route to chaos in thermo-acoustic oscillations', *Ph.D. thesis*, (2012).

51. Kabiraj L., Saurabh A., Wahi P., Sujith R. I., 'Route to chaos for combustion instability in ducted laminar premixed flames', *Chaos*, 22, 023129 (1-12), (2012a).

52.　　Kabiraj L., Sujith R. I., 'Nonlinear self-excited thermo-acoustic oscillations: intermittency and flame blowout', *Journal of Fluid Mechanics*, Vol 713, 376-397, (2012b).

53.　　Karimi N., Jin S.H., Brear M.J., 'An experimental study of the transfer function of a ducted, laminar premixed flame', *Sixteenth Australasian Fluid mechanics conference*, Gold coast, 2-7 December, (2007).

54.　　Karimi N., Brear M. J., Jin S.H., Monty J.P., 'Linear and non-linear forced response of a conical, ducted, laminar premixed flame', *Combustion and Flame*, 156, 2201-2212, (2009).

55.　　Kato S., Fujimori T., Dowling A. P., Kobayashi H., 'Effect of heat release distribution on combustion oscillation', *Proceedings of the Combustion Institute*, 30, 1799-1806, (2005).

56.　　Khanna, V. K., 'A Study of the Dynamics of Laminar and Turbulent Fully and Partially Premixed Flames', *Ph.D. thesis, Virginia Polytechnic Institute and State University,* (2001).

57.　　Khanna V. K., Vandsburger U., Saunders W. R., Baumann W. T., 'Dynamic Analysis of Swirl Stabilized Turbulent Gaseous Flames', *ASME Turbo Expo*, GT2002-30061, 285-297, (2002).

58.　　Kim K. T., Santavicca D. A., 'Linear stability analysis of acoustically driven pressure oscillations in a lean premixed gas turbine combustor', *Journal of Mechanical Science and Technology*, Vol 23, 3436-3447, (2009).

59.　　Kinsler L.E., Frey A.R., Coppens A.B., Sanders J.V., 'Fundamentals of Acoustics', *John Wiley & Sons*, Fourth edition, (2000).

60.　　Kosztin B., 'Linear and non-linear modeling of thermo-acoustic instabilities in a laboratory burner', *Ph.D. thesis, Keele Univeristy*, (2013).

61.   Kreyszig E., 'Advanced engineering mathematics', Tenth edition, *John Wiley Publications*, (2011).

62.   Lamarque N., Poinsot T., 'Boundary conditions for acoustic eigenmode computations in gas turbine combustion chambers', *AIAA Journal,* 46(9), 2282–2292, (2008).

63.   Langhorne, P. J., Dowling A. P., Hooper N., 'Practical active control system for combustion oscillations', *Journal of Propulsion and Power*, Vol. 6, No. 3, 324-333, (1990).

64.   Le Conte J., *Philosophy Magazine*, page HP. 235, (1958).

65.   Lee, R.C., Wimmer, D.B., 'Exhaust emission abatement by fuel variations to produce lean combustion', *SAE Trans.*, 77, 175, (1968).

66.   Levine H., Schwinger J., 'On the radiation of sound from an unflanged circular pipe', *Phys. Rev.*, **73**, 383–406, (1948).

67.   Lieuwen T., Zinn B. T., 'The role of equivalence ratio oscillations in driving combustion instabilities in low NOx gas turbines', *Twenty-Seventh International Symposium on Combustion, The Combustion Institute,* 1809-1816, (1998).

68.   Lieuwen T., Torres H., Johnson C., Zinn B. T., 'A mechanism of combustion instability in lean premixed gas turbine combustors', *Journal of Engineering for Gas Turbine and Power*, Vol (123), 182-189, (2001).

69.   Lieuwen T., 'Modeling premixed combustion–acoustic wave interactions: A review', *Journal of Propulsion and Power*, Vol 19(5), (2003).

70.   Lieuwen T., Yang V., 'Combustion instabilities in gas turbine engines: Operational experience, fundamental mechanisms, and modeling', *AIAA Progress in Astronautics and Aeronautics*, Vol. 210, (2005).

71.   Lieuwen T., McDonell V., Petersen E., Santavicca D., 'Fuel flexibility influences on premixed combustor blowout, flashback, auto-ignition and stability', *Journal of Engineering for Gas Turbine and Power*, Vol (130), 011506 (1-10), (2008).

72.   Lores M. E., 'A theoretical study of non-linear longitudinal combustion instability in liquid propellant rocket engines', *Ph.D. thesis, Georgia Institute of Technology*, (1972).

73.   Marble, F., Candel, S., 'Acoustic disturbances from gas nonuniformities convected through a nozzle', *Journal of Sound and Vibration*, Vol. 55, 225–243, (1977).

74.   Mariappan S., 'Theoretical and experimental investigation of the non-normal nature of thermo-acoustic interactions', *Ph.D. thesis, IIT Madras*, (2012).

75.   Markstein G. H., 'Instability phenomena in combustion waves', *In Proc. of the 1952 4th International Symposium on Combustion*, 44-59, Cambridge, Mass, (1952).

76.   Markstein G. H., 'Nonsteady Flame Propagation', *The Macmillann Company, Pergamon Press Ltd.*, Oxford, England, (1964).

77.   Martin C., Benoit L., Nicoud F., Poinsot T., 'Analysis of acoustic energy and modes in a turbulent swirled combustor', *Centre for Turbulence Research, Proceedings of the summer program*, (2004).

78.   Matveev K., 'Thermo-acoustic instabilities in the Rijke tube: Experiments and modeling', *Ph.D. thesis, California Institute of Technology*, California, (2003).

79.   McAllister S., Chen J., Fernandez P., Carlos A., 'Fundamentals of Combustion Processes', *Springer Science*, (2011)

80.   Mcmanus, K., Poinsot, T., Candel, S. M., 'A review of active control of combustion instabilities', *Progress in Energy and Combustion Science*, 19, 1–29, (1993).

81.   Merk H. J., 'An analysis of unstable combustion of premixed gases', *Sixth International Symposium on Combustion, The Combustion Institute,* (1957).

82.   Mukherjee, N., Heckl, M. A., 'Analysis of modal frequencies of tubes with internal constriction using the blockage integral', *International Congress on Sound and Vibration 21*, Beijing, 13-17th July, (2014).

83.   Mukherjee N., Heckl M. A., Bigongiari A., Vishnu R., Pawar S., Sujith R. I., 'Nonlinear dynamics of a laminar V flame in a combustor', *International Congress on Sound and Vibration 22*, Florence, 12-16th July, (2015).

84.   Mukherjee, N. K., Heckl, M. A., Shrira, V., 'Analysis of flame intrinsic modes in a resonator', *International Congress on Sound and Vibration 23*, Athens, 10-14th July, (2016).

85.   Munjal M. L., 'Acoustics of ducts and mufflers', *John Wiley*, New York, (1987).

86.   Munjal M. L., Mukherjee N. K., '1-D Acoustical analysis of axial-inlet, transverse-outlet air cleaners of rectangular and circular cross-section', *International Journal of Acoustics and Vibrations*, 15(2), 55-64, (2010).

87.   Munjal M. L., Mukherjee N. K., 'Plane wave analysis of rectangular axial-inlet, axial-outlet and transverse-inlet, transverse-outlet air cleaners', *Noise Control Engineering Journal*, 59(5), 447-463, (2011).

88.   Munt R. M., 'The interaction of sound with a subsonic jet issuing from a semi-infinite cylindrical pipe', *Journal of Fluid Mechanics*, Vol. 83, 609-640, (1977).

89.   Munt R. M., 'Acoustic transmission properties of a jet pipe with subsonic jet flow: 1. The cold jet reflection coefficient', *Journal of Sound Vibration*, 142, 413–436, (1990).

90.   Nagaraja S., Kedia K., Sujith R. I., 'Characterizing energy growth during combustion instabilities: Singularvalues or eigenvalues?', *Proceedings of the Combustion Institute*, 32, 2933–2940, (2009).

91.   Nayfeh A. H., 'Introduction to perturbation techniques', *John Wiley and Sons*, (1993).

92.   Nayfeh A. H., Mook D. T., 'Nonlinear oscillations', *John Wiley and Sons*, (1995).

93.   Noiray N., 'Linear and non-linear analysis of combustion instabilities, application to multipoint injection systems and control strategies', *Ph.D. thesis, Ecole Centrale Paris*, (2007).

94.   Noiray N., Durox D., Schuller T., Candel S., 'A unified framework for nonlinear combustion instability analysis based on the flame describing function', *Journal of Fluid Mechanics*, 615, 139-167, (2008).

95.   Noiray N., Durox D., Schuller T., Candel S., 'Dynamic phase converter for passive control of combustion instabilities', *Combustion and Flame*, 32, 3163-3170, (2009a).

96.   Noiray N., Durox D., Schuller T., Candel S., 'A method of estimating the noise level of unstable combustion based on the flame describing function', *International Journal of Aeroacoustics*, Vol 8, number 1 and 2, 157-176, (2009b).

97.   Noiray N., Schuermans B., 'Theoretical and experimental investigations on damper performance for suppression of thermo-acoustic oscillations', *Journal of Sound and Vibration*, 331, 2753–2763, (2012).

98.   Paschereit C. O., Gutmark E., Weisenstein W., 'Control of combustion driven oscillations by equivalence ratio modulations', *ASME Turbo Expo*, Indianapolis, Indiana, June 7-10, (1999a).

99.   Paschereit C. O., Gutmark E., Weisenstein W., 'Coherent structures in swirling flows and their role in acoustic combustion control', *Physics of Fluids*, 9, 2667-2678, (1999b).

100.   Peerlings L. B. W., Manohar, Kornilov V. N., Goey P., 'Flame ion generation rate as a measure of flame thermo-acoustic response', *Combustion and Flame*, 160, 2490-2496, (2013).

101.   Poinsot T., Chatelier C. L., Candel S. M., Esposito E., 'Experimental determination of the reflection coefficient of a premixed flame in a duct', *Journal of Sound and Vibration*, 107(2), 265-278, (1986).

102.   Poinsot, T. J., Trouv´e, A., Veynante, D., Candel, S., Esposito, E., 'Vortex-driven acoustically coupled combustion instabilities', *Journal of Fluid Mechanics*, 177, 265-292, (1987).

103.   Poinsot T. J., Veynante D., Bourienne F., Candel S., Esposito E., Surget J., 'Initiation and suppression of combustion instabilities by active control', *Twenty-Second International Symposium on Combustion, The Combustion Institute*, 1363-1370, (1988).

104.   Poinsot T. J., Veynante D. P., 'Combustion', *John Wiley and Sons, Ltd*, (2004).

105.   Poinsot T., Selle L., 'LES and acoustic analysis of combustion instabilities in gas turbines', www.cerfacs.fr/~cfdbib/repository/TR_CFD_05_19.pdf

106.   Poinsot T., Veynante D., 'Theoretical and numerical combustion', *R. T. Edwards*, third edition, (2011).

107. Polifke W., Kopitz J., Serbanovic A., 'Impact of the fuel time lag distribution in elliptical premix nozzles on combustion stability', *American Institute of Aeronautics and Astronautics*, 2104, (2001).

108. Polifke W., Lawn C., 'On the low-frequency limit of flame transfer functions', *Combustion and Flame*, 151, 437–451, (2007).

109. Polifke, W., 'Thermo-acoustic system modeling and stability analysis: Conventional approaches', *Workshop on advanced instability methods*, IIT Madras, Jan 27-29, (2009).

110. Powell E. A., 'Nonlinear combustion instability in liquid propellant rocket engines', *Ph.D. thesis, Georgia Institute of Technology*, (1970).

111. Putnam A. A., 'Combustion driven oscillations in industry', *American Elsevier Publishers*, New York, (1971).

112. Rabinovich M. I., Trubetskov D. I., 'Oscillations and waves: in linear and nonlinear systems', *Kluwer Academic Publishers*, (1989).

113. Rämmal H., Lavrentjev J., 'Sound reflection at an open end of a circular duct exhausting hot gas', *Noise Control Eng. Journal*, 56 (2), March-April (2008).

114. Rayleigh Lord, 'The explanation of certain acoustical phenomena', *Royal Institution Proceedings*, 8: 536-542, (1878).

115. Richards G. A., Janus M., 'Control of flame oscillations with equivalence ratio modulation', *Journal of propulsion and power*, Vol 15, No 2, Mar-Apr (1999).

116. Richards G. A., Straub D. L., Robey E. H., 'Passive control of combustion dynamics in stationary gas turbines', *Journal of Propulsion and Power*, 19, (5), 795–810, (2003).

117. Rijke P. L., 'On the vibration of the air in a tube open at both ends', *Philosophical Magazine*, Vol. 17, 419-422, (1859).

118.	Roux A., Reichtadt S., Bertier N., Gicquel L. Y. M., Vuillot F., Poinsot T., 'Comparison of numerical methods and combustion models for LES of a ramjet configuration', *Second Colloque INCA*, 23-24 Oct (2008).

119.	Sattelmayer, T., 'Influence of the combustor aerodynamics on combustion instabilities from equivalence ratio fluctuations', *International Gas Turbine and Aero Engine Congress & Exposition*, ASME 2000-GT-82, Munich, (2000).

120.	Saunders W. R., Nord L., Fannin C. A., Huang X., Baumann W. T., Vandsburger U., Khanna V., Haber L., Eisenhower B., Liljenberg S., 'Diagnostics and modeling of acoustic signatures in a tube combustor', *International Congress on Sound and Vibration 6*, Copenhagen, Denmark, July (1999).

121.	Schadow, K. C., Gutmark, E., 'Combustion instability related to vortex shedding in dump combustors and their passive control', *Progress of Energy and Combustion Science*, Vol. 8, 117-132, (1992).

122.	Schluter J.H., 'Large-eddy simulations of combustion instability suppression by static turbulence control', *Center for Turbulent Research, annual research brief*, (2001).

123.	Schuermans B., Polifke W., Paschereit C. O., 'Modelling transfer matrices of premixed flames and comparison with experimental results', *ASME, International Gas Turbine and Aeroengine Congress and Exhibition*, (1999).

124.	Schuermans B., 'Modelling and control of thermo-acoustic instabilities', *Ph.D. thesis, Ecole Polytechnique Federale De Lausanne*, Switzerland, (2003).

125.	Schuermans B., Bellucci V., Guethe F., Meili F., Flohr P., Paschereit C. O., 'A detailed analysis of thermo-acoustic interaction mechanisms in a turbulent premixed flame', *Proceedings of ASME Turbo Expo*, GT2004-53831, Vienna, (2004).

126.   Schuller T., Ducruix S., Durox D., Candel S., 'Modelling tools for the prediction of premixed flame transfer functions', *Proceedings of the Combustion Institute*, Vol 29, 107–113, (2002).

127.   Schuller T., Durox D., Candel S., 'A unified model for the prediction of laminar flame transfer functions: comparisons between conical and V-flame dynamics', *Combustion and Flame*, 134, 21-34, (2003).

128.   Schuller T., Tran N., Noiray N., Durox D., Ducruix S., Candel S., 'The role of nonlinear acoustic boundary conditions in combustion/acoustic coupled instabilities', *Proceedings of ASME turbo expo*, GT2009-59390, (2009).

129.   Schuller T., Durox D., Palies P., Candel S., 'Acoustic decoupling of longitudinal modes in generic combustion systems', *Combustion and Flame*, 159, 1921-1931, (2012).

130.   Silva C., Duran I., Nicoud F., Moreau S., 'Boundary conditions for the computation of thermo-acoustic modes in combustion chambers', *AIAA Journal, American Institute of Aeronautics and Astronautics*, 52 (6), 1180-1193, (2014).

131.   Silva C. F., Emmert T., Jaensch S., Polifke W., 'Numerical study on intrinsic thermo-acoustic instability of a laminar premixed flame', *Combustion and Flame*, 162, 3370-3378, (2015).

132.   Sirignano W. A., 'Nonlinear combustion instability: Liquid propellant rockets', www.signup4.net/Upload/ANAD10A/BRIA30E/Tuesday%20Sirignano.pdf

133.   Soloviev A., Lukas R., 'The near-surface layer of the ocean: Structure, dynamics and applications', *Atmospheric and Oceanographic Sciences Library*, Vol 48, Springer, (2014).

134.   Sonntag R. E., Borgnakke C., Wylen G. J. V., 'Fundamentals of thermodynamics', Wiley, (2002).

135.   Straub, D. L., Richards, G. A., 'Effect of fuel nozzle configuration on premix combustion dynamics', *International Gas Turbine and Aeroengine Congress & Exposition*, ASME 98- GT-492, Stockholm, Sweden, (1998).

136.   Strogatz S. H., 'Non-linear dynamics and chaos', *Perseus books publishing*, (1994).

137.   Sujith R. I., Waldherr G. A., Zinn B. T., 'An exact solution for one-dimensional acoustic fields in ducts with an axial temperature gradient', *Journal of Sound and Vibration*, 184 (3), 389-402, (1995).

138.   Sujith R. I., 'Exact solutions for modeling sound propagation through a combustion zone', *Journal of Acoustical Society of America*, 110(4), October, (2001).

139.   Truffin K., Varoquie B., Poinsot T., 'Measurements of transfer functions using Large Eddy Simulations: Theoretical framework and first tests', www.cerfacs.fr/~cfdbib/repository/TR_CFD_03_61.pdf (2002)

140.   Truffin K., Poinsot T., 'Comparison and extension of methods for acoustic identification of burners', *Combustion and Flame*, 142, 388–400, (2005).

141.   Varoquie B., Legier J.P., Lacas F., Veynante D., Poinsot T., 'Experimental analysis and Large Eddy Simulation to determine the response of non-premixed flames submitted to acoustic forcing', *Proceedings of the Combustion Institute*, 29, 1965-1970, (2002).

142.   Vishnu R., 'Experimental study on combustion dynamics of a ducted lean premixed V-flame', *Master of Science thesis, IIT Madras*, October, (2013).

143.   Vishnu R., Sujith R.I., Aghalayam Preeti, 'Role of flame dynamics on the bifurcation characteristics of a ducted V-flame', *Combustion Science and Technology*, 187, issue 6, 894-905, (2015).

144. Warren G.B., 'Fuel-economy gains from heated lean air-fuel mixtures in motorcar operation', 65-WA/APC-2. Mech. Eng. 88(4), 84, (1966).

145. Watson K. M., West B. J., Cohen B. I., 'Coupling of surface and internal gravity waves: A mode coupling model', *Journal of Fluid Mechanics*, 77, 185–208, (1976).

146. Watson K. M., 'The coupling of surface and internal gravity waves: revisited', *Journal of Physical Oceanography*, 20, 1233–1248, (1990).

147. Zhao D., Morgans A. S., 'Tuned passive control of combustion instabilities using multiple Helmholtz resonators', *Journal of Sound and Vibration*, Vol 320, Issue 4-5, 744-757, (2009).

148. Zhao D., 'Transient growth of flow disturbances in triggering a Rijke tube combustion instability', *Combustion and Flame*, 159, 2126-2137, (2012).

149. Zinn B. T., Powell E. A., 'Nonlinear combustion instability in liquid-propellant rocket engines', *Thirteenth International Symposium on Combustion, The Combustion Institute*, 491-503, (1971).